University of Stavanger

**Faculty of Science and Technology**

# MASTER'S THESIS

| | |
|---|---|
| Study program/ Specialization:<br><br>*Master in Petroleum Engineering*<br>*Reservoir technology* | Spring semester, 2011.<br><br>Open access |
| Author:<br>*Andreas Davidsen* | ……<br>(Author's signature) |
| Faculty supervisor: *Merete Vadla Madland*<br><br>External supervisor(s):<br>*Merete Vadla Madland*<br>Reidar Inge Korsnes | |
| Title of thesis:<br><br>A Mechanical Study of the effect of Sulphate | |
| Credits (ECTS): *30* | |
| Key words:<br>- Water weakening of chalk<br>- *High Porosity chalk*<br>- *Triaxial compressive*<br>- *Brazilian tests*<br>- *Creep tests*<br>- *Effect of sulphate*<br>- *Temperature effects*<br>- *Failure envelope*<br>- Aging | Pages: ……<br><br>+ Appendix: ……<br><br>Stavanger, ……..<br>Date/year |

# A mechanical study of the effect of sulphate

**Master Thesis by**

**Andreas Davidsen**

**Spring 2011**


University of Stavanger

Faculty of Science and Technology

Department of Petroleum Engineering

## Acknowledgements

With this I would like to express my gratitude to the members of the chalk group at the University of Stavanger, fellow students, family and to my dear girlfriend Therese Dyrø for the help and motivation I have received during the work with this thesis.

First of all I would like give a special thank to associate professor Merete Vadla Madland and Dr.Philos Reidar Inge Korsnes for once again including me in their research group at the University of Stavanger. Merete and Reidar have helped me with both technical and theoretical questions and given me exceptional follow-up throughout the last six months. They have truly been a source of great help and motivation.

I would also like to thank senior engineer Kim André Vorland for the technical support I have received at the chalk lab.

I would also like thank to Kim André Øvstebø for the great collaboration throughout the work with this thesis. His eye for details has been a great source of help during the writing phase of this thesis. I would also like to thank Dagny Hamsø, Harald Frette Littlehamar and Johann Helleren for helping me keep up the motivation during long days at the school and the lab.

Finally I would like give a special thank to my family and to my dear girlfriend for inspiring talks during times with low motivation and frustration. Without our their help the fulfilment of thesis would have been difficult.

*Andreas Davidsen. Stavanger 2011*

## Abstract

In this study the presence of sulphate in seawater was examined from a mechanical point of view. As test material an outcrop chalk from the Hallembaye area in Belgium called Liegé was used. This is a high porosity outcrop chalk with an average porosity of approximately 40 %. To study the effect sulphate has on chalks mechanical strength synthetic seawater (SSW) and synthetic seawater without sulphate (SSW-($SO_4^{2-}$)) was used as saturation and flooding fluids. Two different test temperatures (ambient temperature and 130 °C) was used to study if reduction in mechanical strength caused by the presence of sulphate in the brine would be dependent on temperature.

Hydrostatic, deviatoric (with varying degree of radial support) and Brazilian tests were conducted such that an estimate of the failure envelopes for the different test parameters (temperature and flooding fluid) could be obtained. By comparing such failure envelopes for one can study how the resistance against shear failure and pore collapse is affected by the presence sulphate and temperature. In total three creep tests at 130 °C were included to study how the resistance against hydrostatic compression were affected by the presence of sulphate in the flooding fluid.

On the basis of the results obtained from the different triaxial tests it was shown that chalk cores tested at 130 °C were weaker against both shear failure and pore collapse in the presence of sulphate. The largest overall reduction in mechanical strength was observed for stress situations where pore collapse was the dominant failure mechanism (deviatoric tests performed with a high degree of radial support). The yield points and Young's modeli for tests performed without any presence of sulphate in the flooding fluid were a factor 1.3 higher than for the tests performed with sulphate present flooding fluid. A reduction in mechanical strength due to the presence of sulphate was not observed for tests performed at ambient temperature. In fact a somewhat higher resistance against shear failure was observed when sulphate was present in the brine. It was also shown that the weakening caused by sulphate was dependant on the test temperature, while tests performed in the absence of sulphate appeared to be unaffected by temperature. The yield points and Youngs modeli for tests performed at ambient temperature in the presence of sulphate were a factor 1.5 higher than for the tests performed at 130 °C.

Results obtained from the creep tests at 130 °C showed that the axial strain experienced was to a large extent dependant on the sulphate in the flooding fluid. The axial creep strain experienced during synthetic seawater flooding (SSW) was shown to be a factor 1.62 higher compared to the axial creep strain experienced during flooding of synthetic seawater without sulphate (SSW-($SO_4^{2-}$)). It was also shown that introduction of sulphate in the flooding fluid induced a significant increase in compaction. Removing sulphate from the flooding fluid was shown to have the opposite effect were a reduction in deformation rate was observed. Chemical analysis performed on effluent samples collected during creep showed a large reduction in magnesium concentration which was shown to most likely be a result of precipitation of magnesium bearing minerals inside the core. A reduction in sulphate concentration was also observed and which was shown to be dependent on the composition of the prior flooding fluids.

# 1 Contents

# 2 Introduction

Chalk is a very exciting high porosity sedimentary rock that can be found in the southern parts of the Norwegian Continental Shelf (NCS). It is a pure sedimentary rock that mainly consists of calcium carbonate ($CaCO_3$). The high preserved porosity of chalk implies that a large volume of oil may be present in such reservoirs which make them of great importance on a local scale. But in fact as much as 61 % of the worlds known hydrocarbon reserves are located in carbonate reservoirs (*Roehl and Choquette, 1985*). On the Norwegian Continental Shelf (NCS) the two most important chalk fields are Ekofisk and Valhall.

During the primary production of the Ekofisk field oil production was a result of oil expansion, solution gas drive, reservoir compaction and limited natural gas injection *(Gauer et al., 2002).* In 1987 seawater injection was started which was designed as a production enhancement mechanism. Voidage balance was achieved in 1994 leading to a stabilization of the reservoir pressure, and in the following year's the reservoir pressure started to increase (*Doornhof et al., 2006*). An increase in reservoir pressure should in theory reduce the compaction due to reduction in effective stress, but despite a pressure increase high subsidence rates were observed at the Ekofisk field. During the reservoir pressure increase following the voidage balance in 1994 subsidence rates of 40 cm/yr was observed until 1998 when the rate sharply declined and stabilized at a rate of 10 cm/yr *(Gauer et al., 2002)*. This persistent compaction rate even after re-pressurization has been shown to be a result of the seawater flooding and is referred to as water weakening of chalk.

Since the water weakening effect was observed in the 1980's a vast amount research has been conducted in an effort to understand the mechanism behind this water weakening effect experienced on chalk. In the early phases it was believed that the mechanical strength of chalk was dependant on two parameters namely the silica content and the porosity *(Da Silva et al., 1985)*. But from flooding experiments performed on chalk it was shown that the mechanical properties was in fact dependant on the flooding fluid. Mechanical tests performed on water saturated chalk were considerably weaker compared to oil saturated and dry chalk *(Risnes, 2001; Delage et al., 1996).* These results pointed in the direction that there might be some physical processes behind the water weakening effect experienced during seawater flooding.

One such physical process that was believed to be the driving mechanisms behind water weakening was capillary forces. Capillary forces are physical forces working between fluids of different composition at the grain surface. It was believed that there were strong capillary forces working between water as a wetting phase, and oil/gas as a non wetting phase. This theory was disproved from flooding experiments on chalk with different water and glycol mixtures (*Risnes et al., 2003; Risnes et al., 2005*). Glycol is fully miscible with water; hence there will be no capillary forces working between these two fluids. Similar mechanical strength was observed for such tests indicating that capillary forces could not be the main driving mechanism behind water weakening of chalk.

*Rinses and Flaageng (1999)* concluded that when considering water effects on chalk focus should be on the properties of the chalk surface. The scope of chalk research was changed to also include physico-chemical effects like repulsive forces from different dipole layers, van der Waals forces and electric surface charges which are all processes related to the surface properties of chalk. Further research concluded that these processes were not strong enough to cause the significant water weakening observed.

In the resent years the water weakening effect of chalk has been linked to chemical reaction between chalk and the injected fluid. *Korsnes et al. (2006)* proposed that the weakening effect observed when chalk was flooded with seawater at high temperatures could be a result of ion substitution between calcium ($Ca^{2+}$) and magnesium ($Mg^{2+}$) on the chalks surface in the presence of sulphate ($SO_4^{2-}$). But from flooding experiments performed with pure magnesium chloride brines ($MgCl_2$) large chemical weakening was observed in the absence of sulphate in the flooding fluid (*Madland et al. (2009a). Madland et al. (2011)* showed by calculations that the amount of magnesium ($Mg^{2+}$) lost during flooding experiments could not be a result of ion substitution alone and the enhanced weakening experienced was described as a result of precipitation of magnesium bearing minerals inside the chalk.

*Hiorth et al. (2008)* showed that for a situation where chalk is flooded with seawater (SSW) at high temperature several minerals may be supersaturated which can precipitate as solid minerals. Precipitation of supersaturated minerals may result in enhanced dissolution of calcium carbonate ($CaCO_3$) which again may affect the mechanical strength of chalk. But due to the complexity of the seawater (SSW) more than one process affecting the mechanical strength can take place at the same time. The presence of sulphate ($SO_4^{2-}$) in the flooding fluid has been shown to have quite a significant effect on chalks mechanical strength *(Heggheim et al., (2004); Megawati et al., (2011)). Heggheim et al. (2004*) showed that the enhanced weakening observed during flooding experiments with high sulphate concentrations were a result of precipitation of anhydrite inside the chalk core. From flooding experiments with pure sodium sulphate brines ($Na_2SO_4$) brines *Megawati et al. (2011)* showed that sulphate may adsorbed on the chalk surface. The chemical weakening observed was described by *Megawati et al. (2011)* as a result of a total disjoining pressure acting at the intergranular contacts. As shown above there are several processes taking place when chalk is flooded with seawater which may contribute to the reduction in mechanical strength. All the different mechanisms and the effect of these are not fully understood, but from performing thorough studies on the effect of the different ions present in seawater one can gradually build up a model which includes the different processes affecting the mechanical strength.

The scope of this thesis was to study the effect of sulphate from a mechanical point of view by using synthetic seawater with and without sulphate as saturation and flooding fluids. Tests were conducted at two different temperatures (ambient temperature and 130$^{o}$C) to also study if any weakening caused by the presence of sulphate would be temperature dependant. Hydrostatic, deviatoric (with varying degree of radial support) and Brazilian tests were performed such that an estimate of the failure envelope at the two different test temperatures could be obtained.The basis for comparison was provided by a parallel master thesis by Øvstebø (2011) where similar tests saturated and flooded with synthetic seawater without sulphate ($SO_4^{2-}$) were performed. To fully study the effect of sulphate and temperature the results provided by Øvstebø (2011) will also be included in this thesis. Creep tests will also be conducted to study how the creep behaviour is affected by the presence of sulphate. By performing chemical analysis on effluent samples collected during creep tests the chemical reactions taking place between chalk and the flooding fluid can also be studied.

# 3 Theory

## 3.1 Chalk

Chalk is a sedimentary rock that belongs to the carbonate family, which are recognized by their high content of calcium carbonate ($CaCO_3$). Carbonates are consists mainly of calcium carbonate ($CaCO_3$) and dolomite ($CaMg(CO_3)_2$), and can be divided into two sub-groups; limestone and dolomite on the basis of the mineral composition. Usually carbonates are found naturally as sediments or reefs in tropic and marine environments as a result of biological, chemical and detrial processes *(Ahr, 2008).* Unlike sandstone carbonates does not owe its mineral composition to weathered parent rocks, and the structure is not a result of sediment transport from rivers and streams (detrial). Carbonates consist mainly of skeletal remains from microorganisms, but other sources of calcium carbonate ($CaCO_3$) may be from calcified algae or foraminifers.

Chalk is a type of limestone with a very high content of calcium carbonate (>90%), which is a very important reservoir rock on the Norwegian Continental Shelf (NCS). It has been estimated that as was much as 61% of the world's hydrocarbon reserves are located in carbonate reservoirs (*Roehl and Choquette, 1985*) which shows that these reservoirs are of great importance both on a local and global scale.

The North Sea chalk is mainly build up from skeletal debris from a calcareous nanofossil called coccoliths, with a minor contribution from foraminifers, calcispheres and macrofossil fragments *(Hjuler and Fabricius, 2009).* In *Fig.3.1* an intact coccolith-ring is seen when examining a chalk sample in a scanning electron microscope (SEM). Chalk will mainly consist of fragmented parts of such coccoliths and not intact rings.


*Fig.3.1: An intact coccolith-ring found in a Stevens Klint outcrop chalk sample from the Sigerslev quarry in Denmark. The main building blocks for this chalk are fragmented parts of coccolith rings (from Læknes (2009)).*

Chalk has a very open and complex structure as can be seen in *Fig.3.1*. Porosities in North Sea chalk sediments range between 30-50%, which is significantly higher compared to what may be expected in chalk sediments 2000-3000 m below sea level (*Hancock, 1985*). High porosity is preserved due to early invasion of oil and overpressure which is a result of the low permeability found in chalk (*Fabrizius 2003).*

The main building block is small fragmented parts of coccolith-rings which has a typical dimension of 1 μm. A consequence of this is that the pore throats will be narrow making it difficult for fluid to flow. Typical permeability found in North Sea chalk is between 1-5 mD which are very low compared to other reservoir rocks.

## 3.2 Rock mechanics

The science of rock mechanics was defined by the Committee on Rock Mechanics of the Geological Society of America in the following way; *" Rock mechanics is the theoretical and applied science of the mechanical behaviour of rock; it is that branch of mechanics concerned with the response of rock to the force field of its physical environment" (Judd, 1964).*
General theory about rock mechanic is taken from *Fjær et al. (2008).*

### 3.2.1 Porosity

Porosity is defined as the volume occupied by the pore fluid relative to the total volume or bulk volume. By estimating both the pore volume and the bulk volume for a given test sample, the porosity can be determined by the use of the following equation:

$$\Phi = \frac{V_p}{V_b} \tag{3.1}$$

where:
$\Phi$ = porosity [%]
$V_p$ = the volume occupied by the pore fluid [ml]
$V_b$ = the total volume of the sample [ml]

Bulk volume for cylindrical test samples are found by first measuring the length and diameter of the core. With the length and diameter as input data the following equation can then be used to calculate the bulk volume of the samples.

$$V_b = \frac{1}{4}\pi L D^2 \tag{3.2}$$

where:
L= length of the sample [mm]
D = diameter of the test sample [mm]

The pore volume can be determined by measuring the dry and saturated weight of each test-sample. To be able to measure the dry weight of a tests sample all the fluid occupying the pore space must be removed. This is done by placing the test-cores in a heating chamber at 130 °C for approximately 24 hours. The next step will be to measure the saturated weight of the test-cores. This is done by saturating the cores with distilled water, which has a density equal to 1 g/ml at ambient temperature. By using the following relation the pore volume will be given as the difference in saturated and dry weight divided by the density (ρ) of the pore fluid.

$$V_p = \frac{m_{sat} - m_{dry}}{\rho_{distilled\ water}} \tag{3.3}$$

The porosity is usually presented as percent; hence Eq.3.1 has to be multiplied with 100%.

### 3.2.2 Stress

Stress (σ) is defined as a force working through a given area or surface:

$$\sigma = \frac{F}{A} \tag{3.4}$$

where:
F= total force [N]
A= area where the force is acting [$m^2$]

In this thesis stress will be defined by using SI units where stress is expressed in Pa or MPa ($10^6$ Pa). In rock mechanics compressive stresses are defined as positive, while in solid mechanics compressive stresses are defined as negative. The reason for using this definition is because rocks usually are exposed to compressive stresses in the earth's crust and; hence these stress conditions are of most interest. Tensile stresses will, following the definition above, be denoted as negative stresses.

The orientation of the area (surface) where the force is acting is of great importance when considering stress. On a tilted arbitrary surface (A`) stress will be decomposed into two components, one component working normal to the surface and one component working parallel to the surface like illustrated in *Fig.3.2*.

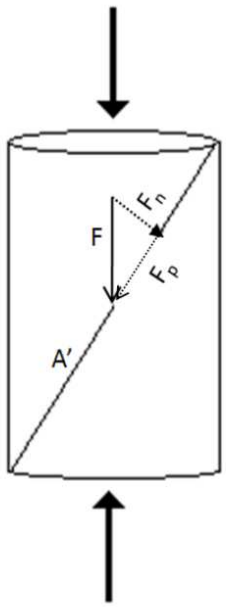


*Fig.3.2: A cylindrical test sample exposed to a uniaxial compressive stress, which can be decomposed into a normal ($F_n$) and parallel ($F_p$) stress component for a diagonal surface A'.*

By the use of the normal stress component ($F_n$) the normal stress will be defined by the following equation:

$$\sigma = \frac{F_n}{A'} \tag{3.5}$$

From the component working perpendicular to the surface ($F_p$) the shear stress will be defined by:

$$\tau = \frac{F_p}{A'} \tag{3.6}$$

*Eq. 3.5* and *Eq. 3.6* will only be valid in homogenous solid materials. Sedimentary rocks like chalk will be inhomogeneous on a microscopic scale due to its porosity. The response when put under stress will be dependent on the contribution from the non- solid part of the material. In solid homogeneous materials the whole stress is carried by the solid part of the material, whereas in porous materials the total stress will have a contribution from both the forces transmitted through the solid framework and the force transmitted through the fluid in the pore space. *Fig.3.3* illustrates how these different forces act in a porous material such as chalk.

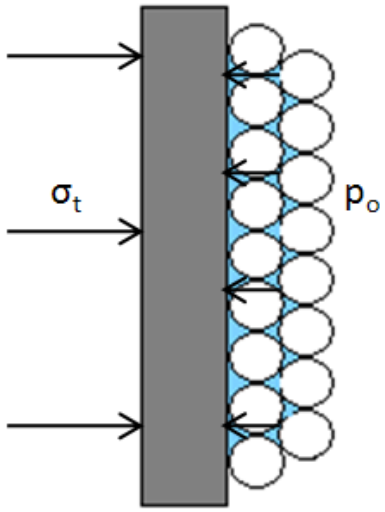


*Fig.3.3: Illustration of a porous material under stress where the grains only experiences the effective stress. The effective stress will be the difference between the total stress ($\sigma_t$) and the pore pressure ($p_o$) working in the opposite direction. As the pore pressure increased the effective stress is reduced.*

As indicated in *Fig.3.3* the total stress experienced by the grain to grain contacts will be a function of the pore pressure, and following the total deformation will be dependent on the effective stress and not the total stress. For porous materials where there exist grain to grain contacts effective stress will be defined by the following equation:

$$\sigma_p' = \sigma_p - \alpha p_f \tag{3.7}$$

where:
$\sigma_p'$ = effective stress
$\sigma_p$ = total stress
$\alpha$ = Biot coefficient (also called the effective stress coefficient)
$p_f$ = pore pressure.

The Biot coefficient will be defined by the following equation.

$$\alpha = 1 - \frac{K_{fr}}{K_s} \tag{3.8}$$

Where:
$K_{fr}$ = bulk modulus of the framework
$K_s$ = bulk modulus of the solid

The inverse of the bulk modulus will give the compressibility (C) for the framework and solid respectively.

$$C_{fr} = \frac{1}{K_{fr}} \tag{3.9}$$

$$C_s = \frac{1}{K_s} \tag{3.10}$$

The compressibility of the solid ($C_s$) will be significantly higher compared to the compressibility of the framework ($C_{fr}$), hence the Biot coefficient will be restricted to the region $0 \leq \alpha \geq 1$ where a value close to 1 represent a unconsolidated rock.

Chalk, as used in this present study, is often characterised as a weak rock where a Biot coefficient close to 1 has been used to calculate the effective stress. It has been has shown that the effective stress coefficient for high porosity chalk depends on the applied stress and the pore fluid, a result of this is that the effective stress coefficient can't be regarded as a constant (*Omdal et al., 2009).* But for a pure strength perspective it has been shown that the conventional effective stress concept ($\alpha$ =1) will be applicable for mechanical tests on high porosity chalk *(Madland et al., 2009b),* and will therefore be used consistently throughout this thesis.

### 3.2.3 Strain

When a test sample is exposed to an external stress it will start to deform. This deformation leads to movement of the particles inside the sample. In *Fig.3.4* a sample has been exposed to an external stress and the position of an arbitrary point inside the sample has shifted.


*Fig.3.4: A test sample has deformed due to an applied stress, and the position of an arbitrary point inside the sample has shifted*

By introducing a displacement vector the movement of the point can be monitored. The shift in x direction is denoted *u*, the shift in y direction is denoted *v* and finally the shift in z direction is denoted *w*.

$$\vec{u} = (u, v, w) \tag{3.11}$$

By using the same sign convention as for stresses, the new position of the point will be given by the following equations:

$$x' = x - u \tag{3.12}$$

$$y' = y - v \tag{3.13}$$

$$z' = z - w \tag{3.14}$$

In a situation where the displacements *u*, *v* and *w* have a constant value, the displacement is said to be a translation of a rigid body. But if the relative position of all the particles inside a sample changes, and position of a given point can't be returned to its initial position the sample has been strained. In *Fig.3.5* a test sample has been put under stress and experienced strain.

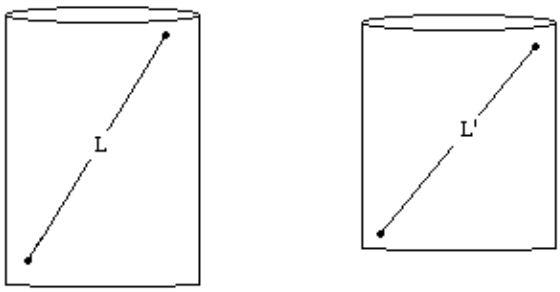


*Fig.3.5: A test sample has deformed and the relative position of every particle inside the sample has shifted.*

By measuring the change in length the subsequent strain, in percent, can be calculated by the use of the following equation.

$$\varepsilon = \frac{L-L'}{L} \cdot 100\% \tag{3.15}$$

where:
ε = strain [%]
L= initial length [m]
L'= length after deformation [m]

To be consistent with the definition of stress a reduction in length, due to compaction, will be denoted as positive. An elongation of a test sample will thus result in negative strain.

Rock mechanical tests are usually performed on three dimensional samples which will deform in all three directions. It is therefore convenient to express the deformation with respect to a change in volume or volumetric strain. The volumetric strain can be found by adding up the strains experienced in the different orthogonal directions.

$$\varepsilon_v = \frac{\Delta V}{V} = \varepsilon_x + \varepsilon_y + \varepsilon_z \tag{3.16}$$

where:
$\varepsilon_v$ = volumetric strain
$\varepsilon_x$ = strain in x-direction
$\varepsilon_y$ = strain in y-direction
$\varepsilon_z$ = strain in z-direction

In this present study cylindrical test samples where used in all performed tests. Due to the samples symmetrical shape there will be deformation both in axial and radial direction like indicated in *Fig.3.6*.

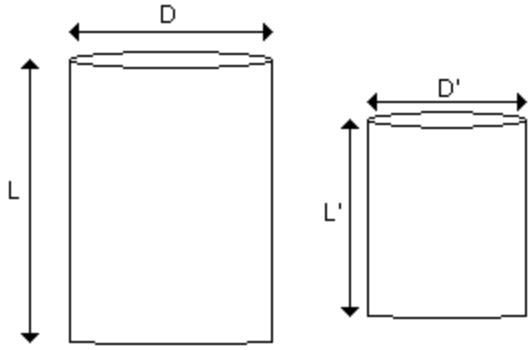


*Fig.3.6: When a cylindrical test sample is strained there will be a relative change n both radial and axial direction. The volumetric strain is found by adding up strain from axial and radial direction.*

Due to the external stress the core has been exposed to, there has been a reduction in both length and diameter. The axial strain is determined by use of *Eq.3.14*, while the radial strain is determined by the following equation.

$$\varepsilon_r = \frac{D-D'}{D} \tag{3.17}$$

The equation for volumetric strain will simplify due to the radial symmetry.

$$\varepsilon_v = \varepsilon_a + 2\varepsilon_r \tag{3.18}$$

where:
$\varepsilon_a$ = strain in axial direction
$\varepsilon_r$ = strain in radial direction.

For a pure isotropic material the deformation will be equal in all direction during isotropic loading; hence the volumetric strain can be determined form the axial deformation directly.

$$\varepsilon_v = 3 \cdot \varepsilon_x \tag{3.19}$$

In a situation where no radial measurements are available, the volumetric strain is calculated by using *Eq.3.18.* By using this simplification one has to assume that the material behaves as an isotropic material. The assumption of isotropy is not completely correct for a sedimentary material like chalk because there can be large variation in physical properties within one test sample. Such variations in physical properties may lead to different stress responses for different areas in one sample. This in-homogeneity is also known as anisotropy.

### 3.2.4 Stress Strain relations

When test samples are put under stress, they usually start to deform. A method of treating data obtained from such tests is to plot the applied stress versus the resulting strain like illustrated in *Fig.3.7*. In this case the core is first loaded isotropic, also called a hydrostatic phase, to a predetermined stress level. Following this phase the test sample is loaded in axial direction, keeping the confining pressure constant, until the sample yields. This period of increasing axial load is known as a deviatoric phase. By studying the stress strain response from such tests valuable information about the materials mechanical strength can be obtained.

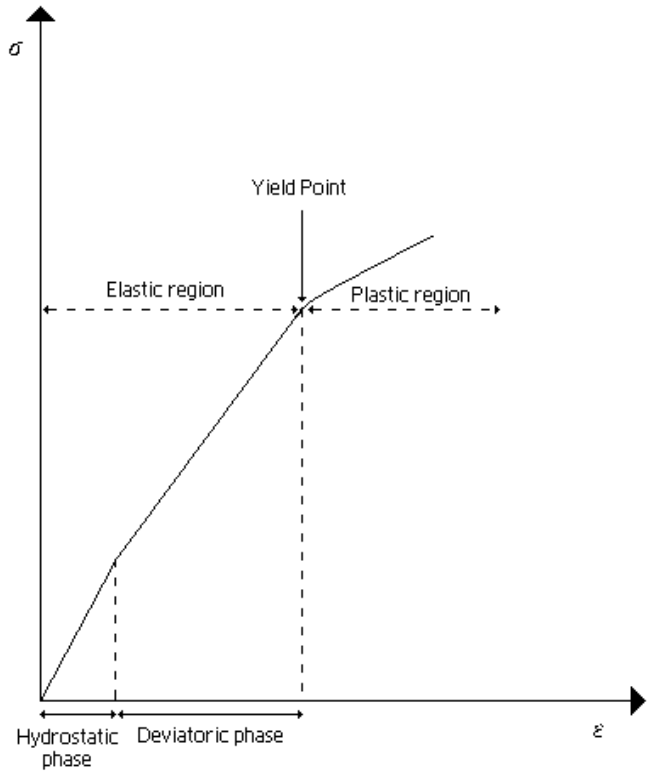


*Fig.3.7: Illustration of a standard triaxial test where the test sample first is loaded hydrostatically to a predetermined stress level. Following this phase axial load is applied until the sample yields. The yield point will be a critical limit between the elastic and plastic region.*

In *Fig.3.7* a hydrostatic phase and a deviatoric are illustrated. The elastic region is the area where there is a linear relationship between applied stress and the resulting strain. In the following plastic region there will be a non linear relationship between stress and strain. This transition point between the elastic and plastic region is known as the materials yield point. The yield point is determined as the point where the stress strain curve starts to deviate from a linear trend

In the elastic region the stress and strain relationship can be expressed by using the theory of linear elasticity. This theory will be valid as long as there is a linear relationship between stress and strain. For the non linear stress strain relationship experienced in the plastic phase the mathematical treatment will be much more complicated compared to linear elastic behaviour.

In this present study the theory of linear elasticity is used to describe the behaviour before the test sample yields or goes into failure. The axial strain experienced due to external stress can be found by using Hooks law:

$$\varepsilon_x = \frac{1}{E}\sigma_x \tag{3.20}$$

where:
$\varepsilon_x$ = axial strain
E =Young's modulus [GPa]
$\sigma_x$ = axial stress [MPa]

Young's modulus is an elastic parameter that indicates the materials strength against uniaxial compression.

By rearranging *Eq.3.19* the Young's modulus can be expressed with respect to axial stress and strain respectively.

$$E = \frac{\sigma_x}{\varepsilon_x} \tag{3.21}$$

The Young's modulus is found from the linear slope of the stress strain curve in the deviatoric phase and the result is expressed in GPa.

Another important strength parameter is the materials bulk modulus (K). The Bulk modulus is defined as a materials resistance against hydrostatic compression. Unlike the Young's modulus the bulk modulus is determined from the data obtained in the hydrostatic phase. Since the sample is loaded uniformly in all directions the strain experienced in all directions have to be included. For a hydrostatic test, or phase, the bulk modulus will be defined by the following equation.

$$K = \frac{\sigma_h}{\varepsilon_v} \tag{3.22}$$

where;
$\sigma_h$ =hydrostatic stress [MPa]
$\varepsilon_v$ =volumetric strain [MPa]

The bulk modulus is determined in the region where there is a linear relationship between stress and strain and is usually expressed in GPa. In an axial stress strain plot the bulk modulus can be found as 1/3 of the slope during hydrostatic loading before yield is initiated.

### 3.2.5 Failure mechanisms

In mechanical tests core samples are put under increasing stress and at a sufficient stress level the test sample will eventually start to yield. In *Fig.3.7* the materials yield point was defined as critical limit between the elastic and plastic phase. At this point the test material will have experienced a permanent deformation, and will not return to its initial shape during pressure depletion. A consequence of going into failure is a reduction in the materials ability to carry external stress; hence the material will deform more for a given stress increase compared to pre-yield conditions.
The process of failure in its self is a very complex process which is not fully understood. Methods used to describe mechanical failure are based on mathematical descriptions of the

observed behaviour during increasing stress. When discussing a materials yield strength, or failure strength, it is therefore important to specify the different test parameters used. This because the type of failure will be dependent on the type of test performed.

The most important tests, when estimating the materials strength, are uniaxial and triaxial tests. In *Fig.3.9* the main difference between these two types of tests are illustrated.

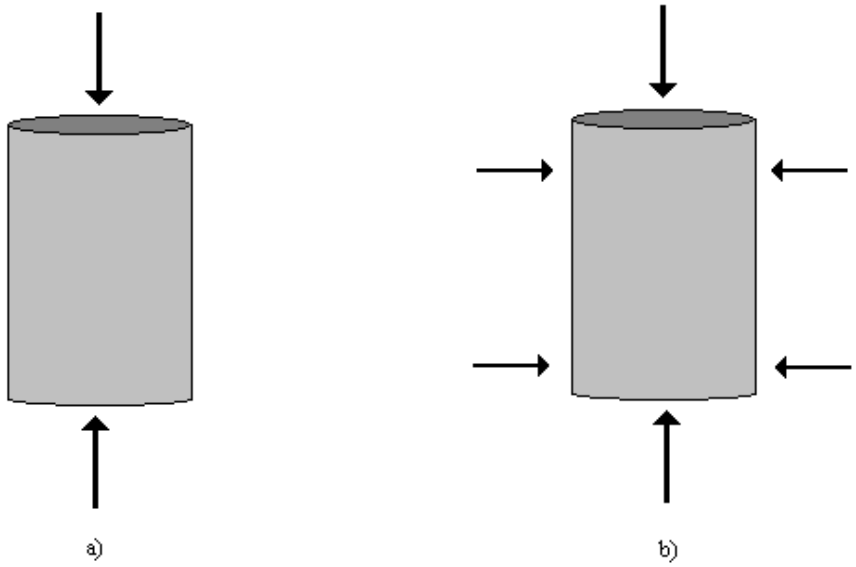


*Fig.3.9: Illustration of the main difference between a) a uniaxial tests and b) a triaxial test. Load is only applied in axial direction for the uniaxial tests while for the triaxial tests there will be a stress component in all of the orthogonal directions*

For the uniaxial test presented in *Fig.3.9 a)* the stress will be applied in only axial direction and there will not be any stress component in radial direction. Such a test is also called an unconfined compression test. *Fig.3.9 b)* illustrates a triaxial where there will be stress components in all orthogonal directions. The main difference between a uniaxial and triaxial test will be the degree of radial support, i.e. the failure mechanism will depend on the degree of radial support the test is performed with. In the tests performed in this study the effective radial stress component will be given by the difference between confining pressure and pore pressure for the given test.

**Shear failure**

In uniaxial compression and triaxial tests with low or no radial support the test samples will fail in shear failure. This type of failure is a result of high shear stresses, which is the difference between effective axial and radial stress. Shear failure in general is a result of high shear stresses along a failure plane inside the sample resulting in relative movement of the bodies opposite to the failure plane like illustrated in *Fig.3.10*.

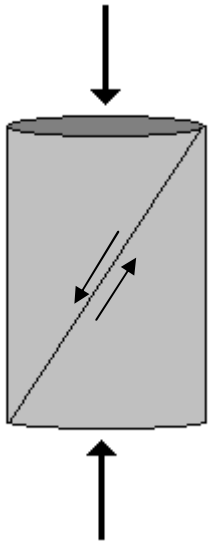

*Fig.3.10: Core sample loaded axially with no radial support until shear failure occurs a long a failure plane.*

These two bodies separated by the failure plane in *Fig.3.10* will move in a frictional process. The frictional force acting against this relative movement will be dependent on the total force pressing these bodies together.

**Pore collapse**

In hydrostatic and triaxial tests with a large degree of radial support, a second failure mechanism called pore collapse can be observed *(Blanton 1981).* This type of failure is mostly seen in high porosity materials such as chalk. Chalk has a relative open structure were the grains can be forced into the pore space in situations where no excessive shear stresses are present such as during hydrostatic loading. On a microscopic level pore collapse quite similar to shear failure, because pore collapse is actually a result of excessive shear stresses between grains resulting in shear failure at the grain to grain contacts. This motion can be a result of breakage of frictional bonds between the grains, or due to sliding on frictional contacts inside the material (*Risnes 2000).*

### 3.2.6 Mohr Coulomb criteria

In *Section 3.2.5* it was shown that the frictional forces working against shear failure was dependent on a normal stress component (σ´) working over the failure plane. In other words there will be a critical shear stress where shear failure is initiated. This critical shear stress will be a function of the normal stress (σ´) working over a failure plane and will be given by;

$$|\tau_{max}| = f(\sigma') \tag{3.23}$$

where:
$\tau_{max}$ =critical shear stress
σ´ =effective normal stress component working

The relation in *Eq.3.23* is also known as the Mohr's hypothesis. Shear failure like defined by Mohr's hypothesis will depend solely on the minimum and maximum principal stresses and not the intermediate principal stress. In a situation where cylindrical tests samples are used there will not be any intermediate stress component due to the radial symmetry around the circumference. In *Fig.3.11* the stress situation for a compression test on a cylindrical sample is illustrated. Here normal and shear stresses will work on an arbitrary failure plane inside the sample.

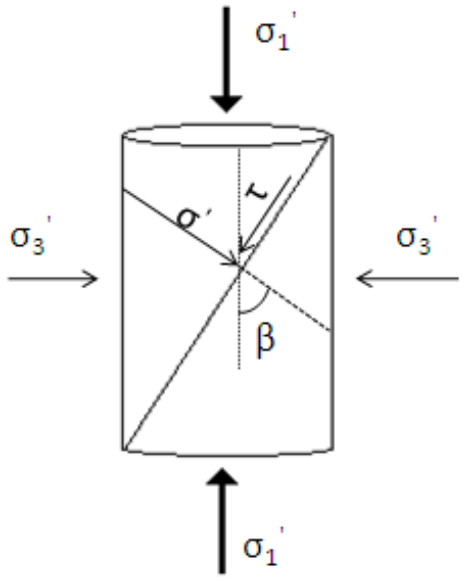


*Fig.3.11: Illustration of the different forces acting on an arbitrary failure-plane inside a cylindrical test sample during triaxial compression. There will be a normal stress component (σ´) working on the failure plane pressing the two bodies together. Parallel to the failure plane there will act a shear force (τ) which trying to initiate shear failure. The failure angle is defined as the angle between the normal (σ´) force and the largest effective stress ($\sigma_1$´).*

Where $\sigma_1$´ and $\sigma_3$´ from *Fig.3.11* will be the maximum and minimum principal stresses respectively. On the diagonal failure surface in *Fig.3.11* there will work a normal stress component (σ´) which presses the two bodies together. The shear stress component (τ) will try to separate the two bodies by initiating shear failure. The angle β between the normal stress component *(σ`)* and the largest effective stress component ($\sigma_1$´) is known as the material failure angel.

The Mohr Coulomb criterion is based on the assumption that the function given in *Eq.3.23* is a linear function with respect to the normal stress component σ`;

$$|\tau| = S_o + \mu\sigma' \tag{3.24}$$

where:
$S_o$ = the materials cohesion or inherent shear stress
μ = coefficient of internal friction,

The cohesion ($S_o$) will give information about the cohesive forces present in the test material. This force reflects the shear stress needed to initiate shear failure in a case where no normal force is present. The coefficient of internal friction (μ) is a measure of the strength against shear failure at an incipient failure surface. This parameter will be dependent on the strength of intact areas and the resistance against frictional sliding in damaged areas along the failure plane. *Savage et al. (1996)* showed that the coefficient of internal friction is in fact related to the strength against friction sliding in areas of the test sample that are damaged.

The linear line given by *Eq.3.24* is also known as the failure line. When used in a $\tau$-$\sigma'$ space this line represent a critical limit between an elastic area and a plastic area. For a stress configuration below the line given by *Eg.3.24* failure occur for any plane inside the test sample. Stress configurations outside the elastic region will result in permanent deformation. In *Fig.3.12* a Mohr circle is drawn by using the maximum ($\sigma_1'$) and minimum principle stress ($\sigma_3'$) obtained from a mechanical test. The failure line given by *Eq.3.24* is drawn such that in tangents the Mohr circle as shown in *Fig.3.12.* The angle φ of the failure line is known as the angle of internal friction or simply the friction angel while the point of intersection with the ordinate will give the materials cohesion ($S_o$).

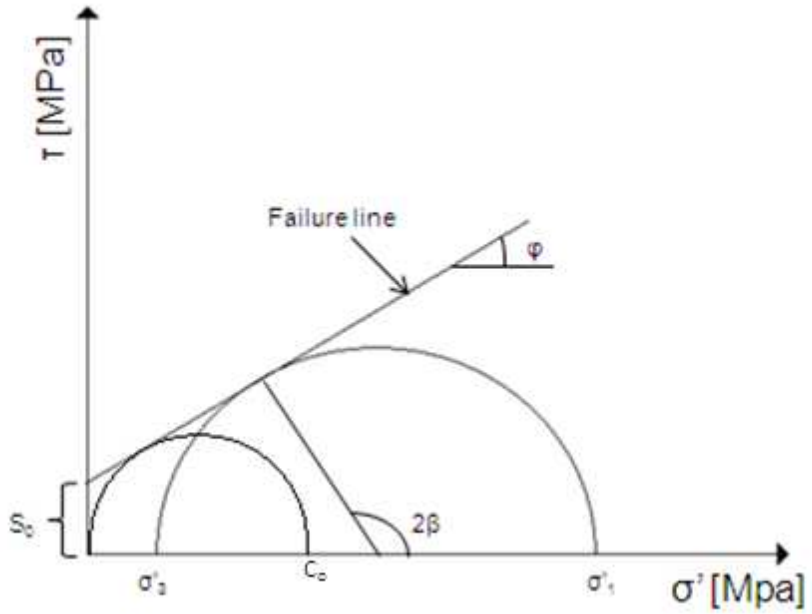


*Fig.3.12: Illustrates a Mohr circle drawn with respect to the maximum ($\sigma_1'$) and minimum ($\sigma_3'$) principle stresses with failure line drawn according to the Mohr-Coulomb criteria in Eg.3.24. From the inclination of the failure line the friction angle (φ) can be determined. The point of intersection with the ordinate will give the materials cohesion ($S_0$). The Mohr circle drawn by using the uniaxial compressive strength ($C_o$) will start in the origin and tangent the failure line.*

For the case illustrated in *Fig.3.12* the material will behave as an elastic material where no permanent strain will occur for stress configurations inside the elastic area. But for complex structure like high porosity chalk this will not be the case. Permanent strains and even creep deformation may occur inside the elastic area *(Risnes and Nygaard 2001).* Strain experienced inside the elastic area may be a result of frictional sliding between the grains, while failure as given by the yield point in Fig.3.7 will be a result of breakage of grain to grain bonds. The stress strain response will be linear inside the elastic area for tests performed on chalk; hence the theory of linear elasticity and the Mohr Coulomb criterion will be valid and can be used.

The material friction angle is related to the internal friction (μ) by the following equation:

$$tan\varphi = \mu \tag{3.25}$$

In Fig.3.12 the failure line tangents the Mohr circle at a point with coordinates (τ,σ´). This point represents the stress configuration at the point of failure. The shear stress (τ) at the failure plane as failure occurs will be given by the following equation:

$$|\tau| = \frac{1}{2}(\sigma_1' - \sigma_3')sin2\beta \tag{3.26}$$

The normal stress (σ´) at the failure plane will be given by the following equation:

$$\sigma' = \frac{1}{2}(\sigma_1' + \sigma_3') + \frac{1}{2}(\sigma_1' - \sigma_3')cos2\beta \tag{3.27}$$

The friction given by the inclination of the failure line will be related to the failure angle (β) by the following equation:

$$\beta = \frac{\pi}{4} + \frac{\varphi}{2} \tag{3.28}$$

Another strength parameter that can be determined by the use of the Mohr Coulomb criteria is the materials uniaxial compressive strength ($C_O$). The uniaxial compressive strength is the axial stress needed to initiate failure in a case where no radial support is present. In this case the minimum principle stress ($\sigma_3$´) would be equal to zero, and the maximum effective stress ($\sigma_1$´) would be the stress value where failure was initiated. The corresponding Mohr circle for this situation and how the failure line tangents this circle is shown *Fig.3.12*. Uniaxial compressive strength can also be determined by using the following equation;

$$C_o = 2S_o \frac{cos\varphi}{1-sin\varphi} = 2S_o tan\beta \tag{3.29}$$

Due to the relation between the friction angle and the failure angle showed in *E.q.3.28*, the value of the uniaxial compressive strength could be determent by using the materials cohesion and failure angle like shown in *Eg.3.29*. It must be emphasized that the expression for the uniaxial compressive strength is only valid in cases where the failure mechanism is pure shear failure; hence it will not be applicable in situations where pore collapse is the dominant failure mechanism.

If both the materials cohesion and failure angle is known the Mohr Coulomb criteria, with respect to the maximum and minimum principle stress, will be given by the following equation:

$$\sigma_1' = S_o tan\beta + \sigma_3' tan^2\beta \tag{3.30}$$

The Mohr Coulomb criterion is only valid in cases where the failure mechanism is pure shear failure. As the degree of radial support increases there will be a transition from shear failure to pore collapse as the dominant failure mechanism. When considering the failure envelope for a high porous material like chalk, it can be expressed by the use of the Mohr Coulomb with an end cap like presented in *Fig.3.13*. *Jones et al., 1989* showed that a high porous material like chalk will have a failure envelope with an end cap.

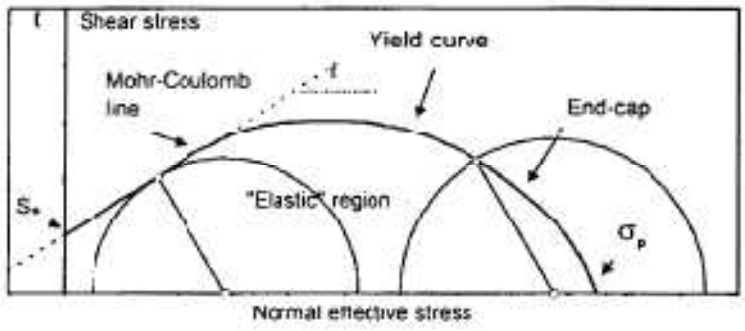


*Fig.3.13: Illustration of how the failure envelope for a high porous material with an end cap will be in the τ-σ´ plane (from Risnes, (2001)).*

The type of plot in *Fig.3.13* is not very practical when considering the end cap, because it is difficult to analyse the end cap behaviour in a Mohr plot. Mohr plots are therefore mostly used to analyse data where shear failure is the dominant failure mechanism. Another plotting technique is therefore needed to be able to analyse both shear failure and pore collapse in the same plot.

### 3.2.7 q-p' plot

When determining the mechanical properties for a given rock, several series of triaxial tests with varying degree of radial support are performed. As mentioned in *Chapter 3.2.6* it is difficult to analyse end cap data in a Mohr plot. One way to analyze such data is by plotting the obtained strength data in what is called a q-p´ plot. This plotting technique is originally from another technical discipline called soil mechanics, but it has been shown that it can also be used in the case of weakly cemented sedimentary rocks like chalk *(Jones and Leddra, 1989)*.In this type of plot the generalized effective shear stress (q) is plotted against the mean effective stress (p´) given by the following equations:

$$q = \frac{1}{\sqrt{2}}\sqrt{(\sigma_1' - \sigma_2')^2 + (\sigma_2' - \sigma_3')^2 + (\sigma_1' - \sigma_3')^2} \tag{3.31}$$

$$p' = \frac{1}{3}(\sigma_1' + \sigma_2' + \sigma_3') = \bar{\sigma}' \tag{3.32}$$

where:
$\sigma_1'$ = maximum principle stress
$\sigma_2'$ = intermediate principle stress

$\sigma_3'$ = the minimum principle stress.
For cylindrical cores tested under triaxial conditions the equations above will simplify. This because there will be an isotropic stress field over the circumference as a result of the cylindrical shape, ensuring that the intermediate and the minimum principle stresses will be similar:

$$\sigma_2' = \sigma_3' \tag{3.33}$$

The equations for the generalized shear stress and the mean effective stress will then become;

$$q = \sigma_1' - \sigma_3' \tag{3.34}$$

$$p' = \frac{1}{3}(\sigma_1' + 2\sigma_3') \tag{3.35}$$

The test cores are first loaded hydrostatically to a predetermined stress level, and then axial load is applied until failure occurs..During this phase with increasing axial load the confining pressure, or the radial stress, is kept constant. The stress path for each of the triaxial tests can be plotted in the q-p´ plane like presented in *Fig.3.14* where the endpoint will represent the stress configuration at failure. Stress paths for the different triaxial tests will all have a constant slope of 3:1. These stress paths will, if all are plotted in the same q p´ plot, make up the materials failure envelope as illustrated in *Fig.3.14*. This failure envelope can be regarded as a critical limit between the elastic and the plastic area. For an elastic material stress configurations inside the failure envelope will not cause any permanent deformation while stress configurations outside the failure envelope will cause permanent deformation as pressure is depleted.

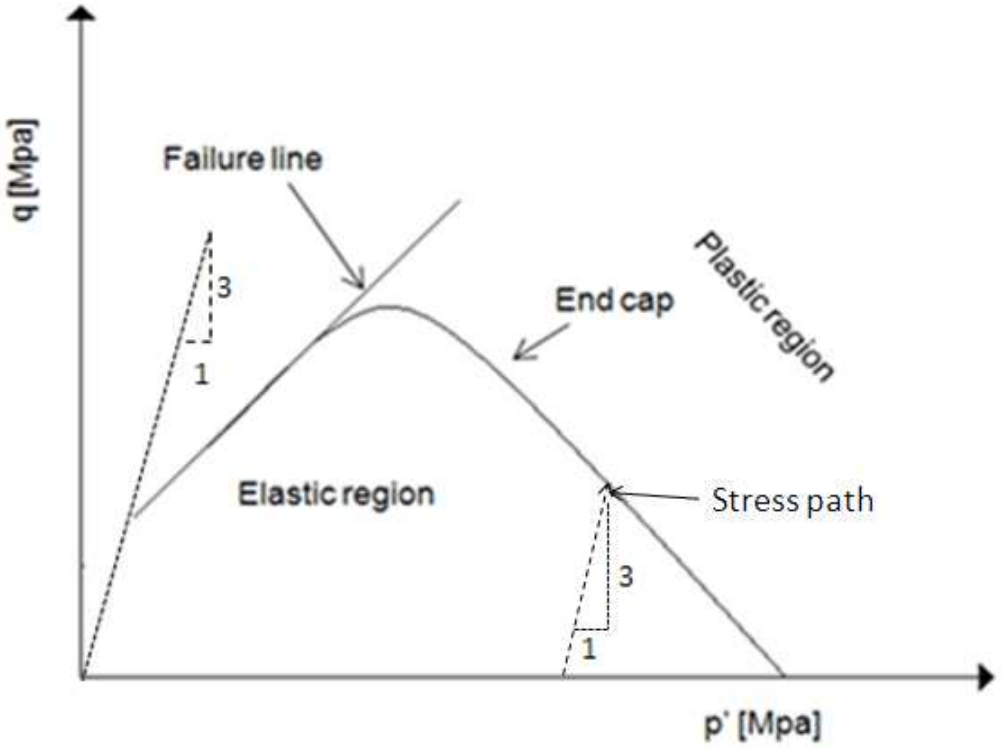


*Fig.3.14: Illustration of the failure envelope for a porous material like chalk. Shear failure will be the dominant failure mechanism at the failure line, while pore collapse will be the failure mechanism at the end cap. The failure envelope will be a critical limit between the elastic and plastic region. The failure line is limited by a line with a slope equal to 3:1.*

Tests performed with low degree of radial support will give points that fall on or close to the failure line. Here the dominant failure mechanism will be pure shear failure. As the degree of radial support increases with higher confining pressures the points will fall on what is called the end cap. In this end cap section the dominant failure mechanism will be pore collapse which is shear failure on a microscopic level like presented in *Chapter 3.2.5.*The Mohr Coulomb criteria can be translated so that is also can be used in the q-p´ plot. In the q-p´ plot the failure line will be given by the following equation:

$$q = \left(\frac{6sin\varphi}{3-sin\varphi}\right)p' + \left(\frac{6S_o cos\varphi}{3-sin\varphi}\right) \tag{3.36}$$

where:
φ = friction angel
$S_0$ = cohesion of the material

*Eg.3.36* is a linear equation that can be written in the following form:

$$q = Ap' + B \tag{3.37}$$

Where A will be the slope of the failure line:

$$A = \frac{6sin\varphi}{3-sin\varphi} \tag{3.38}$$

B will be the point of intersection with the ordinate in the q p' plot:

$$B = \frac{6S_o cos\varphi}{3-sin\varphi} \tag{3.39}$$

By rearranging *Eq.3.38* and *Eq.3.39* an estimate of the friction angle and the cohesion can be determined directly from the q p' -plot. These values can then be used in the Mohr Coulomb criterion which will give an expression for a calculated failure line that can be compared to a drawn failure line such as in *Fig.3.12*.

The failure line will be limited by a line that starts in the origin with a slope equal to 3:1 like shown in *Fig.3.14*. This limiting line is found by elimination the maximum principle stress ($\sigma_1'$) from *Eq.3.34* and *Eq. 3.35* resulting in the following equation:

$$p' = \frac{1}{3}q + \sigma_3' \tag{3.40}$$

Eq.3.40 shows why this limiting line will have a constant slope of 3:1.

By performing tensile strength tests data points closer to the ordinate can be obtained. The failure line will then no longer be limited by the line given from *Eq.3.40*, resulting in a better estimate of the point of intersection with the ordinate axis and the materials cohesion. In the following chapter such a method for measuring the materials tensile strength, and how this relates to the maximum and minimum principle stress, will be presented.

### 3.2.8 Indirect measurement of tensile strength - Brazilian tests

The triaxial apparatus used in this present study made it difficult to perform deviatoric tests resulting in data points close to the ordinate axis both in the Mohr and q-p´ plots. A result of this has been the development of different indirect methods to determine the tensile strength of the material. Such methods are called indirect because they do not create a homogeneous state of tensile stress inside the test sample, but due to the experimental setup an inhomogeneous state of stress will be created which is tensile in some regions of the sample *(Jaeger et al., 2007).* In this present study a method called a Brazilian test is used as an indirect measurement of the tensile strength of chalk.

The tests are performed by using an apparatus like the one illustrated in *Fig.3.15*. A small cylindrical test sample is placed between two loading plates. The thickness of the test sample is between the length of the radius and the diameter of the test samples used in the triaxial cell. Load is then applied in axial direction until failure is initiated as shown in *Fig.3.15*.

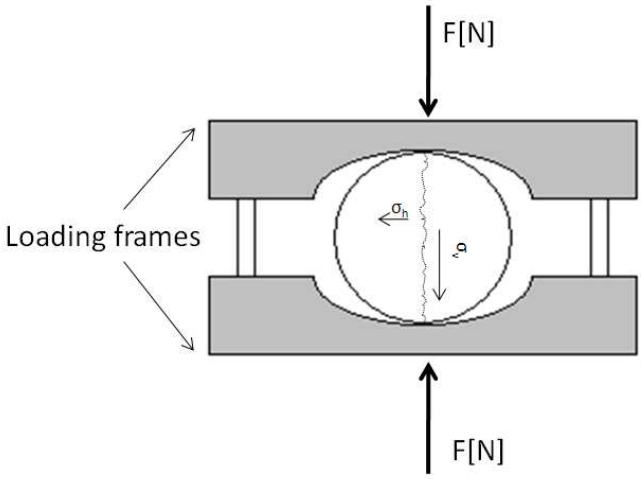


*Fig.3.15: An illustration of the Brazilian apparatus and how the different forces will act as load is increased. At failure a fracture will propagate in vertical direction as a result of the tensile stress in horizontal direction.*

By studying the stresses for a point close to the centre of the test sample the following relationship between horizontal and vertical stresses will be valid:

$$\sigma_h = -\frac{2F}{\pi DL} \tag{3.41}$$

$$\sigma_v = \frac{6F}{\pi DL} \tag{3.42}$$

where:
F = applied force [N]
L = thickness of the test-sample [m]
D = diameter [m]

The reason why the horizontal stress component in *Eg.3.41* has a negative sign in front of the expression is because this stress component will be in tension. The vertical stress component will thus be in compression. In *Fig.3.16* the stress situation for an arbitrary point close to the centre of the test sample is illustrated:

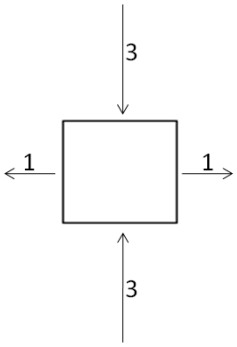


*Fig.3.16: Illustration of the stress situation for an arbitrary point close to the centre of a test sample during a Brazilian test. The relation between the compressive and tensile stress will be equal to 3:1.*

As shown in *Fig.3.16* there will be a 3 to 1 relationship between the horizontal and vertical stress components for a point close to the centre of the sample. In a Brazilian test the sample is loaded until failure is initiated and a fracture will propagate in vertical direction. This type of failure will be a result of the tensile stresses close to the centre of the sample. The tensile strength measured from a Brazilian ($T_{ob}$) test will be found from the maximum force of the peak force at failure ($F_c$) by the use of the following equation.

$$T_{ob} = -\frac{2F_c}{\pi DL} \tag{3.43}$$

Where:
$F_c$ = peak force at failure

In fact the horizontal and vertical stress components in *Eq.3.41* and *Eq.3.42* will give the minimum ($\sigma_3'$) and maximum ($\sigma_1'$) principle stresses. By including the Brazilian tensile strength ($T_{ob}$) obtained from the Brazilian tests, the maximum and minimum principle stresses will be given by the following equations:

$$\sigma_1 = 3 \cdot T_{ob} \tag{3.44}$$

$$\sigma_3 = -T_{ob} \tag{3.45}$$

By using the principle stresses calculated from the equations above, the data obtained from the Brazilian tests can be included in Mohr and q-p´ plots. It has been shown that there is a close connection between the cohesion ($S_o$) and the Brazilian tensile strength ($T_{ob}$) *(Madland et al., 2002).*

$$S_o \approx \sqrt{3}T_{ob} \tag{3.46}$$

### 3.2.9 Creep Behaviour

Creep tests are defined as time-dependant deformation tests performed under constant stress. These types of tests are often used to study the mechanical behaviour of rocks post failure i.e. after the material has yielded. In *Fig. 3.17* it is illustrated how a creep tests may look like in a strain versus creep time plot. The creep phase can be divided into three different sub phases, a transient creep period, a steady state period and an accelerating creep period.

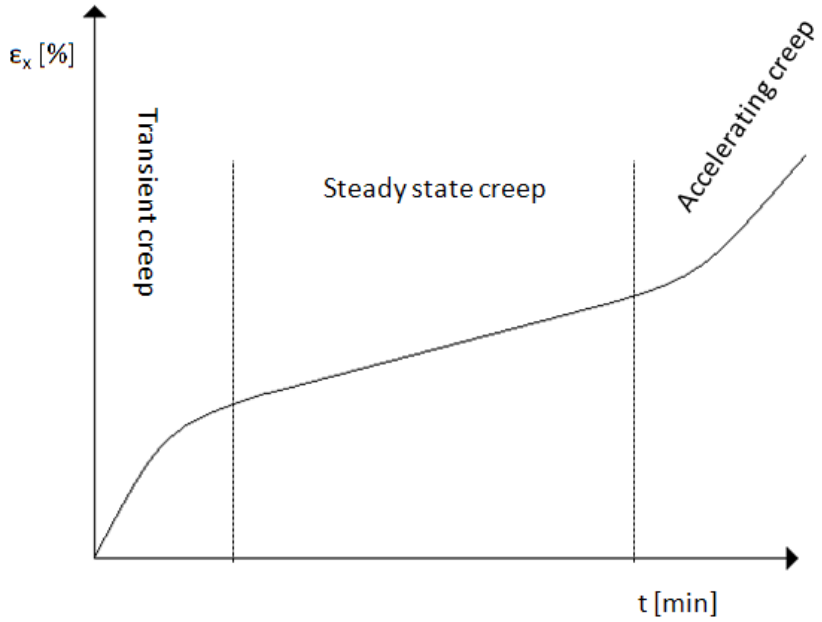


*Fig.3.17: Illustration of a creep test with a period of transient creep, a period with steady state creep and a period with accelerating creep.*

As indicated in *Fig.3.17* the deformation rate during a creep test will be time dependant. In the transient period the deformation rate will decrease with time. This period is then followed by a steady state period where the rate of deformations will be constant with respect to time. As a result of chemical weakening the deformation rate may start to increase with time such as when synthetic seawater (SSW) is introduced in a chalk core that has been flooded with distilled water (DW). As the synthetic seawater displaces the distilled water present in the pore space a significant increase in creep strain is observed which can be regarded as a period of accelerating creep.

The creep strain data obtained from creep tests can be used to estimate the creep rate. This is done by plotting the axial creep strain data versus logarithmic time as illustrated in Fig.3.18.

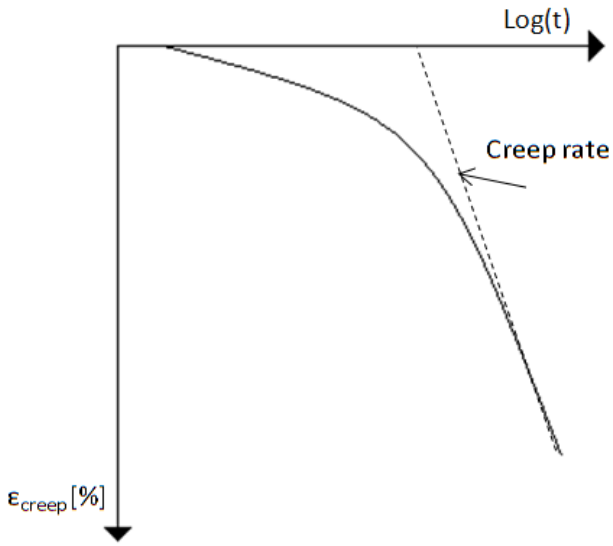


Fig.3.18: Creep deformation plotted against logarithmic time. The creep rate of the material can be determined from the tangent in the steady state period.

The creep rate is determined from the tangent drawn from a steady state period like shown in Fig.3.18. By choosing two data points (($\varepsilon_1$,$t_1$) and ($\varepsilon_1$,$t_1$)) close to each other the creep rate will be given by the following equation:

$$m = \frac{\varepsilon_2 - \varepsilon_1}{\log(t_2) - \log(t_1)} \tag{3.47}$$

where:
m= creep rate [%/decade]
ε = strain [%]
t= creep time [min]

## 3.3 Chemical aspects

### 3.3.1 Dissolution and Precipitation

The solubility of a mineral will be temperature dependant and usually increase as the temperature increases. This is not the case for calcium carbonate ($CaCO_3$); here the overall solubility will decrease as temperature is increased. In *Fig.3.19* the solubility of calcium carbonate ($CaCO_3$) is plotted against temperature ($^oC$) for a system that has reached chemical equilibrium. As the temperature increases there is a reduction in overall solubility of calcium carbonate ($CaCO_3$) (*from Miller 1952).*

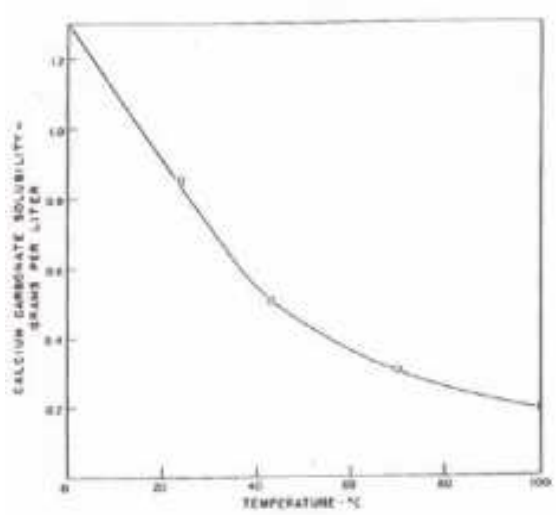


*Fig.3.19: Solubility of calcium carbonate ($CaCO_3$) as a function of temperature ($^0C$) at a $CO_2$ pressure equal to 0.987 atm (from Miller, (1952)).*

A reduction in the overall solubility for an equilibrium solution may lead to re-precipitation of $CaCO_3$ as a solid material. In fact for complex brines like synthetic seawater (SSW) precipitation of several supersaturated minerals may increase the dissolution of calcium carbonate ($CaCO_3$) *(Hiorth et al., 2008)*. One way to determine if a mineral is supersaturated in a solution is by studying the ratio between the ionic product (Q) and the equilibrium constant (K):

$$\frac{Q}{K} \tag{3.48}$$

If the ratio from *Eq.3.48* is larger than one for a given mineral, the mineral will be supersaturated in the solution and may precipitate as a solid mineral. Calculations performed for seawater injection in chalk at 130 °C show that several minerals will be supersaturated which may precipitate as solid minerals *(Hiorth et al., 2008*). The results for the calculations performed on seawater and Ekofisk formation brine (EF) flooding are shown in Fig.3.20 (from *Hiorth et al. (2008*)).

| Mineral | $Log_{10}$ Q/K | |
|---|---|---|
| | Seawater | EF |
| Dolomite $CaMg(CO_3)_2$ | 2.16 | 0.7 |
| Dolomite(ordered) $CaMg(CO_3)_2$ | 2.17 | 0.7 |
| Dolomite(disord.) $CaMg(CO_3)_2$ | 1.18 | -0.29 |
| Huntite $CaMg_3(CO_3)_4$ | 1.98 | -2.42 |
| Brucite $Mg(OH)_2$ | 1.37 | -0.1 |
| Magnesite $MgCO_3$ | 1 | -0.46 |
| Anhydrite $CaSO_4$ | 0.22 | - |
| Calcite $CaCO_3$ | 0 | 0 |

Fig.3.20: Table over minerals that may be supersaturated when chalk is flooded with seawater and Ekofisk formation brine (EF) at 130 °C *(from Hiorth et al., 2008*).

As seen from the table in *Fig.3.20* several of the minerals that may precipitate contains calcium, which will reduce the overall concentration of calcium ($Ca^{2+)}$ present in the solution. In an effort to reach equilibrium more calcium carbonate ($CaCO_3$) must be dissolved from the core material. It is reasonable to assume that this increased dissolution of calcium carbonate ($CaCO_3$) will take place at the intergranular contacts which will be in a higher state of stress *(Hiorth et al., 2008*.). This increased dissolution of calcium carbonate ($CaCO_3$) may again lead to an increased weakening of the material.

Increased solubility of calcium carbonate ($CaCO_3$) during seawater flooding has been linked to the removal of one of the common ions, $Ca^{2+}$ and $CO_3^{2-}$, in the solution due to precipitation. *Heggheim et al. (2004)* showed that the presence of sulphate in the flooding fluid at high temperatures may lead to precipitation of anhydrite ($CaSO_4$). This removes calcium ($Ca^{2+}$), which is a common ion from the solution, which increases the overall dissolution of chalk. It has been shown that this precipitation process is temperature dependant and related to the solubility of anhydrite ($CaSO_4$) (*Heggheim et al., 2004).* As temperature is increased the solubility of anhydrite is reduced hence a lower concentration dissolved anhydrite can be present in the solution. As anhydrite ($CaSO_4$) precipitates calcium ($Ca^{2+}$) is removed from the solution increasing the dissolution of calcium carbonate in an effort to reach chemical equilibrium.

### 3.3.2 Surface processes

Dissolution and precipitation is not the only processes that may affect the mechanical strength of chalk. Other mechanisms, which are related to surface processes, may also have an effect on the strength. In the following sections some of these processes will be briefly introduced.

**Ion substitution**

One process that has been proposed as a possible weakening mechanism for chalk is an ion substitution process between magnesium ($Mg^{2+}$) and calcium ($Ca^{2+}$). From experimental tests at high temperatures (130 °C), where outcrop chalk was flooded with seawater, it was shown that magnesium from the flooding fluid could substitute calcium in a one to one relationship on the chalk surface creating dolomite ($MgCO_3$) *(Korsnes et al., 2006).*Such a substitution process would lead to structural changes on the chalk surface due to difference in ion size *($Ca^{2+} > Mg^{2+}$)* which may affect the mechanical strength. For a weak material like chalk, the mechanical strength will be related to the stability of the intergranular contacts between the chalk grains. It has been shown that for a material like chalk that these intergranular contacts are weakly cemented *(Risnes et al., 1999);* hence a reduction in mechanical strength due to ion substitution will be a result of a substitution process at the intergranular contacts *(Korsnes et al., 2006).* In *Fig.3.21* this process is illustrated for a situation where sulphate ($SO_4^{2-}$) is present in the solution *(from Korsnes et al., 2006).*

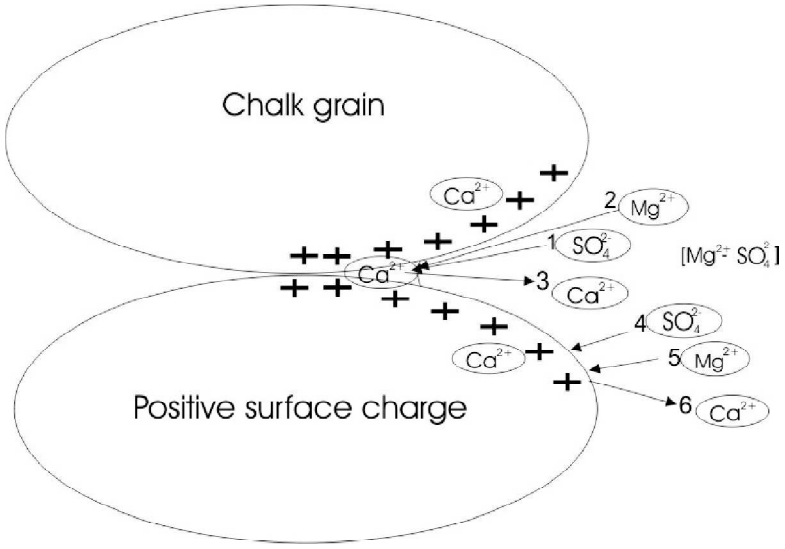


*Fig.3.21: Illustration of the ion substitution processes where calcium ($Ca^{2+}$) substitute magnesium ($Mg^{2+}$) on the chalk surface in the presence of sulphate ($SO_4^{2-}$) (from Korsnes et al., 2006).*

When chalk is flooded with seawater the surface charge of the grains will be positive (*Korsnes et al., 2006)* as indicated in *Fig. 3.21*. Divalent magnesium ions from the solution will also have positive charges which prevent ion substitution due to repulsive. Adsorption of sulphate on the chalk surface will reduce the positive surface charge which reduced the repulsive forces. This makes it possible for magnesium to substitute calcium on the chalk surface. But from chemical analysis of effluent water samples collected during creep tests a larger reduction in magnesium concentration that could be explained by pure ion substitution process was observed. These results indicate that ion substitution can not be the only processes causing a reduction in the magnesium concentration.

**Intergranular Pressure Solution (IPS)**

Another possible mechanism that can reduce the mechanical strength of chalk is intergranular pressure solution (IPS). This weakening mechanism is based on three material transfer processes occurring in series; first dissolution of material from stressed intergranular regions, diffusion or transport of material along stressed grain to grain boundaries and precipitation of solid material in the pore space *(Hellmannet al., 2002).* The slowest of these three processes will control the overall deformation.

The increase in solubility which eventually leads to dissolution of a solid material at intergranular regions with high effective stress is a process which is driven by the difference in chemical potential. *Hellmann et al. (2002)* showed that the chemical potentials for an interphase subjected to high compressive normal stress and an interphase subjected to high hydrostatic stress will be given by the following equations.

$$\mu_\sigma = F_\sigma + \sigma V_\sigma \tag{3.49}$$

$$\mu_{Pore} = F_{Pf} + P_f V_{Pf} \tag{3.50}$$

where:
μ = chemical potential
F=Helmholtz free energy
σ = normal stress at interphase
$V_\sigma$= molar volume of the normal stressed interphase
$P_f$ = hydrostatic stress (or pore fluid stress)
$V_{pf}$ = molar volume hydrostatic stressed interphase

The variation in the molar volumes of the stressed interphases are usually very small and can be neglected; hence the difference between the chemical potential for these two stressed interphases can then be written as:

$$\Delta\mu = \big(\sigma - P_f\big)V + (F_\sigma + F_{pf}) \tag{3.51}$$

This difference in chemical potential is in fact the thermodynamic driving force behind the increased dissolution of solid material in the IPS model. As can be seen from *Eq.3.51* an increase in the compressive normal stress will increase the difference in chemical potential. This will again lead to an increase in the overall dissolution of material at the interphase in compression.

The structure of the interphases between grains is crucial when considering the IPS model because it will affect dissolution and diffusion (transport) of minerals. Two different models have been proposed which are the “thin film” and “islands and channels” model *(Zhang and Spiers, 2006)*. The difference between these two models is presented in *Fig.3.22* (from *Zhang and Spiers, 2006).* In the “thin film” model there is a small water film between the two grains. This thin water film is trapped between the grains and can’t be squeezed out by increased the effective normal stress *(Rutter, 1983)*. In the “channel and island” model the interphase between the grains will be naturally roughened which means that there will be solid-solid contacts or “islands” which is surrounded by a network of “channels” with fluid *(Schutjens and Spiers, 1999)*. The dissolved material will be diffused through this thin water film or the channels and out in the pore space where it will precipitate due to a reduction in chemical potential.

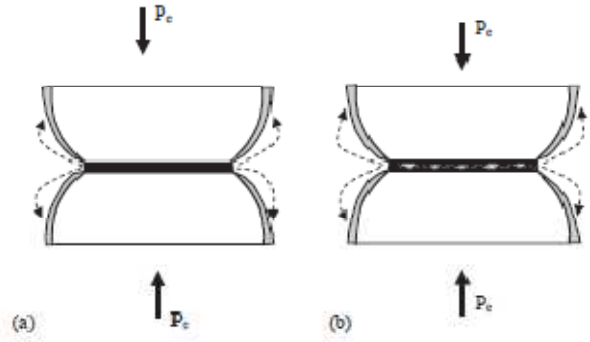


Fig.3.22: Figure illustrating the main difference between a) the "thin film model" and b) the "islands & channel model" (from *Zhang and Spiers (2006))*

Experimental studies performed on different materials exposed to the same differential stress deform with different rates. A more correct approach to the IPS mechanism will be to express the grain to grain convergence as a function of a force flux relation *(Hellmann et al., 2002).* The dissolution process at a stressed interphase can be expressed, by using a linear force-flux relation, by the following equation (*Lehner, 1995).*

$$\dot{m} \propto K[\Delta\mu] \tag{3.52}$$

where:
$\dot{m}$ = mass flux
K = rate constant
Δμ = difference in chemical potential between the intergranular surface and the pore space

A similar linear force-flux relation can also be written for precipitation of the dissolved material in the pore space by performing an appropriate reduction to the difference in chemical potential.

Diffusion of the dissolved material can also be expressed by using a force-flux relation as for the dissolution and precipitation processes. This is done on the basis on Fick's law which will lead to the following equation.

$$\dot{m} \propto \frac{C_o D^{gb} \delta}{a^2[\Delta\mu]} \tag{3.53}$$

Where:
$C_o$ = reference concentration for the solubility of the solid matter
$D^{gb}$ = grain boundary diffusivity
δ= main grain boundary thickness,
$a$ = grain radius boundary
Δμ= difference in chemical potential for the system.

In *Eq.3.52* and *Eq.3.53* there are two so called rate-determining parameters which are the rate constant (K) and the reference concentration for the solubility of material ($C_o$). These parameters vary with material and will determine the rate for the difference processes.

**Sulphate adsorption**

As indicated in *Chapter 3.3.1* sulphate ($SO_4^{2-}$) present in the flooding may precipitate as anhydrite ($CaSO_4$) which reduces the overall concentration of sulphate in the solution. But the reduction in sulphate ($SO_4^{2-}$) can also be a result of adsorption on the chalk surface. This type of process will depend on the materials surface charge. Chalk will have a positive surface charge when seawater is present due higher concentrations of divalent cations compared to anions ($[Ca^{2+}] + [Mg^{2+}] > [SO_4^{2-}]$) *(Korsnes, 2007)*. Negative charged sulphate ions can create surface complexes with calcite sites at the chalk surface, which reduces the positive charge of the surface. The concentration of negative charged sulphate ions in the vicinity of the surface will decrease exponentially as the distance from the surface increases following a Boltzmann type of distribution *(Hiort et al., 2010)*. *Hiorth et al. (2010)* showed that this adsorption process will be dependent on temperature and the fluids pH. The adsorption will be largest when the pH is between 8-11. The adsorption will also increase as the temperature increases.

In a present study by *Megawati et al. (2011)* such adsorption was detected when chalk was flooded with pure sulphate brines (Brines with varying amounts of $Na_2SO_4$). The presence of sulphate also reduced the mechanical strength of the test material which was explained as a result of a disjoining pressure working at the granular contacts. This disjoining pressure is a result of interactions between charged surfaces due to electrical double layers in the intergranular contacts.

# 4 Test material and preparation

## 4.1 Liegé chalk

The chalk used in this present study is an outcrop chalk from Lixie near Liegè in Belgium, which will be called Liegé chalk in this study. This is a pure outcrop chalk with a carbonate content measured to 95 % *(Megawati et al., 2011).* The non-carbonate content for Liegè chalk mostly consists of quartz and clinoptilolite (*Hjuler and Fabrizius, 2009*).

The age of this outcrop chalk is late Campanien which corresponds to an age of 83.5 million years. This makes this chalk formation somewhat older compared to the chalk found on the Norwegian Continental Shelf (NCS). Other main characteristics of this type of chalk are the porosity and permeability usually exhibited. Porosities usually range between 40-43 %, and permeability between 1-2 mD. This low permeability is a result of low average grain diameter (1.3 µm) (*Hjuler and Fabrizius, 2009*).

## 4.2 Core preparation

### 4.2.1 Drilling

All tests in this study were performed on cylindrical cores from the same block of outcrop Liegè chalk. The first step in preparing these cores was to drill out cylindrical samples from a rectangular piece of the chalk by the use of the machine in *Fig.4.1*.

*Fig.4.1: Machine used to drill out cylindrical samples from a block of outcrop chalk. Water was used as cooling fluid to prevent the drill bit from overheating.*

The machine has an oversized drill bit that can drill out tests samples with a diameter of approximately 40 mm and with a typical length of 180 mm. To prevent the bit from overheating during drilling water is used as a cooling fluid. A result of using water is that the samples have to be dried in a heating camber before they can be shaped. On each sample the drilling direction was marked ensuring that all tests were performed with the same orientation.

### 4.2.2 Shaping

The triaxial cells require that the test samples have a uniform diameter such that an isotropic stress field will be created around the radial circumference. A lathe like the one in *Fig.4.2* was used to uniformly shape the diameter of the individual cores.

*Fig.4.2: The lathe used to reduce the diameter to a predetermined value, to ensure a uniform diameter that will give an isotopic stress field in radial direction during testing.*

Before shaping the samples have a diameter of approximately 40 mm. The diameter of the samples is then reduced in two steps, first down to 39 mm and finally down to 37 mm. Some of the samples had a length between 160-200 mm which made it difficult to reduce the diameter of the entire sample in one run. If such large samples are mounted in the lathe slightly off centre this may cause the specimen to fail as rotation is started. Therefore such large samples are shaped in two runs. This is done by first measuring the length of the sample and marking of the centre. This point indicates where to stop when the first part of the sample has been shaped. The sample is then turned around such that the next half section can be shaped. A result of using this method is that the two half sections are shaped with a slightly different centre axis. This will not cause any problem because the samples have to be cut into the desired length before being tested. Cutting removes any effect that different centre axis may have.

### 4.2.3 Cutting

To cut the samples into desired lengths a cutting machine like the one in *Fig.4.3* was used. This machine has a diamond blade that can easily cut the soft chalk and ensure that the cut angle is exactly 90 degrees.


*Fig.4.3: Cutting machine used to cut the chalk cores into desired lengths. The cutting machine is equipped with a diamond blade which can cut trough hard materials like flint which often occur in outcrop chalk.*

When cutting one have to keep in mind that chalk is a very soft sedimentary rock which may break if two much force is applied to the blade. It is therefore recommended to cut with low applied force and with a gentle movement of the cutting arm. Flint is a very hard quartz-mineral that is often found in outcrop chalk. The diamond blade, which the cutting machine is equipped with, is hard enough to cut trough any small pieces of flint that may be in the cores without causing any damage to the cores. For cores prepared for the creep tests a small piece of the top and bottom section was cut off. These end samples will be used later as a reference to study the chemical effect of flooding brine through the cores.

### 4.2.4 Estimating porosity

The porosity of the test samples where estimated by the use of a simple weight analysis described in *Chapter 3.2.1*. The cores where first placed in a heating chamber at 130 °C for approximately 24 hours to remove any water that may be in the cores. To get a proper estimate of the bulk volume a digital vernier calliper was used to measure both diameter and length. The cores were then placed inside the vacuum vessel in *Fig.4.4*, and pressure was then reduced to approximately 2-4 Pa absolute pressure.

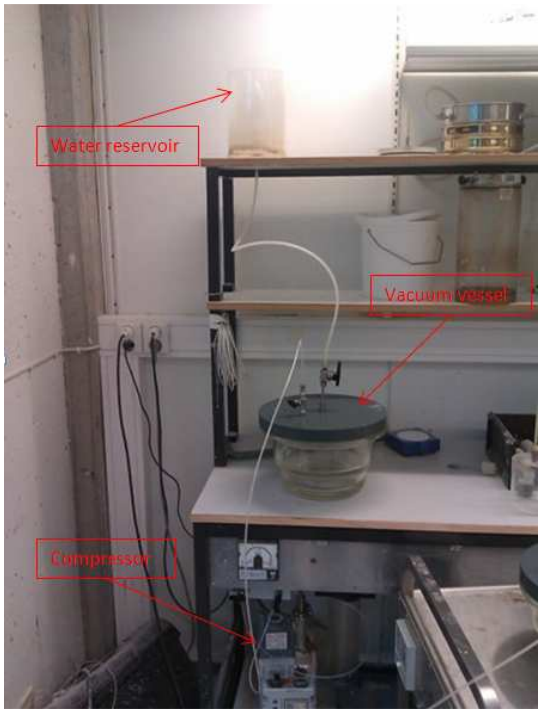


*Fig.4.4: Apparatus used to saturate the cores. Cores are placed inside the vacuum vessel and pressure is reduced to 2-4 kPa absolute pressure by the use of the compressor. Water is then poured into the water reservoir and injected into the vacuum vessel.*

After reaching the desired pressure the water reservoir is filled with distilled water, and air present in the flooding line is bleed off at the top of the vacuum vessel. Slowly water is injected into the vacuum vessel preventing any air from entering. The water will imbibe into the pore space displacing any air inside the pores. After the cores are fully submerged in the injected water, they are left to rest in the fluid for approximately 15 minutes before being remove. By measuring the saturated weight of the cores the porosity of each sample could be calculated. After measuring the saturated weight the cores where placed inside a heating chamber at 130 °C to dry. The cores could now be saturated with brine and tested.

When saturating the cores with the respective brine the same procedure as described above will be used. The only difference is that brine is filled in the water reservoir instead of distilled water.

## 4.3 Saturation fluids

To study the effect of sulphate two different brines were used; synthetic seawater (SSW) and synthetic seawater without sulphate (SSW-($SO_4^{2-}$)). Preparation of the SSW was done according to the recipe presented in *Table 4.1* while SSW-($SO_4^{2-}$) was prepared according to the recipe in *Table 4.2*. To ensure that the ionic strength of SSW-($SO_4^{2-}$) is the same as for SSW the amount of sodium chloride (NaCl) was modified as seen when comparing *Table 4.1* and *Table 4.2*.

*Table 4.1: Recipe for SSW*

| Salt | Mixing order | Mass [g/l] | Concentration [mol/l] |
|---|---|---|---|
| NaCl | 1 | 23.38 | 0.4000 |
| $Na_2SO_4$ | 5 | 3.41 | 0.0240 |
| $NaHCO_3$ | 6 | 0.17 | 0.0020 |
| KCl | 2 | 0.75 | 0.0100 |
| $MgCl_2 \cdot 6H_2O$ | 3 | 9.05 | 0.0045 |
| $CaCl_2 \cdot 2H_2O$ | 4 | 1.91 | 0.0130 |

*Table 4.2: Recipe for* SSW-($SO_4^{2-}$)

| Salt | Mixing order | Mass [g/l] | Concentration [mol/l] |
|---|---|---|---|
| NaCl | 1 | 27.58 | 0.4000 |
| $NaHCO_3$ | 5 | 0.17 | 0.0020 |
| KCl | 2 | 0.75 | 0.0100 |
| $MgCl_2 \cdot 6H_2O$ | 3 | 9.05 | 0.0045 |
| $CaCl_2 \cdot 2H_2O$ | 4 | 1.91 | 0.0130 |

As solvent nanopure distilled water was used, which has a toxicity of approximately 3 ppb. Some of the distilled water is first added in a conical flask, and then the salts are added according to the mixing orders of *Table 4.1* and *Table 4.2* for SSW and SSW-($SO_4^{2-}$) respectively. Sodium sulphate ($Na_2SO_4$) reacts strongly with water, and it is often convenient to dissolve the salt before adding it to the conical flask. This prevents the salt from clumping which increases mixing time. The conical flask is placed on a magnetic stirrer like shown in *Fig.4.5*. The magnetic stirrer has a small magnetic element which rotates inside the conical flask due to an alternating magnetic field. After all salts have been added the solution is left to mix for approximately 2 hours before being filtrated. This removes any impurities that may contaminate the solution.

*Fig.4.5: The conical flask is placed on a magnetic stirrer. A small magnetic element is placed inside the flask which will rotate due to a alternating magnetic.*

The filtrate-apparatus used consist of a filter assembly by Millipore as presented in *Fig. 4.6.* A vacuum pump creates a small under-pressure blow the filter plate which reduced the time needed to filtrate the solution. All brines prepared were filtrated with 0.65 µm filter from Millipore.

*Fig.4.6: Filtrate-apparatus from Millipore used to filtrate the brine. A 0.65 µm filter was used consistently for all the brine prepared.*

After being filtrated the pH of the brine was measured to ensure that the brine was prepared correctly with a pH similar to that of seawater.

## 4.4 Aging

All the cores tested at high temperature were first aged in a heating chamber at 130 °C for three weeks. The reason for aging the cores prior to testing was to let the brine equilibrate with the. When these cores are flooded the equilibrium between the brine and chalk is disturbed further increasing any chemical reactions between chalk and brine. First the cores were saturated with the respective brine following the same saturation procedure described in *Chapter 4.2.4* and then placed in the aging cell, also called an autoclave, presented in *Fig.4.7*. The same aging cell was used to age cores saturated with SSW and SSW-($SO_4^{2-}$).

*Fig. 4.7: The autoclave used to age cores saturated with both SSW and SSW-($SO_4^{2-}$) in a heating chamber at 130 °C for three weeks. A back pressure of 0.7 MPa was used to prevent the brine from evaporating.*

By using an aging cell as large as the autoclave in *Fig.4.7* one can age as much as 20 cores at the same time. After being saturated with the correct brine the cores where placed inside the autoclave and brine was added until all cores where fully submerged. To prevent the brine from evaporating at high temperature, a back pressure was applied through a vent on the side of the cell. The laboratory is equipped with a gas pressure of 0.7 MPa, which is beneath the design pressure of 1.5 MPa for the autoclave.

After three weeks the cores were removed from the autoclave and placed in individual core holders. The cores were then placed in a refrigerator at 4$^{o}$C until being tested. This was done to slow down any chemical reactions which again could affect the mechanical strength.

# 5 Test equipment and procedure

## 5.1 Test equipment

### 5.1.1 The Triaxial cell

All the triaxial and creep-tests were performed in a specially designed HP/HT triaxial cell frequently used to perform mechanical tests. The main building blocks of such a triaxial cell is the piston assembly, a confining chamber and a loading frame as illustrated in *Fig.5.1*. In total six steel bolts are used so that the apparatus can withstand high internal pressures inside the confining chamber.

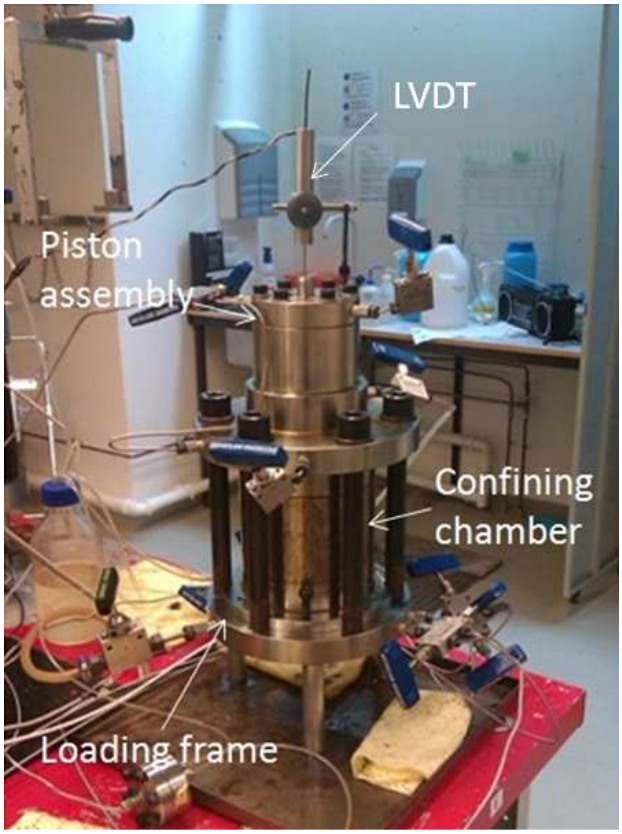


*Fig.5.1: The same triaxial cell model was used to perform both triaxial and creep-tests. The apparatus consist of three main segments; the piston assembly, the confining chamber and the loading frame. Six steel bolts are used to ensure a closed system for high pressure tests.*

This robust testing cell is designed so that it can perform high pressure tests over a long period of time. Heat resistant o-rings are used to ensure that the system remains closed during high temperature tests. Inside the piston assembly there is a piston that is placed between two small oil chambers, as indicated in *Fig.5.2*. This makes it possible to move the piston up and down by simply pumping oil into the upper or lower piston chamber. There is also a connection between the confining chamber and the piston chambers, which makes it possible to perform hydrostatic test with only a small additional axial pressure ensuring contact between the piston and the test sample. The axial movement of the piston is measured by the use of a linear voltage displacement transducer (LVDT) which is mounted on the top of the piston assembly (See *Fig.5.1*). This measures the axial movement of the piston which is related to the axial deformation of the test sample. The LVDT has an uncertainty in the measurements of ±0.05 mm.

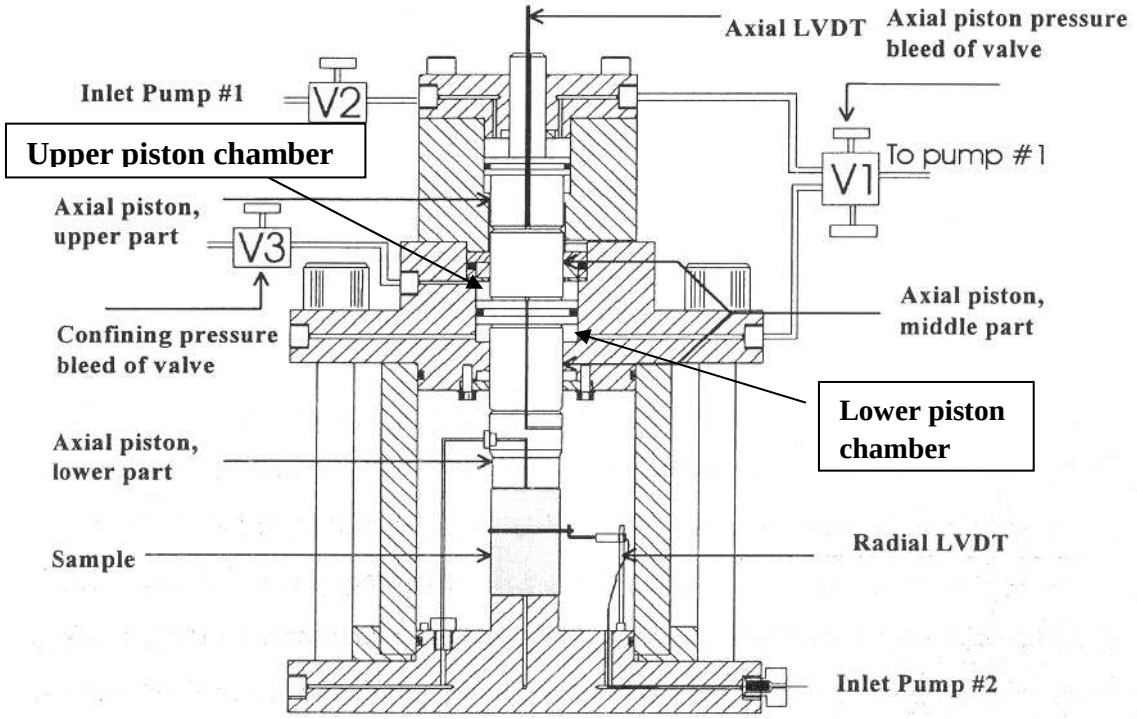


*Fig.5.2: Illustration of the triaxial cells internal component. The picture also shows how the different pumps are connected to the test cell.*

The test core is placed between two small pistons with an internal flooding system which make it possible to perform both drained and un-drained tests. To pressurize the system a synthetic oil is used in the confining chamber. This oil is pumped into the confining chamber trough the valve marked inlet pump #2 in *Fig.5.2*. The pressure in the confining chamber can be bleed off through the confining pressure bleed of valve. To prevent this confining oil from intruding into the core when pressure is increased, a plastic shrinking sleeve is used around the test sample. This ensures a closed system and fluid can be flooding through the test sample without any contamination from oil.

### 5.1.2 Pumps

There is in total three pumps connected to the triaxial apparatus as seen in *Fig.5.2*. One pump is used to regulate the confining pressure, one pump is used to pump oil into the piston chambers and one pump is connected to the flooding line. Three different experimental setups (test cells) were used in this study. Which pumps that are connected to the different cell is shown in *Table 5.1*.

*Table 5.1: Overview of what type of pumps that is connected to the different tests cells*

| Pumps | Test cell #1 | Test cell #2 | Test cell #3 |
|---|---|---|---|
| ***Piston pump*** | Quizix Qx | Teledyne ISCO 260 D | Gilson 307 |
| ***Confining pump*** | Quizix Qx | Gilson 307 | Gilson 307 |
| ***Flooding pump*** | Gilson 307 | Gilson 307 | Gilson 307 |
| ***Back pressure*** | Teledyne ISCO 260 D | Gas Pressure | Gas Pressure |

All the deviatoric tests performed in this study were tested with the set up described for *Test cell #1* in *Table 5.1*. The creep test flooded with SSW-($SO_4^{2-}$) was performed with the set up described for *Test cell #2*, while the creep tests flooded with SSW were performed with the set up for *Test cell #3*. For all the creep tests a manual regulated back pressure regulator was used while for the deviatoric tests a Teledyne ISCO 260 D pump was used to regulate the back pressure (pore pressure).

The Gilson 307 pump, shown in *Fig.5.3*, is a constant rate pump which can deliver a constant flooding rate between 10 ml/min and 0.01 ml/min. This makes the pump ideal as a flooding pump where a constant flooding rate is needed. The maximum flooding pressure for such pumps is 60 MPa.


*Fig.5.3: Picture of the Gilson 307 pump connected to the flooding line. The pump can pump with a constant flooding rate between 0.010 and 10.0 ml/min. Maximum pressure for this pump is 60 MPa.*

For *Test cell #1* a Quzix Qx pump, shown in *Fig. 5.4*, is used to control and regulate the piston and confining pressures. This pump can maintain a constant pressure by pumping and retrieving oil from the different oil chamber. The flooding rate of such pumps is between 10 ml/min and 0.001 ml/min. It is also possible to perform ramping operations on such pumps, which makes it possible to perform loading phases with equal loading rates. This ensures that the isotropic loading phases for all the deviatoric tests are performed with the same stress rate.

*Fig.5.4: Picture of the Quizix QX pumps used to regulate the confining and piston pressures. This pump can flood with a constant rate and maintain a constant pressure.*

A pump with similar specifications as the Quzix QX pump is the Teledyne ISCO 260 D syringe pump in *Fig.5.5*.

*Fig.5.5: Teledyne ISCO 260 D syringe pump used to regulate the back pressure. This type of pump can also pump with constant flooding rate and maintain a constant pressure*

The Teledyne ISCO 260 D syringe pump can pump with a constant flooding rate, retrieve oil and maintain a constant pressure much like the Quizix QX pump.

### 5.1.3 Pressure gages

Digital pressure gauges were used to measure the confining pressure, the piston pressure and the differential pressure over the test sample. All the pressure gauges were Emerson Rosemount 3051 pressure gauges like shown in *Fig.5.6*. These pressure gauges send an analogue signal to the logging card on the computer connected to the test apparatus.

*Fig.5.6: Pressure gauge used to monitor confining and piston pressures. Pressure data is sent from the gauges to the logging card on the computer.*

The analogue signals are a series of electric currents for representing the different pressure values. In fact as much as ten thousand signals are sent to the logging card each second, where the average value is presented in the software. The uncertainty of such pressure gauges is 0.0075% of the maximum pressure the gauge can measure.

### 5.1.4 Heating system

Some of the tests are performed at high temperatures, hence a heating system is needed to increase the temperature and maintain a constant temperature. This is done by using a PT 100 heating element. A heating jacket is mounted on the outside the confining chamber which is regulated by an Omron control box. Due fluctuations in the room temperature, there will also be some small fluctuations in the temperature inside the test cell. These temperature fluctuations will be approximately ± 0.02 $^{o}$C.

### 5.1.5 Software

The different tests are controlled by a computer through a software called LabVIEW. LabVIEW is a programming code used to design software's for experimental use. In this case the program is specially designed to run triaxial tests. By using the program one can easily control flow rates and change maximum pressures. It also logs all changes in pressures, axial movement of piston and the temperature. The system is designed so that any logged value can be displayed on the ordinate and abscissa in a plot presented in the software. For example during a deviatoric test it is preferred to monitor the piston pressure versus the axial movement of the piston. Live values of the different pressures, which are updated every second, are also displayed. This makes it possible for the operator to register any sudden changes in pressures. Data logged by the program is written to a data file that can be opened in *Microsoft Excel*. The amount of data written to this data file is controlled by the logging rate. During a short test like the deviatoric data high resolution is desirable which is obtained by a frequent logging rate. A typical logging rate for such test is every 30 seconds. In creep tests which can run for several thousand minutes lower resolution is needed. For such test a typical logging rate is every third minute.

Another software is used to control the Quzix Qx pumps. This program makes it possible to control flooding rates and pressures. Hydrostatic ramping operations can also be designed in this program ensuring that all operations are carried out with similar loading rates.

### 5.1.6 Brazilian cell

The indirect tensile strength measurements are performed by using what is called a Brazilian test cell. This cell is build after a design by *Korsnes (2000).* In *Fig.5.7* a picture of the experimental apparatus is presented. The test sample is placed between two loading frames inside the housing. On the front and back cover heating elements are attached which makes it possible to perform high temperature tests as well as tests at ambient temperature.

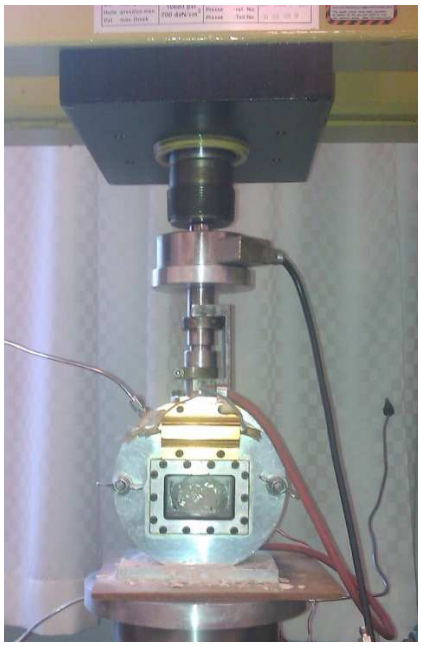

*Fig.5.7: Brazilian test cell equipped with a heating element making it possible to perform tests at high temperatures. The test cell is placed in a test rack with a hydraulically operated piston.*

A steal rod is fitted through a bore in the top of the housing. A load cell is placed on the top of this steal road which measures the axial load applied from a hydraulically operated piston in the test rack. The piston is driven by a Gilson 307 pump controlled by a similar software introduced in *Chapter 5.1.5*. When performing high temperature test a back pressure of 0.7 MPa is used to prevent the brine in the test sample from evaporating as the test cell is heated up.

## 5.2 Test procedure

### 5.2.1 Mounting test

The saturated core is first placed between the upper and lower flooding piston like illustrated in *Fig.5.8*. Between the pistons and the core a paper filter is placed ensuring that any impurities inside the core do not enter the flooding lines. Around the upper and lower flooding piston small rubber seals are used. These rubber seals are greased with vacuum grease to ensura closed system when the sleeve is attached.

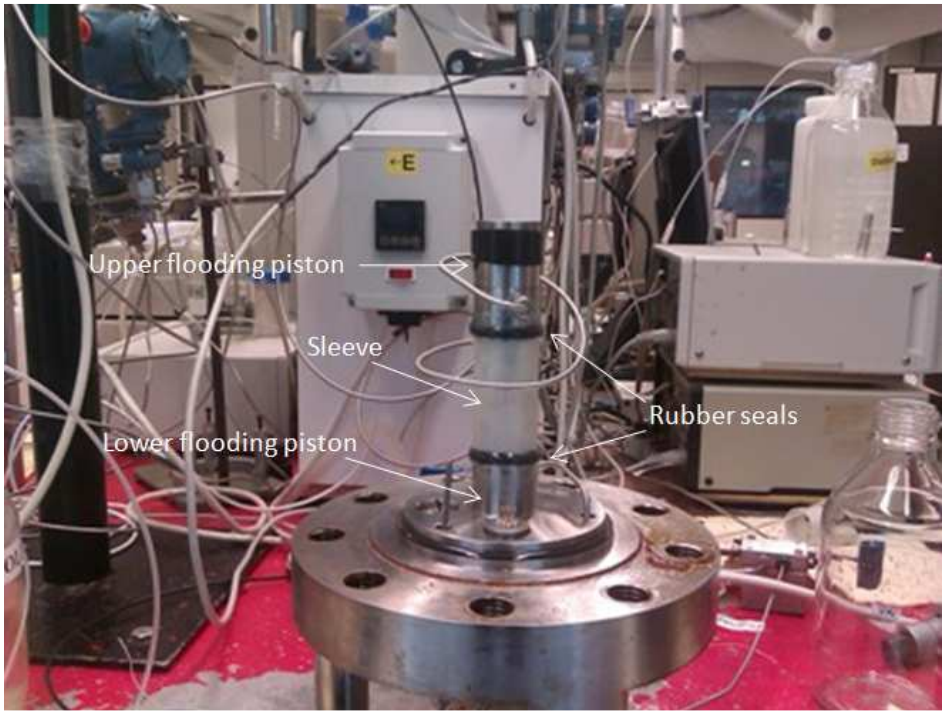


*Fig.5.8: The core is placed between the upper and lower flooding piston. Between the core and the pistons paper filters are used to prevent any impurities from entering the flooding line. Rubber seals are placed above and below the core ensuring a proper seal with the sleeve.*

The sleeve is a Teflon plastic sleeve which shrinks as heat is applied. The sleeve is cut into a length of approximately 110 mm so that it reaches well over core. Heat is gently applied around the bottom so that the sleeve first is attached properly at the bottom. The process is then continued from the bottom and up until the entire sleeve is properly attached.

The next step is to tighten the flooding lope and attach the steal jacket which makes up the confining chamber. For high temperature tests the heating element must be mounted on the outside of the confining chamber before attaching the piston assembly. Confining oil is purred into the confining chamber until the core is fully submerged in confining oil. The piston assembly is attached to the loading frame by six steal bolts which is tighten in an alternating manner. After tightening the bolts the linear voltage displacement transducer (LVDT) is attached at the top of the piston assembly as seen in *Fig.5.1*.

The confining pump is then started with a constant flooding rate equal to 2.0 ml/min with the confining pressure bleed of valve open. Before building any confining pressure it is important to remove any air that may be in the confining chamber. After all air has been removed the confining pressure bleed off valve (See *Fig.5.2*) is closed and the confining pressure is

increased to 0.5 MPa. This is done to apply stress on the sleeve which reduces the chance for any influx of confining oil into the closed flooding system. After reaching the predetermined stress level of 0.5 MPa the confining pump is put on constant pressure cycle which keeps the confining pressure constant at 0.5 MPa.

### 5.2.2 Increasing pore pressure

When increasing the pore pressure a difference of 0.5 MPa is kept between the confining and pore pressure. The flooding pump is started with a constant flooding rate of 3.0 ml/ min and distilled water is flooded into the upper chamber in the flooding cell as illustrated in *Fig.5.9.* This makes the piston inside the flooding cell move downwards. Brine inside the lower chamber will then be pushed out with the same rate as distilled water is pumped into the upper chamber. The reason for using such a flooding cell is to prevent any precipitation of salt inside the piston chamber in the Gilson 307 pump which may damage the pump.

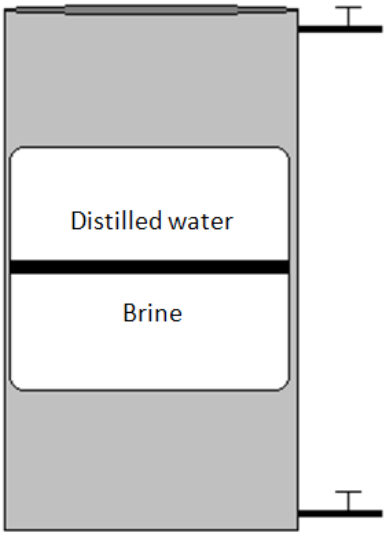


*Fig.5.9: Illustration of the flooding cell used to flood brine. Distilled water is pumped into the upper chamber which pushes the piston downwards. Brine is pushed out from the lower chamber with the same rate as distilled water enters the upper chamber.*

The brine is pumped through the flooding line bypassing the core. In other words brine will not flow through the core but be deflected at the inlet. This makes is possible for a more rapid pore pressure increased compared to a case where fluid is flooded through the core. A pumping rate of 3.0 ml/min is kept until all air is removed from the flooding line. Then the rate is reduced to 2.0 ml/min and the pump connected to the back pressure regulator is put on a constant pressure cycle at 0.4 MPa. Pore pressure inside the system will increase gently up to the pre set pressure of the back pressure regulator. As the pore pressure increases the confining pressure is increased maintaining a difference of 0.5 MPa between the confining pressure and the pore pressur. After reaching 0.4 MPa the flooding rate is reduced to 1.0 ml/min and the pump connected to the back pressure regulator is increased to a constant pressure cycle of 0.7 MPa. When the pore pressure reaches 0.7 MPa the confining pressure will be equal to 1.2 MPa. The flooding rate is reduced to 1 PV/day which usually corresponds to a flooding rate of 0.021 ml/min. Flooding is continued for 24 hours before the next step in the test procedure can be started.

### 5.2.3 Increasing temperature

The next step in the test procedure is to increase the test temperature for tests that should be performed at high temperatures. All high temperature tests were performed at 130 °C. For tests performed at ambient temperature the next step in the test procedure will be introduces *Chapter 5.2.4*. The temperature is increased by the use of a heating element attached to the outside of the confining chamber. Inside the confining chamber a temperature sensor measures the temperature close to the core which the control box uses to regulate the effect of the heating element.

As the temperature increases the oil inside the confining chamber will start to expand due to thermal expansion. This oil expansion will lead to apressure build-up inside the confining chamber if oil is not bled off. A spring pressure valve is connected to the confining pressure bleed of valve (see *Fig.5.2*) which is set to bleed off excess pressures above 1.2 MPa. During this time period the Quizix Qx pump is switched off.

### 5.2.4 Lowering piston

After flooding the core for 24 hours, which corresponds to one pore volume displaced, the piston could be lowered. The piston is lowered by pumping oil into the upper piston chamber as presented in *Fig.5.10*. Oil is pumped into the upper piston chamber with a constant pumping rate equal to 2.0 ml/min with the bleed of valve open.

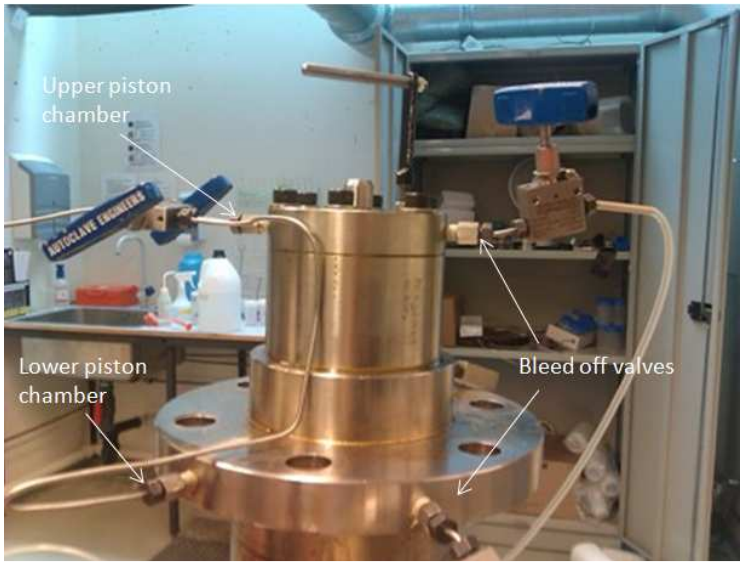


*Fig.5.10: Oil is pumped into the upper piston chamber which increases the pressure on the top of the piston. This pressure pushed the piston downwards slowly. Piston pressure is depleted by opening the upper bleed of valve*

When oil flows continuously out the bleed of valve all the air has been removed from the system and the valve can be closed. The upper piston chamber is a small closed volume and a high pumping rate may cause a very sudden pressure increase; hence a low flow rate of 0.3 ml/min is used. As oil is pumped into the piston chamber the pressure will start to increase slowly. When the frictional force between the piston and the cylinder is overcome the piston will start to move. The pressure needed to initiate movement of the piston will be the friction pressure and used to correct the axial stress. Movement of the piston is measured by the

linear voltage displacement transducer (LVDT) and is plotted against piston pressure in LabVIEW. When contact is established between the piston and the upper flooding piston a sudden increase in piston pressure can be seen. To prevent any damage to the core the maximum pressure that can be reached in the piston chamber is set 0.3 MPa above the friction pressure. After contact is established the Quzix Qx pump is set on constant pressure cylcle which keeps the piston pressure constant at 0.8 MPa.

### 5.2.5 Increasing stress

With contact between the piston and the lower piston assembly the test can be started. All tests that require a higher degree of radial support then 0.5 MPa, need to be loaded isotropic to the desired stress level. This is done by increasing the confining pressure with a constant loading rate. The stress rate used for all isotropic loading phases are based on the loading rate during hydrostatic tests. Hydrostatic tests are loaded isotopic 2-3 MPa above the materials yield point, which in this case equals a confining pressure of 12,7 MPa. The hydrostatic tests performed in this thesis where loaded to 12.7 MPa in 430 minutes which correspond to a loading rate of 0.0295 MPa/min. This type of ramping operation could only be performed on the tests cells that were connected to a Quizix QX pump.

The creep tests were performed in a different tests-cells compared to the triaxial tests. Here a Gilson 307 pump was used to regulate the confining pressure and this pump can only pump with a constant flooding rate. A constant flooding rate of 0.050 ml/min was used to increase the confining pressure to 12.0 MPa. This flooding rate gives a loading rate close to the loading rate for the ramping operations performed by the Quizix QX pumps.

In all loading phases the piston pump was set to in constant pressure cycle 0.2-0.3 MPa above the friction pressure for the different test cells. As the confining pressure increases this frictional pressure sometime increases which may cause the piston to get stuck. This is solved by increasing the piston pressure 0.1-0.2 MPa above the current piston pressure.

After reaching the desired level of radial support for the triaxial tests, axial load can be applied until failure is initiated. Axial load is increased by slowly increasing the pressure inside the piston chamber. This is done by putting the piston pump in constant flow rate cycle with a constant flooding rate of 0.010 ml/min.

### 5.2.6 Dismantling test

When the test is finished the cell is dismantle. The first thing that is done is to move the piston up to its initial position. This is done by first depleting the piston pressure by opening the upper bleed of valve in *Fig.5.2*. Then the inlet valve to the upper piston chamber is closed while the inlet valve for the lower piston chamber is opened. As for lowering the piston *(Chapter 5.2.4)* any air present in the chamber must be removed before the pressure can be increased. This is done by pumping oil into the chamber with the lower bleed of valve open. When a continuous flow of oil is exits the bleed of valve the valve is closed. A constant flooding rate of 1.0 ml/min is used to move the piston back up. When the piston is back to its initial position the confining pressure is reduced slowly to 1.2 MPa.

For high temperature tests the temperature must be removed before the test cell can be dismantled. This is done by turning off the heating element. As the temperature decreases the volume of oil inside the confining chamber will decrease, which leads to a reduction in

confining pressure. To cope for the reduction in oil volume the confining pump is put on constant pressure cycle which allows the flooding rate to increase as much as needed to maintain a constant pressure. As mentioned earlier this can only be done on the test cells connected to a Quizix Qx pump. When a Gilson 307 pump is used to regulate the confining pressure, a constant flooding rate of 2.0 ml/min is used to cope for the reduction in oil volume.

When the temperature inside the test cell reaches ambient temperature the pore pressure can be depleted. This is done by reducing the back pressure from the Teledyne 260 D syringe pump to 0.7 bars which is the lower limit for this pump. The fluid inside the flooding line is then allowed to pass freely through the back pressure regulator removing the pore pressure. The next step is then to deplete the remaining confining pressure and drain the oil from the confining chamber. By applying air pressure through the confining bleed off valve drainage of confining oil will be faster. When all oil inside the confining chamber has been removed the piston assembly is lifted off.

The core is then removed and any excess oil is cleaned up. To prevent any corrosion in the flooding lines distilled water (DW) is pumped through removing all SSW.

### 5.2.7 Brazilian test

All the Brazilian tests were performed by the use of the apparatus presented in *Fig.5.7*. The samples are prepared from cores which have a length of 70 mm and a diameter of 37mm. Each core is divided into three smaller samples with a length between the radii and the diameter (18.5-37 mm) by the use of the cutting machine presented in *Fig.4.3*. Before cutting the core a vertical line is drawn on the core. This line will be used to ensure that each sample is tested with the same orientation. The preferred number of samples which is needed to obtain a good estimate of the indirect tensile strength is around 10.

Test samples that should be tested at ambient temperature were prepared from cores that were un-aged, so after cutting the samples the length and diameter was measured and the bulk volume is calculated. The samples were then placed in a heating chamber at 130 $^0$C for 24 hours and saturated with distilled water so that porosity could be determined (*See Chapter 4.2.4*). After porosity had been determined the cores were placed in a heating chamber and saturated with brine (SSW of SSW-($SO_4^{2-}$)) 24 hours before the tests should be performed.

Test samples tested at 130 °C were prepared from cores that already had been aged for three weeks at 130 °C. These cores were already saturated with brine so porosity could not be determined in the same manner as for the un-aged cores.

Ambient test were performed by placing a saturated sample between the loading frames which then was placed inside the housing. The test samples were placed inside the loading frame with the marked line facing up. Then the piston in the external loading frame was pumped gently down to a point right above the load sensor by the use of a hand pump. *LabVIEW* was then started and the flooding rate of the Gilson 307 pump was set to 0.5 ml/min. These types of tests are very short; hence a high data resolution is needed. The program was set to log values every 0.001 minutes. Tensile failure is recognized by a sudden drop in piston pressure which terminates the tests. Peak load at failure is then used to calculate the indirect tensile strength ($T_{ob}$).

Test samples that should be tested at 130 °C where first placed inside a small aging cell in a heating chamber at 130 °C the day before the tests should be performed. The next morning the aging cell was removed from the heating chamber and allowed to cool down before the tests were started. When the temperature in the tests cell had stabilized at 130 °C the front panel was removed and the loading frame was taken out. Below the loading frame there is a small beaker that was filled with brine before the loading frame with the test sample was placed back in the housing. The front panel was then mounted back on and a gas pressure of 0.7 MPa was applied. The air pressure in combination with the brine in the small cup below the loading frame will prevent the sample from drying as temperature increases and stabilizes. After temperature is stabilized the system is left to equilibrate for 30 minutes before the tests were started following the same procedure as for ambient tests.

### 5.2.8 Chemical analysis of water samples

Water samples of the effluent were collected daily during the creep tests. These samples were analysed so that any chemical processes inside the core could be detected. The water samples are placed in a refrigerator at 4$^{o}$C until the day chemical analysis is performed. First a small fraction of the effluent sample is diluted 200 times by a Gilson Gx-271 diluter shown in *Fig.5.11*. By using this apparatus a higher degree of accuracy is obtained compared to a case where the dilution is done manually. The reason for diluting the effluent prior to the chemical analysis is to get the ion concentration within the detection range of the ion chromatograph (IC).

*Fig.5.11: A Gilson Gx-271 diluter was used to dilute the effluent samples 200 times. This was done to ensure that the ion concentrations are within the detection range of the IC.*

The diluted samples are then filtrated by the use of a 5 ml syringe with a PALL filter. This filter removes any impurities that may be in solution. The filtrated solution is injected into 1.5 ml glasses that are used in the IC.

Chemical analyses of effluent samples were performed by the use of the Dionex ICS-3000 ion chromatograph by Dionex Corporation in *Fig.5.12*.

*Fig.5.12: A Dionex ICS-3000 ion chromatograph by Dionex Corporation is used to measure the concentration of cations and anions in the effluent samples.*

The IC can measure the concentration of both anions and cations present in the effluent samples. By comparing these concentrations to the initial concentration of anions and cations in the brine prior to flooding one can study and quantify the chemical reactions taking place inside the core.

# 6 Results

In the following chapters the first results that will be presented are the data obtained from the stress strain plots like the yield points, the Young's-moduli and the bulk moduli. The data from the stress strain plots are then used to determine the cohesion ($S_o$) and the friction angle ($\varphi$) from a Mohr plot and finally to draw the full failure envelope in a qp´-plot.

In total 57 cores were prepared and tested according to the procedure described in *Chapter 5*. The cores are named LK followed by a number. LK is an abbreviation for Liegè chalk and the name of the person that drilled out the cores samples. The number represent in which order the cores were prepared.The first core prepared got the number 1 and the last 99. Of these 57 cores 29 cores were used for synthetic seawater (SSW) tests. *Table 6.1* shows an overview of these 29 cores where 17 cores were used for tests at 130 °C while the remaining 12 cores were tested at ambient temperature.

*Table 6.1: Table of all cores used SSW test*

| Core | Diameter [mm] | Length [mm] | Pore Volume [ml] | Bulk Volume [ml] | Porosity [%] | Test Temp. [°C] |
|---|---|---|---|---|---|---|
| *LK4* | 36.96 | 72.70 | 30.97 | 78.00 | 39.71 | Ambient temp. |
| *LK71* | 36.97 | 70.08 | 30.03 | 75.23 | 39.92 | Ambient temp. |
| *LK75* | 37.00 | 70.17 | 28.61 | 75.45 | 37.92 | Ambient temp. |
| *LK80* | 36.95 | 70.32 | 28.85 | 75.40 | 38.26 | Ambient temp. |
| *LK82* | 36.95 | 70.19 | 29.24 | 75.27 | 38.85 | Ambient temp. |
| *LK84* | 36.97 | 70.16 | 29.76 | 75.31 | 39.51 | Ambient temp. |
| *LK85* | 36.99 | 69.93 | 29.59 | 75.15 | 39.38 | Ambient temp. |
| *LK87* | 36.97 | 69.90 | 29.18 | 75.04 | 38.89 | Ambient temp. |
| *LK89* | 37.03 | 70.09 | 30.05 | 75.48 | 39.81 | Ambient temp. |
| *LK96* | 37.01 | 70.05 | 29.88 | 75.36 | 39.65 | Ambient temp. |
| *LK97* | 36.98 | 70.22 | 30.13 | 75.42 | 39.95 | Ambient temp. |
| *LK99* | 36.99 | 70.18 | 30.08 | 75.42 | 39.88 | Ambient temp. |
| *LK7* | 37.04 | 70.00 | 29.95 | 75.43 | 39.71 | 130°C |
| *LK11* | 37.05 | 70.07 | 29.42 | 75.54 | 38.94 | 130°C |
| *LK15* | 36.99 | 69.86 | 29.33 | 75.07 | 39.07 | 130°C |
| *LK17* | 37.02 | 70.11 | 29.59 | 75.46 | 39.21 | 130°C |
| *LK18* | 36.96 | 70.07 | 29.97 | 75.18 | 39.87 | 130°C |
| *LK19* | 37.05 | 70.25 | 30.12 | 75.74 | 39.77 | 130°C |
| *LK20* | 36.97 | 70.15 | 29.27 | 75.30 | 38.87 | 130°C |
| *LK21* | 37.03 | 70.11 | 29.73 | 75.51 | 39.37 | 130°C |
| *LK25* | 36.99 | 69.98 | 29.79 | 75.20 | 39.61 | 130°C |
| *LK26* | 37.09 | 70.17 | 29.95 | 75.81 | 39.50 | 130°C |
| *LK28* | 36.93 | 69.41 | 29.20 | 74.35 | 39.27 | 130°C |
| *LK29* | 37.00 | 69.98 | 30.18 | 75.24 | 40.11 | 130°C |
| *LK32* | 36.98 | 69.78 | 29.95 | 74.95 | 39.96 | 130°C |
| *LK34* | 37.10 | 70.30 | 29.34 | 76.00 | 38.61 | 130°C |
| *LK35* | 36.99 | 69.95 | 29.54 | 75.17 | 39.30 | 130°C |
| *LK94* | 37.00 | 70.18 | 29.52 | 75.46 | 39.12 | 130°C |
| *LK95* | 36.98 | 69.91 | 29.73 | 75.09 | 39.59 | 130°C |

All cores tested at 130 °C were aged for three weeks at the same temperature prior to testing as described in *Chapter 4.4*. The cores tested at ambient temperature were saturated with brine the day before being mounted in the test cell. Each core was flooded with a flooding rate equal to 1 PV/day for 24 hours before the test was started.

The 28 cores in *Table 6.2* were used for synthetic seawater (SSW-($SO_4^{2-}$) tests. Of these in total 18 cores were tested at high temperature, while the remaining 10 cores were tested at ambient temperature.

*Table 6.2: Table of all cores used for SSW-($SO_4^{2-}$) tests*

| Core | Diameter [mm] | Length [mm] | Pore Volume [ml] | Bulk Volume [ml] | Porosity [%] | Test Temp. [$^oC$] |
|---|---|---|---|---|---|---|
| *LK38* | 36.99 | 68.28 | 29.49 | 73.38 | 40.19 | Ambient temp. |
| *LK46* | 36.99 | 66.34 | 28.16 | 71.29 | 39.50 | Ambient temp. |
| *LK48* | 36.97 | 70.12 | 29.89 | 75.27 | 39.71 | Ambient temp. |
| *LK64* | 37.01 | 70.22 | 30.38 | 75.54 | 40.22 | Ambient temp. |
| *LK66* | 37.02 | 68.84 | 29.77 | 74.10 | 40.18 | Ambient temp. |
| *LK67* | 36.99 | 70.32 | 30.20 | 75.57 | 39.96 | Ambient temp. |
| *LK68* | 36.96 | 68.99 | 29.48 | 74.02 | 39.83 | Ambient temp. |
| *LK92* | 36.99 | 70.19 | 29.49 | 75.43 | 39.10 | Ambient temp. |
| *LK93* | 37.01 | 70.05 | 30.11 | 75.36 | 39.96 | Ambient temp. |
| *LK98* | 37.00 | 70.15 | 30.12 | 75.43 | 39.93 | Ambient temp. |
| LK27 | 37.13 | 68.93 | 29.39 | 74.64 | 39.38 | 130$^o$C |
| *LK41* | 37.00 | 65.81 | 28.55 | 70.76 | 40.35 | 130$^o$C |
| *LK47* | 37.03 | 70.03 | 29.47 | 75.42 | 39.07 | 130$^o$C |
| LK49 | 37.01 | 68.85 | 29.32 | 74.07 | 39.59 | 130$^o$C |
| *LK50* | 36.96 | 69.53 | 29.49 | 74.60 | 39.53 | 130$^o$C |
| *LK51* | 37.03 | 70.01 | 30.30 | 75.40 | 40.19 | 130$^o$C |
| *LK52* | 37.00 | 70.10 | 30.23 | 75.37 | 40.11 | 130$^o$C |
| *LK57* | 36.99 | 70.18 | 30.17 | 75.42 | 40.00 | 130$^o$C |
| *LK58* | 36.97 | 70.13 | 30.21 | 75.28 | 40.13 | 130$^o$C |
| *LK59* | 37.02 | 70.10 | 30.02 | 75.45 | 39.79 | 130$^o$C |
| *LK62* | 37,00 | 70.36 | 30.43 | 75.65 | 40.22 | 130$^o$C |
| LK63 | 36.96 | 70.24 | 29.41 | 75.36 | 39.03 | 130$^o$C |
| *LK65* | 37.03 | 70.22 | 29.70 | 75.62 | 39.27 | 130$^o$C |
| *LK69* | 36.97 | 70.17 | 29.45 | 75.33 | 39.10 | 130$^o$C |
| *LK70* | 36.94 | 70.16 | 29.89 | 75.19 | 39.75 | 130$^o$C |
| *LK72* | 36.92 | 70.16 | 30.22 | 75.11 | 40.23 | 130$^o$C |
| *LK74* | 36.96 | 70.13 | 29.78 | 75.24 | 39.58 | 130$^o$C |
| LK79 | 38.08 | 70.03 | 32.07 | 79.76 | 40.21 | 130$^o$C |

The average porosity based on all cores prepared was calculated to 39.57 % with a standard deviation of 0.51 %

## 6.1 Synthetic Seawater (SSW)

### 6.1.1 Ambient temperature

By performing a lot of different triaxial tests (both hydrostatic and deviatoric tests with varying degree of radial support) one can obtain a good estimate of the materials failure envelope. This failure envelope is regarded as a critical limit between the elastic and the plastic region.

**Mechanical results in tables**

In total 12 different triaxial tests with varying degree of radial support was performed and the results of these tests are listed in *Table 6.3*. Brazilian tests were included so that a data point closer to the ordinate axis could be obtained.

*Table 6.3: Table over the mechanical result obtained at ambient temperature*

| Test type | Test core | Unaged/Ambient or Aged/130 °C | Porosity [%] | $\sigma'_1$ [MPa] | $\sigma'_3$ [MPa] | q [MPa] | p' [MPa] | E-modulus [GPa] | K-modulus [GPa] |
|---|---|---|---|---|---|---|---|---|---|
| Brazilian | | Unaged/Ambient | | 1.83 | -0.61 | 2.43 | 0.20 | | |
| 0.3 MPa Dev. | LK80 | Unaged/Ambient | 38.26 | 5.60 | 0.30 | 5.30 | 2.07 | 1.465 | |
| 0.5 MPa Dev. | LK71 | Unaged/Ambient | 39.92 | 5.80 | 0.50 | 5.30 | 2.27 | 1.320 | |
| 0.8 MPa Dev. | LK87 | Unaged/Ambient | 38.89 | 6.80 | 0.80 | 6.00 | 2.80 | 1.302 | |
| 1.0 MPa Dev. | LK82 | Unaged/Ambient | 38.85 | 7.00 | 1.00 | 6.00 | 3.00 | 1.597 | |
| 1.5 MPa Dev. | LK89 | Unaged/Ambient | 39.81 | 7.40 | 1.50 | 5.90 | 3.47 | 1.394 | |
| 2.0 MPa Dev. | LK75 | Unaged/Ambient | 37.92 | 8.40 | 2.00 | 6.40 | 4.13 | 1.450 | |
| 3.0 MPa Dev. | LK85 | Unaged/Ambient | 39.38 | 9.50 | 3.00 | 6.50 | 5.17 | 1.622 | |
| 4.0 MPa Dev. | LK84 | Unaged/Ambient | 39.51 | 9.50 | 4.00 | 5.50 | 5.83 | 1.534 | |
| 7.0 MPa Dev. | LK96 | Unaged/Ambient | 39.65 | 12.00 | 7.00 | 5.00 | 8.67 | 1.349 | |
| 8.0 MPa Dev. | LK99 | Unaged/Ambient | 39.88 | 12.30 | 8.00 | 4.30 | 9.43 | 1.540 | |
| Hydr. | LK97 | Unaged/Ambient | 39.95 | 10.30 | 10.20 | 0.10 | 10.23 | | 0.703 |
| Hydr. | LK4 | Unaged/Ambient | 39.71 | 10.10 | 9.60 | 0.50 | 9.77 | | 0.907 |

The yield points for the different tests are listed in *Table 6.3* as the maximum effective stress ($\sigma_1'$) while the minimum effective stress ($\sigma_3'$) will be the difference between the confining and the pore pressure.

The tensile strength ($T_{ob}$) for the material is found by using the peak force ($F_c$) obtained for each individual test and found by *Eq.3.43*. Based on the average tensile strength ( $\overline{T_{ob}}$ ), from in total 10 individual tests, the maximum and minimum principle stress can be calculated by using *Eq.3.44* and *Eq.3.45* respectively. In *Table 6.4* the results from the Brazilian tests performed on SSW saturated samples at ambient temperature are listed.

*Table 6.4: Results from 10 Brazilian tests performed on SSW saturated Liegé chalk samples at ambient temperature*

| Core | Diameter [mm] | Length [mm] | Pore Volume (ml) | Bulk Volume (ml) | Porosity (%) | Peak force (kN) | Tob [Mpa] |
|---|---|---|---|---|---|---|---|
| *LK (1.1)* | 37.00 | 21.60 | 9.21 | 23.22 | 39.66 | 0.82 | 0.65 |
| *LK (1.2)* | 37.00 | 20.43 | 8.71 | 21.97 | 39.65 | 0.64 | 0.54 |
| *LK (1.3)* | 37.00 | 22.00 | 9.55 | 23.65 | 40.37 | 0.83 | 0.65 |
| *LK (2.1)* | 36.96 | 21.06 | 8.95 | 22.60 | 39.48 | 0.68 | 0.56 |
| *LK (2.2)* | 36.96 | 22.49 | 9.66 | 24.13 | 40.03 | 0.82 | 0.63 |
| *LK (2.3)* | 36.96 | 20.78 | 8.93 | 22.29 | 40.05 | 0.71 | 0.59 |
| *LK (3.1)* | 36.93 | 19.80 | 8.40 | 21.21 | 39.61 | 0.67 | 0.58 |
| *LK (3.2)* | 36.93 | 20.76 | 8.86 | 22.24 | 39.84 | 0.72 | 0.60 |
| *LK (4.1)* | 36.95 | 23.30 | 9.92 | 24.99 | 39.70 | 0.91 | 0.67 |
| *LK (4.2)* | 36.95 | 20.34 | 8.68 | 21.81 | 39.80 | 0.74 | 0.63 |

The average tensile strength ( $\overline{T_{ob}}$ ) was calculated to be 0.61 MPa with a standard deviation of ±0.04 MPa.

**Example of determination of yield and elastic modeli**

The maximum principle stress ($\sigma_1'$) is found by studying stress strain plots for each individual test. In *Fig.6.1* the stress strain plot for 0.5 MPa deviatoric test is shown. The yield-point will the point where the stress-strain relation starts to deviate from a linear like presented in *Chapter 3.2.4*.

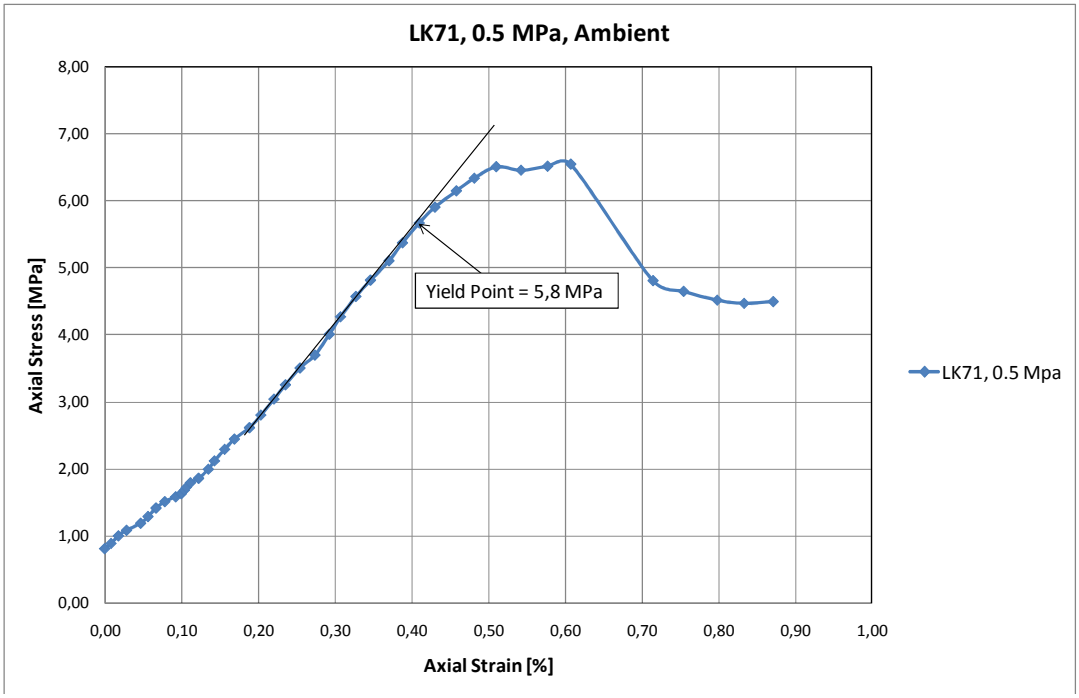


*Fig.6.1: Stress strain plot for a deviatoric test performed with 0.5 MPa in difference between the confining pressure and the pore pressure at ambient temperature. The yield point for is determined as the point where the stress strain curve starts to deviate from a linear trend. For this case the yield point was determined to 5.8 MPa.*

Another parameter that can be found from stress strain plots is the materials Young's modulus. The Young's modulus is determined from the slope of the stress strain curve before yield is initiated. In *Fig.6.2* a small section of the stress strain curve in *Fig.6.1* is shown. The Young's modulus is determined from the slope by performing a linear regression on the chosen data points.

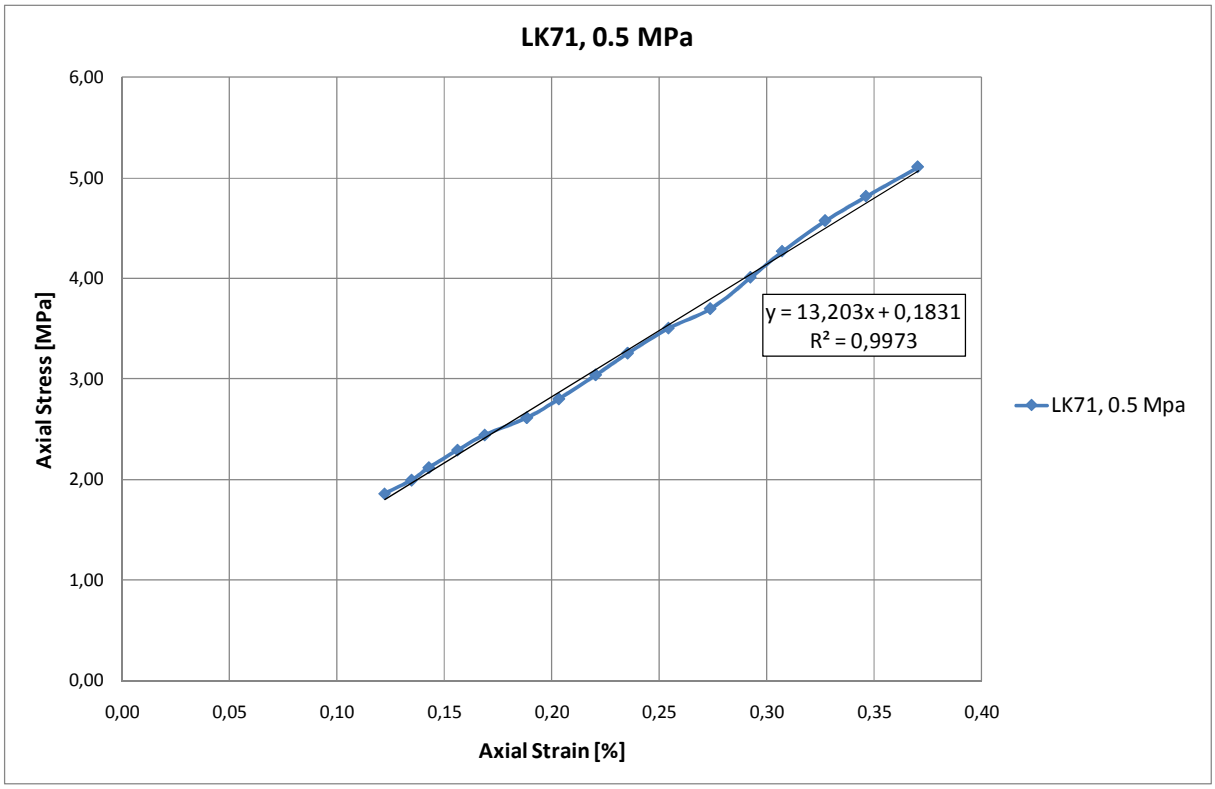


*Fig.6.2: A section of the linear stress strain relation is used to estimate the Young's modulus. By performing a linear regression on the chosen data points the Young's modulus will be given as the slope of the regression line. The $R^2$ value give information on how good the curve fit is.*

Since the strain is expressed in percent the value obtained from the linear regression must be multiplied with 100 to get the Young's modulus expressed in MPa. Usually the Young's modulus is expressed as GPa which means that the value has to be divided by 1000 to get the values presented in *Table 6.1*. An equivalent method will be to just divide the value of the slope found by the linear regression with 10 to get the Young's modulus expressed in GPa.

The bulk modulus is determined from stress versus volumetric strain plots from hydrostatic loading phases as shown in *Fig.6.3*.The stress increase is plotted against volumetric strain given by *Eq.3.19*. A linear regression is performed on a section of the stress strain curve prior to yield. From the slope of this regression line the bulk modulus can be found. The slope is divided by 10 (as for the Young's modulus) so that the value of the bulk modulus is expressed in GPa.

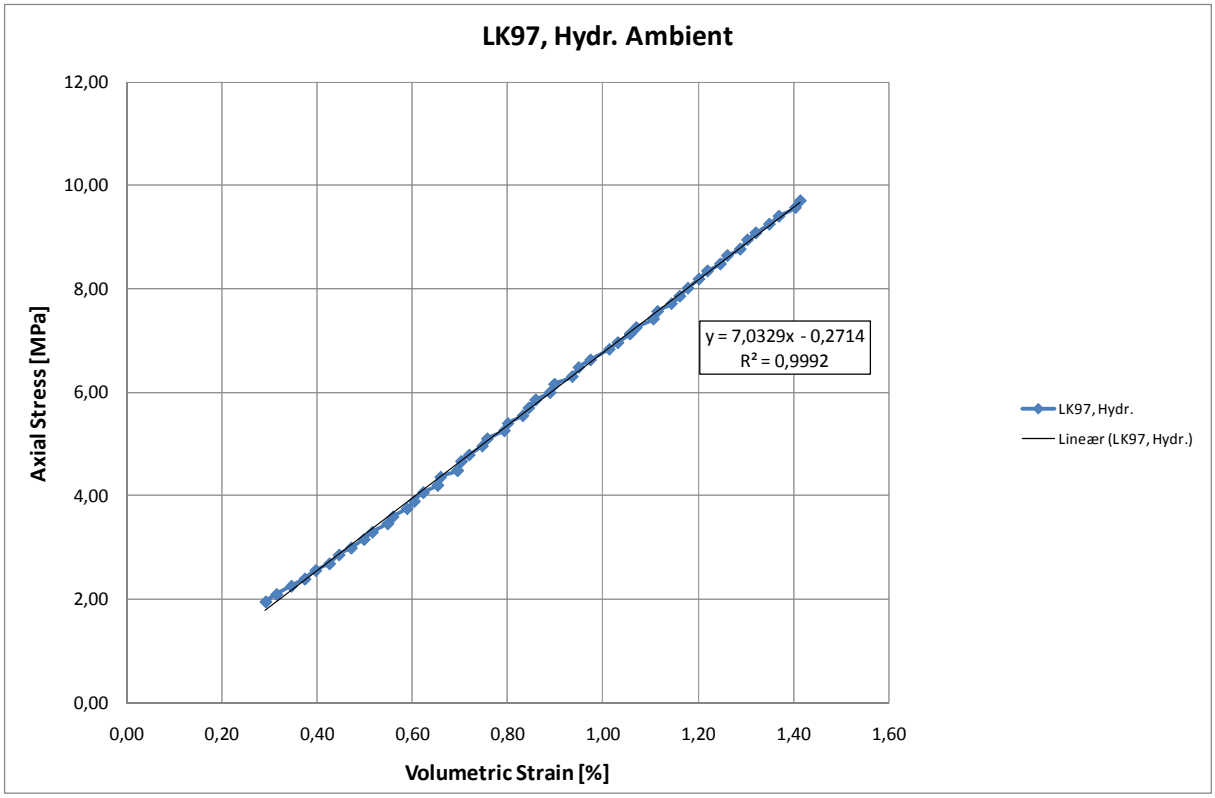


*Fig.6.3: A section of the stress versus volumetric strain plot for the hydrostatic loading phase of LK97. The bulk modulus is determined by performing a linear regression on a set of data points prior to yield.*

**Mohr and q-p´ plots**

The hydrostatic tests are not plotted in the τ σ-plane due to the small difference between the maximum and minimum principle stress. Mohr circles drawn for hydrostatic tests will be small circles to the right of the failure line. From the maximum ($\sigma_1'$) and minimum ($\sigma_3'$) principle stress the corresponding Mohr circles can be drawn in the τ σ-plane as shown in *Fig.6.4* where the Mohr circles for all the different deviatoric tests are drawn. A linear line is drawn in such a manner that it tangents the first Mohr circles which will be regarded as the failure line. From this line the materials cohesion ($S_o$) and friction angle (φ) can be determined as shown in *Fig.3.12*.

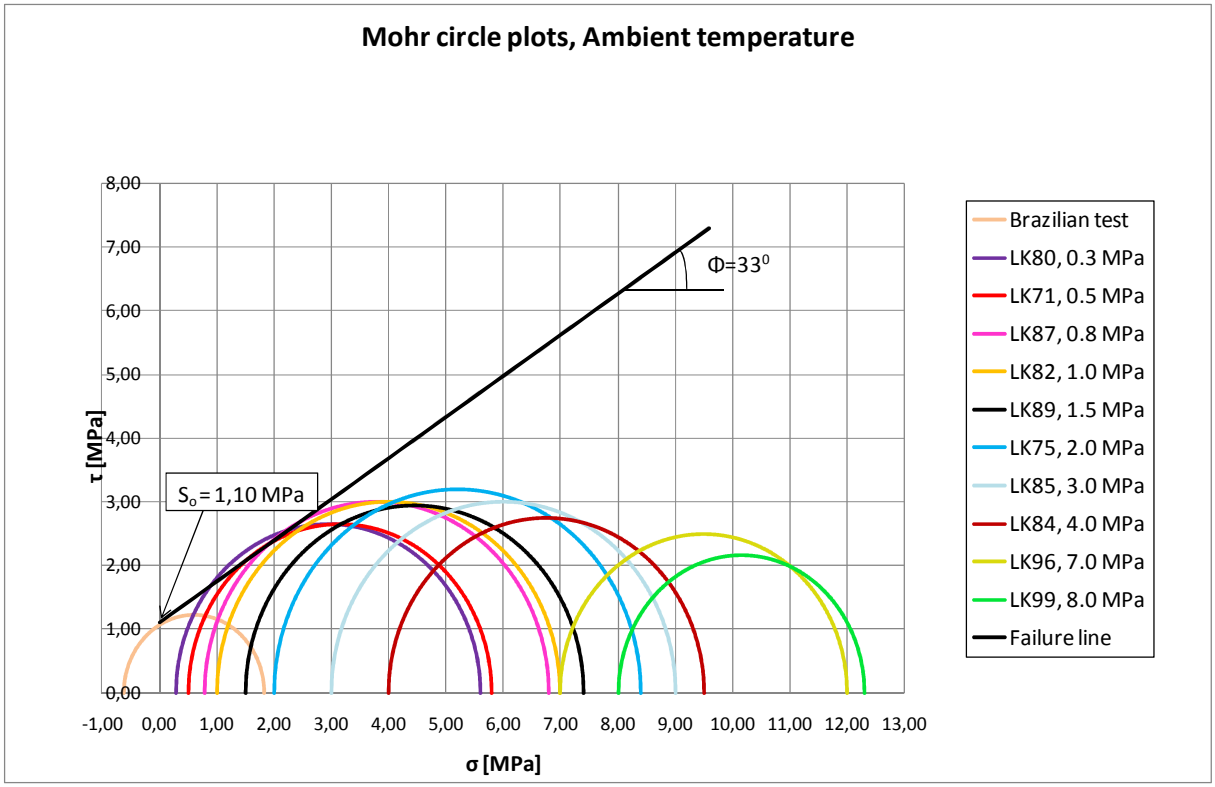


*Fig.6.4: Mohr circles drawn on basis of the results from the deviatoric tests performed at ambient temperature. A failure line is drawn manually such that it tangents the first Mohr circles. Cohesion is determined as the point of intersection with the ordinate axis while the friction angle will be the inclination of the failure line.*

Another way of plotting the data obtained from the different deviatoric tests is by using a q-p´ plot (*Chapter 3.2.7*). q-p´ values are calculated on basis of the maximum ($\sigma_1$´) and minimum ($\sigma_3$´) principle stress and are calculated by the use of *Eq. 3.34* and *Eq.3.35*. By plotting enough deviatoric tests one can obtain a good estimate of the entire failure envelope as shown in *Fig.6.5*.

A linear regression is performed on the data points that fall on or close to the failure line. On the end cap side a second order polynomial regression is used to obtain an expression that gives the shape of the end cap. By plotting these regression lines in the q-p´ plot as shown in *Fig.6.5* one obtains an estimate of the critical limit between the elastic and plastic region. Brazilian tests are indirect tensile strength tests that give a point close to the ordinate axis. The failure line will therefore not be limited by a line from the origin with a slope equal to 3:1 (*chapter 3.2.7*). Hydrostatic tests are included to obtain data points close to the abscissa.

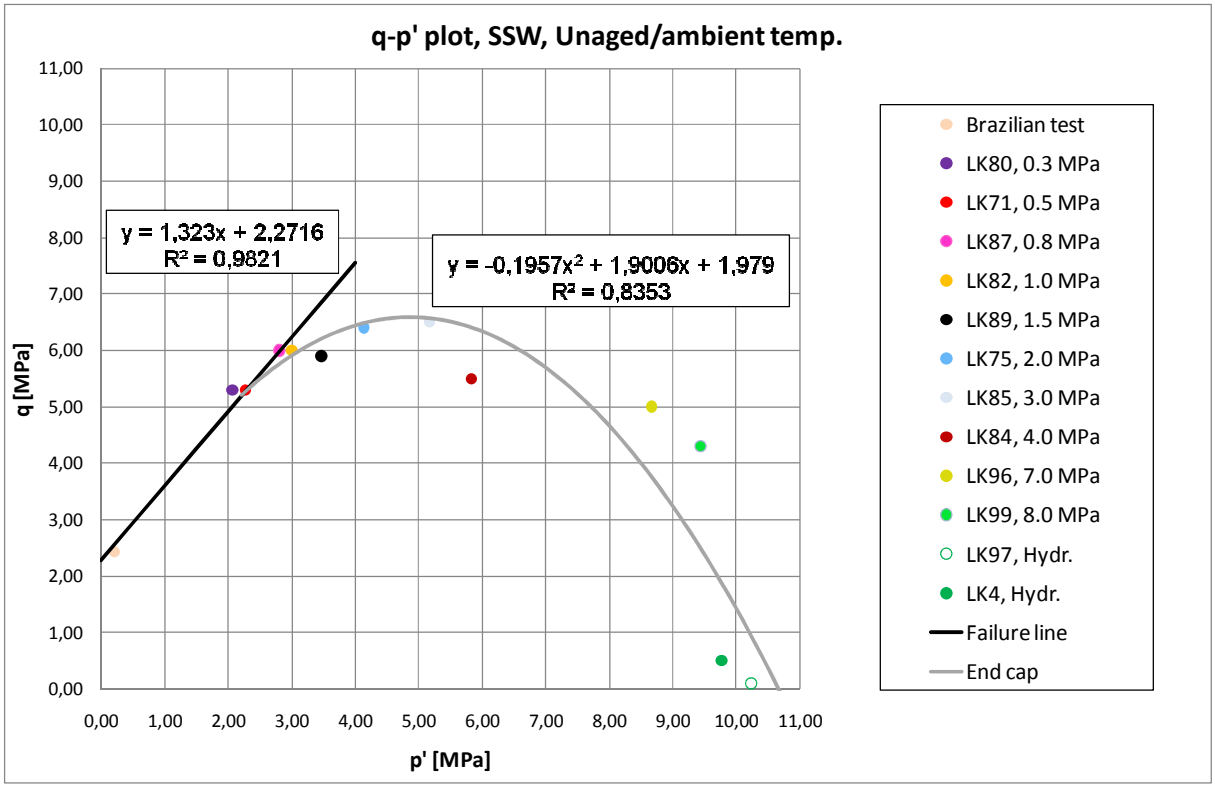


*Fig.6.5: q-p´ plot for the data obtained from deviatoric tests at ambient temperature. The failure line is found by performing a linear regression on the results from the five first tests. On the end cap a second order polynomial regression is used on the remaining data points to give an estimate of the shape of the end cap curve. The $R^2$ value gives information about the quality of the regression.*

From the linear regression performed on the first data point's one obtain an expression for the failure line. By using the slope of the line and the point of intersection with the ordinate axis the cohesion ($S_o$) and friction angle ($\varphi$) can be determined by the use of *Eq.3.38* and *Eq.3.39*.The materials internal friction is found by using *Eq. 3.25*. These values can be used in the Mohr Coulomb criterion given by *Eq.3.24* to draw a new failure line in the Mohr plot as shown in *Fig.6.6* where both the calculated failure line from the q-p´ plot and the drawn failure line from *Fig.6.4* are included.

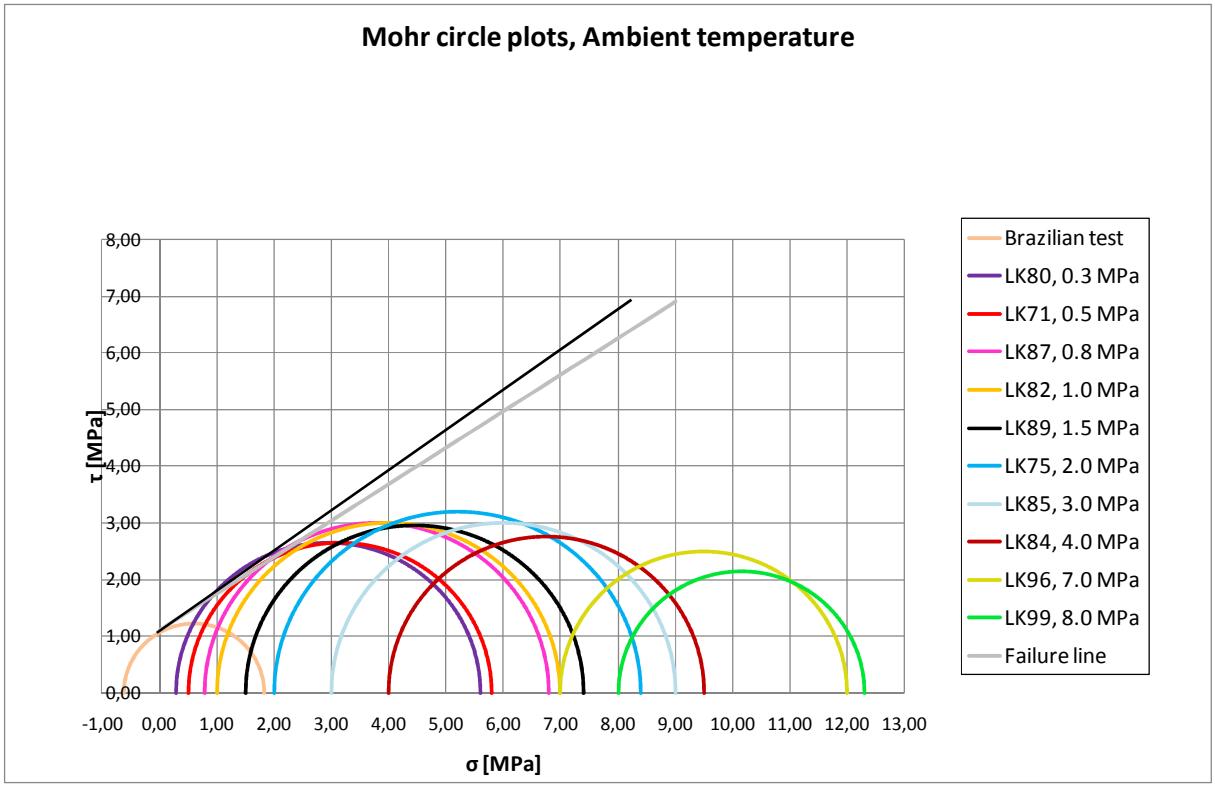


*Fig.6.6: Mohr plot for all deviatoric tests performed at ambient temperature. The black failure line will be the drawn failure line from Fig.6.3 while the grey line will be the calculated failure line from the q-p´ plot in Fig.6.5. Both lines give a very similar point of intersection with the ordinate but with different inclinations.*

As can be seen from *Fig.6.6* there is some difference between the failure line drawn from the Mohr plot in *Fig.6.4* and the calculated failure line from the q-p´ plot in *Fig.6.5*. *Table 6.4* shows the main difference between the calculated and the manually drawn failure line.

*Table 6.4: Table over the main differences between the drawn failure line from the Mohr plot in Fig.6.4 and calculated failure line from the q-p´ plot in Fig.6.5*

| Mechanical parameters | Failure line drawn from Mohr plot | Failure line calculated from q-p´plot |
|---|---|---|
| $S_o$ [MPa] | 1.10 | 1.11 |
| $\varphi^o$ | 36 | 33 |
| $\mu$ | 0.73 | 0.64 |
| $\beta^o$ | 63 | 61 |

The main difference between these two methods in *Table 6.4* will be in the friction angle. Cohesion is very similar for these two methods which is mostly a result of the Brazilian tests. From *Fig.6.6* it is evident that calculating the cohesion and friction angle from the q-p´ plot in *Fig.6.5* is an applicable method which in this case gives a better estimate of the mechanical parameters in *Table 6.4* compared to the drawn failure line from the Mohr plot in *Fig.6.4*.

### 6.1.2 130 ℃

**Mechanical results in tables**

The cores tested at 130 °C were aged at the same temperature for three weeks prior to testing. In total 12 different triaxial tests (including both deviatoric and hydrostatic) were performed. *Table 6.5* show the results obtained from the tests performed at 130 °C on Liegé chalk saturated and flooded with SSW.

*Table 6.5: Table over the results obtained from the tests performed at 130 °C on chalk saturated and flooded with SSW*

| Test type | Test core | Unaged/Ambient or Aged/130 °C | Porosity [%] | $\sigma'_1$ [MPa] | $\sigma'_3$ [MPa] | q [MPa] | p' [MPa] | E-modulus [GPa] | K-modulus [GPa] |
|---|---|---|---|---|---|---|---|---|---|
| Brazilian test. | | Aged/130 °C | | 0.80 | -0.27 | 1.10 | 0.09 | | |
| 0.3 MPa Dev. | LK28 | Aged/130 °C | 39.27 | 3.40 | 0.30 | 3.10 | 1.33 | 0.794 | |
| 0.5 MPa Dev. | LK17 | Aged/130 °C | 39.21 | 4.20 | 0.50 | 3.70 | 1.73 | 0.947 | |
| 0.8 MPa Dev. | LK11 | Aged/130 °C | 38.94 | 5.20 | 0.80 | 4.40 | 2.27 | 0.810 | |
| 1.0 MPa Dev. | LK29 | Aged/130 °C | 40.11 | 5.40 | 1.00 | 4.40 | 2.47 | 0.998 | |
| 1.2 MPa Dev. | LK26 | Aged/130 °C | 39.50 | 5.60 | 1.20 | 4.40 | 2.67 | 0.932 | |
| 1.5 MPa Dev. | LK7 | Aged/130 °C | 39.71 | 6.10 | 1.50 | 4.60 | 3.03 | 0.930 | |
| 2.3 MPa Dev. | LK15 | Aged/130 °C | 39.07 | 6.50 | 2.30 | 4.20 | 3.70 | 1.116 | |
| 4.0 MPa Dev. | LK18 | Aged/130 °C | 39.87 | 8.10 | 4.00 | 4.10 | 5.37 | 1.097 | |
| 6.0 MPa Dev. | LK21 | Aged/130 °C | 39.37 | 9.20 | 6.00 | 3.20 | 7.10 | 1.150 | |
| 6,5 Mpa Dev. | LK19 | Aged/130 °C | 39.77 | 8.80 | 6.50 | 2.30 | 7.27 | 1.022 | |
| Hydr. | LK20 | Aged/130 °C | 38.87 | 7.60 | 7.14 | 0.46 | 7.29 | | 0.478 |
| Hydr. | LK34 | Aged/130 °C | 38.61 | 7.40 | 6.87 | 0.53 | 7.05 | | 0.556 |

Yield points, Young's modulus and bulk modulus are determined according to *Fig.6.1*, *Fig.6.2* and *Fig.6.3.*

The average tensile strength ( $\overline{T_{ob}}$ ) is used to calculate the maximum ($\sigma_1'$) and minimum ($\sigma_3'$) effective stress. In *Table 6.6* the results for in total 9 individual tests are shown. A back pressure of 0.7 MPa was used to ensure that the samples remained saturated during the test. This made it necessary to correct the peak force before calculating the tensile strength. The correction factor was determined individually and subtracted from the total peak force giving the load values presented in *Table 6.6*. Porosity for each sample could not be determined individually since these tests samples were prepared from aged cores already saturated with brine. The porosities for these samples are therefore assumed to be similar to the porosity of the core that the samples were prepared from.

*Table 6.6: Results from in total 9 Brazilian tests on SSW saturated samples at 130$^0$C*

| Core | Diameter [mm] | Length [mm] | Porosity [%] | Peak force (kN) | Tob [Mpa] | Correction factor |
|---|---|---|---|---|---|---|
| *LK25 (1)* | 37.02 | 22.42 | 39.61 | 0.15 | 0.12 | 0.277 |
| *LK25 (2)* | 37.02 | 22.23 | 39.61 | 0.21 | 0.16 | 0.241 |
| *LK25 (3)* | 37.02 | 23.01 | 39.61 | 0.36 | 0.27 | 0.261 |
| *LK32 (1)* | 36.89 | 23.53 | 39.96 | 0.59 | 0.44 | 0.250 |
| *LK32 (2)* | 36.89 | 18.74 | 39.96 | 0.24 | 0.22 | 0.289 |
| *LK32 (3)* | 36.89 | 25.36 | 39.96 | 0.54 | 0.36 | 0.260 |
| *LK35 (1)* | 36.97 | 22.77 | 39.30 | 0.51 | 0.38 | 0.241 |
| *LK35 (2)* | 36.97 | 23.71 | 39.30 | 0.23 | 0.17 | 0.265 |
| *LK35 (3)* | 36.97 | 21.23 | 39.30 | 0.33 | 0.27 | 0.268 |

The average tensile strength ( $\overline{T_{ob}}$ ) was calculated to be 0.27 MPa with a standard deviation of ±0.10 MPa.

**Mohr and q-p´ plots**

On the basis of the maximum ($\sigma_1'$) and minimum ($\sigma_3'$) effective stress values in Table.6.5 the Mohr circles for the tests can be drawn as shown in *Fig.6.7*. The hydrostatic tests are not included. A failure line is drawn manually in such a manner that it tangents the first four Mohr circles. From the point of intersection with the ordinate axis the cohesion is determined while the friction angle will determined from the inclination of the drawn failure line.

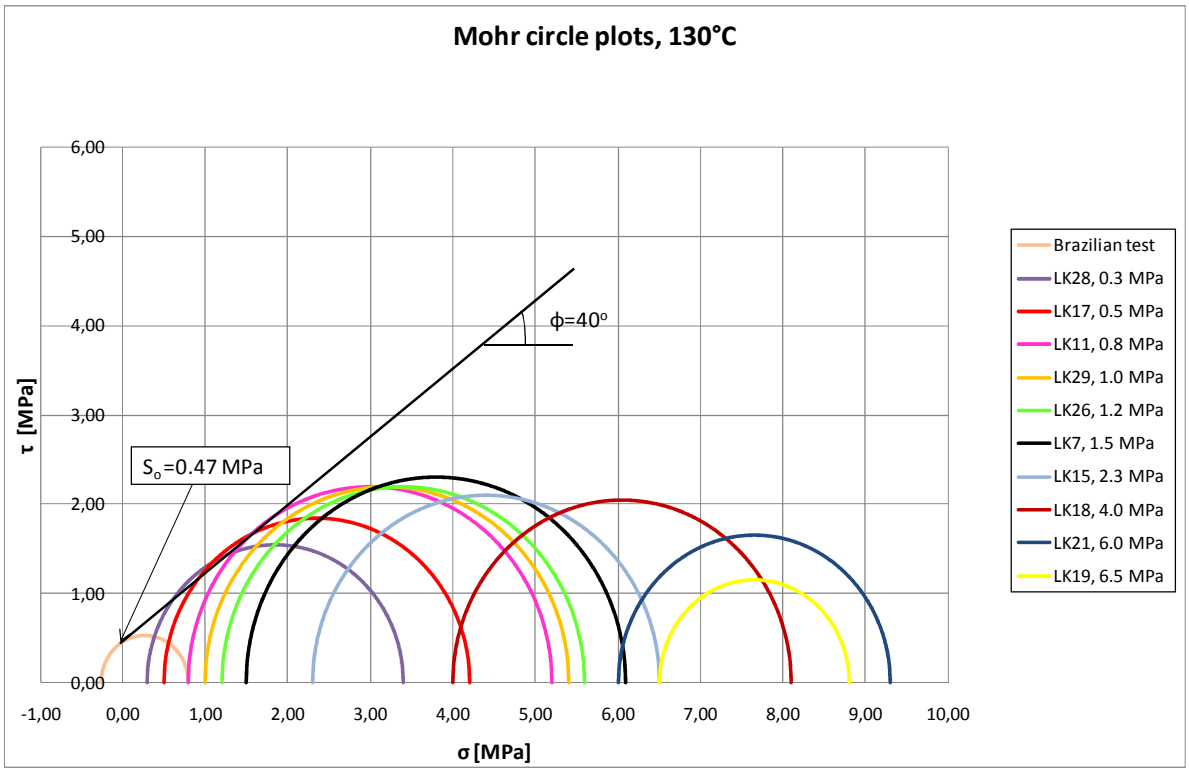


*Fig.6.7: Mohr circles for all the deviatoric tests performed at 130$^0$C. A failure line is drawn manually so that it tangents the first four Mohr circles. Cohesion is found from the point of intersection with the ordinate axis while the friction angle will be determined from the inclination of the failure line.*

In *Fig.6.8* the results from Table 6.5 are shown in a q-p´ plot.

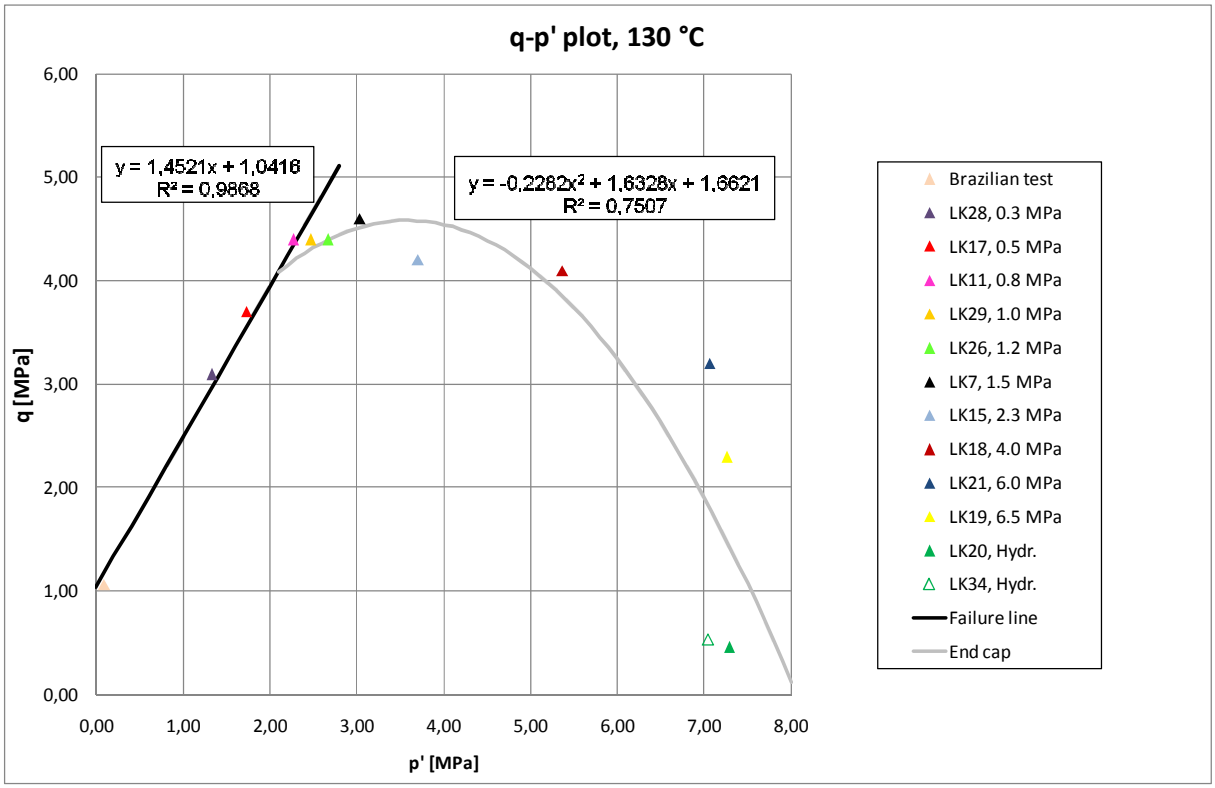


*Fig.6.8: q-p´ plot of all the tests performed at 130 °C. A Linear regression is performed on the results from the first 4 tests to obtain an expression of the failure line, while the shape of the end cap is obtained by performing a second order polynomial regression on the results from the remaining tests.*

A linear regression of the first four data points is used to find an expression for the failure line. The shape of the end cap is found by performing a second order polynomial regression on the results from the remaining tests.

The cohesion and friction angle can be determined from the slope and point of intersection with the ordinate axis for the failure line in *Fig.6.8*. These values are used in the Mohr Coulomb criterion to give an expression for the calculated failure line. In *Fig.6.9* the calculated failure line from the q-p´ plot in *Fig.6.8* is compared to the drawn failure line in *Fig.6.7*.

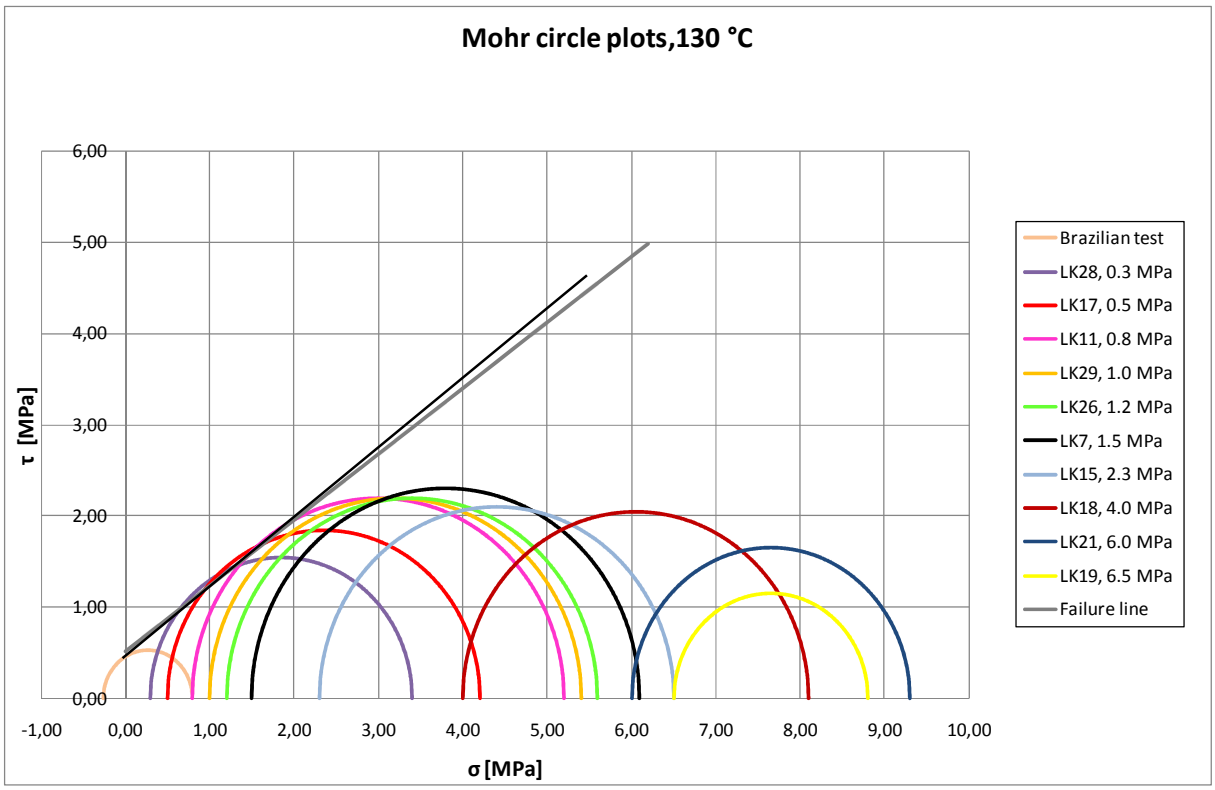


*Fig. 6.9: Mohr plot of all the tests performed at 130$^0$C. The gray failure is the calculated failure line from the q-p´ plot in Fig.6.8, while the black is the drawn failure line from the Mohr plot in Fig.6.7.*

Due Brazilian tests the cohesion will be quite similar for the two failure lines in *Fig. 6.9*. The main difference between these two lines will be in the inclination. In *Table 6.7* the influence that this difference in inclination has on mechanical parameters like cohesion, friction angle, coefficient of internal friction (μ) and failure angle (β) are shown.

*Table 6.7: Table over the main differences between the calculated failure line from the q-p´ plot in Fig.6.8 and the drawn failure in Fig.6.7*

| Mechanical parameters | Failure line drawn from Mohr plot | Failure line calculated from q-p´plot |
|---|---|---|
| $S_o$ [MPa] | 0.47 | 0.52 |
| $\varphi^o$ | 40 | 36 |
| μ | 0.84 | 0.72 |
| $\beta^o$ | 65 | 63 |

As for the tests performed at ambient temperature the friction angle for the calculated failure line from the q-p´ -plot in Table 6.7 will be higher than the drawn failure line from the Mohr plot. The friction angle calculated from the q-p´ plot in *Fig.6.8* is more realistic compared to the drawn failure line from the Mohr plot in *Fig.6.7*. These results also confirm that using the q-p´ plot to estimate cohesion and friction angle is an applicable method which also here give more accurate results compared to the drawn failure from a Mohr plot.

### 6.1.3 Creep tests

In total two cores were prepared for creep tests where SSW should be used as saturation and flooding fluid. These cores were not aged prior testing but the tests were performed at $130^0$C. The first creep tests performed on LK94 was flooded with SSW through the entire test while the creep test performed on LK95 was first flooded with SSW after 9602 minutes. This was a result of a closed valve on the flooding cell which first was detected after 9602 minutes. As soon as this was detected SSW flooding was started. The DW flooding affected both the yield point and the strain experiences as creep stress was reached as seen in Table.6.8.

*Table 6.8: Table of the mechanical parameters determined from the hydrostatic phase up to the creep stress of 12MPa for LK94 and LK95*

| Core | Porosity [%] | Yield Point [MPa] | K-modulus [GPa] | Strain at creep stress [%] |
|---|---|---|---|---|
| LK94 | 39.12 | 8.40 | 0.655 | 0.85 |
| LK95* | 39.59 | 9.60 | 0.814 | 0.52 |

** Flooded with distilled water (DW) due to a mistake*

Yield points were determined in the hydrostatic phases at the point where the stress strain curve starts to deviate from a linear trend as shown in *Fig.6.1*. The Bulk modulus was determined from the slope of the stress versus volumetric strain curve prior to yield as shown in *Fig.6.3*. When comparing the yield points for the two tests in *Table 6.8* a clear difference in strength is observed. LK95 which was flooded with DW yields at a higher stress level and is stronger against hydrostatic compression (K-modulus) compared to LK94 which was flooded with SSW. The strain experienced as the creep stress of 12.0 MPa was reached is a factor 1.64 higher for LK94 compared to LK95. The results in Table 6.8 gives a strong impression of the impact SSW has on the mechanical strength of chalk.

The test procedure for the second creep tests was initially to flood with SSW until steady state creep was obtained and then introduce SSW-($SO_4^{2-}$) to see how this affects the creep curve. Because if the presence of sulphate ($SO_4^{2-}$) in the flooding fluid has a weakening effect on chalk during creep deformation the deformation rate should decrease if sulphate is removed. During the experimental work with this thesis it also became interesting to study the effect dissolution of calcium carbonate ($CaCO_3$) has on the creep behaviour. If creep deformation is solely a result of increased dissolution of calcium carbonate a significant increase in calcium concentration in the flooding fluid should decrease the deformation rate considerably or even cease it. The plan was therefore to introduce a new SSW-($SO_4^{2-}$) solution with ten times the concentration of calcium after a period of pure SSW-($SO_4^{2-}$) flooding to see how this affected the creep behaviour. The reason for flooding synthetic seawater *without* sulphate was to remove sulphate from the synthetic seawater present in the pore space. Sulphate reacts strongly with calcium which results in precipitation of anhydrite ($CaSO_4$). Such precipitation can block the pore throats making it difficult to flood fluid through the core. But due to the flooding of distilled water and time limitations it was decided to continue the creep tests on LK95 with a short period of SSW followed by SSW-($SO_4^{2-}$) to see what effect this would have on the creep behaviour. In *Fig.6.10* the creep phases for both the tests performed on LK94 and LK95 are included.

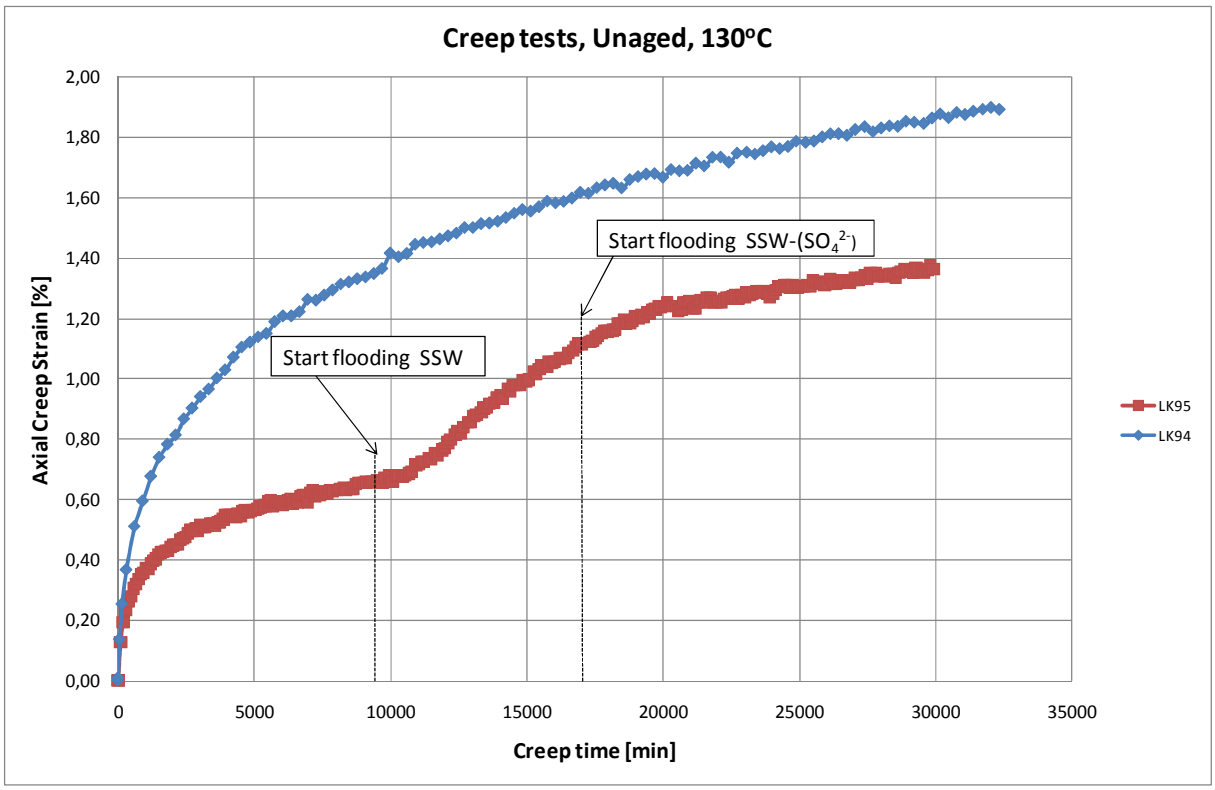


*Fig.6.10: Creep curves for LK94 and LK95 flooded with a constant flooding rate equal to 1 PV/day at 130 °C. Due to a mistake LK95 was flooded with distilled water until SSW flooding was started after 9602 minutes. SSW flooding was continued until* SSW-($SO_4^{2-}$) *was started after 16811 minutes. The test performed on LK94 was terminated after 32040 minutes when the outlet was blocked due to precipitation of anhydrite ($CaSO_4$). This core was initially flooded with a constant flooding rate equal to 1 PV/day, but due to precipitation of anhydrite the pumping rate was reduced to 0.5 PV/day after 19 447 minutes in an effort to flood the core as long as possible.*

The test performed on LK94 was terminated after 32 040 minutes when the outlet was blocked due to precipitation of anhydrite ($CaSO_4$) at the outlet. Evidence of precipitation of anhydrite was seen after approximately 18 000 minutes when the differential pressure started to increase significantly. In an effort to continue the tests as long as possible the flooding rate was reduced to 0.5 PV/day 19 447 minutes into the creep. From *Fig.6.10* it appears that the reduction in flooding rate did not have any visale effects on the creep behaviour.

When comparing the two creep curves for LK94 and LK95 in *Fig.6.10* it is visible that flooding with distilled water had a significant effect on the overall creep behaviour for LK95. The overall creep deformation for LK94, which was flooded with SSW during the whole tests, is significantly higher compared to LK95 which was flooded with distilled water. As SSW flooding was started a significant increase in creep strain is visible which also can be regarded as a period of accelerating creep. As SSW-($SO_4$) is flooded through the core the deformation rate decreases which indicate an increase in the resistance against hydrostatic compression. By plotting the axial creep strain against logarithmic time one can estimate the creep rate for the given tests as shown in *Fig.6.11*. The creep rates are found from the slope of the last data points. One requirement for estimating the creep rate is that the core experiences steady state deformation.

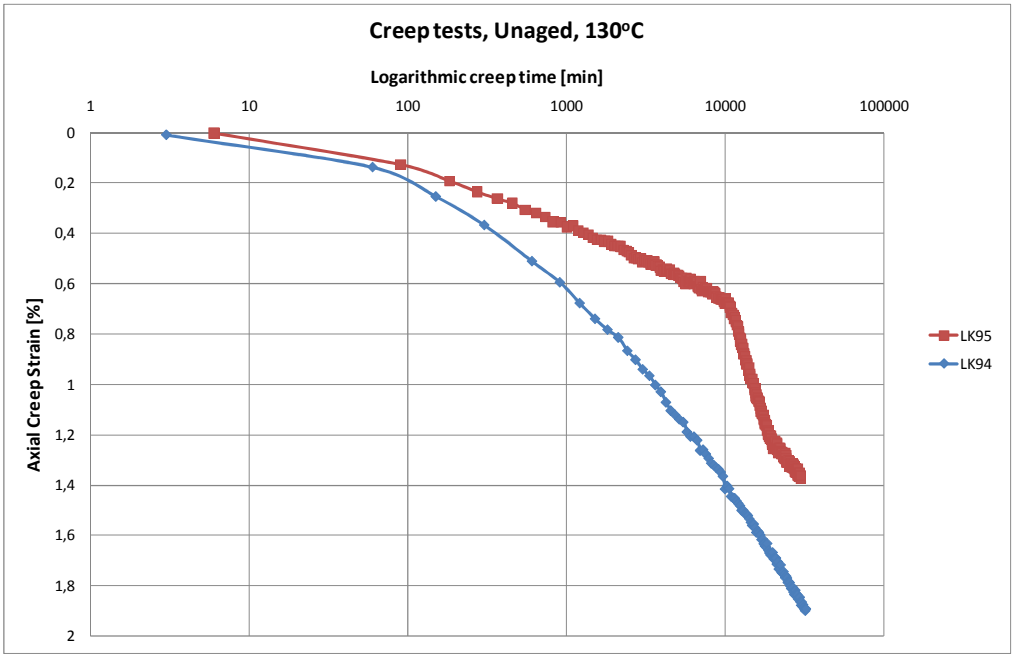


*Fig.6.11: The axial creep strain experienced for LK94 and LK95 plotted against logarithmic time. From the slope of the last data points the creep rate for the material can be determined. For LK95 three different flooding phases was included and the creep rate was estimated for each of these phases.*

The creep rate is determined from the slope of the last points in the steady state period. For the test performed LK95 three different flooding phases were included. For each of these phases the creep rate is determined from the last data points before changing the flooding fluid. In *Table 6.9* these calculated creep rates are shown with the chosen creep time at end point. The second data point needed to calculate the creeps rates were chosen at a logged data point which was somewhat earlier than the end point shown in *Table 6.9*

*Table 6.9: Overview of the calculated creep rates obtained for the tests performed on LK94 and LK95 with the end point used in the calculation included*

| Core | Flooding fluid | Creep time at end point [min] | Creep rate [%/decade] |
|---|---|---|---|
| LK94 | SSW | 31 086 | 0.98 |
| LK95 | DW | 9 006 | 0.36 |
| | SSW | 16 416 | 1.46 |
| | SSW-(SO42-) | 29 910 | 0.81 |

From the results in Table 6.9 the effect of changing flooding fluids for the test performed on LK95 is very clear. The lowest creep rate is obtained when distilled water (DW) is flooded trough the core, when SSW is introduced the creep rate increases significantly. As SSW-($SO_4$) is flooded through the core is the creep rates decreases to almost half the deformation rate seen during SSW flooding. When comparing the creep rates for the SSW flooding phases for LK94 an LK95 in *Table 6.9* it is seen that the creep rate for LK95 is lower compared to the creep rate for LK94. This indicates that steady state creep behaviour for LK95 is not that well defined as for LK94. Had the SSW flooding been continued for a longer period of time such a large difference in creep rates may not have been seen.

## 6.2 Synthetic Seawater without sulphate SSW-(SO42-)

The results from the tests saturated and flooded with SSW-($SO_4^{2-}$) were provided from a parallel master thesis (*Øvstebø, 2011*). Since the only difference between these two theses is the presence of sulphate ($SO_4^{2-}$) the data obtained by *Øvstebø, (2011)* could be used to thoroughly study the effect sulphate has on the mechanical strength of Liegé outcrop chalk. The results from *Øvstebø (2011)* will be presented in following chapters.

### 6.2.1 Ambient temperature

**Mechanical results in tables**

In total 9 different deviatoric tests were performed at ambient temperature. Brazilian and hydrostatic tests were included to obtain data points close to the ordinate and abscissa in the Mohr and q-p´ plots. The mechanical results obtained from these tests are listed in *Table 6.10.*

*Table 6.10: Table over mechanical results obtained at ambient temperature*

| Test type | Test core | Unaged/Ambient or Aged/130 °C | Porosity [%] | $\sigma'_1$ [MPa] | $\sigma'_3$ [MPa] | q [MPa] | p' [MPa] | E-modulus [GPa] | K-modulus [GPa] |
|---|---|---|---|---|---|---|---|---|---|
| Brazilian test | | Unaged/Ambient | | 1.38 | -0.46 | 1.84 | 0.15 | | |
| 0.3 MPa Dev. | LK68 | Unaged/Ambient | 39.83 | 5.20 | 0.30 | 4.90 | 1.93 | 1.376 | |
| 0.5 MPa Dev. | LK48 | Unaged/Ambient | 39.71 | 4.20 | 0.50 | 3.70 | 1.73 | 1.480 | |
| 0.5 MPa Dev. | LK46 | Unaged/Ambient | 39.50 | 4.80 | 0.50 | 4.30 | 1.93 | 1.234 | |
| avg(0.5 MPa Dev.)* | LK48/LK46 | Unaged/Ambient | | 4.50 | 0.50 | 4.00 | 1.83 | | |
| 1.0 MPa Dev. | LK38 | Unaged/Ambient | 40.19 | 6.20 | 1.00 | 5.20 | 2.73 | 1.262 | |
| 1.2 MPa Dev. | LK93 | Unaged/Ambient | 39.96 | 6.20 | 1.20 | 5.00 | 2.87 | 1.299 | |
| 2.3 MPa Dev. | LK67 | Unaged/Ambient | 39.96 | 8.40 | 2.30 | 6.10 | 4.33 | 1.577 | |
| 4.0 MPa Dev. | LK64 | Unaged/Ambient | 40.22 | 9.30 | 4.00 | 5.30 | 5.77 | 1.508 | |
| 7.0 MPa Dev. | LK92 | Unaged/Ambient | 39.10 | 11.40 | 7.00 | 4.40 | 8.47 | 1.907 | |
| 8.0 MPa Dev. | LK98 | Unaged/Ambient | 39.93 | 12.50 | 8.00 | 4.45 | 9.50 | 1.805 | |
| Hydr. | LK66 | Unaged/Ambient | 40.18 | 10.70 | 10.20 | 0.60 | 10.37 | | 0.689 |

* *Average value calculated from the two 0.5 MPa deviatoric tests performed at ambient temperature*

Yield points for the different triaxial tests are presented as the maximum principle stress ($\sigma_1'$) in *Table 6.10* while the minimum principle stresses ($\sigma_3'$) are the difference between the confining pressure and the pore pressure. Yield points, E-moduli and bulk moduli are determined according to *Fig.6.1*, *Fig.6.2* and *Fig.6.3* respectively. The results from the Brazilian tests presented in *Table 6.10* are determined from an average tensile strength ( $\overline{T_{ob}}$ ) calculated on the basis of 12 individual tests performed on SSW-($SO_4^{2-}$) saturated cores at ambient temperature shown in *Table 6.11*.

*Table 6.11: Overview of the result obtained from 12 individual Brazilian tests performed on SSW-($SO_4^{2-}$) saturated samples at ambient temperature*

| Core | Diameter [mm] | Length [mm] | Pore volume [ml] | Bulk volume [ml] | Porosity [%] | Peak force [kN] | Tob [MPa] |
|---|---|---|---|---|---|---|---|
| LK (5.1) | 36.98 | 24.30 | 10.25 | 26.10 | 39.27 | 0.614 | 0.435 |
| LK (5.2) | 36.96 | 24.89 | 10.70 | 26.70 | 40.07 | 0.801 | 0.554 |
| LK (5.3) | 36.95 | 21.62 | 9.40 | 23.18 | 40.55 | 0.676 | 0.538 |
| LK (6.1) | 36.98 | 22.83 | 9.75 | 24.52 | 39.76 | 0.732 | 0.552 |
| LK (6.2) | 36.97 | 24.04 | 10.30 | 25.81 | 39.91 | 0.758 | 0.543 |
| LK (7.1) | 36.99 | 22.06 | 9.54 | 23.71 | 40.24 | 0.414 | 0.323 |
| LK (7.2) | 36.98 | 19.91 | 8.48 | 21.38 | 39.66 | 0.495 | 0.428 |
| LK (7.3) | 36.98 | 21.18 | 8.92 | 22.75 | 39.21 | 0.564 | 0.458 |
| LK (8.1) | 36.96 | 21.90 | 9.10 | 23.50 | 38.73 | 0.460 | 0.362 |
| LK (8.2) | 36.97 | 20.39 | 8.30 | 21.89 | 37.92 | 0.460 | 0.388 |
| LK (8.3) | 37.00 | 20.43 | 8.63 | 21.97 | 39.29 | 0.455 | 0.383 |
| LK (9.1) | 36.96 | 22.84 | 9.62 | 24.50 | 39.26 | 0.760 | 0.573 |

The average tensile strength ( $\overline{T_{ob}}$ ) for these tests were calculated to be 0.46 MPa with a standard deviation of ±0.08 MPa.

**Mohr and q-p´ plots**

By using the yield point values in *Table 6.10* the Mohr circle for each individual test can be drawn in the τ σ-plane like shown in *Fig.6.12*. The failure line is drawn manually so that it tangents the Mohr circles for the Brazilian tests, the 0.5 MPa deviatoric test and the 1.0 MPa deviatoric test.

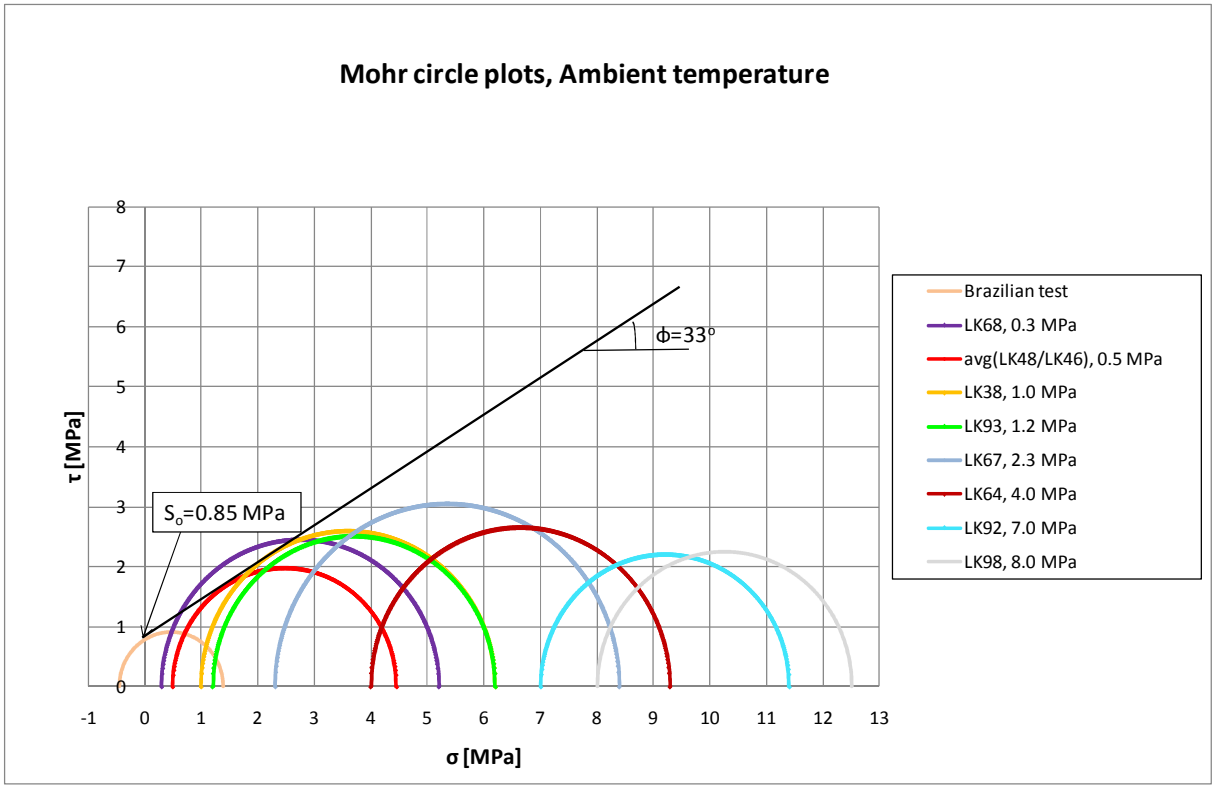


*Fig.6.12: Mohr circles for tests performed at ambient temperature. The failure line is drawn manually so that it tangents the Mohr circles for the Brazilian tests, the 0.5 MPa deviatoric test and the 1.0 MPa deviatoric test. The Mohr circle for the 0.3 MPa deviatoric tests is neglected as it appears to deviate from the linear trend which the other deviatoric tests up to 1.0 MPa follows. Cohesion ($S_o$) and friction angle ($\varphi$) is determined from the drawn failure line.*

The failure line in *Fig.6.12* in such a manner that it does not tangent the 0.3 MPa deviatoric test. This because core LK68 appears to be somewhat stronger than the other cores which makes is difficult to compare the results obtained from this test with the other tests performed with low effective radial stress. The result for the 0.3 MPa deviatoric test is therefore neglected and will not be used further in this thesis. In total two 0.5 MPa deviatoric tests were performed and the Mohr circle in *Fig.6.12* is the drawn on basis of the average yield point for these two tests.

The results in *Table 6.10* can also be plotted in a q-p´ plotlike shown in *Fig.6.13* such that the entire failure envelope for the material can be drawn. Here the hydrostatic test is also included to obtain a data point close to the abscissa.

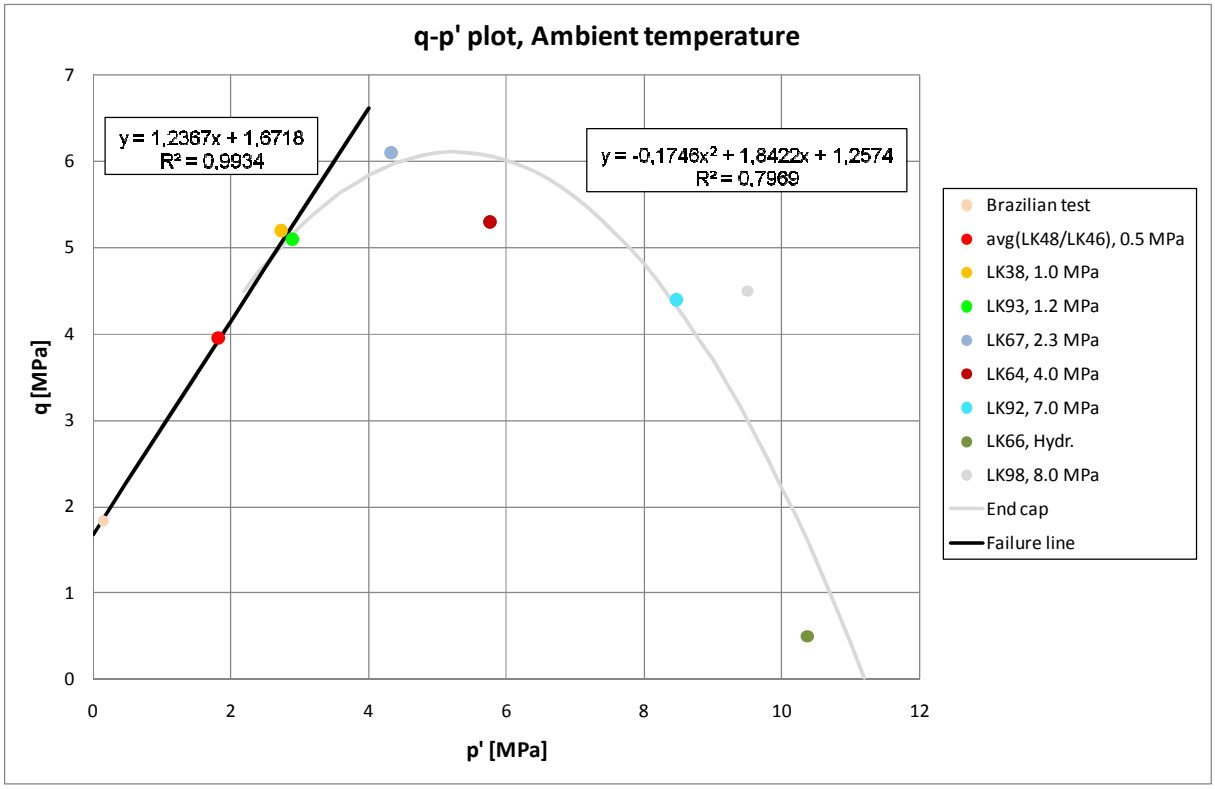


*Fig.6.13: q-p´ plot for all the tests performed ambient temperature. The failure line is found by performing a linear regression on the results from the four first tests while the shape of the end cap section is found by performing a second order polynomial regression on the results from the remaining tests.*

A linear regression is performed on the first four data points in *Fig.6.13*. From the expression obtained from this regression the failure line can be drawn in the q-p´ plot. The shape of the end cap is found by performing a second order polynomial regression on the results for the remaining tests. From the slope and point of intersection of the failure line in the q-p´ plot the cohesion ($S_o$) and friction angle ($\varphi$) can be determined. These calculated values can then be used in the Mohr Coulomb criterion such that an expression for the failure line can be obtained. In *Fig.6.14* this calculated failure line from the q-p´ plot in *Fig.6.13* is compared to the drawn failure line from the Mohr plot in *Fig.6.12*.

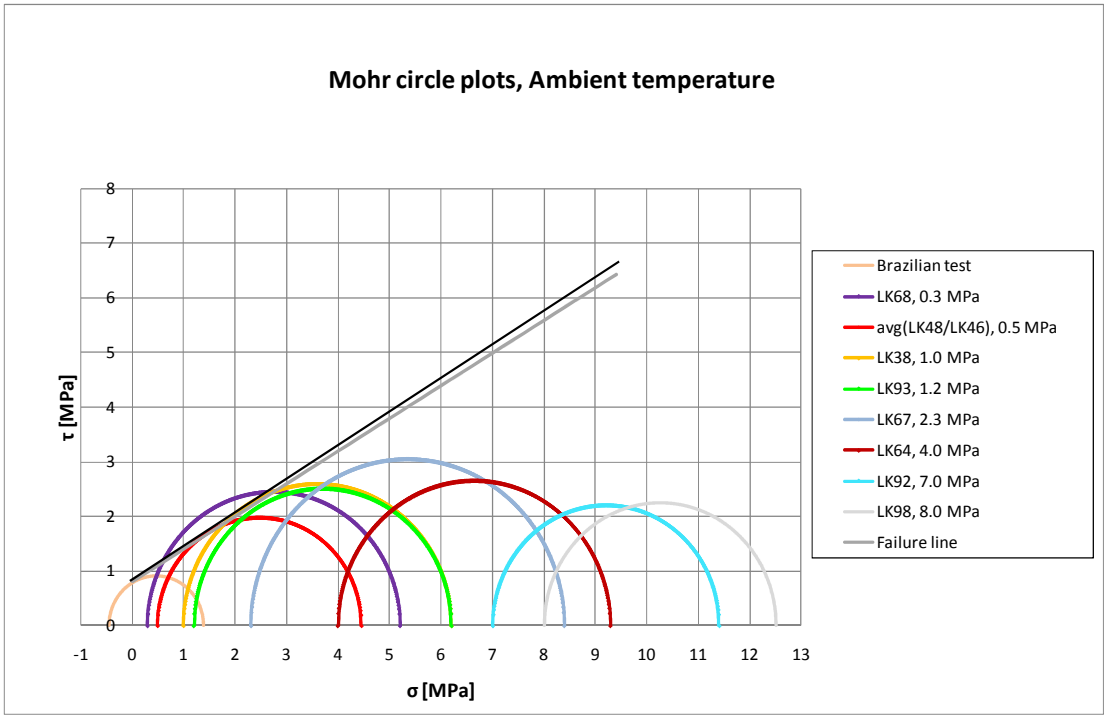


*Fig.6.14: Mohr plot for tests performed at ambient temperature with both the calculated failure line from the q-p´ plot in Fig.6.13 (grey line ) and the drawn failure line from the Mohr plot in Fig.6.12 included (black line)*

As can be seen in *Fig.6.14* there is only minor differences between the calculated failure line found from the q-p´ plot in *Fig.6.13* and drawn failure line from the Mohr plot in *Fig.6.12*. This is a result of neglecting the 0.3 MPa deviatoric test which appear to be somewhat stronger than the other deviatoric tests with low effective radial stress. Cohesion which is determined from the point of intersection with the ordinate will be very similar for the two failure lines in *Fig.6.14*. The main difference will be in how these lines tangents the Mohr circles which again affect the inclination. *Table 6.12* shows how mechanical properties like cohesion, friction angle, coefficient of internal friction (μ) and failure angle (β) are affected by the inclination of the failure lines.

*Table 6.12: Overview of the main differences between the calculated failure line from the q-p´ plot in Fig.6.14 and the drawn failure line from the Mohr plot in Fig.6.13*

| Mechanical parameters | Failure line drawn from Mohr plot | Failure line calculated from q-p´plot |
|---|---|---|
| $S_o$ [MPa] | 0.85 | 0.81 |
| $\varphi^o$ | 33 | 31 |
| μ | 0.65 | 0.60 |
| $\beta^o$ | 62 | 61 |

As for the SSW tests the calculated friction angle from the q-p´ plot in Table 6.12 are lower than the drawn failure line from the Mohr plot. The difference between the two methods in Table 6.12 are not that significant as for the SSW tests but the calculated failure line from the q-p´ plot in *Fig. 6.13* appear to give a failure line that tangents the Mohr circles in *Fig.6.14* somewhat better than the drawn failure line from *Fig. 6.12*.

### 6.2.2 130 ℃

**Mechanical results in tables**

In total 12 triaxial tests were performed on at 130 °C, 11 of these tests were deviatoric tests with varying degree of radial support while the last test was a hydrostatic test. Brazilian and hydrostatic tests are included such that data points close to the ordinate and abscissa can be obtained. In *Table 6.13* the results from all the tests performed at 130 °C are listed.

*Table 6.13: Table of the mechanical results obtained for tests performed at 130 °C*

| Test type | Test core | Unaged/Ambient or Aged/130 °C | Porosity [%] | $\sigma'_1$ [MPa] | $\sigma'_3$ [MPa] | q [MPa] | p' [MPa] | E-modulus [GPa] | K-modulus [GPa] |
|---|---|---|---|---|---|---|---|---|---|
| Brazilian test | | Aged/130 °C | | 1.56 | -0.52 | 2.08 | 0.17 | | |
| 0.3 MPa Dev. | LK50 | Aged/130 °C | 39.53 | 4.40 | 0.30 | 4.10 | 1.67 | 1.155 | |
| 0.5 MPa Dev. | LK62 | Aged/130 °C | 40.22 | 4.90 | 0.50 | 4.40 | 1.97 | 1.277 | |
| 0.8 MPa Dev. | LK69 | Aged/130 °C | 39.10 | 5.40 | 0.80 | 4.60 | 2.33 | 1.378 | |
| 1.0 MPa Dev. | LK57 | Aged/130 °C | 40,00 | 6.20 | 1.00 | 5.20 | 2.73 | 1.346 | |
| 1.2 MPa Dev. | LK70 | Aged/130 °C | 39.75 | 6.70 | 1.20 | 5.50 | 3.03 | 1.094 | |
| 1.5 MPa Dev. | LK65 | Aged/130 °C | 39.27 | 7.40 | 1.50 | 5.90 | 3.47 | 1.169 | |
| 1.8 MPa Dev. | LK74 | Aged/130 °C | 39.58 | 8.30 | 1.80 | 6.50 | 3.97 | 1.172 | |
| 2.3 MPa Dev. | LK58 | Aged/130 °C | 40.13 | 7.10 | 2.30 | 4.80 | 3.90 | 1.186 | |
| 3.0 MPa Dev. | LK59 | Aged/130 °C | 39.79 | 8.10 | 3.00 | 5.10 | 4.70 | 1.355 | |
| 4.0 MPa Dev. | LK47 | Aged/130 °C | 39.07 | 9.00 | 4.00 | 5.00 | 5.67 | 1.134 | |
| 7.0 MPa Dev. | LK51 | Aged/130 °C | 40.19 | 11.80 | 7.00 | 4.80 | 8.60 | 1.360 | |
| Hydr. | LK52 | Aged/130 °C | 40.11 | 10.80 | 10.30 | 0.50 | 10.47 | | 0.587 |

Yield points were determined according to *Fig.6.1*. The yield points are presented as the maximum principle stress ($\sigma_1'$) in *Table 6.13*. Minimum principle stress ($\sigma_3'$) will be the difference between the confining and pore pressure also known as the effective radial stress. The results for the Brazilian tests are calculated from an average tensile strength ( $\overline{T_{ob}}$ ) determined from in total 10 individual tests performed on SSW-($SO_4^{2-}$) saturates samples at 130 °C as shown in *Table 6.14*

*Table 6.14: Table of the results obtained from in total 10 individual Brazilian tests on SSW-($SO_4^{2-}$) saturated sample at 130 °C*

| Core | Diameter [mm] | Length [mm] | Porosity [%] | Peak force (kN) | Tob [Mpa] | Correction factor |
|---|---|---|---|---|---|---|
| LK27 B | 36.95 | 24.36 | 39.38 | 0.65 | 0.46 | 0.237 |
| LK41 B | 36.96 | 21.82 | 40.35 | 0.70 | 0.55 | 0.270 |
| LK41 M | 36.96 | 20.66 | 40.35 | 0.61 | 0.51 | 0.233 |
| LK41 T | 36.96 | 20.95 | 40.35 | 0.58 | 0.47 | 0.254 |
| LK49 M | 36.94 | 20.12 | 39.59 | 0.67 | 0.57 | 0.242 |
| LK49 T | 36.94 | 22.54 | 39.59 | 0.80 | 0.60 | 0.223 |
| LK63 B | 36.95 | 22.68 | 39.03 | 0.87 | 0.66 | 0.208 |
| LK63 M | 36.95 | 22.51 | 39.03 | 0.52 | 0.39 | 0.248 |
| LK63 T | 36.95 | 22.76 | 39.03 | 0.64 | 0.48 | 0.255 |
| LK72 B | 36.95 | 23.47 | 40.23 | 0.62 | 0.45 | 0.238 |

The average tensile strength from these 10 tests where calculated to be 0.52 MPa with a standard deviation of ± 0.08 MPa.

**Mohr and q-p´ plots**

From the results in *Table 6.13* Mohr circles can be drawn for each individual test as shown in *Fig. 6.15*. A failure line is drawn manually so that it tangents the first six Mohr circles. From the point of intersection with the ordinate axis the materials cohesion can be determined while the friction angle is determined from the inclination of the drawn failure line.


*Fig.6.15: Mohr circle plot for all the tests performed at 130 °C. A failure line is manually drawn such that it tangents the firs sixt Mohr circles. From this line the cohesion (So) is determined at the point of intersection with the ordinate and the friction angle (φ) is determined from the inclination*

The data from *Table 6.13* can also be plotted in a q-p´ plot like shown in *Fig.6.16*. The hydrostatic test is included such that a point close to the abscissa is obtained, while the Brazilian tests gives a data point close to the ordinate.

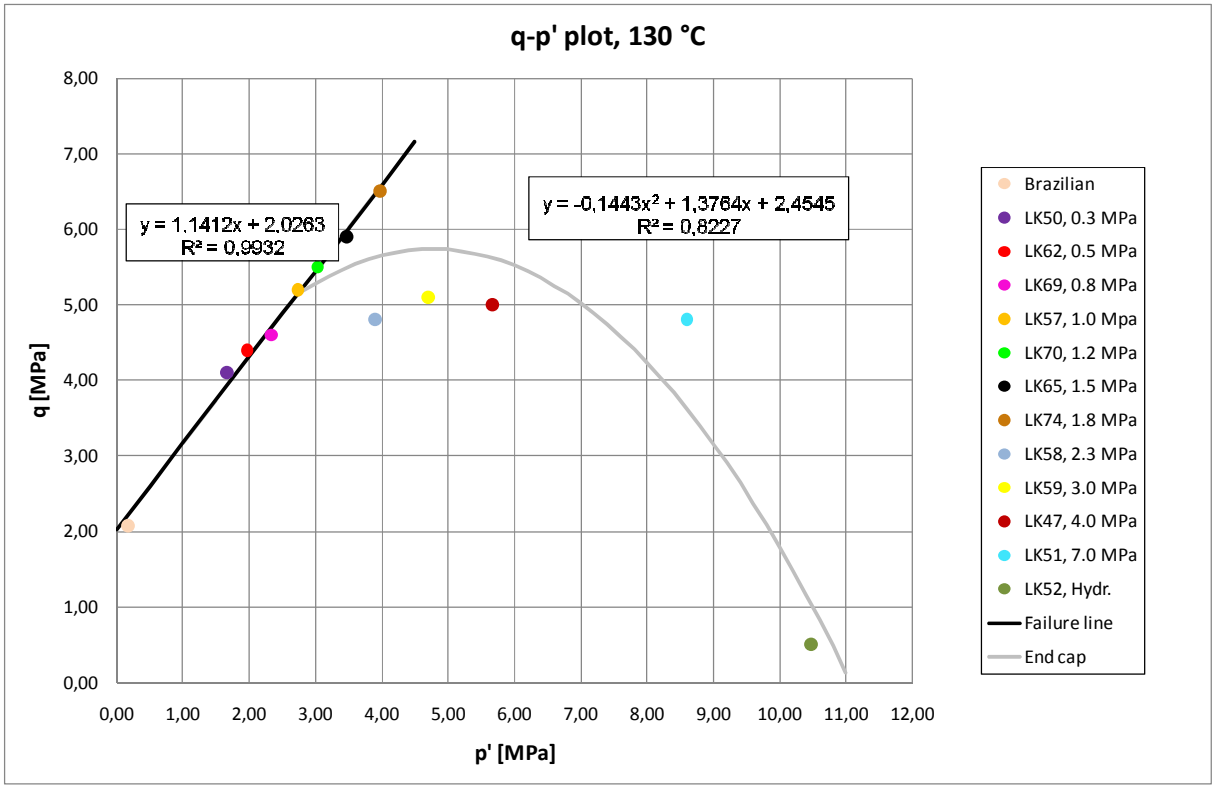


*Fig.6.16: q-p´ plot for all the tests performed at 130 °C. The failure line is found by performing a linear regression on the results from the first eight tests while the shape of the end cap is found by performing a second order polynomial regression on the results for the remaining tests.*

As can be seen in *Fig.6.16* all the data points up to the 1.8 MPa deviatoric tests appear to fall on or very close to the failure line. Between the 1.8 MPa deviatoric tests and the 2.3 MPa deviatoric tests there is a quite significant drop in strength which makes it difficult to draw the shape of the end cap. If the results of the tests performed on LK58, LK59 and LK47 are regarded as abnormally weak the whole end cap section would be lifted up towards the results from LK74. This recognition increases the uncertainty for the shape of the end cap section. The end cap curve presented in *Fig.6.16* is the best curve fit that can be obtained from the current dataset.

The failure line is found by performing a linear regression on the first eight data points. From this line the cohesion ($S_o$) and friction angle can be determined ($\varphi$). By using these values in the Mohr Coulomb criterion an expression for the failure line is obtained. This calculated failure line base on the results from the q-p´ plot in *Fig.6.16* can be compared to the drawn failure line in the Mohr plot in *Fig.6.15* as in *Fig.6.17*.

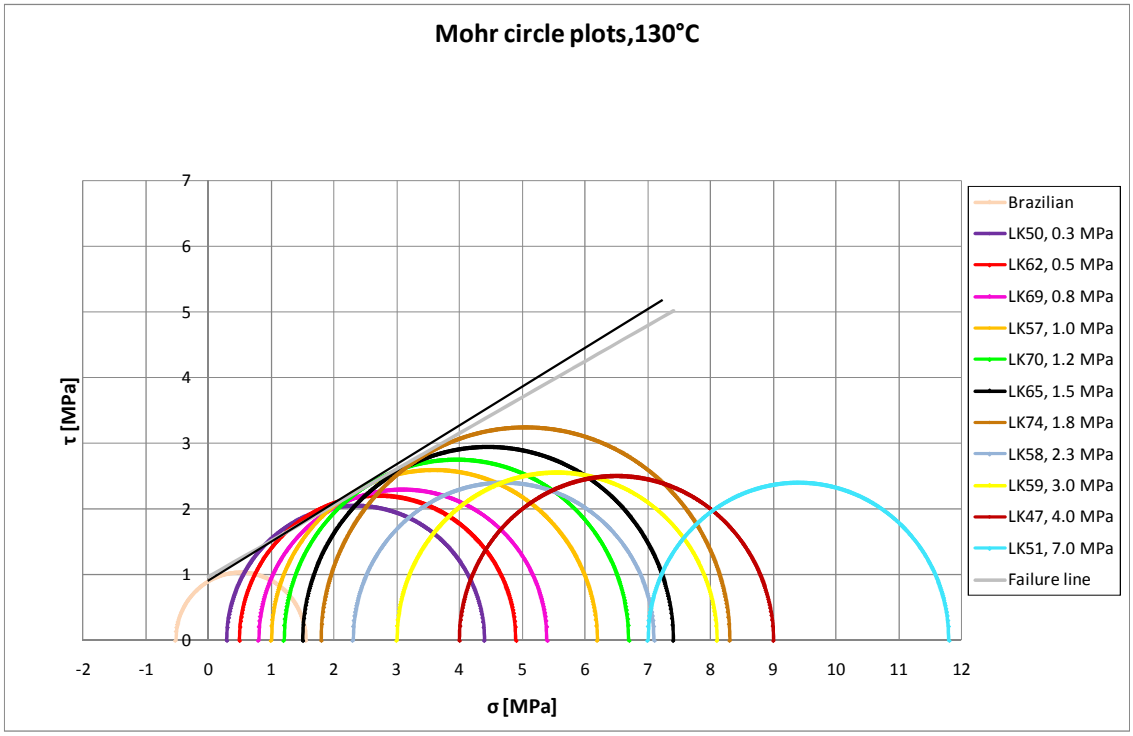


*Fig.6.17: Mohr plot for all the tests performed at 130 °C where both the calculated failure line from the q-p´ plot (gray line) and the drawn failure line from the Mohr plot in Fig.6.17(black line) are included.*

The main difference between the two failure lines in *Fig.6.17* will be in the inclination. Due to the Brazilian test the point of intersection with the ordinate axis will be quite similar for both the failure lines. *Table 6.15* lists the main difference between the calculated failure line from the q-p´ plot in *Fig.6.16* and the drawn failure line for the Mohr plot in *Fig.6.15*.

*Table 6.15: Table over the main differences between the calculated failure line from the q-p´ plot in Fig.6.17 and the drawn failure in Fig.6.16*

| Mechanical parameters | Failure line drawn from Mohr plot | Failure line calculated from q-p´plot |
|---|---|---|
| $S_o$ [MPa] | 0.93 | 0.97 |
| $\varphi^o$ | 32 | 29 |
| $\mu$ | 0.62 | 0.55 |
| $\beta^o$ | 61 | 59 |

Also in *Table 6.15* the calculated failure line based on the q-p´ plot in *Fig.6.16* will have a lower friction angle compared to the failure line drawn in the Mohr plot in *Fig.6.15*. As expected the cohesion will be quite similar for the two failure lines in *Fig.6.17*. The reason for the lower friction angle for the calculated failure line is a lower inclination compared to the drawn failure. From *Fig.6.17* it also appears that the calculated failure line from the q-p´ plot tangents the first eight Mohr circles in a more accurate way compared to the drawn failure line from the Mohr plot in *Fig.6.15*. These results conclude that calculating the cohesion and friction angle from q-p´ plots is a more accurate way compared to solely determining these parameters from Mohr plots.

### 6.2.3 Creep test

One creep tests was performed with a period of SSW-($SO_4^{2-}$) followed by a period of SSW flooding. The test was performed to study the mechanical behaviour of Liegé chalk post failure. Flooding of SSW was included to see how the creep behaviour was affected when a fluid containing sulphate ($SO_4^{2-}$) was introduced. The test was performed on LK79 which was not aged prior to testing but the entire creep test was performed at 130 °C. Mechanical parameters determined during the hydrostatic loading up to the predetermined creep stress of 12.0 MPa is shown in *Table 6.16*.

*Table 6.16: Table over the mechanical parameters determined from the hydrostatic phase up to the creep stress at 12.0 MPa for LK79*

| Core | Porosity [%] | Yield Point [MPa] | K-modulus [GPa] | Strain at creep stress [%] |
|---|---|---|---|---|
| LK79 | 40.21 | 8.20 | 0.924 | 0.55 |

Yield point and bulk modulus was determined according to *Fig.6.1* and *Fig.6.3*.

The creep curve for the tests performed on LK79 is shown in *Fig.6.18*. SSW-($SO_4^{2-}$) flooding was performed until the flooding water was changed to SSW after 50 110 minutes.

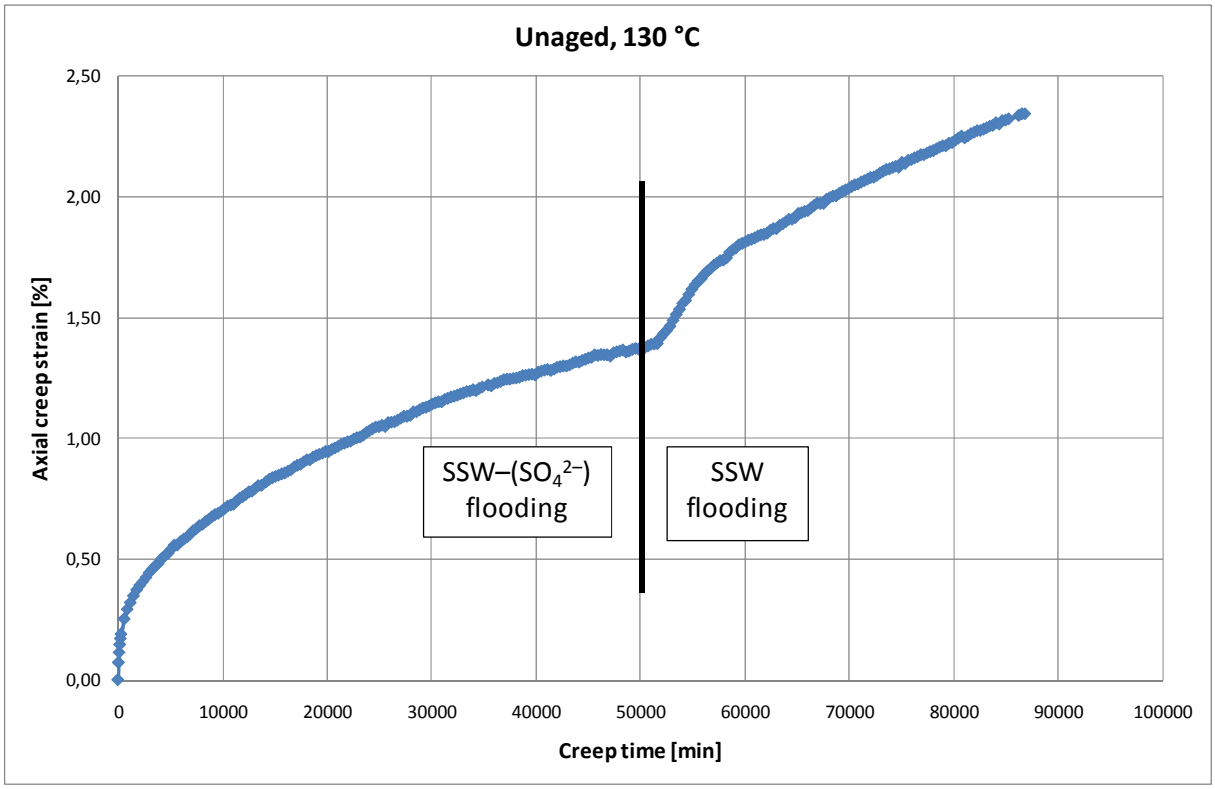


*Fig.6.18: Axial creep strain versus creep time for the test performed on LK79 at 130 °C. The creep test had two different flooding phases. In the first phase SSW-($SO_4^{2-}$) was flooded through the core. After 50 110 minutes the flooding fluid was changed to SSW. A significant increase in axial strain was detected immediately after SSW flooding was started.*

A significant increase in axial creep strain in *Fig.6.18* as SSW flooding was started. Comparing the steady state creep deformation rates for the two flooding phases it can observed that a higher deformation rate is found in the SSW flooding phase. These differences are clearer when comparing the two phases in the axial creep strain versus logarithmic time plot shown in *Fig.6.19.*

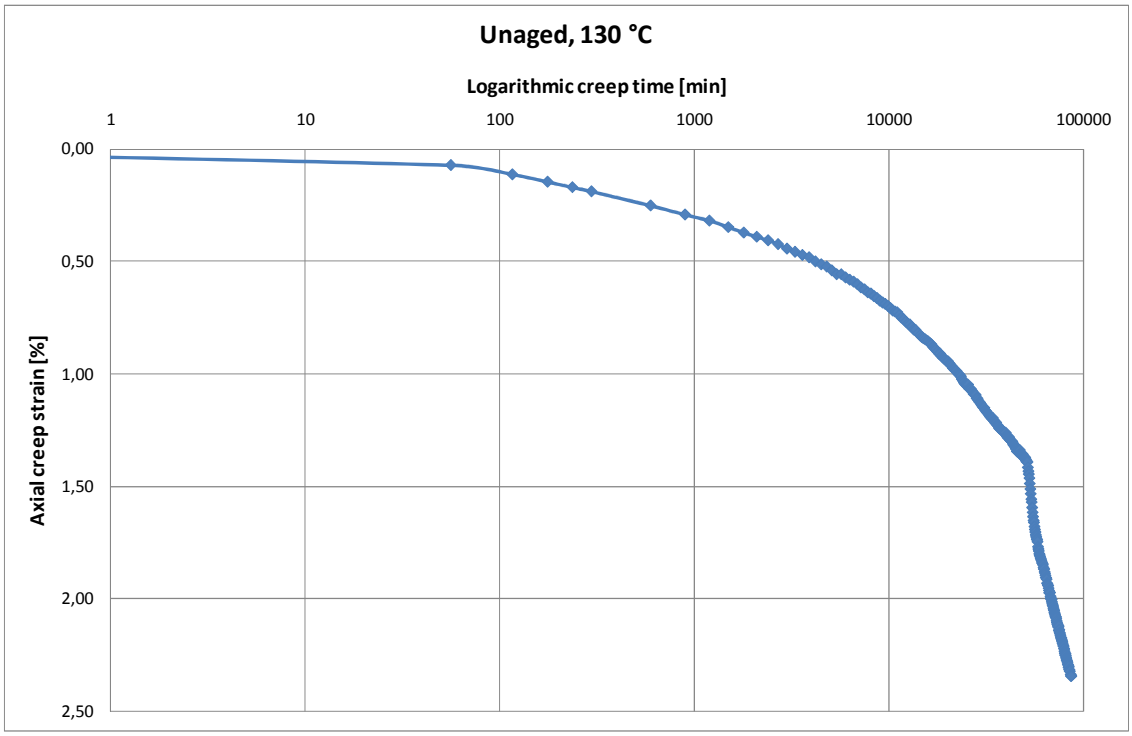


*Fig.6.19: Axial creep strain versus logarithmic time plot for the creep test performed on LK79 at 130 °C. The entire test was performed with a constant flooding rate equal to 1 PV/day. The creep rates were determined by choosing two of the last data points for each of the two flooding phases.*

The creep rates are calculated on the basis of two of the last data points for each of the flooding phases in *Fig.6.19.* In *Table 6.17* the calculated creep rates for the two flooding phases for the tests performed on LK79 is shown with the end points used in the calculation included.

*Table 6.17: Overview of the creep rates calculated for the two different flooding phases with the end point chosen for the calculation included*

| Flooding fluid | Creep time at end point [min] | Creep rate [%/decade] |
|---|---|---|
| SSW-($SO_4^{2-}$) | 45 016 | 1.15 |
| SSW | 84 306 | 3.21 |

When comparing the creep rates obtained for the two flooding phases in *Table 6.17* a significant difference is observed. The creep rate for the SSW flooding phase is almost a factor 3 higher than the creep rate obtained in the SSW-($SO_4^{2-}$) flooding phase. The data in *Table 6.17* show that the presence of sulphate in the flooding fluid for creep tests performed in Liegé chalk has a significant effect on the overall creep behaviour.

## 6.3 Chemical results

### 6.3.1 Chemical changes during aging

Chemical analysis was performed on samples taken of both SSW and SSW-($SO_4^{2-}$) brine before and after aging. In *Table 6.18* the measured ion concentrations for the SSW samples are listed.

*Table 6.18: Table over measured ion concentration before and after aging for SSW*

| Ion | Ion concentration [mol/l] | | Difference ratio ion concentraion |
|---|---|---|---|
| | Before aging | After aging | |
| $Na^+$ | 0.450 | 0.455 | 1.010 |
| $K^+$ | 0.010 | 0.010 | 1.000 |
| $Ca^{2+}$ | 0.013 | 0.035 | 2.692 |
| $Mg^{2+}$ | 0.045 | 0.020 | 0.444 |
| $Cl^-$ | 0.525 | 0.545 | 1.040 |
| $SO_4^{2-}$ | 0.024 | 0.015 | 0.625 |

When studying the results in *Table 6.18* there are three ion concentrations that appear to remain unchanged. Sodium ($Na^+$), potassium ($K^+$) and chloride ($Cl^-$) concentrations remain constant and do not appear to react with the chalk during the aging process. While magnesium ($Mg^{2+}$) and sulphate ($SO_4^{2-}$) concentrations are significantly reduced indicating a reaction between these ions and the chalk. In fact more than half the amount of the initial magnesium concentration is removed from the solution. Calcium concentration increases significantly during the aging process and is almost three times larger than the original concentration of calcium in the SSW.

Also aging chalk cores in SSW-($SO_4^{2-}$) resulted in changes in ion concentrations as shown in *Table 6.19*.

*Table 6.19: Table over measured ion concentration before and after aging for SSW-($SO_4^{2-}$)*

| Ion | Ion concentration [mol/l] | | Difference ratio ion concentraion |
|---|---|---|---|
| | Before aging | After aging | |
| $Na^+$ | 0.474 | 0.491 | 1.036 |
| $K^+$ | 0.010 | 0.010 | 1.000 |
| $Ca^{2+}$ | 0.013 | 0.042 | 3.231 |
| $Mg^{2+}$ | 0.045 | 0.020 | 0.444 |
| $Cl^-$ | 0.597 | 0.629 | 1.054 |

Also for the results in *Table 6.19* it appears that sodium, potassium and chloride remain unchanged in the brine during aging. The small variation shown in the difference ration for these ions in *Table 6.19* is within the uncertainty of the ion chromatograph used to analyse samples. The calcium concentration measured after aging was more than three times higher than the original concentration of calcium in SSW-($SO_4^{2-}$). Magnesium concentration measured after aging is less than half the initial magnesium concentration before aging.

### 6.3.2 Chemical analysis of water samples collected during creep tests

In total three creep tests were performed, where effluent water samples were collected daily. These water samples were analysed to study any chemical reactions that might take place inside the chalk cores during flooding. In *Fig.6.20* the result of the chemical analysis from the water samples collected during the creep tests on LK94 is presented. This core was flooded with SSW throughout the test.

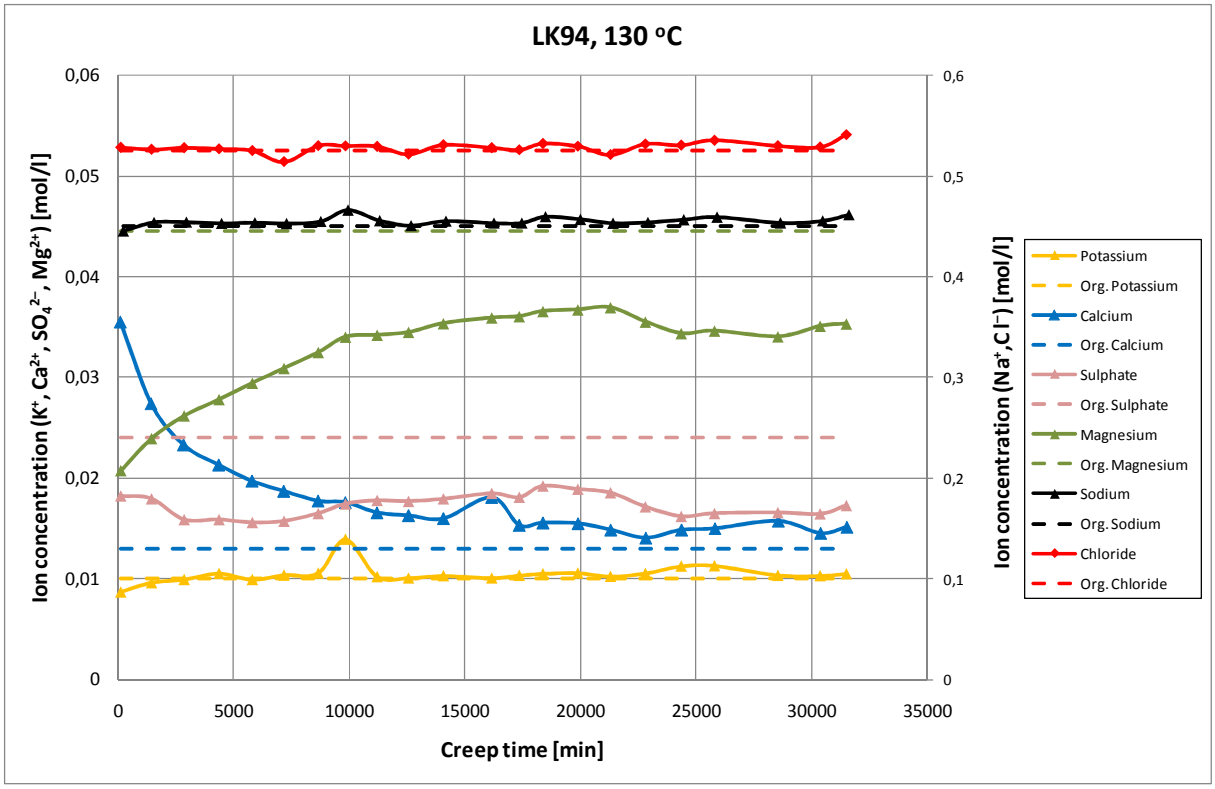


*Fig.6.20: Results of the chemical analysis performed on water samples collected during the creep test performed on LK95 which was flooded with SSW throughout the test.*

During the first 10 000 minutes of the creep test a lot of magnesium ($Mg^{2+}$) is lost inside the core as seen in *Fig.6.20*. At the same time a lot of calcium ($Ca^{2+}$) is produced. The minimum magnesium concentration measured at the start of the creep tests is 2.25 times lower than the original concentration of magnesium in the brine. For calcium the maximum concentration measured at the start of the creep tests is 2.7 times larger compared to the original concentration of calcium in SSW. Sodium ($Na^{+}$), Potassium ($K^{+}$) and chloride ($Cl^{-}$) concentrations remain constant during the entire creep tests indicating that there are no reactions taking place between these ions and the chalk. Measured sulphate ($SO_4^{2-}$) concentration remains below the original concentration of sulphate in SSW throughout the creep test indicating that a lot of sulphate is retained in the core. When the flooding rate was reduced to 0.5 PV/day after 19 447 minutes, in an effort to reduce the precipitation of anhydrite ($CaSO_4$) in the outlet, it appears to affect the ion concentrations of magnesium, calcium and sulphate as seen in *Fig.6.20*. A reduction in the measured ion concentrations for magnesium and sulphate and calcium are observed when the flooding rate was reduced.

Due to a mistake core LK95 was flooded with distilled water (DW) the first 9602 minutes of the creep test. Following this phase flooding of SSW was started. After 16811 the flooding

fluid was changed to SSW-($SO_4^{2-}$). In Fig.6.21 the chemical results from the effluent samples collected during the creep tests performed on LK95 are shown.

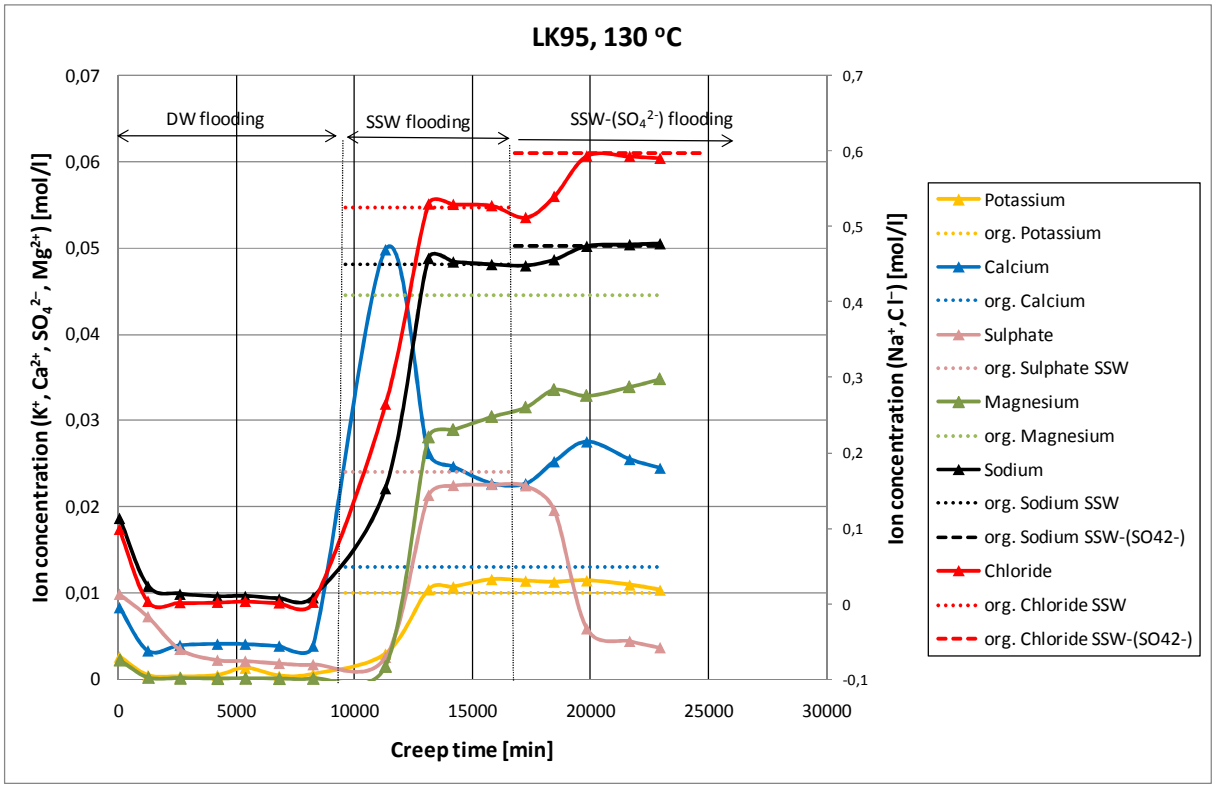


*Fig.6.21: Chemical results obtained from the analysis of water samples collected during the creep test performed on LK95. This core was flooded with three different fluids. First distilled water (DW) was flooded followed by a period of SSW flooding which was started after 9602 minutes. SSW-($SO_4^{2-}$) flooding was started after 16811 minutes.*

Core LK95 was initially saturated with SSW and as distilled water displaced the initial SSW present in the pore space the concentrations of the different ions reduce as shown in *Fig.6.21*. After seawater injection was started a large jump in all ion concentrations are observed. Calcium, chloride and sodium concentrations increase faster than the concentrations for the remaining ions indicating earlier breakthrough. During the period of SSW flooding a lot of calcium is produced from the core while magnesium and sulphate are removed. The largest reduction in ion concentration is seen for magnesium during the whole period of SSW flooding. As SSW-($SO_4^{2-}$) start to break through the core an increase in sodium and chloride concentration is observed. This increase is a result of the higher content of sodium chloride (NaCl) in SSW-($SO_4^{2-}$). As SSW-($SO_4^{2-}$) displaces the SSW in the pore space the sulphate concentration will gently reduce as shown in *Fig.6.21*. The reduction in calcium production observed at 20 000 minutes in *Fig.6.21* can be related to the reduction in deformation rate observed at the same creep time in *Fig.6.10*.

The creep test performed on LK79 consisted of two flooding periods with different flooding fluids. In the first period the core was flooded with SSW-($SO_4^{2-}$) which was changed to SSW after 50 071minutes. The chemical results from the water samples collected during the entire creep period for the tests performed on LK79 is shown in Fig.6.22.

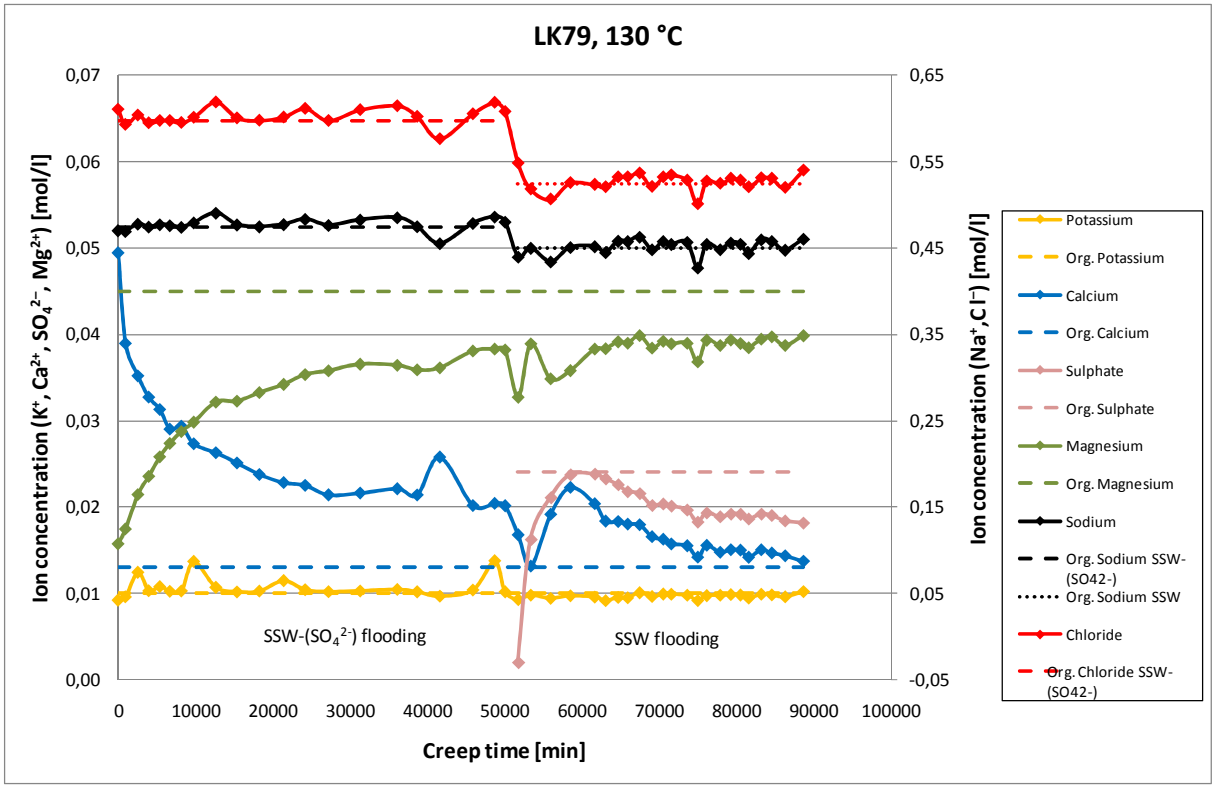


*Fig.6.22: Chemical results from the water samples collected during the creep test performed on LK79 at 130 °C. The core was flooded with SSW-($SO_4^{2-}$) until the flooding fluid was changed to SSW after 50 110 minutes.*

During the period of SSW-($SO_4^{2-}$) flooding in *Fig.6.22* a significant increase in calcium concentration is observed. At the same time a lot of magnesium is removed from the brine. The measured calcium concentration decreases through the course of the SSW-($SO_4^{2-}$) flooding phase. An opposite behaviour is seen for magnesium where the concentration increases trough the course of the SSW-($SO_4^{2-}$) flooding phase. At approximately 42 000 minutes a peak in the calcium concentration and a clear reduction in both sodium and chloride concentrations. This deviation is most likely a result of an unexpected error in the diluting process. After 50 110 minutes SSW flooding was started. The sulphate concentration starts to increase as SSW starts to break through at outlet. At the same time a reduction is sodium and chloride concentrations are observed as a result of a lower content of sodium chloride (NaCl) in SSW. As the concentration of sulphate increases an increase in calcium concentration is also observed. After reaching a maximum concentration at approximately 60 000 minutes both these concentration start to decrease with similar trends as shown in *Fig.6.22*.

# 7 Discussion

## 7.1 Effect of temperature

### 7.1.1 SSW

**Results in tables**

One method for studying the effect of temperature is by comparing the yield points for tests performed with similar degree of radial support from *Table 6.3* and *Table 6.5*. In *Table 7.1* the results from such tests both ambient temperature and at 130 °C are listed. Please note that all listed values are obtain from one tests unless otherwise is stated.

*Table 7.1: Table over the differences in yield points for similar tests performed with at ambient temperature and 130 °C*

| Test type | $\sigma_1'$ [Mpa] | | Difference [MPa] | Difference ratio |
|---|---|---|---|---|
| | Ambient | 130°C | | |
| Brazilian | 1.83 | 0.81 | 1.02 | 2.26 |
| 0.3 MPa Dev. | 5.60 | 3.40 | 2.20 | 1.65 |
| 0.5 MPa Dev. | 5.80 | 4.20 | 1.60 | 1.38 |
| 0.8 MPa Dev. | 6.80 | 5.20 | 1.60 | 1.31 |
| 1.0 MPa Dev. | 7.00 | 5.40 | 1.60 | 1.30 |
| 1.5 MPa Dev. | 7.40 | 6.10 | 1.30 | 1.21 |
| 4.0 MPa Dev. | 9.50 | 8.10 | 1.40 | 1.17 |
| Hydrostatic | 10.20* | 7.50* | 2.70 | 1.36 |
| **Average** | | | | **1.46** |

**Average value based on two hydrostatic tests*

As can be seen from *Table 7.1* the yield stress for tests performed at 130 °C are lower compared to tests performed at ambient temperature. The average difference ratio between test performed at 130 °C and ambient temperature is 1.46, i.e. the yield point is on average 1.47 times higher for test performed at ambient temperature compared to tests perform at 130 °C. This same temperature dependency is also seen when comparing the Young's modulus as shown in *Table 7.2*

*Table 7.2: Table over the differences in Young's moduli for similar test performed at ambient temperature and 130 °C*

| Effective radial stress | E-modulus [GPa] | | Difference [GPa] | Difference ratio |
|---|---|---|---|---|
| | Ambient temperature | 130°C | | |
| 0.3 MPa | 1.465 | 0.794 | 0.671 | 1.845 |
| 0.5 MPa | 1.320 | 0.947 | 0.373 | 1.394 |
| 0.8 MPa | 1.302 | 0.810 | 0.492 | 1.607 |
| 1.0 MPa | 1.597 | 0.998 | 0.599 | 1.600 |
| 1.5 MPa | 1.394 | 0.930 | 0.464 | 1.499 |
| 4.0 MPa | 1.534 | 1.097 | 0.437 | 1.398 |
| **Average** | | | | **1.557** |

When comparing the Young's modulus for the different deviatoric tests in *Table 7.1* no dependency on the degree of radial support is visible for tests performed at similar temperature. But when comparing the results from the tests performed at the two different test temperatures a clear temperature dependency is visible. Ambient temperature tests have a higher Young's modulus compared to the tests performed at 130 °C. In fact the Young's modulus at ambient temperature will on average be a factor 1.557 higher than for the tests performed at 130 °C. This gives a direct indication that the mechanical strength of Liegé chalk flooded with SSW will be significantly reduced as temperature is increased to 130$^{o}$C.

Similar temperature dependency is also visible when comparing the bulk modulus for the hydrostatic tests in *Table 7.3*. The data in *Table 7.3* are average values based on two hydrostatic tests performed at both test temperatures.

*Table 7.3: Table of average bulk modulus for the hydrostatic tests performed at ambient temperature and at 130 °C*

| K-modulus [GPa] | | Difference [GPa] | Difference ratio |
|---|---|---|---|
| Ambient temperature | 130$^{o}$C | | |
| 0.805* | 0.517* | 0.288 | 1.557 |

**Average value based on two hydrostatic tests*

From *Table 7.3* it is clear that the tests performed at ambient temperature are more resistant against hydrostatic compression compared the tests performed at 130 °C. The average bulk modulus for the hydrostatic tests at ambient temperature will be 1.557 times higher compared the hydrostatic tests at ambient temperature. This difference ratio is in fact the same as for the Young's modulus in *Table 7.2*.

**Mohr and q-p´ plots**

By comparing the data obtained from the calculated failure lines in *Fig. 6.6* and *Fig.6.9* one can study if temperature has any effect on mechanical properties like cohesion ($S_o$) and friction angle ($\varphi$). *Table 7.4* show the mechanical properties found from the calculated failure line for the tests performed at ambient temperature and at 130 °C

*Table 7.4: Difference in mechanical properties determined from the calculated failure line for tests performed at ambient temperature and at 130 °C.*

| Mechanical parameters | Ambient temperature | 130 °C |
|---|---|---|
| $S_o$ [MPa] | 1.11 | 0.52 |
| $\varphi^{o}$ | 33 | 36 |
| $\mu$ | 0.64 | 0.72 |
| $\beta^{o}$ | 61 | 63 |

When comparing the mechanical properties in *Table 7.4* it is clear that the temperature has an effect on the cohesion. The cohesion found at ambient temperature is 2.14 times larger than

the cohesion found at 130 °C. This same trend is not seen when comparing the friction angel. In fact the friction angle for test performed at 130 °C is somewhat higher compared to the friction angle found at ambient temperature.

By comparing the failure envelopes for tests performed at ambient temperature and 130 °C one can get a clear impression of the effect aging and temperature has on the mechanical properties of Liegé chalk. In *Fig.7.1* the failure envelopes obtained for the two test temperatures are shown.

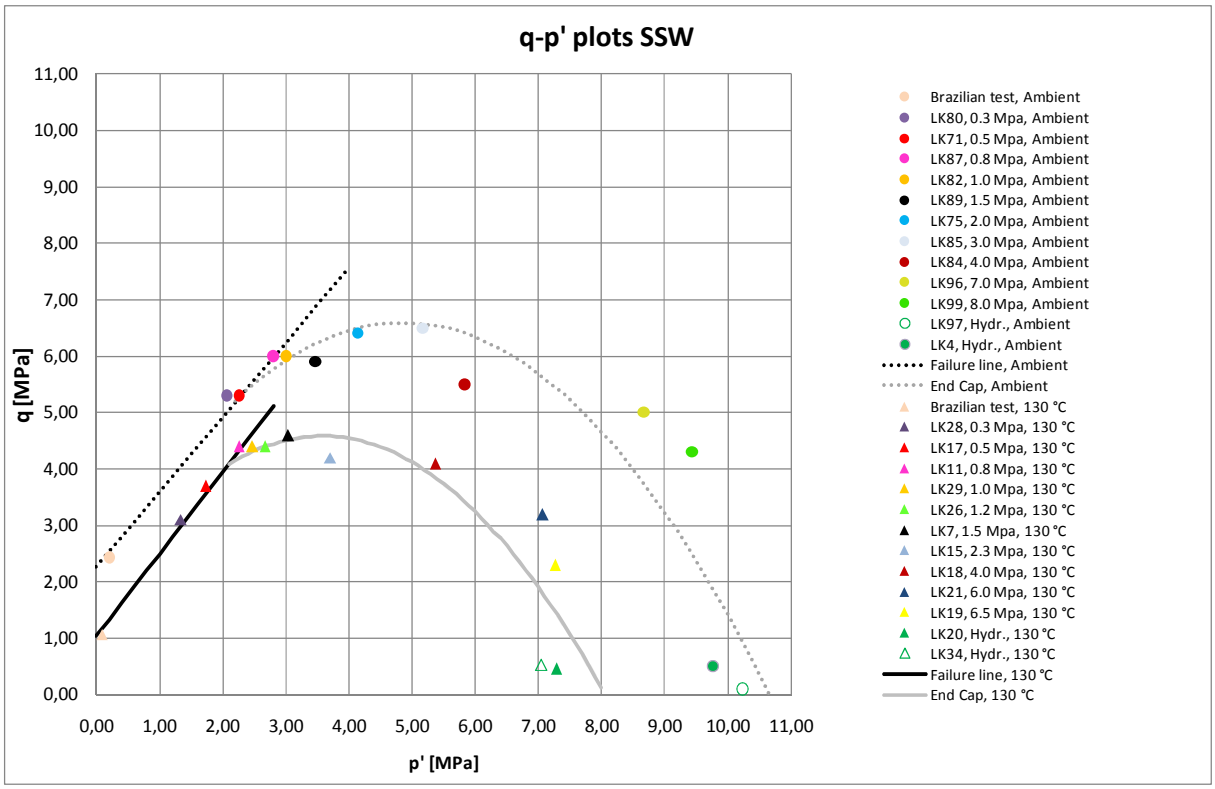


*Fig.7.1: Failure envelopes for tests performed at ambient temperature and at 130 °C. The failure envelope for the tests performed at 130 °C fall below the failure envelope for tests performed at ambient temperature indicating that high temperature tests are weaker against both shear failure and pore collapse. The largest separation between these two curves is found on the end cap indicating that the larges reduction in strength will be against pore collapse.*

The failure envelope for high temperature tests fall below the failure envelope for the test performed at ambient temperature as shown in *Fig.7.1*. This in combination with the results from *Table 7.1* and *Table 7.2* give a clear impression of the effect of temperature for tests saturated and flooded with SSW. Tests performed on aged cores tested at 130 °C are weaker against both shear failure and pore collapse. The largest separation between these two failure envelopes is found on end cap indicating that the largest reduction in mechanical strength will be against pore collapse. The data presented in *Fig.7.1* gives a strong indication that the weakening effect caused by SSW flooding will be temperature dependant and appears to be quite significant at high test temperatures (130 °C).

### 7.1.2 SSW-($SO_4^{2-}$)

**Results in tables**

The yield points for tests performed with the same degree of radial support at ambient temperature and at 130 °C with SSW-($SO_4^{2-}$) as saturation and flooding fluid are shown in *Table 7.5*. Please note that all listed values are obtained from one test unless otherwise is stated.

*Table 7.5: Table over the difference in yield points for similar tests performed at ambient temperature and at 130 °C*

| Test type | $\sigma_1'$ [Mpa] | | Difference [MPa] | Difference ratio |
|---|---|---|---|---|
| | Ambient | 130°C | | |
| Brazilian | 1.38 | 1.53 | -0.15 | 0.89 |
| 0.5 MPa Dev. | 4.50* | 4.90 | -0.40 | 0.92 |
| 1.0 MPa Dev. | 6.20 | 6.20 | 0 | 1.00 |
| 1.2 MPa Dev. | 6.20 | 6.70 | -0.50 | 0.93 |
| 2.3 MPa Dev. | 8.40 | 7.10 | 1.30 | 1.18 |
| 4.0 MPa Dev. | 9.30 | 9.00 | 0.30 | 1.03 |
| 7.0 MPa Dev. | 11.40 | 11.80 | -0.40 | 0.97 |
| Hydrostatic | 10.70 | 10.80 | –0.10 | 0.99 |
| **Average** | | | | **0.99** |

** Average value based on results from two 0.5 MPa deviatoric tests*

When comparing the yield points in *Table 7.5* no clear temperature dependency is observed due to a lot discrepancy in the data. On average the yield points for tests performed at 130 °C are higher compared to the ambient temperature tests. The difference ratio between the yield points for the two temperatures were calculated to 0.99, i.e. the yield points for the ambient temperature tests are on average 0.99 times lower compared to the tests performed at 130 °C. Based on these data alone it is difficult to see if there is any temperature effect for the SSW-($SO_4^{2-}$) tests. In *Table 7.6* the difference in Young's moduli for similar tests performed at ambient temperature and at 130 °C is listed.

*Table 7.6: Table over the difference in calculated Young's moduli for similar tests performed at ambient temperature and at 130 °C*

| Effective radial stress | E-modulus [GPa] | | Difference [GPa] | Difference ratio |
|---|---|---|---|---|
| | Ambient temperature | 130°C | | |
| 0.5 MPa | 1.357* | 1.277 | 0.080 | 1.063 |
| 1.0 MPa | 1.262 | 1.346 | -0.084 | 0.938 |
| 1.2 MPa | 1.299 | 1.094 | 0.205 | 1.187 |
| 2.3 MPa | 1.577 | 1.186 | 0.391 | 1.330 |
| 4.0 MPa | 1.508 | 1.134 | 0.374 | 1.330 |
| 7.0 MPa | 1.907 | 1.360 | 0.547 | 1.405 |
| **Average** | | | | **1.208** |

** Average value based on results from two 0.5 MPa deviatoric tests*

Unlike the results from *Table 7.5*, there is only one test that appears to be stronger at 130 °C (based on the Young's modulus) in *Table 7.6*. On average the Young's modulus for tests performed at ambient temperature are 1.206 times larger than the Young's modulus for tests performed at 130 °C. The calculated Young's modulus for tests performed at ambient temperature appear to increase with increasing radial support, while for the tests performed at 130 °C such dependency is not observed. Based on the Young's modulus the tests performed at ambient temperature appear to be somewhat more resistant against shear failure compared to the tests performed at 130 °C. The calculated bulk modulus for the hydrostatic tests in *Table 7.7* also show a similar picture where a lower bulk modulus is observed for the test performed at ambient 130 °C.

*Table: 7.7: Table over calculated bulk modulus for hydrostatic tests performed at ambient temperature and at 130 °C*

| K-modulus [GPa] | | Difference [GPa] | Difference ratio |
|---|---|---|---|
| Ambient temperatur | 130°C | | |
| 0.689 | 0.587 | 0.102 | 1.174 |

*Table 7.7* shows that the bulk modulus for hydrostatic tests at ambient temperature is 1.174 times higher than the bulk modulus for tests performed at 130 °C. The results in *Table 7.7* are only based on one tests performed at both temperature. More data is needed to be able to determine if temperature affects the bulk modulus for SSW-($SO_4^{2-}$) tests. Based on the data in *Table 7.5-7.7* it is difficult to determine if the discrepancy in the data is from naturally variations in mechanical strength from core to core or an effect of temperature.

**Mohr and q-p´ plots**

Mechanical parameters obtained from the calculated failure lines in *Fig.6.14* and *Fig.6.17* shown in *Table 7.8* show little variations the two test temperatures.

*Table 7.8: Table over the mechanical parameters determined from calculated failure lines in Fig.6.14 and Fig.6.17*

| Mechanical parameters | Ambient temperature | 130 °C |
|---|---|---|
| $S_o$ [MPa] | 0.81 | 0.97 |
| $\varphi^o$ | 31 | 29 |
| $\mu$ | 0.60 | 0.55 |
| $\beta^o$ | 61 | 59 |

Unlike the results in *Table 7.4* the cohesion appears to increase slightly as temperature increases. The cohesion for the tests performed at 130 °C is 1.13 times higher compared to the cohesion found at ambient temperature. This is not a significant difference and may be a result of natural variations in mechanical strength found in chalk blocks, because samples from the same block of chalk may vary in strength dependant on which area in the block the samples are prepared from.

In Fig.7.2 the failure envelopes for SSW-($SO_4^{2-}$) tests performed at ambient temperature and at 130 °C are shown.

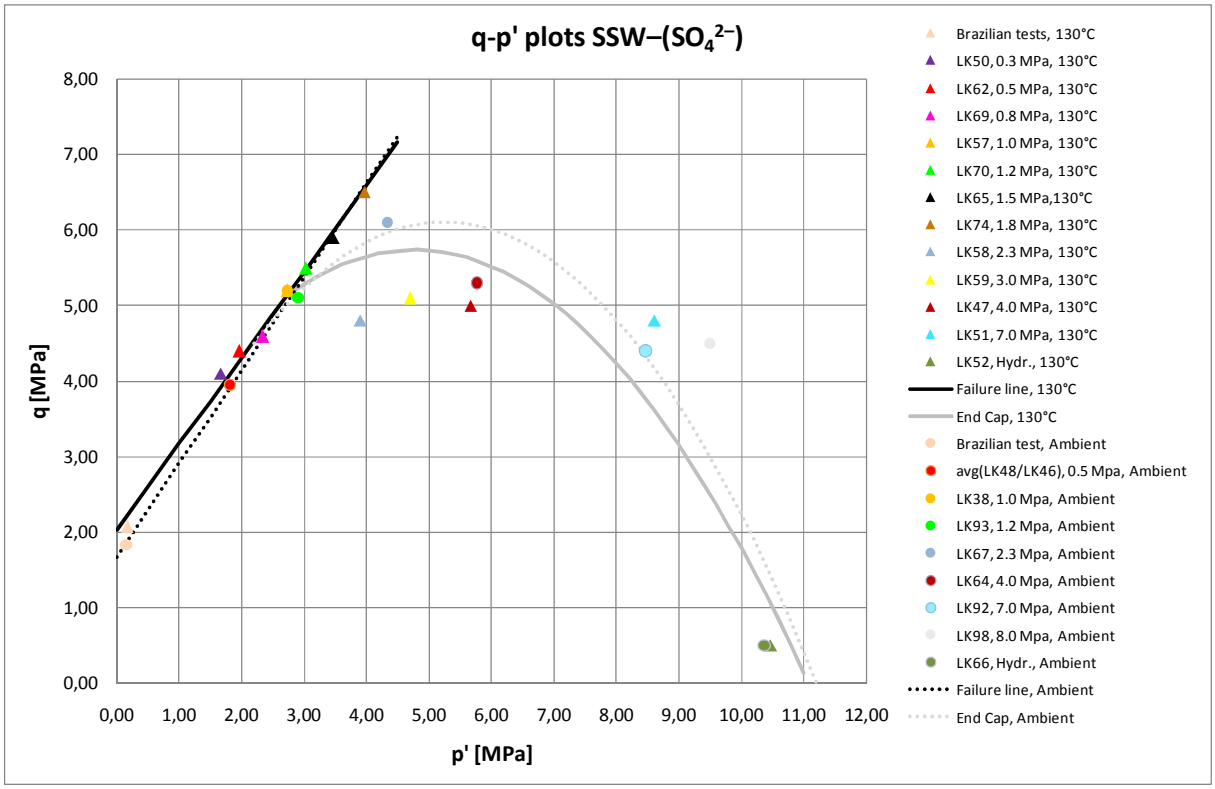


*Fig.7.2: Failure envelopes for tests performed at ambient temperature and 130 °C. The failure envelopes for the two test temperatures appear to be quite similar but some difference in the shape of the end cap is observed. This shape is obtained from a polynomial regression on a limited amount of data points which gives a high uncertainty for this curve. It is therefore difficult to see any clear temperature dependency.*

When comparing the failure envelopes for tests performed at ambient temperature and at 130 °C in *Fig.7.2* no significant differences are observed. The failure lines for the results obtained at the two different temperatures follow the same trend with some difference in the point of the intersection with the ordinate axis. This difference in point of intersection with the ordinate is mainly a result of the difference in maximum principle stress ($\sigma_1'$) obtained from the Brazilian tests. Tests performed at low effective radial stress appear fall in a cluster where it is difficult to distinguish between the results obtained at the two different test temperatures. The end cap for the tests performed at 130 °C in *Fig.7.2* falls below the end cap for the ambient temperature tests, but if the results from the tests performed on LK58, LK59 and LK47 are regarded as abnormally weak the whole end cap section for the 130 °C tests would be lifted up towards the result from the 1.8 MPa deviatoric tests and above the end cap for the ambient temperature tests.

A general trend observed is that the mechanical strength of chalk reduces as the temperature is increased, but for the results in *Fig.7.2* this is not completely the case. Here the failure envelopes are almost un-separable indication the mechanical strength is quite similar for the two test temperatures.

## 7.2 Effect of sulphate

To study what the effect of removing sulphate ($SO_4^{2-}$) in seawater will have on the mechanical strength of chalk one can compare tests performed with similar tests parameters where the only difference is the presence of sulphate. In this study two different tests temperatures were used and by comparing the results obtained for the for tests performed with the different brines (SSW and SSW-($SO_4^{2-}$)) one can study if sulphate affects the mechanical strength and if any weakening effect will be temperature dependant.

### 7.2.1 Ambient temperature

**Results in tables**
In *Table 7.9* the yield points for the tests performed with the same degree of radial support at ambient temperature is listed. If sulphate has a weakening effect at ambient temperature this should have an impact on the yield points for tests saturated and flooded with SSW.

*Table 7.9: Table over the difference in yield points for SSW and SSW-($SO_4^{2-}$) tests performed at ambient temperature*

| Test type | $\sigma_1'$ [Mpa] | | Difference [MPa] | Difference ratio |
|---|---|---|---|---|
| | SSW–($SO_4^{2-}$) | SSW | | |
| Brazilian | 1.38 | 1.83 | 0.45 | 1.33 |
| 0.5 MPa Dev. | 4.50* | 5.80 | 1.30 | 1.29 |
| 1.0 MPa Dev. | 6.20 | 7.00 | 0.80 | 1.13 |
| 4.0 MPa Dev. | 9.30 | 9.50 | 0.20 | 1.02 |
| 7.0 MPa Dev. | 11.40 | 12.00 | 0.60 | 1.05 |
| 8.0 MPa Dev. | 12.50 | 12.30 | –0.20 | 0.98 |
| Hydrostatic | 10.70 | 10.20** | –0.50 | 0.95 |
| **Average** | | | | **1.11** |

** Average yield value calculated from two 0.5 MPa deviatoric tests*
*** Average value calculated from two hydrostatic tests*

When comparing the yield points in *Table 7.9* it is observed most of the yield points for the SSW tests are higher compared to the SSW-($SO_4^{2-}$) tests. Only for the 8.0 MPa deviatoric and hydrostatic tests a higher yield point is observed for SSW-($SO_4^{2-}$) tests. On average the yield points for the SSW tests will be a factor 1.11 higher than the SSW-($SO_4^{2-}$) tests. This is not a significant difference indicating that there is no chemical weakening taking place at ambient temperature. The difference observed in the yield points are therefore most likely a result of natural variations in mechanical strength which can be seen in a block of outcrop chalk.

Little difference in the results for the two different flooding fluids is also observed when studying the results in *Table 7.10*.

*Table 7.10: Table over the differences in calculated Young's moduli for tests performed at ambient temperature*

| Effective radial stress | E-modulus [GPa] | | Difference [GPa] | Difference ratio |
|---|---|---|---|---|
| | SSW–($SO_4^{2-}$) | SSW | | |
| 0.5 MPa Dev. | 1.357* | 1.320 | 0.037 | 1.028 |
| 1.0 MPa Dev. | 1.262 | 1.597 | –0.335 | 0.790 |
| 4.0 MPa Dev. | 1.508 | 1.534 | –0.026 | 0.983 |
| 7.0 MPa Dev. | 1.907 | 1.349 | 0.558 | 1.414 |
| 8.0 MPa Dev. | 1.805 | 1.540 | 0.265 | 1.172 |
| **Average** | | | | **1.077** |

** Average Young's modulus calculated from the result of two 0.5 MPa deviatoric tests*

The Young's moduli for SSW-($SO_4^{2-}$) tests in *Table 7.10* are on average higher than for SSW tests. These results indicate that the SSW-($SO_4^{2-}$) tests were somewhat stiffer or more resistant against uniaxial compression, but the difference is not significant. From these results it appears that the presence of sulphate ($SO_4^{2-}$) in the flooding fluid at ambient temperature does not have any direct effect on the materials Young's modulus.

The calculated bulk modulus values for the hydrostatic tests performed at ambient temperature in *Table 7.11* show a somewhat higher resistance against hydrostatic compression for SSW tests.

*Table 7.11: Table over the differences in bulk moduli for tests performed at ambient temperature*

| K-modulus [GPa] | | Difference [GPa] | Difference ratio |
|---|---|---|---|
| SSW–($SO_4^{2-}$) | SSW | | |
| 0.689 | 0.805* | 0.116 | 0.856 |

** Average bulk modulus calculated from the results of two hydrostatic tests*

The difference in bulk modulus from *Table 7.11* is not a significant difference which makes it difficult to determine if it is related to sulphate or just a result of natural variation in mechanical strength. Had a second repetition of the hydrostatic with SSW-($SO_4^{2-}$) flooding been conducted the difference in bulk modulus could even be further reduced. More tests could also have the opposite effect where an increase in the difference could be seen, but from the available data no clear sulphate effect at ambient temperature is seen. From the yield points in Table 7.9 and the calculated elastic parameters in *Table 7.10* and *Table 7.11* it appears that the presence of sulphate does not have any significant effect on the mechanical strength. The difference observed in mechanical strength for SSW and SSW-($SO_4^{2-}$) tests are most likely a result of naturally variations in mechanical strength.

**Mohr and q-p´ plots**

In *Table 7.12* the mechanical properties from the calculated failure lines in *Fig.6.6* and *Fig.6.14* are compared to study if the presence of sulphate has had any effect on these properties.

*Table 7.12: Table over the mechanical properties determined from the calculated failure lines for SSW and SSW-($SO_4^{2-}$) tests performed at ambient temperature*

| Mechanical parameters | SSW-($SO_4^{2-}$) | SSW |
|---|---|---|
| $S_o$ [MPa] | 0.81 | 1.11 |
| $\varphi^o$ | 31 | 33 |
| $\mu$ | 0.60 | 0.64 |
| $\beta^o$ | 61 | 61 |

The main difference between the results in *Table 7.12* will be in the estimated cohesion ($S_o$). The cohesion for the SSW tests is a factor 1.37 higher than the estimated cohesion for the SSW-($SO_4^{2}$) tests. For the other mechanical properties in *Table 7.12* only minor differences are observed. By comparing the failure envelopes for the SSW and SSW-($SO_4^{2-}$) tests performed at ambient temperature in a q-p´-plot like in *Fig.7.3* one can get a better picture of how the mechanical behavior is affected by the presence of sulphate.

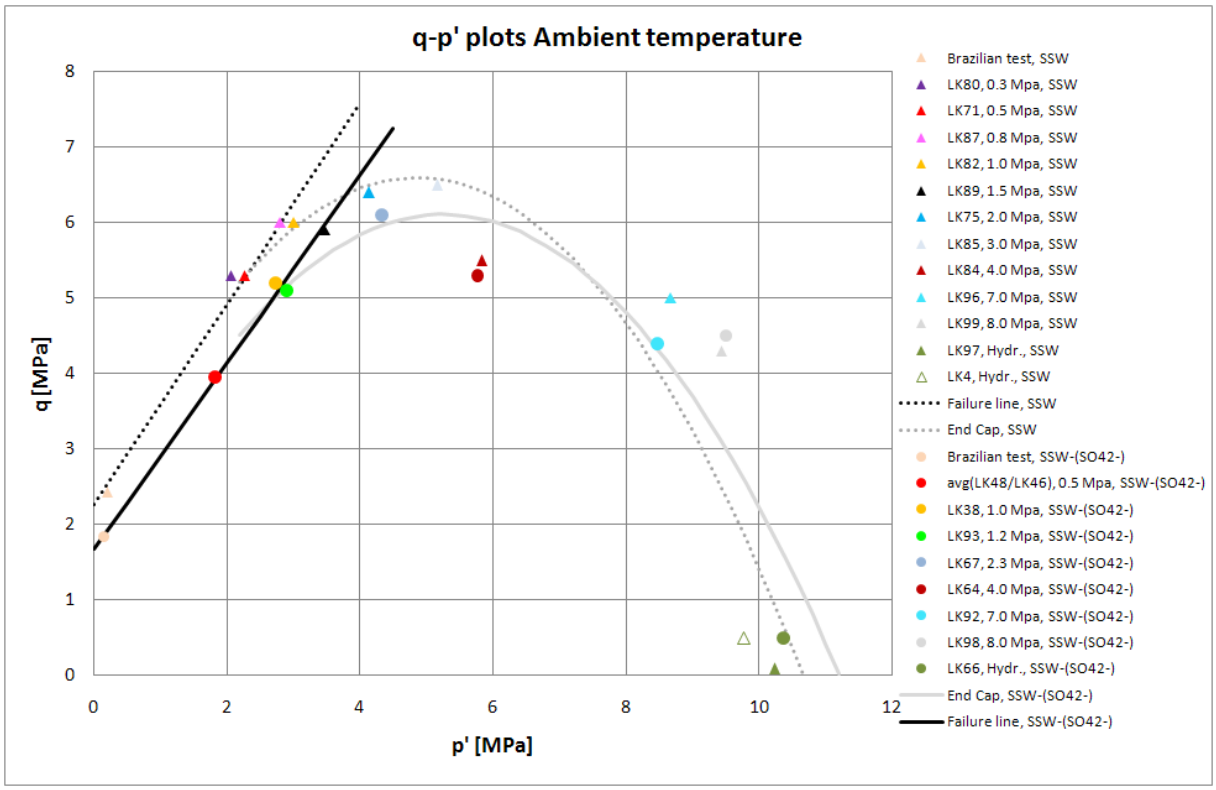


*Fig.7.3: Failure envelopes for tests saturated and flooded with SSW and SSW-($SO_4^{2-}$) at ambient temperature. The failure line for the SSW-($SO_4^{2-}$) tests seems to fall below the SSW failure line indicating that these cores were less resistant against shear failure. Strength against pore collapse which is given by the end cap appears to be quite similar for the SSW and SSW-($SO_4^{2-}$) tests.*

From *Fig.7.3* it is observed that the failure line for the SSW-($SO_4^{2-}$) tests fall below the failure line for the SSW tests which indicates that the SSW-($SO_4^{2-}$) tests were somewhat weaker against shear failure. For increasing degree of radial support the difference in strength reduces which can be seen when comparing the end cap sections for the failure envelopes in *Fig.7.3*. (comment end cap behaviour)

### 7.2.2 130 ℃

**Results in tables**

From the chemical analysis performed on SSW and SSW-($SO_4^{2-}$) samples before and after aging indicated that there was a strong interaction between the chalk and the brine at 130 °C. The results from *Table 6.18* and *Table 6.19* show that there are chemical reactions taking place during the aging process which may affect the mechanical strength of chalk. In *Table 7.13* the yield points for the SSW and SSW-($SO_4^{2-}$) tests performed with similar degree of radial support performed at 130 °C are listed.

*Table 7.13: Table over the difference in yield points for SSW and SSW-($SO_4^{2-}$) tests performed with similar degree of radial support at 130 °C*

| Test type | $\sigma_1'$ [Mpa] | | Difference [MPa] | Difference ratio |
|---|---|---|---|---|
| | SSW–($SO_4^{2-}$) | SSW | | |
| Brazilian | 1.53 | 0.81 | 0.72 | 1.89 |
| 0.3 MPa Dev. | 4.40 | 3.40 | 1.00 | 1.29 |
| 0.5 MPa Dev. | 4.90 | 4.20 | 0.70 | 1.17 |
| 0.8 MPa Dev. | 5.40 | 5.20 | 0.20 | 1.04 |
| 1.0 MPa Dev. | 6.20 | 5.40 | 0.80 | 1.15 |
| 1.2 MPa Dev. | 6.70 | 5.60 | 1.10 | 1.20 |
| 1.5 MPa Dev. | 7.40 | 6.10 | 1.30 | 1.21 |
| 2.3 MPa Dev. | 7.10 | 6.50 | 0.60 | 1.09 |
| 4.0 MPa Dev. | 9.00 | 8.10 | 0.90 | 1.11 |
| Hydrostatic | 10.80 | 7.50* | 3.30 | 1.44 |
| **Average** | | | | **1.26** |

** Average yield value from two hydrostatic tests*

From *Table 7.13* one can observe that the largest difference in yield point will be between the hydrostatic tests, where the yield point for core flooded with SSW-($SO_4^{2-}$) has a yield point that is a factor 1.44 higher than for the hydrostatic tests flooded with SSW. On average the yield points obtained for the SSW-($SO_4^{2-}$) tests will have a yield point that is a factor 1.26 times higher compared to the SSW tests. The largest difference ratio is found for the Brazilian tests where largest effective stress ($\sigma_1'$) is a factor 1.89 times higher than the value obtained from the SSW test. Results from *Table 7.13* give a strong indication that there is a significant reduction in strength due to the presence of sulphate ($SO_4^{2-}$) at 130 °C.

In *Table 7.14* the calculated Young's moduli for SSW and SSW-($SO_4^{2-}$) tests performed at 130 °C are listed. As for the yield points in *Table 7.13* there is a significant difference between the Young's modulus for SSW and SSW-($SO_4^{2-}$) tests. On average the Young's moduli for SSW-($SO_4^{2-}$) tests will be a factor 1.298 higher compared to the SSW tests. The difference between the Young's modulus for SSW and SSW-($SO_4^{2-}$) tests appear to decrease

slightly as the degree of radial support increases. In a general view the data in *Table 7.14* indicates that resistance against uniaxial compression will be higher when sulphate is not present in the seawater at 130 °C.

*Table 7.14: Table over the differences in calculated Young's moduli for SSW and SSW-($SO_4^{2-}$) tests performed with same degree of radial support at 130 °C*

| Effective radial stress | E-modulus [GPa] | | Difference [GPa] | Difference ratio |
|---|---|---|---|---|
| | SSW–($SO_4^{2-}$) | SSW | | |
| 0.3 MPa | 1.155 | 0.794 | 0.361 | 1.455 |
| 0.5 MPa | 1.277 | 0.947 | 0.330 | 1.348 |
| 0.8 MPa | 1.378 | 0.810 | 0.568 | 1.701 |
| 1.0 MPa | 1.346 | 0.998 | 0.348 | 1.349 |
| 1.2 MPa | 1.094 | 0.932 | 0.162 | 1.174 |
| 1.5 MPa | 1.169 | 0.930 | 0.239 | 1.257 |
| 2.3 MPa | 1.186 | 1.116 | 0.070 | 1.063 |
| 4.0 MPa | 1.134 | 1.097 | 0.037 | 1.034 |
| **Average** | | | | **1.298** |

In *Table 7.15* the calculated bulk moduli for the SSW and SSW-($SO_4^{2-}$) tests at 130 °C are compared.

*Table 7.15: Table over the difference in calculated bulk moduli for hydrostatic SSW and SSW-($SO_4^{2-}$) tests performed at 130 °C*

| K-modulus [GPa] | | Difference [GPa] | Difference ratio |
|---|---|---|---|
| SSW–($SO_4^{2-}$) | SSW | | |
| 0.587 | 0.517* | 0.07 | 1.135 |

** Average value calculated from two hydrostatic tests*

Unlike the results in *Table 7.13* and *Table 7.14* no clear weakening effect is observed for the hydrostatic SSW test in Table 7.15. The bulk modulus for the SSW-($SO_4^{2-}$) is a factor 1.135 higher than the average bulk modulus for the SSW tests. Based on the bulk modulus alone no significant difference is observed between calculated bulk modulus for the hydrostatic tests performed with SSW and SSW-($SO_4^{2-}$).

**Mohr and q-p´ plots**

In *Table 7.16* the mechanical properties determined from the calculated failure lines in *Fig.6.9* and *Fig.6.17* are listed. By comparing the results in *Table 7.16* one can determine if the presence of sulphate in the flooding fluid affect the mechanical properties at 130 °C.

*Table 7.16: Table over the difference in mechanical properties determined from the calculated failure lines for SSW and SSW-($SO_4^{2-}$) tests performed at 130 °C*

| Mechanical parameters | SSW-($SO_4^{2-}$) | SSW |
|---|---|---|
| $S_o$ [MPa] | 0.97 | 0.52 |
| $\varphi^o$ | 29 | 36 |
| $\mu$ | 0.55 | 0.72 |
| $\beta^o$ | 59 | 63 |

When comparing the estimated cohesion ($S_o$) for the two flooding fluids in *Table 7.16* a significant difference is observed. The cohesion estimated from the tests flooded with SSW-($SO_4^{2-}$) is a factor 1.87 higher than the estimated cohesion from the SSW tests. Also in the friction angle ($\varphi$) a significant difference is observed. The friction angle determined for the SSW tests is a factor 1.24 higher than the friction angle found for the SSW-($SO_4^{2-}$) tests. Due to the difference in friction angle the other properties listed in *Table7.16* (coefficient of internal friction ($\mu$) and failure angle ($\beta$)) will also be higher for the SSW tests. To get a clearer impression of the effect of sulphate at high 130 °C the failure envelopes for the SSW and SSW-($SO_4^{2-}$) tests are compared in *Fig.7.4*.

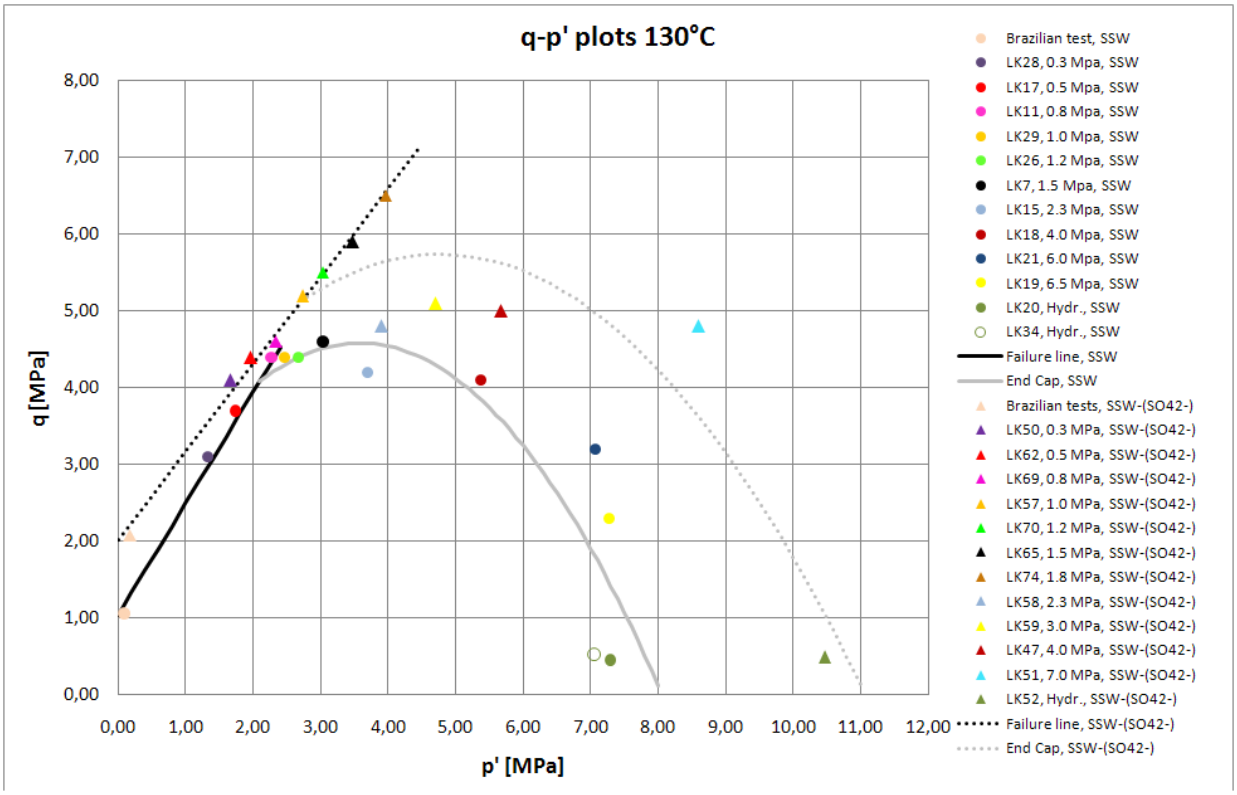


*Fig.7.4: Failure envelopes for the tests performed for SSW and SSW-($SO_4^{2-}$) tests performed at 130 °C. The failure line for the SSW tests falls below the failure line for the SSW-($SO_4^{2-}$). The largest difference is found when comparing the end cap sections for the two brines. Tests performed with SSW as flooding and saturation fluid appear to be weaker against pore collapse compared to the SSW-($SO_4^{2-}$) tests at 130 °C.*

When studying the results in *Fig.7.4* it is evident that the failure envelope for the SSW tests fall below failure envelope for the SSW-($SO_4^{2-}$) tests. These results indicate that the SSW tests are weaker against both shear failure and pore collapse. For the SSW-($SO_4^{2-}$) tests there is a large uncertainty in the shape of the end cap. As can be seen from *Fig.7.4* all tests up to the 1.8 MPa deviatoric tests fall on or very close to the failure line. Then for the next test, which was the 2.3 MPa deviatoric test, there is a large reduction in strength. This makes is very difficult to draw the transition between the failure line and the end cap. Based on the available dataset the failure envelope presented for the SSW-($SO_4^{2-}$) tests in *Fig.7.4* is the best fit that could be obtained. If the results from the tests performed on LK58, LK59 and LK47 are regarded as abnormally weak the whole end cap would be lifted resulting in an even larger separation between the end cap sections for SSW and SSW-($SO_4^{2-}$) tests.

## 7.3 Creep behaviour

In total three different creep tests were performed on un-aged Liegé cores at 130 °C. In *Fig.7.5* the creep plots for the tests performed on LK94, LK95 and LK79 are compared. The different tests were flooded with different flooding fluids at different times which are marked in *Fig.7.5* by small text boxes with the same colour as the creep curves.

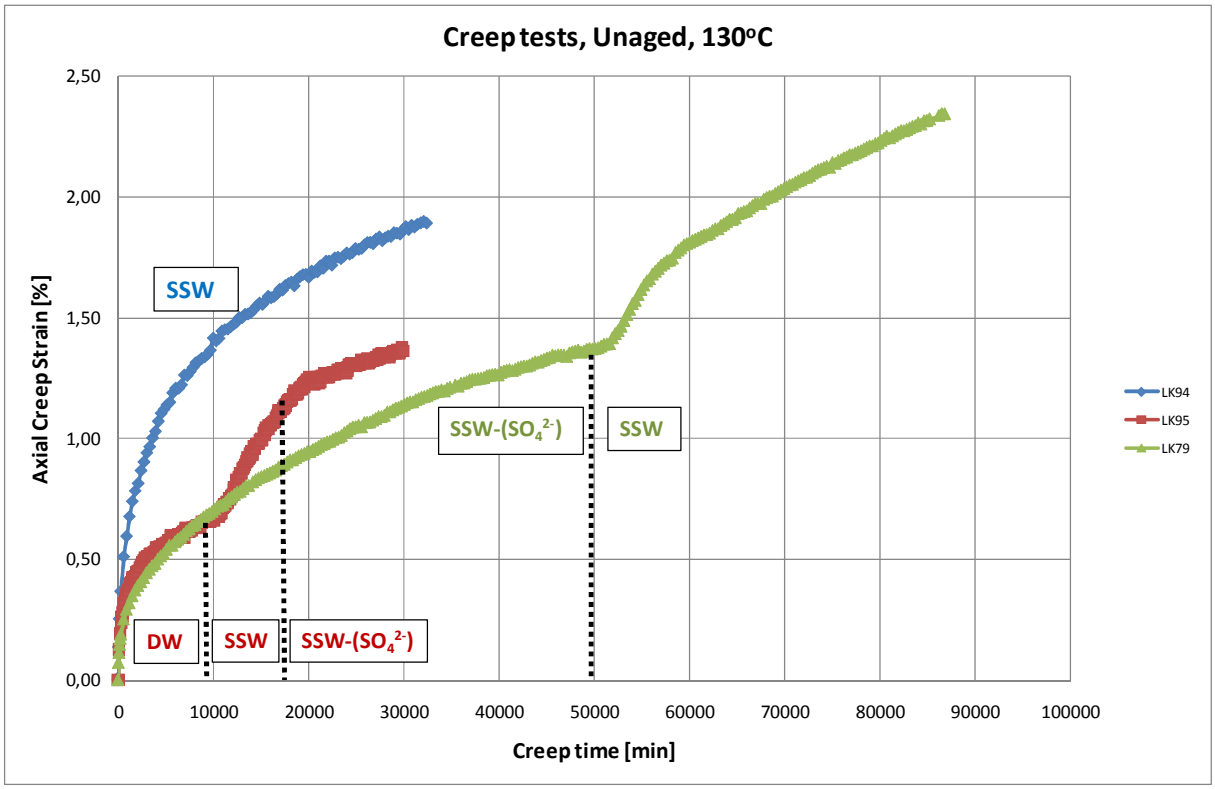


*Fig.7.5: Combined axial creep strain versus creep time plot with the creep phases for the tests performed on LK94, LK95 and LK79 included. The different flooding phases for the different tests are marked in the plot with the same colour as the corresponding creep curve.*

The first thing that is observed when studying the different creep curves in *Fig.7.5* is that the transient period for the creep tests performed on LK79 and LK95 are almost identical. At this time the test performed on LK95 was flooded with distilled water while the test performed on LK79 was flooded with SSW-($SO_4^{2-}$). This similarity indicates that no enhanced chemical weakening occurs during the early stages of a creep tests when flooded with SSW-($SO_4^{2-}$), because the behaviour is almost identical to the creep behaviour observed during distilled water flooding where no chemical interaction between flooding fluid and chalk takes place. By comparing the axial creep strain experienced during the transient period for the three tests a significant difference is observed between the test flooded with SSW and the tests flooded with distilled water and SSW-($SO_4^{2-}$). These results give a strong indication that flooding with SSW has a significant weakening effect on Liegé chalk at 130 °C. As SSW flooding was started in the creep tests performed on LK95 and LK79 a significant increase in creep strain were observed. These results show that a reduction in mechanical strength will occure when SSW is introduced during creep tests on Liegé chalk at 130 °C. To get a better impression of how the different flooding phases affect the mechanical behaviour the accumulated strain experienced at different creep times can be compared.

In *Table 7.17* the accumulated strain experienced for each of the tests are compared at different times. The creep times used for comparison are the creep times where a change in flooding fluid was performed for one of the tests. In example the first creep time used for comparison in *Table 7.17* is a creep time 9 602 minutes which were the creep time where SSW flooding was started in the tests performed on LK95. By presenting the data in such a manner one obtain a better overview of the axial creep strains experienced during the different flooding phases.

*Table 7.17: Table over accumulated axial strain experienced at different creep times for the creep tests performed on LK79, LK94 and LK95. The creep times used for comparison will be the different creep times were changes in the flooding fluid was performed for the different tests.*

| Creep time [min] | LK79 | | LK94 | | LK95 | |
|---|---|---|---|---|---|---|
| | Accumulated ax. creep strain [%] | Flooding fluid | Accumulated ax. creep strain [%] | Flooding fluid | Accumulated ax. creep strain [%] | Flooding fluid |
| 9 602 | 0.687 | SSW–($SO_4^{2-}$) | 1.367 | SSW | 0.660 | DW |
| 16 811 | 0.878 | SSW–($SO_4^{2-}$) | 1.596 | SSW | 1.109 | SSW |
| 29 910 | 1.137 | SSW–($SO_4^{2-}$) | 1.851 | SSW | 1.363 | SSW–($SO_4^{2-}$) |
| 32 040 | 1.171 | SSW–($SO_4^{2-}$) | 1.900 | SSW | | |
| 50 110 | 1.371 | SSW–($SO_4^{2-}$) | | | | |
| 86 778 | 2.342 | SSW | | | | |

From *Table 7.17* the accumulated creep strain for LK94 experienced after 9 602 minutes will be a factor 2 higher than the accumulated strains experienced for LK79 and LK95 at the same creep time. When comparing the accumulated strains experienced at the remaining creep times in *Table 7.17* it is evident that the largest separation will between LK79 and LK94. At 32 040 minutes the accumulated creep strain experienced for LK94 with SSW flooding will be a factor 1.62 higher than the strain experienced for LK79 with SSW-($SO_4^{2-}$) flooding. These results give a strong indication that less creep deformation will occur when sulphate ($SO_4^{2-}$) is not present in the brine. Since the timescales for the three different creep tests are so different it is difficult to compare the total axial creep strain experienced at the end of each test. Another way of studying the effect of the different flooding fluids will be to compare the creep rates experienced during the different flooding phases in the tests performed on LK79, LK94 and LK95. In *Fig.7.6* the axial creep strain experienced for the different creep tests are plotted against logarithmic time.

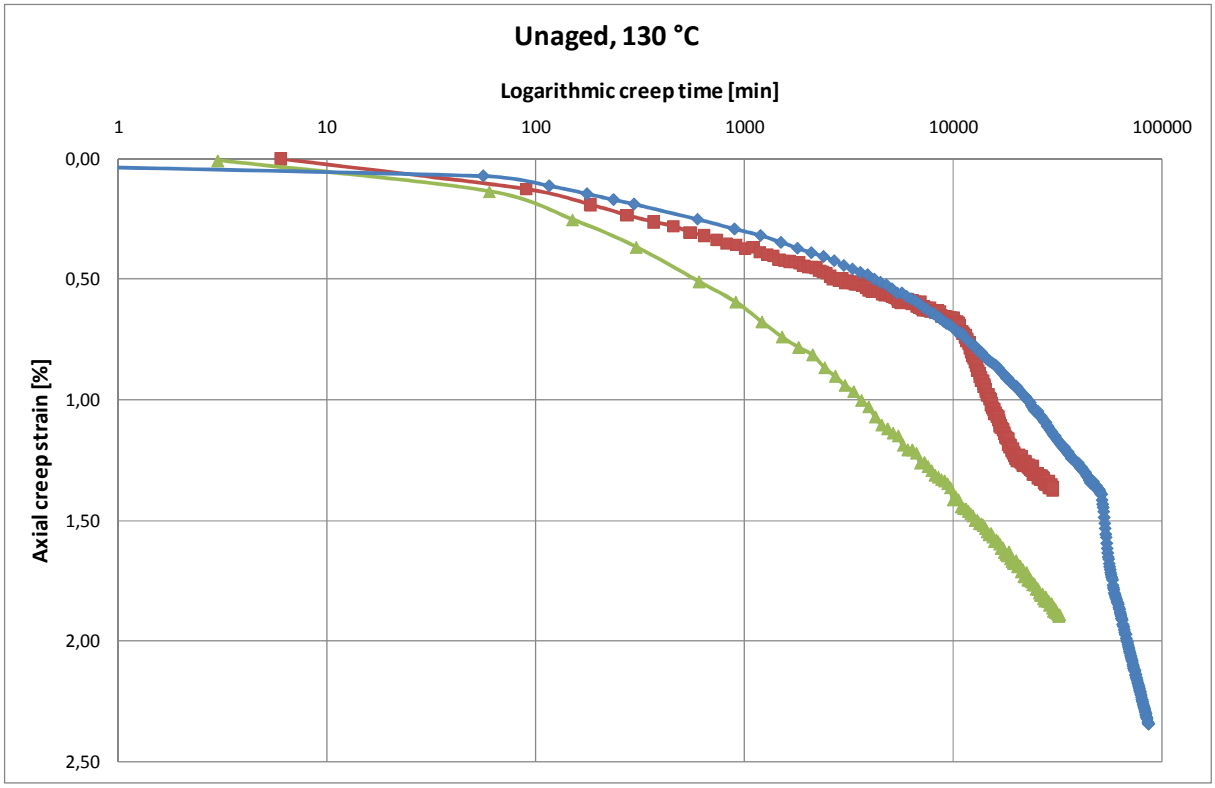


Fig.7.6: Axial creep strain versus logarithmic time plot for the different creep tests. From the two of the last data points in each flooding phase the creep rate can be determined.

In *Table 7.18* the calculated creep rates for the different flooding phases are listed.

*Table 7.18: Table over the calculated creep rates for the different flooding phases in the creep tests performed on LK94, LK95 and LK79*

| Test core | Flooding fluid | Strain rate [ % / Decade ] |
|---|---|---|
| LK94 | SSW | 0.98 |
| LK95 | DW | 0.36 |
| | SSW | 1.46 |
| | SSW–($SO_4^{2-}$) | 0.81 |
| LK79 | SSW–($SO_4^{2-}$) | 1.15 |
| | SSW | 3.21 |

The creep rate calculated for the test performed on LK94 in *Table 7.18* is somewhat lower compared to the creep rates experienced during SSW flooding in the creep tests performed on LK95 and LK94. For the SSW flooding phase on the test performed on LK95 the creep rate is expected to differ as it was calculated from a very short flooding period. But when comparing the creep rates found during SSW flooding for LK94 and LK79 a significant difference is observed. The calculated creep rate for the SSW period on the test performed on LK79 is a factor 5.1 higher than creep rate found during the creep test on LK94. Indicating that a higher deformation rate will be obtained when SSW flooding is performed after a period of SSW-($SO_4^{2-}$) flooding compared to a single flooding phase with SSW. When comparing the

calculated the creep rate for the SSW-($SO_4^{2-}$) flooding periods in *Table 7.18* a small difference is seen. The creep rate obtained for the SSW-($SO_4^{2-}$) flooding period performed on LK79 is a factor 1.4 times higher than the creep rate calculated for the creep tests performed on LK95. A thing to keep in mind is that the creep rate found for the SSW-($SO_4^{2-}$) flooding phase on the test performed on LK79 is calculated at the end of a much longer flooding period. Had the creep test performed on LK95 been continued for a longer period of time the difference in creep rates would perhaps been smaller.

From the data obtained during the three different creep tests it is evident that SSW flooding has a significant effect on the deformation behaviour 130 $^{o}$C. Removing sulphate in the flooding fluid appears to reduce the deformation rate while introducing SSW increased the creep rate significantly. The similar creep behaviour observed for DW and SSW-($SO_4^{2-}$) flooding in the early phases of the creep tests performed on LK79 and LK95 indicate that no enhanced chemical weakening will take place during SSW-($SO_4^{2-}$) flooding.

## 7.4 Chemical aspects

### 7.4.1 Aging water

The results from the chemical analysis performed on SSW and SSW-($SO_4^{2-}$) samples before and after aging in *Table.6.18* and *Table.6.19* show that some variation in the ion concentrations for the two brines occurs as a result of the aging process. In *Table.7.18* the changes in concentrations and the difference ratios for the different ions present in SSW and SSW-($SO_4^{2-}$) are listed.

*Table 7.18: Table over the changes in ion concentrations experienced for SSW and SSW-($SO_4^{2-}$) during aging of Liegé chalk samples at 130°C for three week. Changes in ion concentration are given as the difference between the concentration measured after aging and the initial concentration present in SSW and SSW-($SO_4^{2-}$)*

| Ion | SSW | | SSW-($SO_4^{2-}$) | |
|---|---|---|---|---|
| | Change [mol/l] (after-before) | Difference ratio (after/before) | Change [mol/l] (after-before) | Difference ratio (after/before) |
| $Na^+$ | 0.005 | 1.011 | 0.017 | 1.036 |
| $K^+$ | 0.000 | 1.000 | 0.000 | 1.000 |
| $Ca^{2+}$ | 0.022 | 2.692 | 0.029 | 3.231 |
| $Mg^{2+}$ | -0.025 | 0.444 | -0.025 | 0.444 |
| $Cl^-$ | 0.020 | 1.038 | 0.032 | 1.054 |
| $SO_4^{2-}$ | -0.009 | 0.625 | | |

A negative sign before value in *Table.7.18* indicates that a reduction in the given ion concentration has occurred during the aging process. An increase in concentration will therefore be recognized by a positive sign in *Table 7.18*.

At the first glance of the results in *Table 7.18* it is evident that the concentration of potassium ($K^+$) remains unchanged for both the brines during the aging. The measured concentration of magnesium ($Mg^{2+}$) before and after aging is exactly the same for both brines, which results in a similar reduction in magnesium concentration. For SSW a reduction in sulphate ($SO_4^{2-}$) concentration was also observed, while for SSW-($SO_4^{2-}$) magnesium appears to be the only ion being removed from the aqueous phase during aging. These measured reductions in concentrations for magnesium and sulphate give an indication that these ions react chemically with the chalk. For both brines a significant increase in calcium ($Ca^{2+}$) concentration was observed. This increase in calcium concentration can't be a result of pressure solution because the cores are only exposed to a 0.7 MPa gas pressure during aging which will not result in any high effective stresses at the intergranular contacts. This additional calcium must therefore come from the chalk cores and are most likely related to increased dissolution of calcium carbonate ($CaCO_3$). If this increased dissolution of calcium carbonate occurs at the intergranular contacts this may have an effect the mechanical strength of the aged chalk samples.

An increase in calcium concentration of 0.022 mol/l was measured after aging chalk cores in SSW for three weeks at 130 °C. This increase in calcium concentration is 0.007 mol/l less compared to the increase in calcium concentration measured for SSW-($SO_4^{2-}$) brine after

aging. The only difference between these two brines is the presence of sulphate, indicating that the difference in calcium concentration observed for the two brines may be related to the presence of sulphate. In the SSW aging water a reduction of 0.009 mol/l was measured in the sulphate concentration. By taking the low solubility of anhydrite ($CaSO_4$) at 130 $^oC$ into consideration, precipitation of anhydrite may be the result why a lower calcium concentration is seen in the SSW brine compared to SSW-($SO_4^{2-}$) brine. But a higher reduction in sulphate concentration is measured compared to what could be expected from precipitation of anhydrite alone. From flooding experiments with pure sodium sulphate brines ($Na_2SO_4$) *Megawati et al. (2011)* showed that sulphate was adsorbed as brine was flooded through Liege´ chalk cores at 130 $^oC$. Such sulphate adsorption on the chalk surface may be a reasonable explanation for the additional reduction in sulphate concentration.

For both brines in *Table 7.18* a significant reduction in magnesium concentration was observed. Based in these results the changes in magnesium and calcium concentrations can be a result of ion substitution (*Korsnes et al., 2006*) or precipitation of magnesium bearing minerals (*Madland et al. 2011).* Based on the available data it is difficult to draw any firm conclusion on the mechanism behind the removal of magnesium during aging.

The difference ratios in *Table 7.18* were included such that the relative changes in concentrations could be studied. These ratios give a better picture of the variations in ion concentration compared to the measured changes alone. From *Table 7.18* the concentration of sodium ($Na^+$) and chloride ($Cl^-$) increases with the same order of magnitude as the variation in magnesium and calcium concentrations. But the initial concentrations of sodium and chloride are significantly higher compared to the concentrations of magnesium, calcium and sulphate. Therefore what may be regarded as a high increase in concentration may only result in a minor relative change compared to the initial state. From *Table 7.18* it is evident that measured changes in sodium and chloride concentrations only result in minor relative changes for both brines compared to what is seen for magnesium, calcium and sulphate. In example the concentration of chloride measured after aging in SSW will be 1.038 times higher compared to the initial concentration of chloride in SSW, while the calcium concentration in the SSW aging water increases with a factor 2.692. By comparing the difference ratio for potassium, sodium and chloride in both brines in *Table 7.18* it is evident that these ions do not chemically react with the chalk during the aging process.

### 7.4.2 Creep tests

The results for the chemical analysis performed on the effluent samples collected during the creep tests (*Fig. 6.20, Fig.6.21* and *Fig.6.22*) all show a significant reduction in magnesium concentration. At the same as there is a reduction in magnesium ($Mg^{2+}$) concentration a significant increase in calcium ($Ca^{2+}$) concentration is observed. These results indicate that there are some processes taking place inside the chalk cores that removes magnesium from the aqueous solution and causes a significant calcium production. This additional calcium must come from the chalk cores because there are no other sources of calcium in the system. *Korsnes et al. (2006)* proposed that the water weakening of chalk that was observed during SSW flooding of chalk cores at 130 $^oC$ was a result of an ions substitution mechanism between magnesium and calcium at the chalk surface. This process would therefore depend on the maximum available adsorption sites inside the core. *Madland et al. (2011)* calculated that the maximum number of adsorption sites available for substitution in chalk cores similar to the ones used in this present study was 0.0019 mol. Therefore should the ion substitution

process prevail no more than 0.0019 mol magnesium can be removed from the aqueous phase during the creep tests.

To study this we use the results from the chemical analysis of the collected water samples during SSW-($SO_4^{2-}$) flooding of LK79. To be able to compare the reduction in magnesium concentration to the maximum number of available adsorption sites we need to calculate how many mol's that have been removed from the solution during this flooding period. The reason for using the results for the SSW-($SO_4^{2-}$) flooding phase on LK79 is because there are no other ions present in SSW-($SO_4^{2-}$) that seems to react chemically with the chalk during flooding. During the entire SSW-($SO_4^{2-}$) flooding period of 50 110 minutes a constant flooding rate of 0.022 ml/min was used. From this we can calculate how many litres that have been flooding through the core during this period of time.

$$V_{flooded} = \frac{Q\left[\frac{ml}{min}\right] \cdot t_{flooding}[min]}{1000\ [ml]} = \frac{0.022\left[\frac{ml}{min}\right] * 50\ 110\ [min]}{1000\ ml} = 1.102\ l$$

where:
$V_{flooded}$=Volume flooded through the core [ml]
Q = flooding rate [ml/min]
$t_{flooding}$= total time SSW-($SO_4^{2-}$) has been flooded

The total volume flooded through the entire flooding phase was calculated to 1.102 l. To be able to estimate how much magnesium that has been removed one first have to find the average reduction of magnesium. The average concentration of magnesium was found on bases of the measured magnesium concentration from the effluent samples collected during SSW-($SO_4^{2-}$) flooding phase and was calculated to 0.0311 [mol/l]. By subtracting this average concentration from the initial concentration of magnesium in SSW-($SO_4^{2-}$) (which is 0.045 (mol/l)) one can find the average reduction in concentration.

$$[Mg^{2+}]_{removed} = [Mg^{2+}]_{initiall} - [Mg^{2+}]_{average}$$

$$[Mg^{2+}]_{removed} = 0.045\left[\frac{mol}{l}\right] - 0.0311\left[\frac{mol}{l}\right] = 0.0139\left[\frac{mol}{l}\right]$$

By multiplying the average concentration of removed magnesium by the total flooded volume the amount of magnesium removed in mol's can be estimated.

$$Mg^{2+} = [Mg^{2+}]_{\text{average}}\left[\frac{\text{mol}}{\text{l}}\right] * V_f[\text{l}]$$

$$Mg^{2+} = 0.0139\left[\frac{\text{mol}}{\text{l}}\right] * 1.102[\text{l}] = 0.015\text{mol}$$

The amount of magnesium removed from the aqueous phase during SSW-($SO_4^{2-}$) flooding on LK79 is a factor 7.90 higher than the maximum number of adsorptions sites available for substitution calculated by *Madland et al. (2011).* Similar calculations can also be performed on the chemical results obtained from the analysis of the effluent samples collected during the creep test of LK94. The chemical results obtained from the SSW flooding phase of LK95 are not adequate for performing such calculations and are therefore not included. SSW was

flooded for 32 040 minutes with a constant pump rate equal to 0.021 ml/min in the creep tests performed on LK94. The calculated average magnesium concentration was determined to 0.033 mol/l for this flooding phase. Following the same procedure the amount of magnesium lost during the creep tests on LK94 will be:

$$Mg^{2+} = 0.012\left[\frac{\text{mol}}{\text{l}}\right] * 0.672[\text{l}] = 0.0081 \text{ mol}$$

This removal of magnesium is a factor 4.26 higher than the maximum number of adsorption sides available for substitution calculated by *Madland et al. (2011)*. These data indicate that an ion substitution process can not be the only mechanism behind the removal of magnesium from the aqueous phase. *Madland et al. (2011)* concluded that the removal of magnesium and the high increase in calcium concentration was linked to precipitation of magnesium bearing minerals inside the chalk core. The chemical results obtained from the creep tests performed on LK79 and LK94 support the theory by *Madland et al. (2011*). Had the creep test performed on LK95 been continued for a longer period of time similar calculations could also be conducted on the chemical results obtained from this test.

For the flooding phases with SSW in the tests performed on LK79, LK94 and LK95 sulphate is removed from the aqueous solution (*Fig. 6.20*, *Fig.6.21* and *Fig.6.22*) which is most likely a result of chemical reaction taking place inside the core. From the creep curves in *Fig. 7.5* it is evident the presence of sulphate has a significant effect of the creep behaviour at 130 $^{o}$C *Heggheim et al. (2004)* shows that sulphate would be removed from the solution due to precipitation of anhydrite ($CaSO_4$) when synthetic seawater with 4 times higher content of sulphate was flooded through chalk at 130 $^{o}$C which further increased the dissolution of chalk. The reduction of mechanical strength was described in terms of increased dissolution of chalk. *Megawati et al. (2011)* measured absorption of sulphate at the chalk surface and descried the measured weakening observed in terms of a total disjoining pressure at the intergranular contacts.

By comparing the chemical results obtained from the SSW flooding phase in the tests performed in LK79 and LK94 both these theories can be examined. In *Fig.7.7* the chemical results obtained from the creep tests performed on LK94 are shown. Here the concentration of calcium, magnesium and removed sulphate is compared to the original concentration of calcium and magnesium in SSW. The measured concentration of sodium, potassium and chloride are not included in *Fig.7.7* because they remain approximately constant during the different flooding phases, and do not appear to react chemically with chalk. By excluding these ions one can study the changes of magnesium, calcium and sulphate in greater detail.

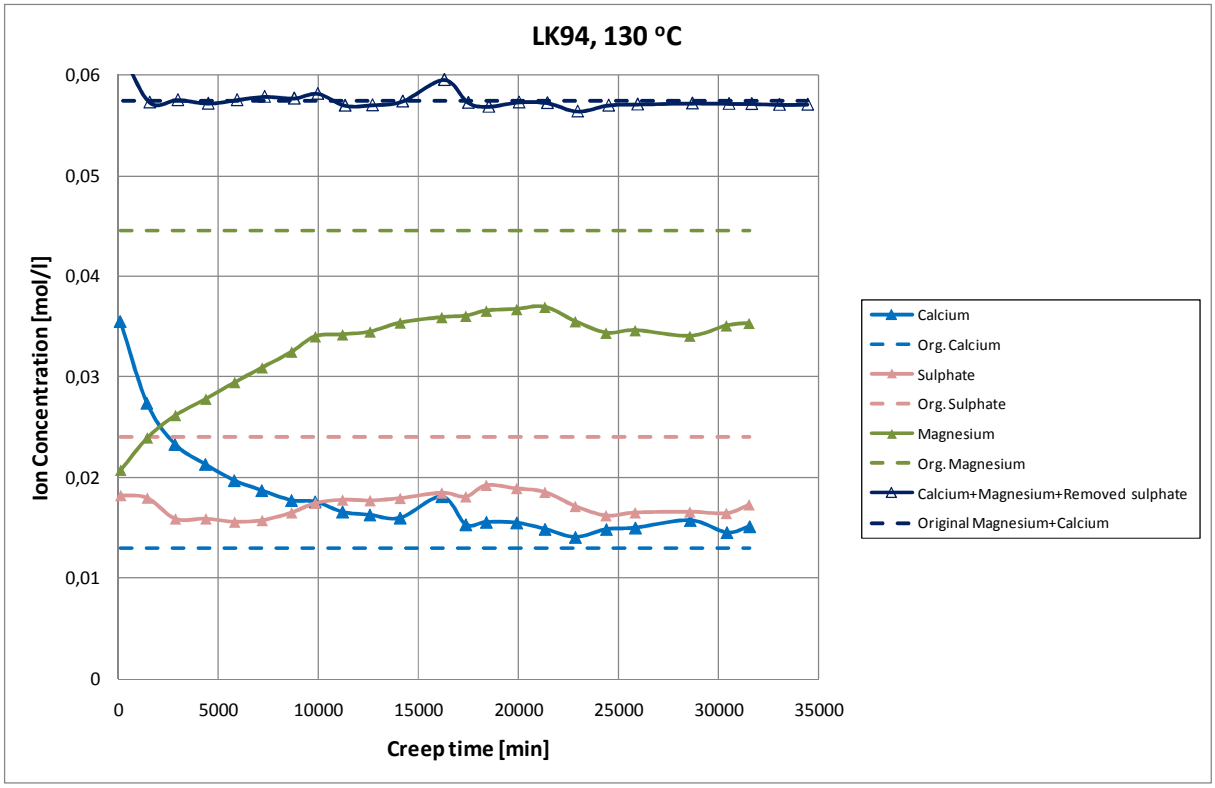


*Fig.7.7: The measured concentrations of calcium, magnesium and sulphate obtained from effluent samples collected during the creep test performed on LK94. A line is included where the measured concentrations of calcium magnesium and the removed sulphate (original concentration of sulphate-the measured concentration of sulphate) is compared to the original concentration of magnesium and calcium (original magnesium +orginial calcium)*

As seen from *Fig.7.7* the line for the original calcium and magnesium concentrations coincide with the line for the calcium, magnesium and removed sulphate. This fact indicates that there is a close relationship between the changes in magnesium, calcium and sulphate concentrations. From the results in *Fig.7.7* it appears that the reduction in sulphate is most likely a result of precipitation process taking place inside the chalk core. One such mineral that can precipitate is anhydrite ($CaSO_4$). Similar observations are also seen when performing the similar comparison on the chemical results for the SSW flooding phase in the test performed on LK79 as shown in *Fig.7.8*. Also here the measured concentrations of sodium, potassium and chloride are excluded such that the changes in magnesium, calcium and sulphate can be studied in greater detail.

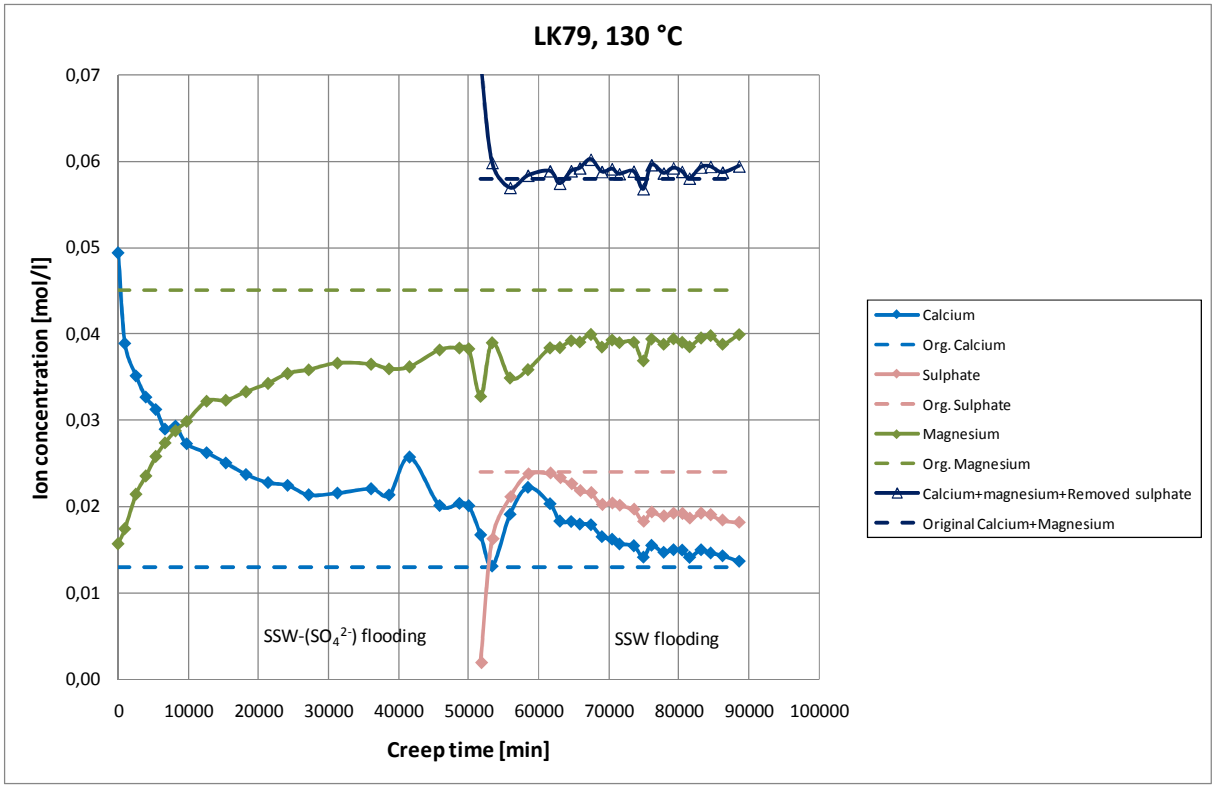


*Fig.7.8: Measured changes in magnesium calcium and sulphate concentrations obtained from the effluent samples collected during the creep test performed on LK79. During the first 50 110 minutes SSW-($SO_4^{2-}$) flooding is performed. As SSW flooding was initiated the measured concentration of sulphate starts to increase. The measured concentrations of calcium, magnesium and removed sulphate (original concentration of sulphate-measured concentration of sulphate) is compared to the original concentration of magnesium and calcium in the brine (original magnesium + original calcium)*

In *Fig.7.8* a clear reduction in calcium concentration is observed as SSW flooding is started. At the same time a very gradual increase in sulphate concentration occurs. This data indicates that there are some processes taking place inside the core which removes calcium and magnesium from the solution. After approximately 8000 minutes the sulphate concentration reaches a maximum level and starts to decline. The measured calcium concentration follows a similar trend as the measured sulphate concentration. The fact that sulphate is removed from the solution gives as indication that sulphate is removed from the aqueous phase due to precipitation. By studying the curves for the measured magnesium, calcium and removed sulphate in *Fig.7.8* one can also see here that this line coincides with the original calcium and magnesium line. These observations in *Fig.7.7* and *Fig.7.8* indicate that sulphate is removed from the solution as a result of precipitation, but due to the complexity of SSW it is difficult to draw any firm conclusions on the basis of the chemical results obtained from the creep tests performed on LK94 and LK95.

Sulphate adsorption at the chalk surface as described by *Megawati et al. (2011)* may still occur in the creep tests performed in this present study but is very difficult to measure due to the complexity of SSW. But indications of sulphate adsorption can actually be seen when studying the results for the chemical analysis performed on effluent samples collected during the creep test performed on LK95 in *Fig.6.21*. As SSW is introduced to LK95 a significant increase in calcium concentration is observed, which is the opposite behaviour compared to what is seen when SSW follows a period of SSW-($SO_4^{2-}$) flooding where a drop in calcium

concentration is observed (see *Fig.7.8*). At the same time there is a gentle increase in both sodium and calcium concentrations. It appears that these ions break through at the outlet somewhat earlier compared to magnesium, potassium and sulphate. From *Fig.6.21* it appears that magnesium, potassium and sulphate are retained in the core. Magnesium and sulphate appear to breakthrough approximately 2000 minutes after SSW flooding was started, while potassium appears to be retained for somewhat longer period of time. This observation gives an indication that adsorption may take place inside the core.

Sulphate adsorption may occur on the positive charged chalk surface due to electrostatic differences while the positive charged ions (magnesium and potassium) can be retained due to two different processes. As sulphate adsorbs on the chalk surface the surface potential will be reduced and may even become negative. Positive charged ions are then attracted to the surface due to electrostatic forces in an effort to neutralize the electrical charge. Another process that may cause retention of positive charged ions is cation exchange due to presence of clay minerals inside the chalk core. Clays tend to have a higher affinity towards magnesium compared to potassium, but due to the higher concentration of magnesium an earlier breakthrough will be expected for magnesium compared to potassium which may be an explanation for the observed behaviour in *Fig.6.21*. But it must be kept in mind that other processes inside core may remove magnesium from the aqueous solution. Magnesium may precipitate as a magnesium bearing mineral inside the core, it can be attracted to the chalk surface due to electro static forces, and it may be removed due to cation exchange as a result of clay minerals present inside the core. Based on this fact it is difficult to draw any firm conclusion based on the available chemical data.

Nonetheless it appears that precipitation of sulphate and magnesium bearing minerals takes place inside the chalk cores during flooding. This precipitation appears to increase the dissolution of calcium carbonate which again seems to have a weakening effect on chalk both during SSW and SSW-($SO_4^{2-}$) flooding.

# 8 Concluding remarks

The main objective for this thesis was to study the effect of sulphate by performing Brazilian tests and triaxial tests (deviatoric and hydrostatic) at both ambient temperature and at 130 $^{o}$C. Similar tests were conducted with synthetic seawater (SSW) and synthetic seawater without sulphate (SSW-($SO_4^{2-}$) as saturation and flooding fluid such that estimates of the failure envelopes in q-p´ plots could be obtained for the different tests parameters (temperature and flooding fluid). Creep tests were included such that the effect of sulphate post failure also could be studied. The experimental work was performed on a high porosity Liegé outcrop chalk with an average porosity of 39.57%. Based on the results obtained from this present study in combination with the results from Øvstebø (2011) the following conclusions can be drawn.

**Triaxial tests**

- Chalk cores tested at 130 $^{o}$C were weaker against both shear failure and pore collapse in the presence of sulphate. The largest overall reduction in strength was observed for stress configurations where pore collapse was the dominant failure mechanism, i.e. for tests performed with a high degree of radial support. The tests performed without any sulphate present in the flooding fluid had yield points and Young's moduli values that were approximately a factor 1.3 higher than for tests where sulphate was present in the flooding fluid.

- For cores tested at ambient temperature no clear reduction in mechanical strength was observed in the presence of sulphate. In fact a higher resistance against shear failure is observed when sulphate is present in the flooding fluid.

- Chalk cores tested by using synthetic seawater (SSW) brine showed a clear reduction in overall mechanical strength when tested at 130 $^{o}$C indicating that the weakening caused by sulphate will be temperature dependant. The largest reduction in strength is seen for stress configurations where pore collapse is the dominant failure mechanism. The tests performed at ambient temperature had yield points and Young's moduli values that were approximately a factor 1.5 higher than tests performed at 130 $^{o}$C.

- For chalk cores tested by using synthetic seawater without sulphate (SSW-($SO_4^{2-}$)) the mechanical strength seems to be unaffected by temperature. Overall the yield points, Young's modulus, bulk modulus and failure envelopes will be very similar for the two different test temperatures.

**Creep tests**

- The axial strain experienced during creep at high temperature is to a large extent dependant on the presence of sulphate in the flooding fluid. Axial creep strain experienced during SSW flooding was found to be a factor 1.62 higher than the axial creep strain experienced during SSW-($SO_4^{2-}$) flooding (after 32 000 minutes of creep). When sulphate is introduced to the flooding fluid during creep a considerable increase in deformation rate is observed. For the opposite case where sulphate is removed from the flooding fluid a reduction is deformation rate will occur.

- Chemical results obtained from effluent samples collected during creep show that precipitation of magnesium bearing minerals may occur both during SSW and SSW-($SO_4^{2-}$) flooding at 130 $^{o}$C.

- The reduction in sulphate concentration measured during creep phases with SSW flooding appears to be a result of precipitation of anhydrite ($CaSO_4$).

- Immediate observations on the changes in sulphate concentration as being introduced to a pore system appear to be dependent on the composition of the prior flooding fluids. For SSW flooding following a period of distilled water flooding indications of sulphate adsorption was seen. This was not observed in the case when SSW was introduced after a long period of SSW-($SO_4^{2-}$) flooding.

# 9 Further work

As a continuation of this study on the effect of sulphate the following points could be included to provide a better foundation for comparison. These recommended points could also result in a more thorough understanding of how the mechanical behaviour of chalk is affected by the presence of sulphate in the flooding fluid.

- First of all repetitions of the different triaxial tests (both hydrostatic and deviatoric) should be performed such that the observation made in this thesis could be confirmed. Repetitions of the different triaxial tests would also result in a better foundation for comparison which would result in a better estimate of the failure envelopes at the different test parameters (temperature end flooding fluid)

- To be study the effect sulphate present in the flooding fluid at the different tests temperatures has on the bulk modulus at least two more hydrostatic tests should be included with SSW-($SO_4^{2-}$) flooding. Such that comparison of bulk modulus can be performed on the same number of tests as for SSW flooding.

- More creep tests should be included where flooding of SSW and SSW-($SO_4^{2-}$) are conducted at different stages in creep tests and in different orders to study in greater detail how introduction and removal of sulphate will affect the overall creep behaviour.

- Chemical analysis should be performed on a larger amount of water samples collected from new creep tests. Effluent samples should be collected more frequently as flooding fluid is changed. This would make it possible study the changes in ion concentration as new brine displaces the fluid present in the pore space with a higher resolution.

- Triaxial tests (both hydrostatic and deviatoric) should be performed on un-aged chalk samples at 130 °C with both SSW and SSW-($SO_4^{2-}$) as flooding fluid such that the effect of aging the cores for three weeks at 130 °C could be determined.

- To study if the chemical weakening observed at 130 °C truly is a result of enhanced dissolution of calcium carbonate ($CaCO_3$) tests should be performed with a flooding fluid that contains a concentration of calcium that is ten times higher than the original concentration of calcium in SSW. For such test sulphate should not be present in the flooding fluid because this would most likely result in precipitation of anhydrite ($CaSO_4$).

# 10 Reference list

Ahr, W. M. 2008. Geology of carbonate reservoirs: The Identification, Description and Characterization of Hydrocarbon Reservoirs in Carbonate Rocks. ISBN: 978-0-470-36925-8

Andersen, M. A., Foged, N. and Pedersen, H. F. 1992. The rate type compaction of weak North Sea Chalk. Rock Mechanics, Tillerson & Wawersik (eds) 1992 Balkema, Rotterdam. ISBN: 905-1-100451

Blanton, T. L., 1981. Deformation of Chalk Under Confining Pressure and Pore Pressure. SPEJ, February 1981

DaSilva, F., Sarda, J. P., Schroeder, C., 1985. Mechanical behaviour of chalks. Second North Sea Chalk Symposium, Book II, Stavanger, Norway.

Delage, P., Schroeder and C., Cui, Y.J. 1996. Subsidence and capillary effects in chalks. EUROCK'96, Torino, Italy.

Doornhof, D., Kristiansen, T. G., Nagel, N., Pattillo, P. and Sayers, C. 2006. Compaction and subsidence. Oilfield Review. Autumn 2006.

Fabrizius, I. L. 2003. How burial digenesis of chalk sediments controls sonic velocity and porosity. AAPG Bulletin, v.87, No.11(November 2003), PP. 1755-1778

Fjær. E., Holt. R.M., Horsrud. P., Raaen. A.M. & Risnes. R. 2008. Petroleum related rock mechanics. 2.nd Edition. ISBN:978-0-444-50260-5.

Gauer, P. R., Sylte, J.E., and Nagel, N. B. 2002. Ekofisk Field Well Log Decompaction. SPE/ISRM 78177.

Hancock, J., 1985. Oil in Chalk. Geology Today, 1:5, 146-150

Heggheim, T., Madland, M. V., Risnes, R. and Austad, T. 2004. A chemical induced enhanced weakening of chalk by seawater. Journal of Petroleum Science and Engineering 46 (2005) pp. 171-184.

Hellmann, R., Renders, P. J. N., Gratier J. P. and Guiguet, R. 2002. Experimental pressure solution compaction of chalk in aqueous solutions. Part 1. Deformation behavior and chemistry. Water-Rock Interactions, Ore Deposits, and Environmental Geochemistry: A Tribute to David A. Crerar. The Geochemical Society, Special Publication No. 7, 2002 . Roland Hellmann and Scott A. Wood (eds)

Hiorth, A., Cathles, L. M., Kolsnes, J., Vikane, O., Lohne, A., Korsnes, R. I., Madland, M. V. 2008. A Chemical model for the seawater- $CO_2$-carbonate system- Aqueous and surface chemistry. International symposium of the society of core analysts in Abu Dhabi, UAE 29 October -2 November, 2008.

Hiorth, A., Cathles, L. M., Madland, M. V. 2010. The impact of Pore Water Chemistry on Carbonate Surface Charge and Oil Wettability. Tranp. Porous Med. (2010) 85:1-21. DOI 10.107/s11242-010-9543-6

Hjuler, M.L. and Fabricius, I. L. 2009. Engineering properties of chalk related to diagenic variations of Upper Cretaceous onshore and offshore chalk in the North Sea area. In: Journal of Petroleum Science and Engineering 68 pp: 151-170.

Jaeger. J. C., Cook N. G. W., Zimmermann R. W. 2007. Fundamentals of Rock Mechanics. 4th edition. ISBN-13: 978-0-632-05759-7.

Jones. M. E. and Leddra. M. J. (1989). “Compaction and flow of porous rocks at depth”. In: Maury, V., Fourmaintraux, D. (Eds.), Rock at Great Depth. Balkema, Rotterdam, pp.891-898.

Jones, M. E., Leddra, M. J., Goldsmoth, A. S., Berget, O. P. and Tappel, I. 1989. The geotechnical characteristic of weak, North Sea Reservoir Rocks. North Sea oil and gas reservoirs - II : proceedings of the 2nd North Sea Oil and Gas Reservoirs Conference organized and hosted by the Norwegian Institute of Technology (NTH), Trondheim, Norway, May 8-11, 1989 / edited by A. T. Buller ... [et al.]

Judd. W.R. (1964). Rock stress, rock mechanics and research, in State of Stress in the Earth’s crust, W.R. Judd, ed., Elsevier, New York, pp. 5-51.

Korsnes, R. I. 2000. Development of a test cell for Brazilian tests at reservoir temperature. Master thesis. Stavanger University College. 2000.

Korsnes, R. I., Madland, M. V. and Austad, T. 2006. Impact of brine composition on the mechanical strength of chalk at high temperatures. EUROCK 2006- Multiphysics Coupling and long term Behavior in Rock Mechanics- Van Cotthem, Charlier, Thimus & Tshibangu (eds). 2006. Taylor & Francis Group, London, ISBN: 0-415-41001-0. pp: 133-140.

Læknes, T. K. 2009. Chalk flooded with simple brines: a rock mechanical and SEM study. Master Thesis. Department of Petroleum Technology. University of Stavanger

Madland, M. V., Korsnes, R. I., Risnes, R. 2002. Temperature effects in Brazilian, uniaxial and triaxial compressive tests with high porosity chalk. SPE-77761.

Madland, M. V., Finsnes, A., Alkafadgi, A., Risnes, R., Austad, T. 2006. The influence of $CO_2$ gas on the mechanical stability of chalk. In: Journal of Petroleum Science and Engineering 51 (2006). pp. 149-168.
Miller JP (1952) A portion of the system calcium carbonate-carbon dioxide-water, with geological implications. Am J Sci 250:161-203

Madland, M. V., Hiorth, A., Korsnes, R. I., Evje, S. and Cathles, L. 2009a. Rock Fluid Interactions in Chalk exposed to Injection of Seawater, $MgCl_2$ and NaCl Brines with equal Ionic Strength. 15th European Symposium on Improved Oil Recovery – Paris, France. 27-29 April. 2009.

Madland, M. V., Omdal, E., Breivik, H., Korsnes, R. I., Hiorth, A., Krisitansen, T. G. Investigation of the Effective Stress Relation for Outcrop Chalk. In: Ling HI, Smyth A, Betti, R (eds) Destech Publications Inc, New York (2009b) Poromechanics IV, Proceedings of the Fourth Biot Conference on Poromechanics pp. 429-434.

Madland, M. V., Hiorth, A., Omdal, E., Megawati, M., Hildebrand-Habel, T., Korsnes, R. I., Evje, S., Cathles, L. M. 2011. Chemical Alterations Induced by Rock- Fluid Interactions When Injecting Brines in High Porosity Chalk. In: Tranp. Porous Med. DOI 10.1007/s11242-010-9708-3.

Megawati, M., Hiorth, A., Madland, M. V. 2011 .The impact of surface charge on the mechanical strength of high porosity chalk. Unpublished paper.

Omdal, E., Madland, M. V., Breivik, H., Næss, K.E., Korsnes, R.I., Hiorth, A., Kristiansen, T.G. Experimental Investigation of the Effective Stress Coefficient for Various High Porosity Outcrop Chalks . ARMA 09-118

Savage. J. C., Byerlee. J. D. and D. Lockner. A. Is internal friction friction? Geophysical Research Letters, Vol. 23, No.5, Pages 487-490. 1996.

Risnes, R. and Flaageng, O. 1999. Mechanical Properties of Chalk with Emphasis on Chalk-Fluid Interactions and Micromechanical Properties. Oil & Gas Science and Technology – Rev. IFP, Vol. 54 (1999), No. 6, pp. 751-758.

Risnes, R. and Nygaard, V. 1999. Elasticity in High Porosity Outcrop Chalk. Second Euroconference on Rock Physics and Rock Mechanics, Heriot-Watt University, Edinburgh, Scotland.

Risnes, R., 2001. Deformation and Yield In High Porosity Outcrop Chalk. In: Phys. Chem. Earth (a), Vol. 26, No. 1-2, pp. 53-57, 2001.

Risnes, R., Haghighi, H., Korsnes, R.I., Natvik, O., 2003. Chalk- Fluid interactions with glycol and brines. Tectonophysics 370, 213-226.

Risnes, R., Madland, M.V., Hole, M., Kwabiah N.K., 2005. Water weakening of chalk- Mechanical effects of water- glycol mixtures. Journal of Petroleum Science & Engineering, 48, 21-36.

Roehl, P.O., Choquette, P.W (Editors), 1985. Carbonate Petroleum Reservoirs. Springer-Verlag, New York, pp 622.

Rutter, E.H. Pressure solution in nature, theory and experiment. J Geol Soc London 1983;140:725–40.

Schutjens, P.M.T.M. and Spiers, C.J. 1999. Intergranular Pressure Solution in NaCl: Grain-to-Grain Contact Experiments under the Optical Microscope. Oil & Gas Science and Technology – Rev. IFP, Vol. 54 (1999), No. 6, pp. 729-750. 1999. Éditions Technip.
*Lehner, F. K. 1995.* A model for intergranular pressure solution in open systems. Tectonophysics 245 (1995) 153-170

Zhang, X. and Spiers, C.J. 2006. Compaction of granular calcite by pressure solution at room temperature and effects of pore fluid chemistry. In: International Journal of Rock Mechanics & Mining Sciences 42 (2005) 950–960.

Øvstebø, K. A. 2011. A mechanical study of sulphate effect on chalk. Department of Industrial Economics, Risk Management and Planning. University of Stavanger

# 11 Appendix A- Tests saturated and flooded with SSW

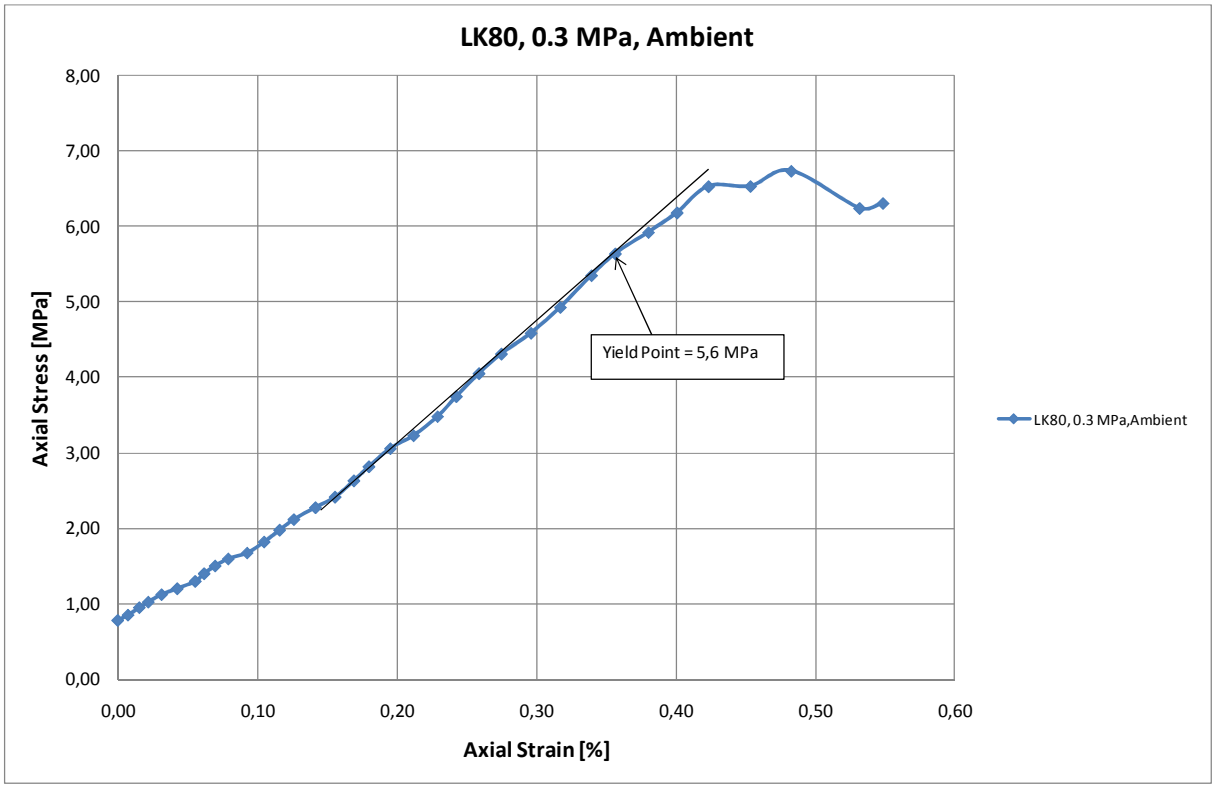


*Fig.A.1: Axial stress versus Axial strain plot for a 0.3 MPa deviatoirc test performed on LK80 with SSW flooding at ambient temperature*

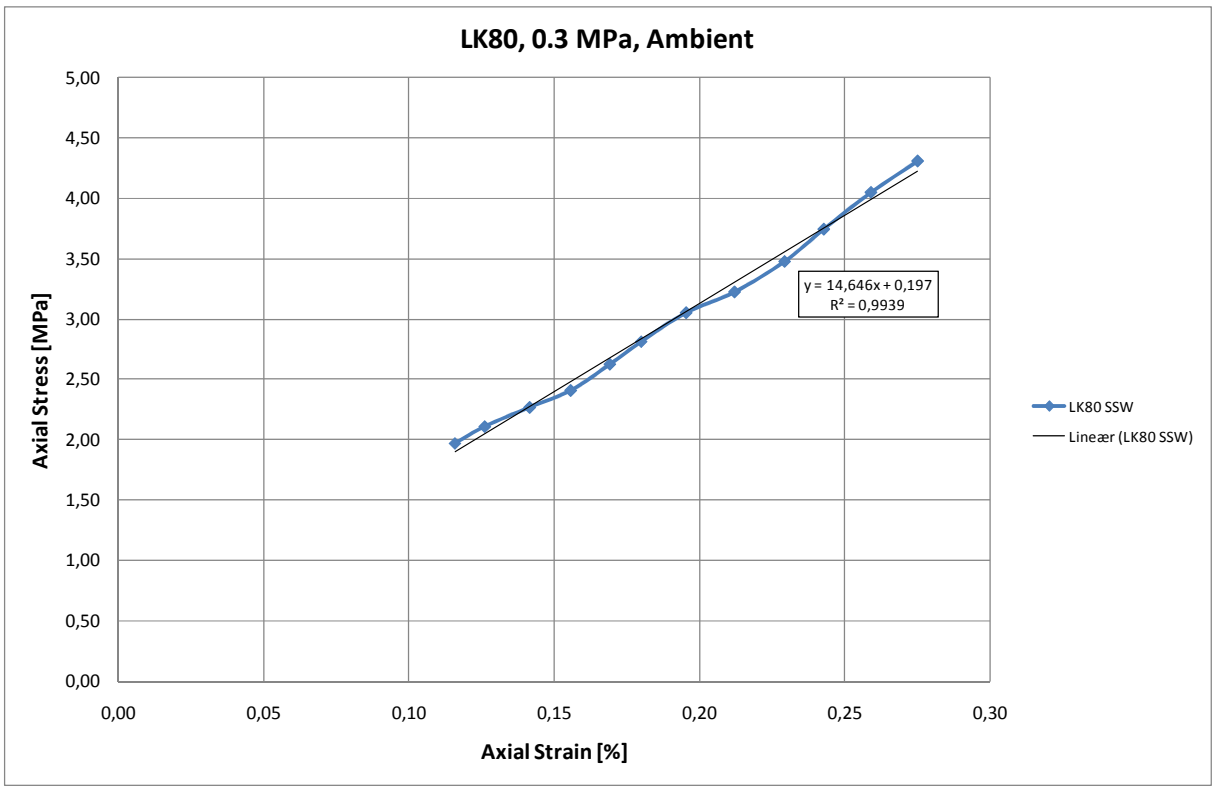


*Fig.A.2: Section of the Axial stress versus Axial strain plot for the 0.3 MPa deviatoirc test performed on LK80 with SSW flooding at ambient temperature used to estimate the Young's modulus.*

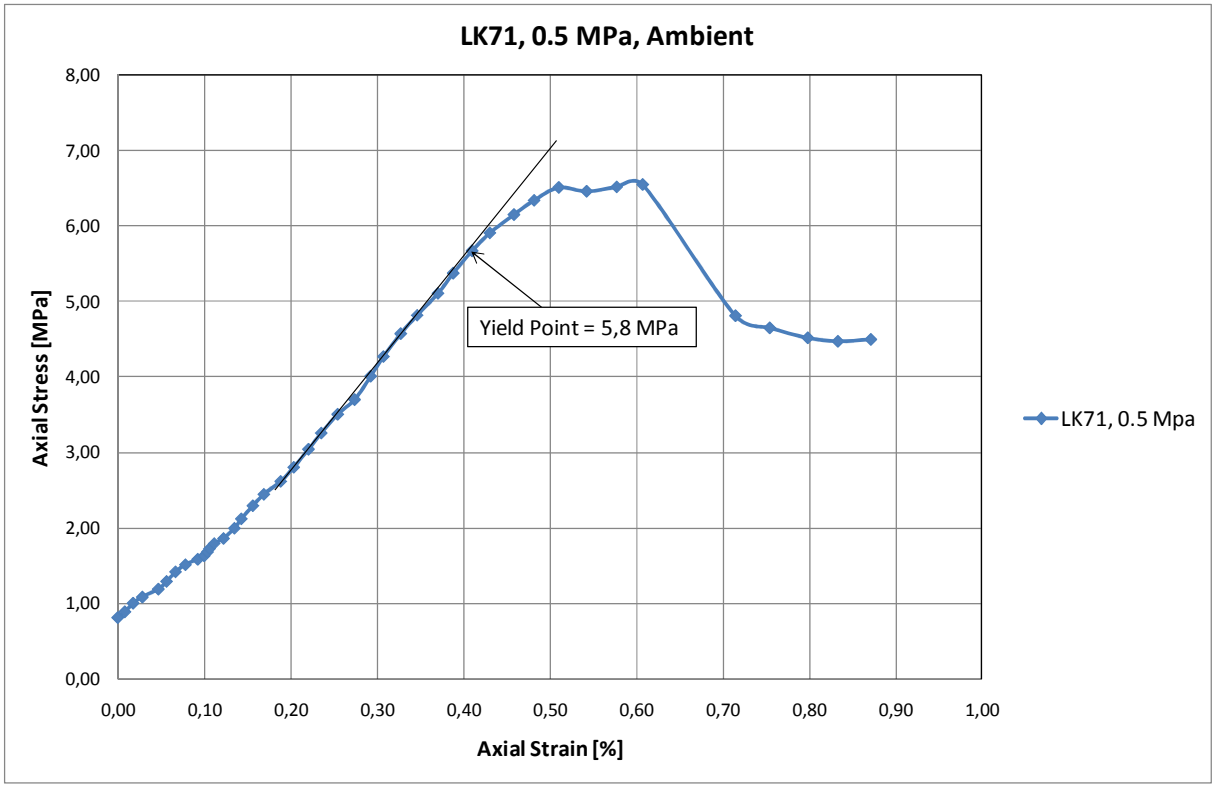


*Fig.A.3: Axial stress versus Axial strain plot for a 0.5 MPa deviatoirc test performed on LK71 with SSW flooding at ambient temperature*

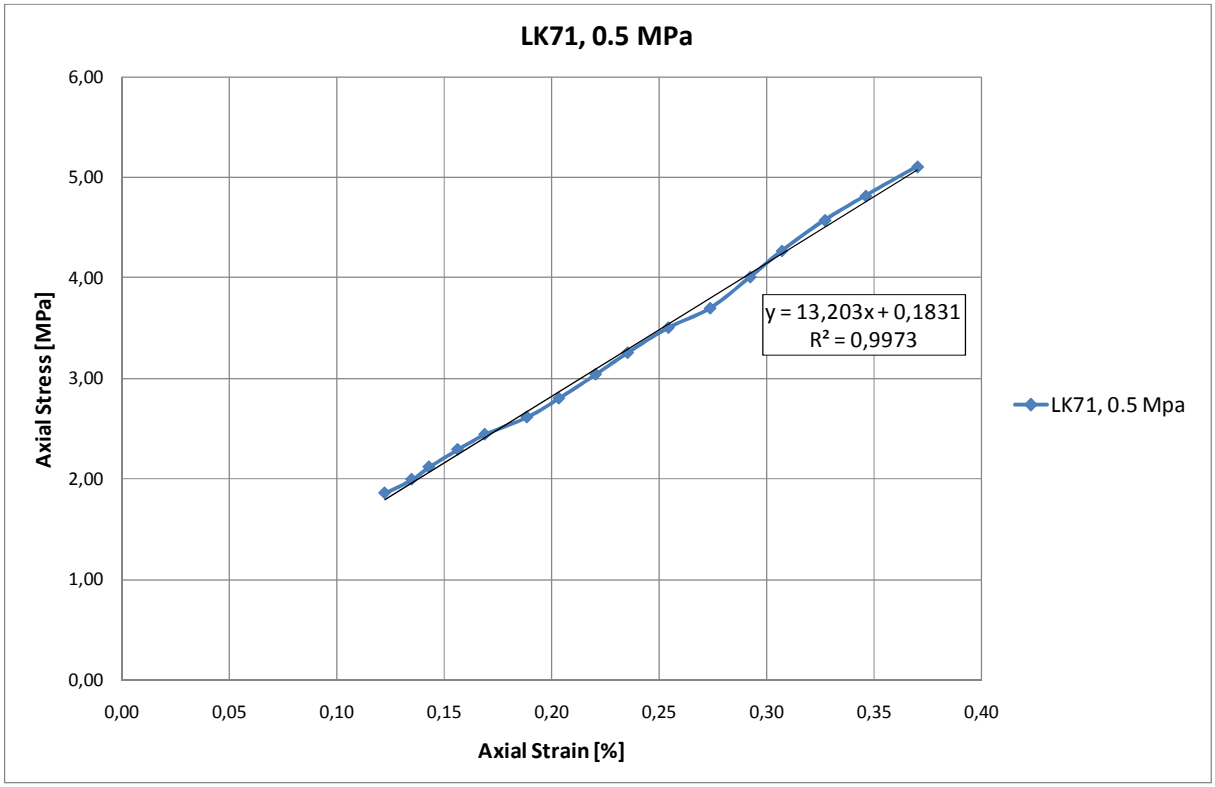


*Fig.A.4: Section of the Axial stress versus Axial strain plot for the 0.5 MPa deviatoirc test performed on LK71 with SSW flooding at ambient temperature used to estimate the Young's modulus.*

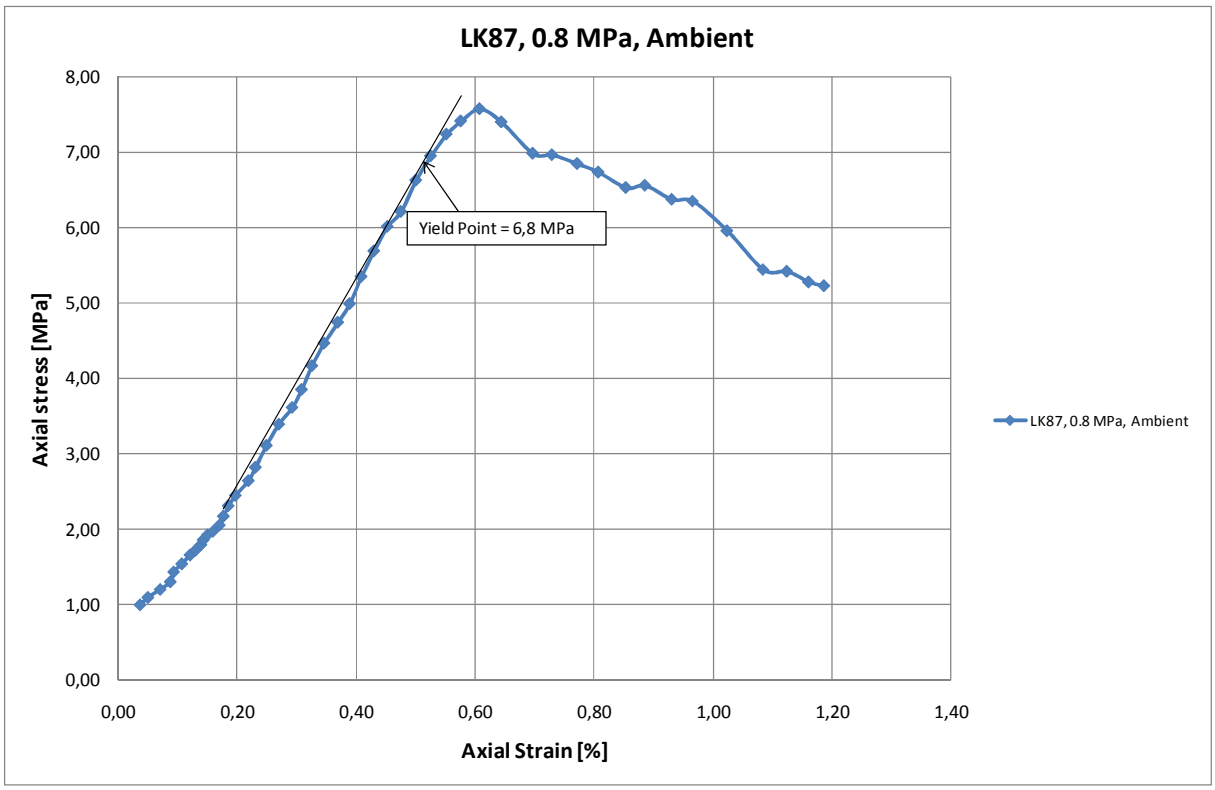


*Fig.A.5: Axial stress versus Axial strain plot for a 0.8 MPa deviatoirc test performed on LK87 with SSW flooding at ambient temperature*

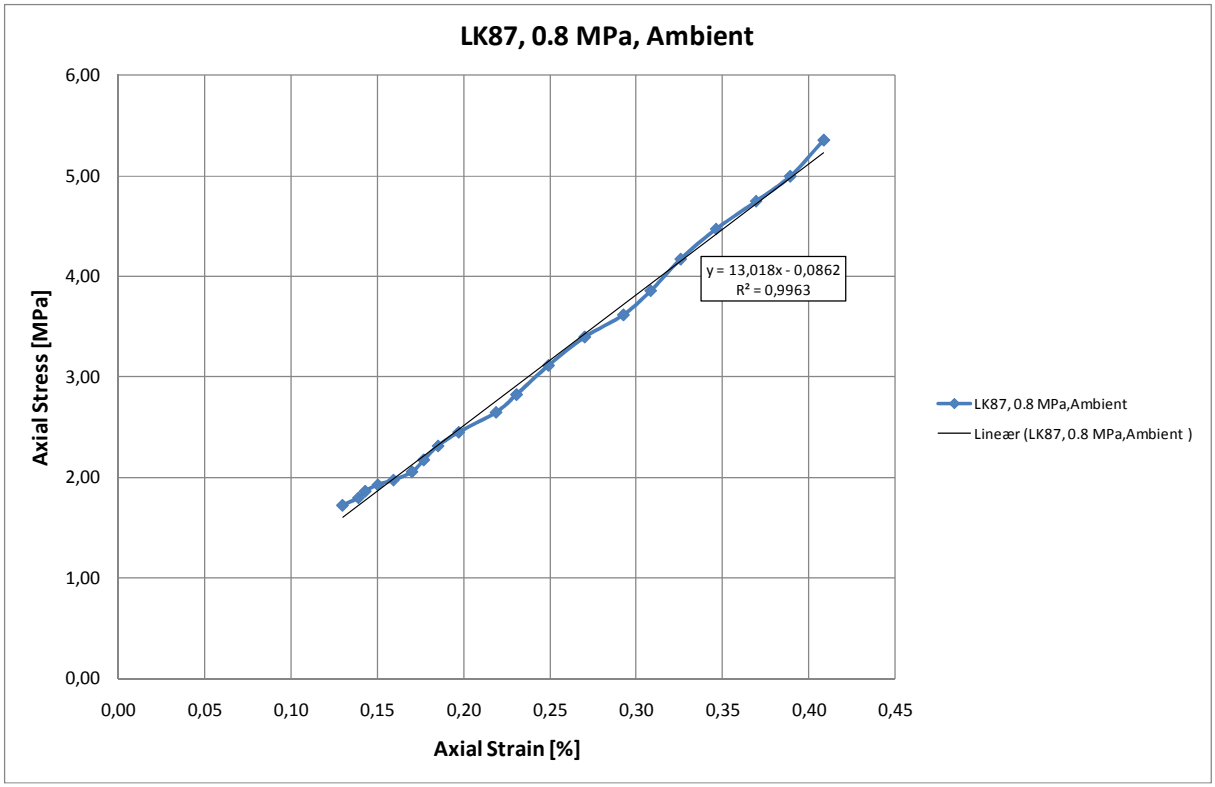


*Fig.A.6: Section of the Axial stress versus Axial strain plot for the 0.8 MPa deviatoirc test performed on LK87 with SSW flooding at ambient temperature used to estimate the Young's modulus.*

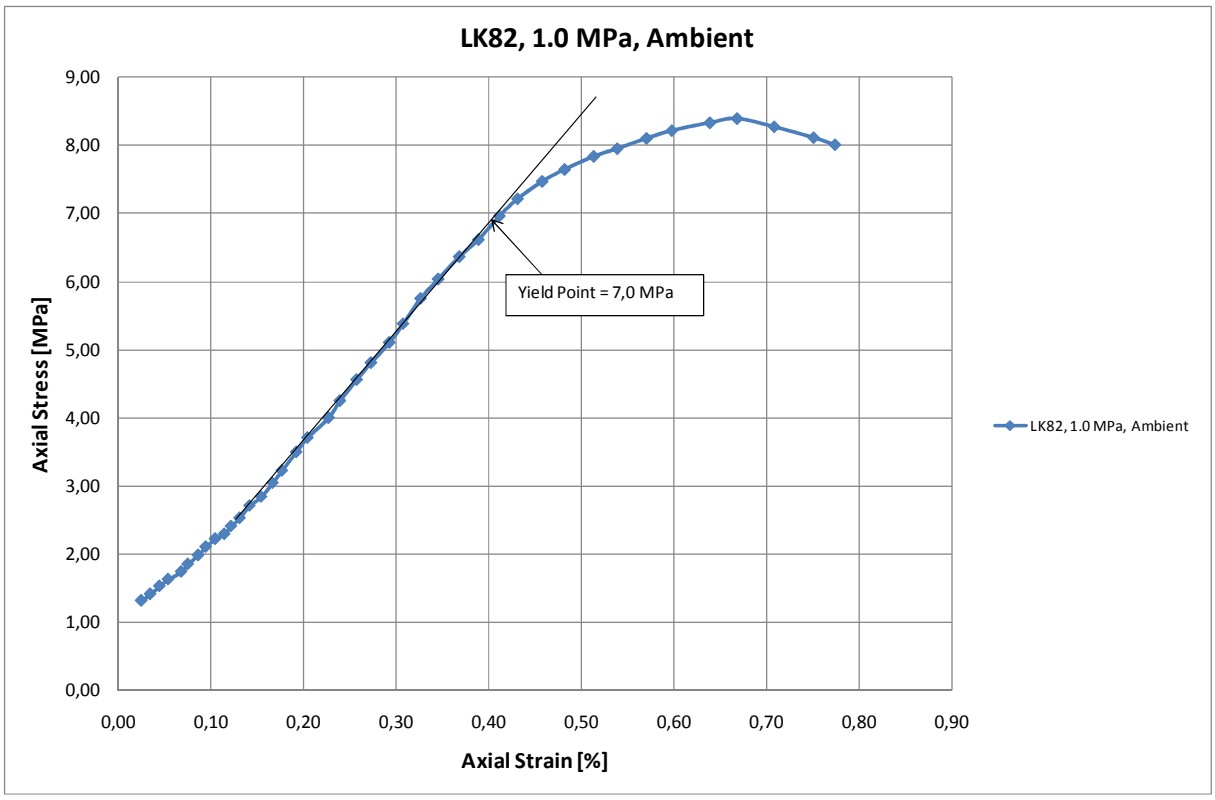


*Fig.A.7: Axial stress versus Axial strain plot for a 1.0 MPa deviatoirc test performed on LK82 with SSW flooding at ambient temperature*

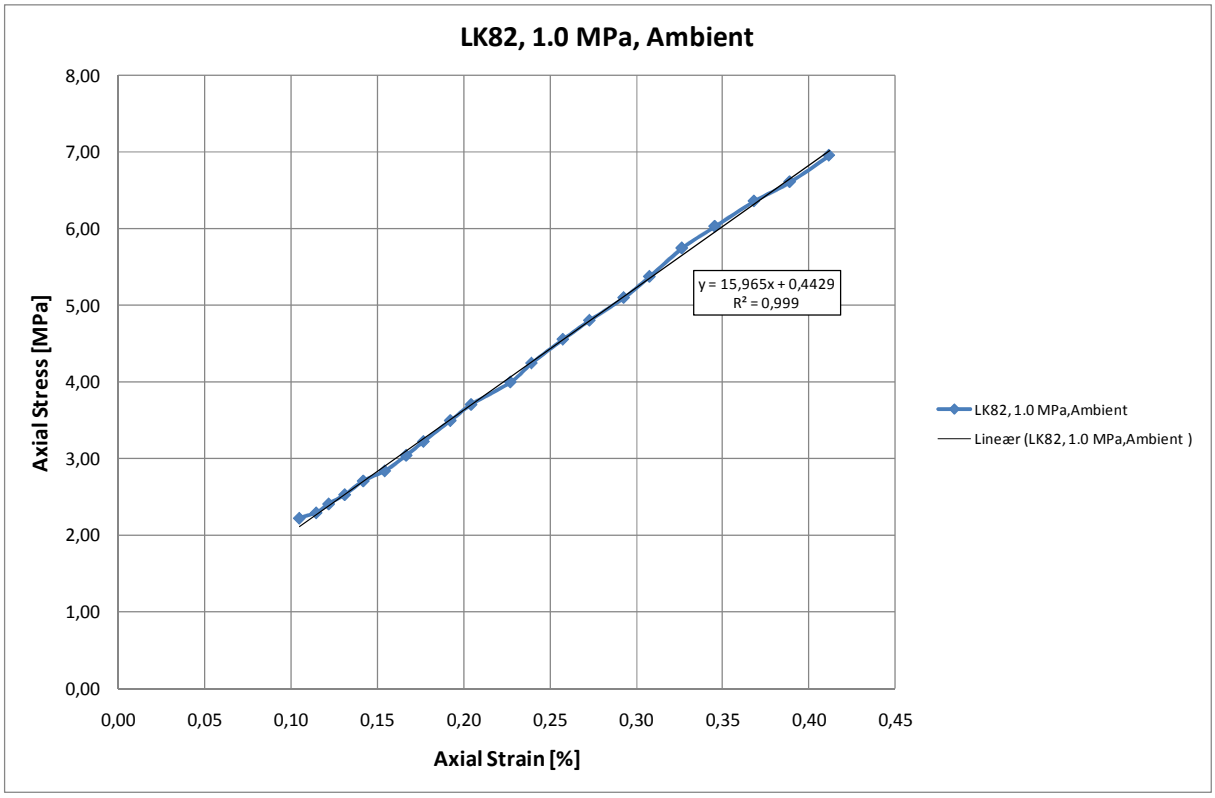


*Fig.A.8: Section of the Axial stress versus Axial strain plot for the 1.0 MPa deviatoirc test performed on LK82 with SSW flooding at ambient temperature used to estimate the Young's modulus.*

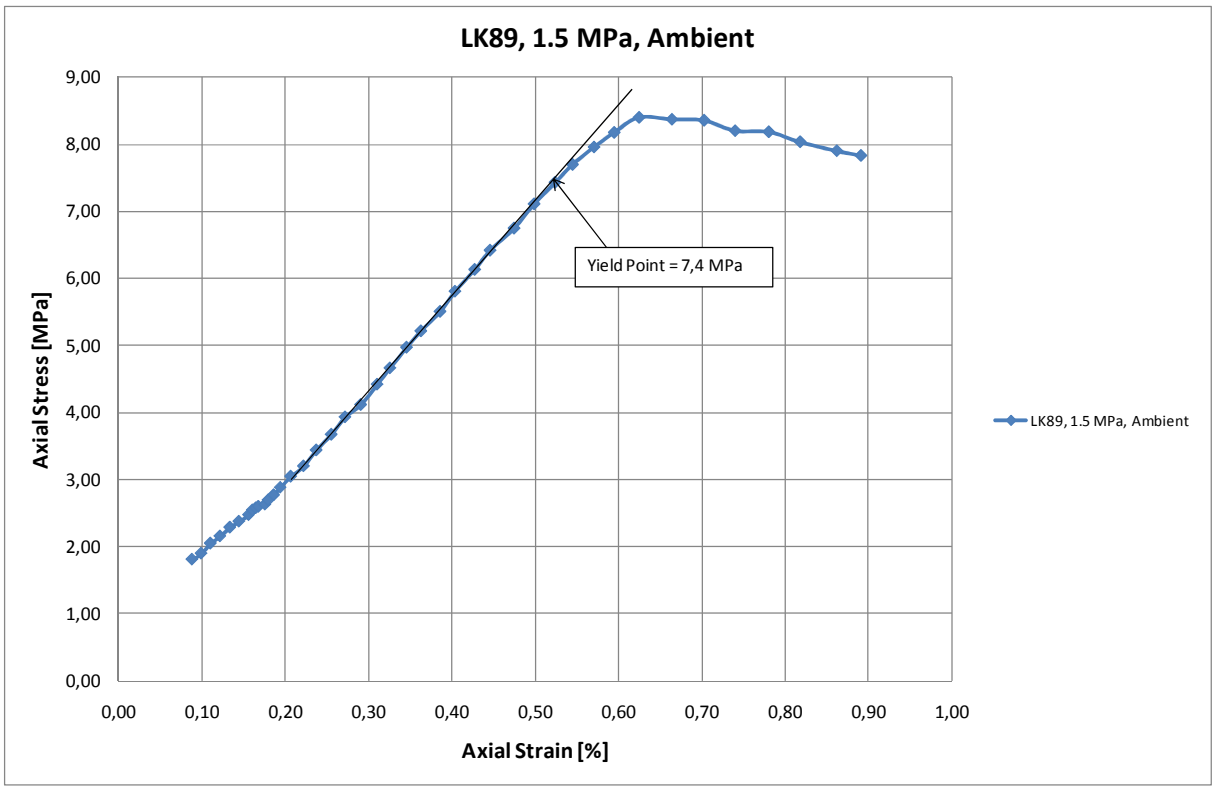


*Fig.A.9: Axial stress versus Axial strain plot for a 1.5 MPa deviatoirc test performed on LK89 with SSW flooding at ambient temperature*

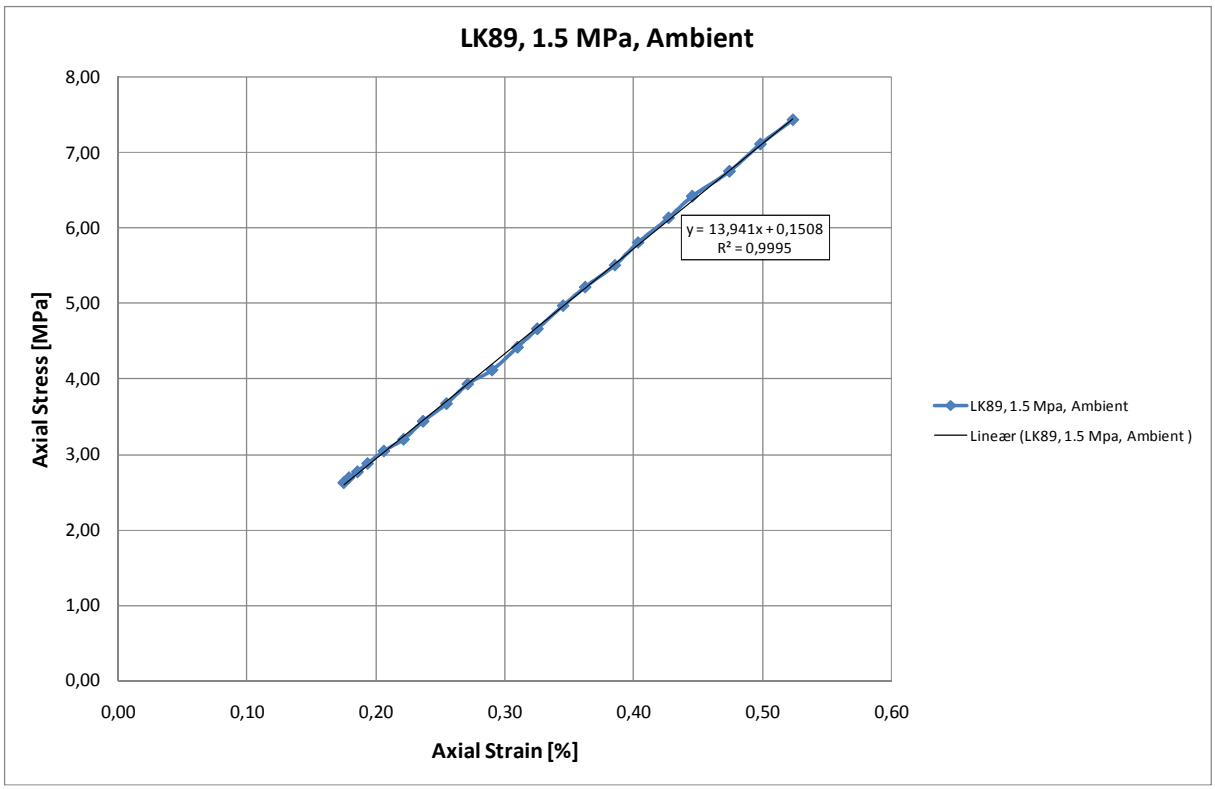


*Fig.A.10: Section of the Axial stress versus Axial strain plot for the 1.5 MPa deviatoirc test performed on LK89 with SSW flooding at ambient temperature used to estimate the Young's modulus.*

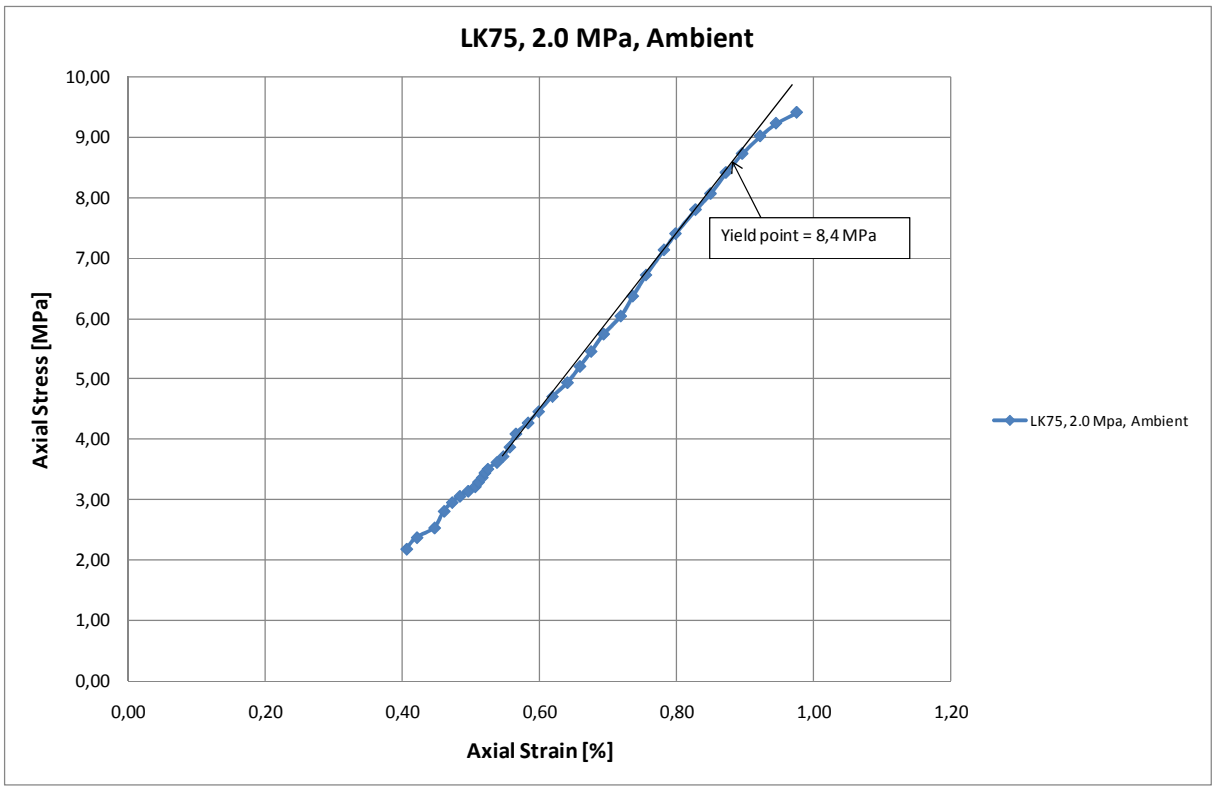


*Fig.A.11: Axial stress versus Axial strain plot for a 2.0 MPa deviatoirc test performed on LK75 with SSW flooding at ambient temperature*

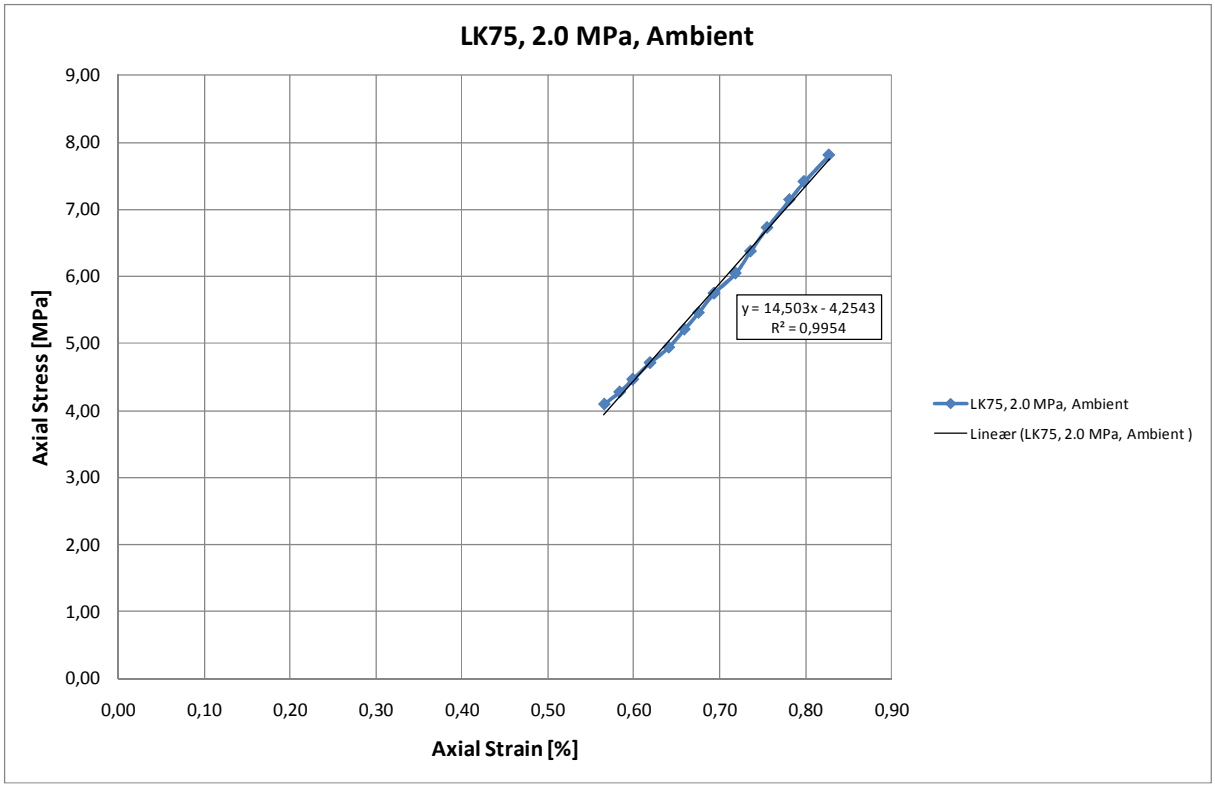


*Fig.A.12: Section of the Axial stress versus Axial Strain plot for the 2.0 MPa deviatoirc test performed on LK75 with SSW flooding at ambient temperature used to estimate the Young's modulus.*

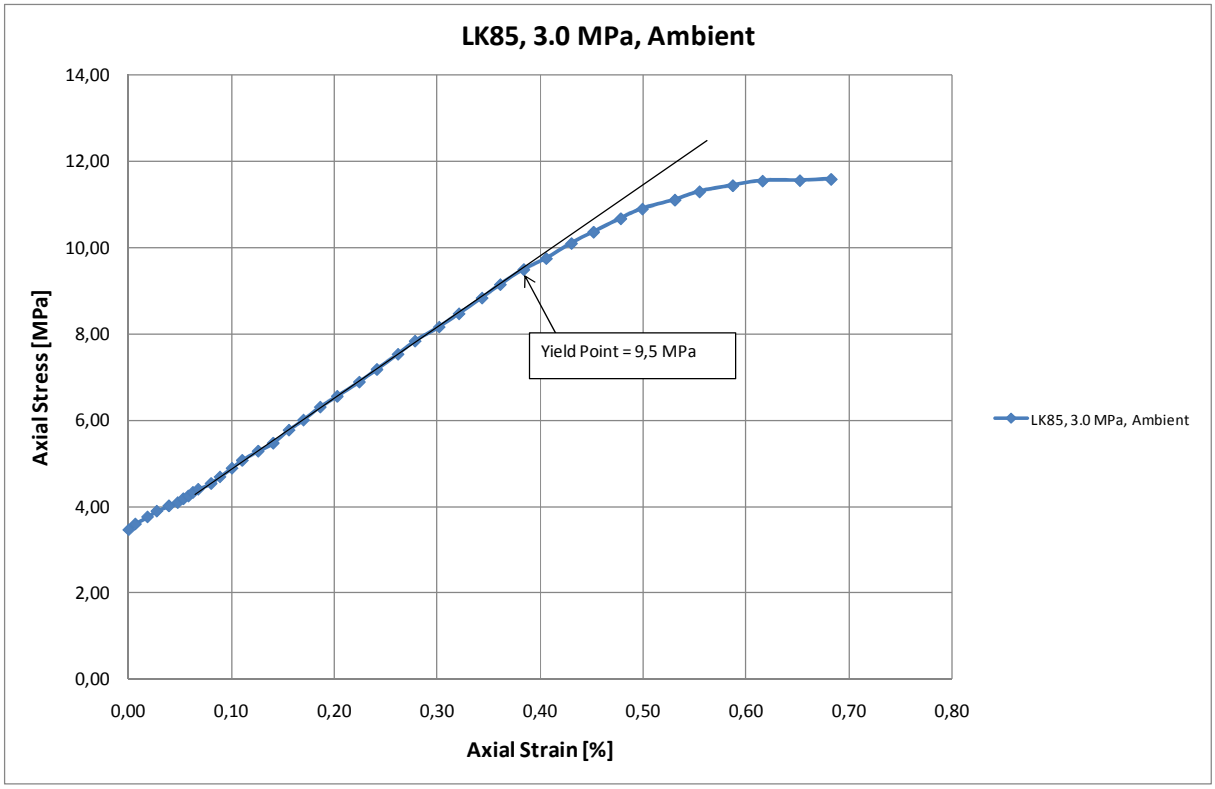


*Fig.A.13: Axial stress versus Axial strain plot for a 3.0 MPa deviatoirc test performed on LK85 with SSW flooding at ambient temperature*

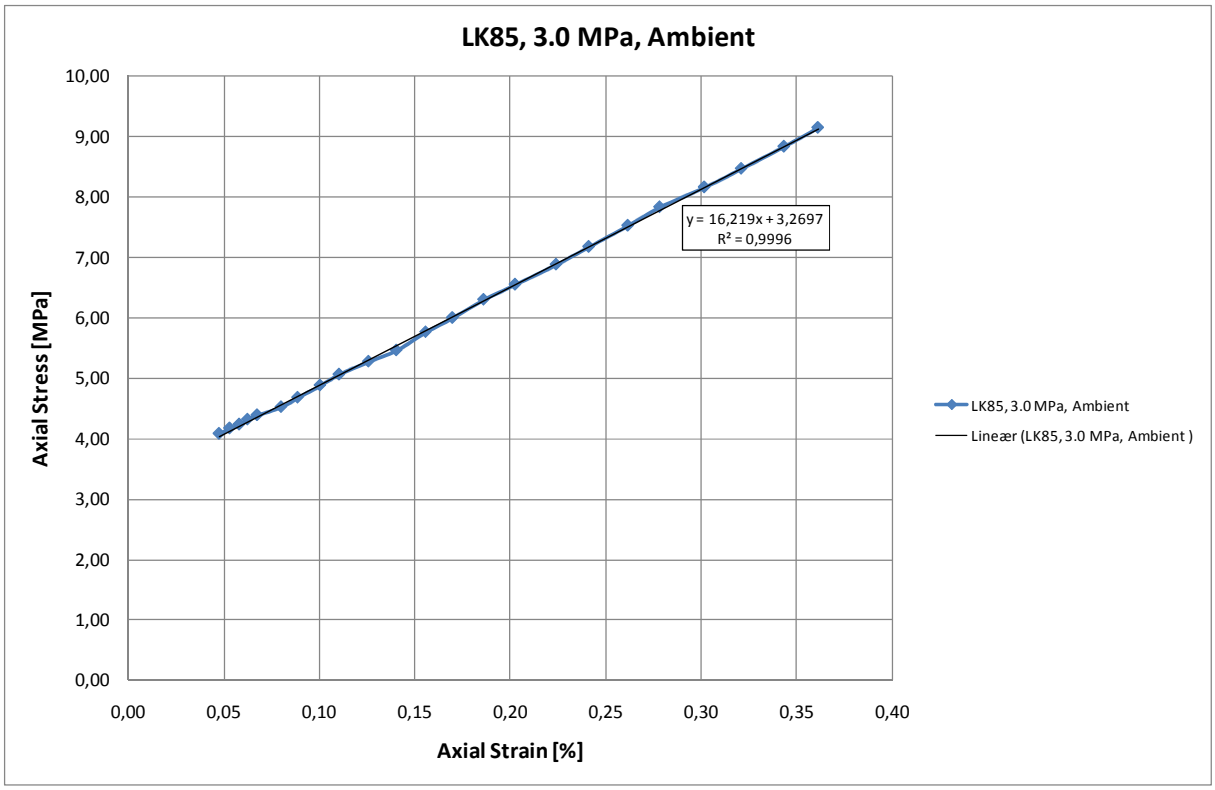


*Fig.A.14: Section of the Axial stress versus Axial strain plot for the 3.0 MPa deviatoirc test performed on LK85 with SSW flooding at ambient temperature used to estimate the Young's modulus.*

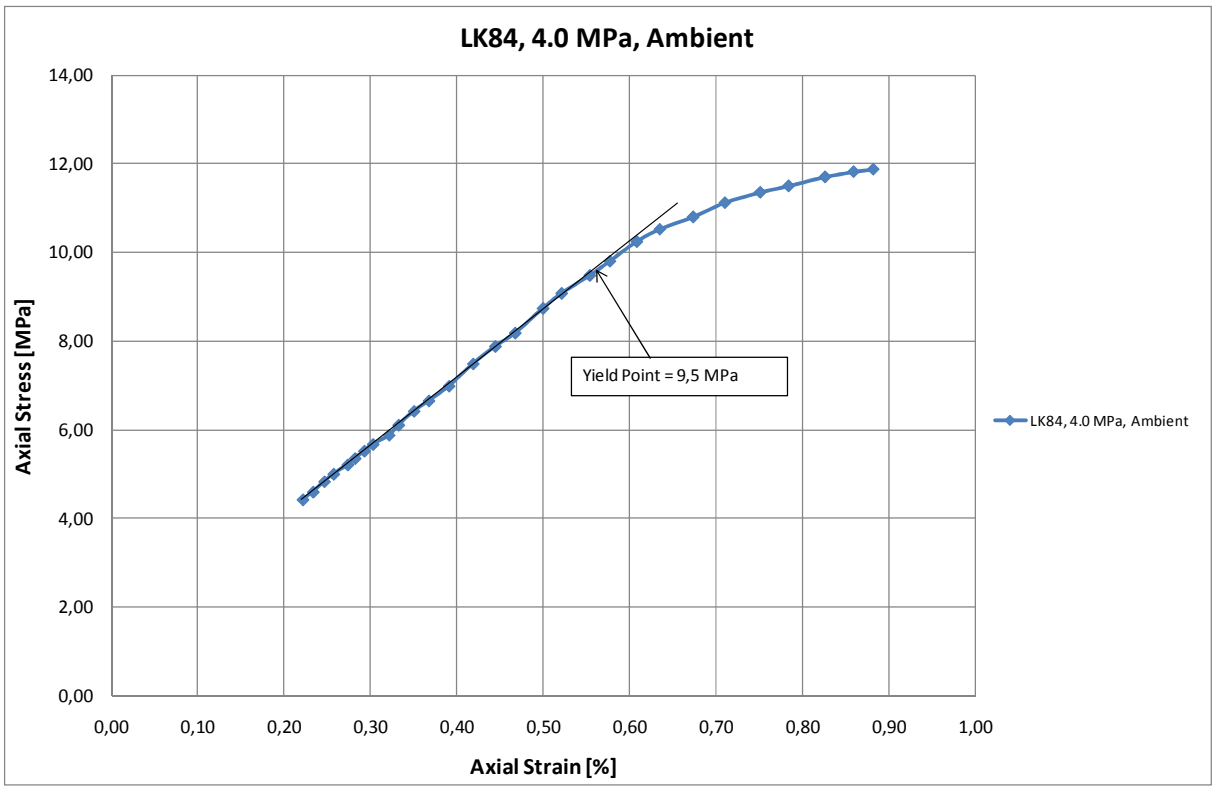


*Fig.A.15: Axial stress versus Axial strain plot for a 4.0 MPa deviatoirc test performed on LK84 with SSW flooding at ambient temperature*

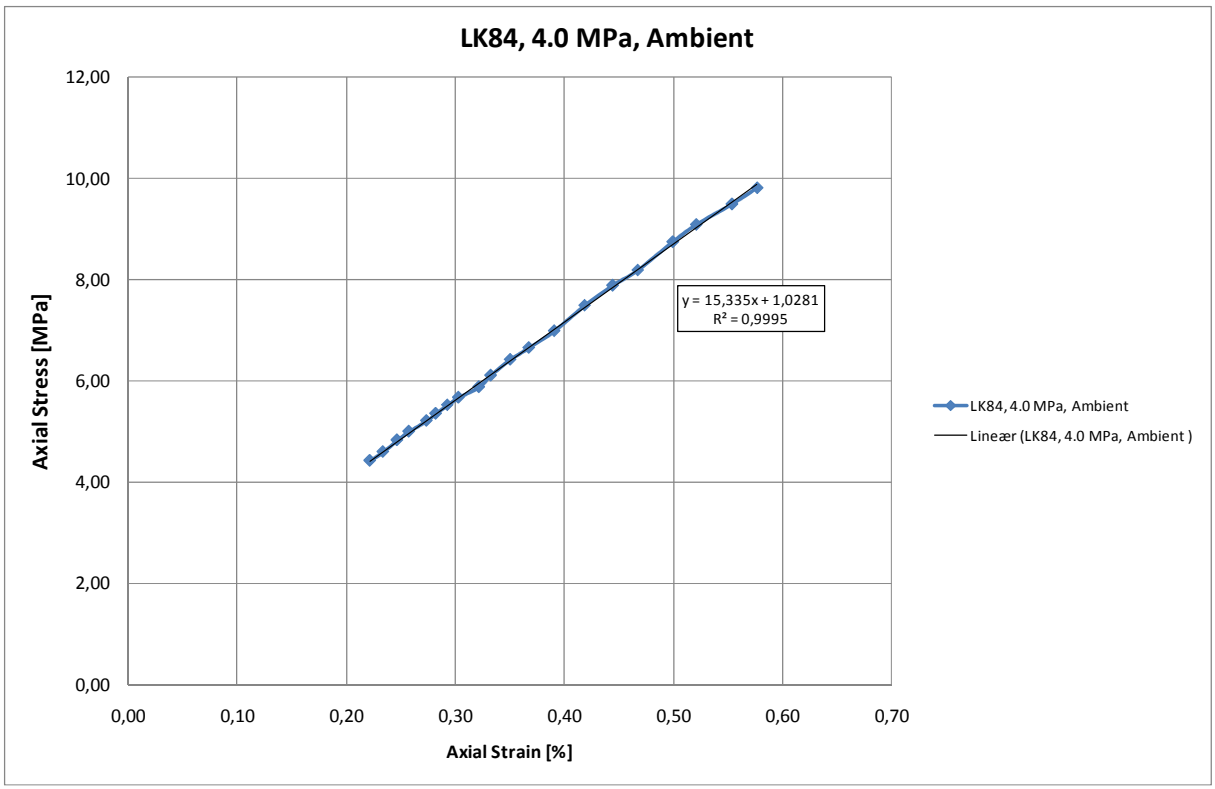


*Fig.A.16: Section of the Axial stress versus Axial strain plot for the 4.0 MPa deviatoirc test performed on LK84 with SSW flooding at ambient temperature used to estimate the Young's modulus.*

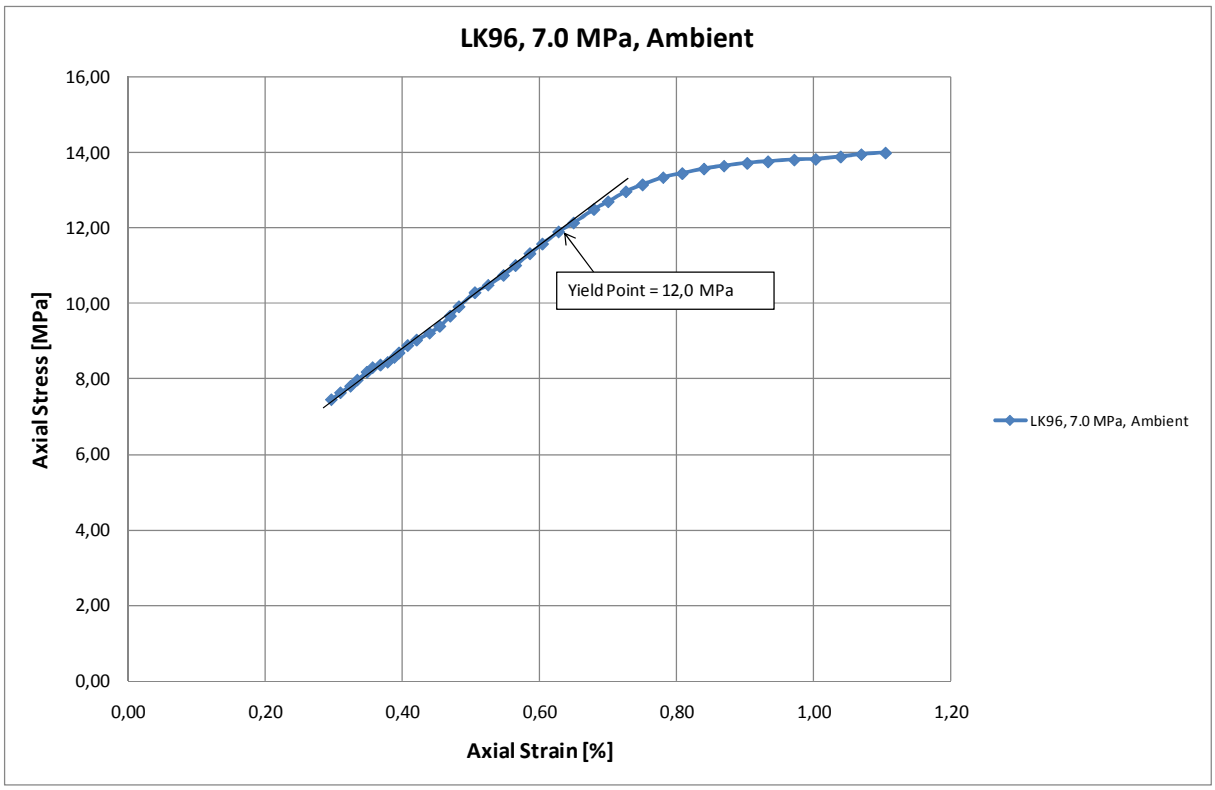


*Fig.A.17: Axial stress versus Axial strain plot for a 7.0 MPa deviatoirc test performed on LK96 with SSW flooding at ambient temperature*

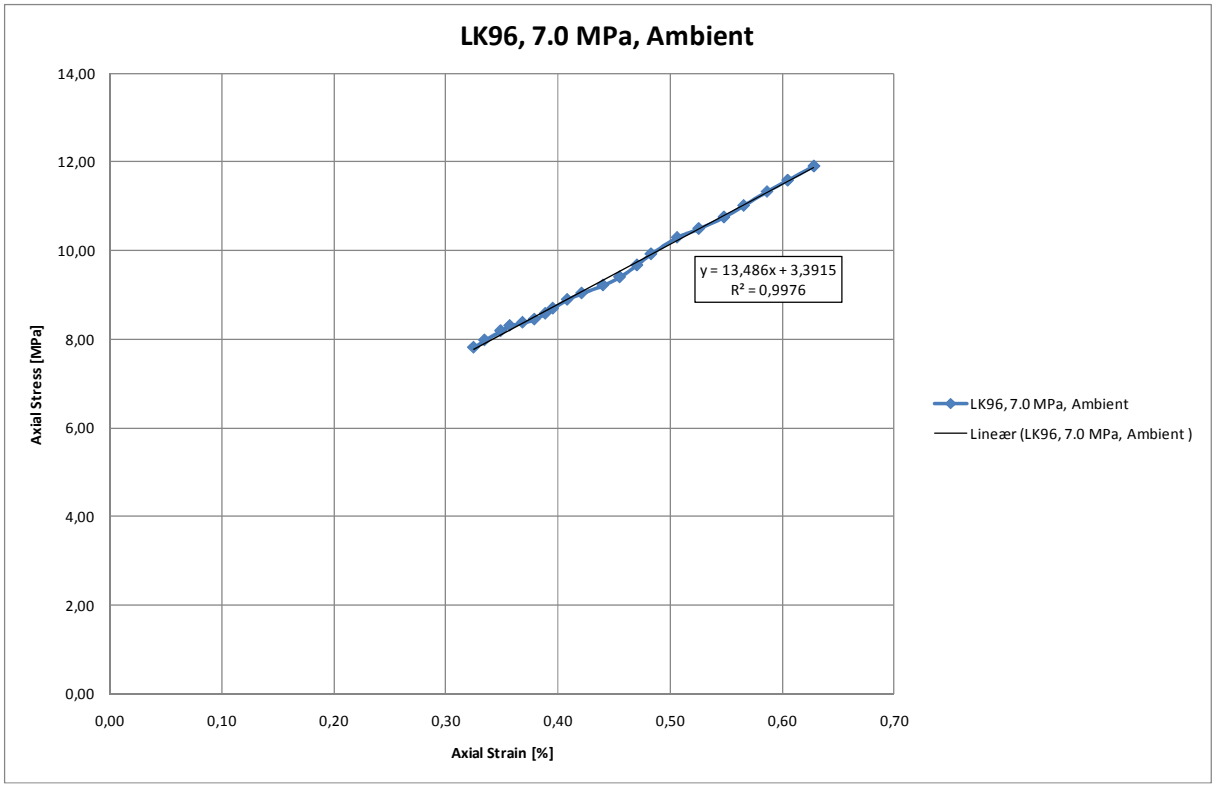


*Fig.A.18: Section of the Axial stress versus Axial strain plot for the 7.0 MPa deviatoirc test performed on LK84 with SSW flooding at ambient temperature used to estimate the Young's modulus.*

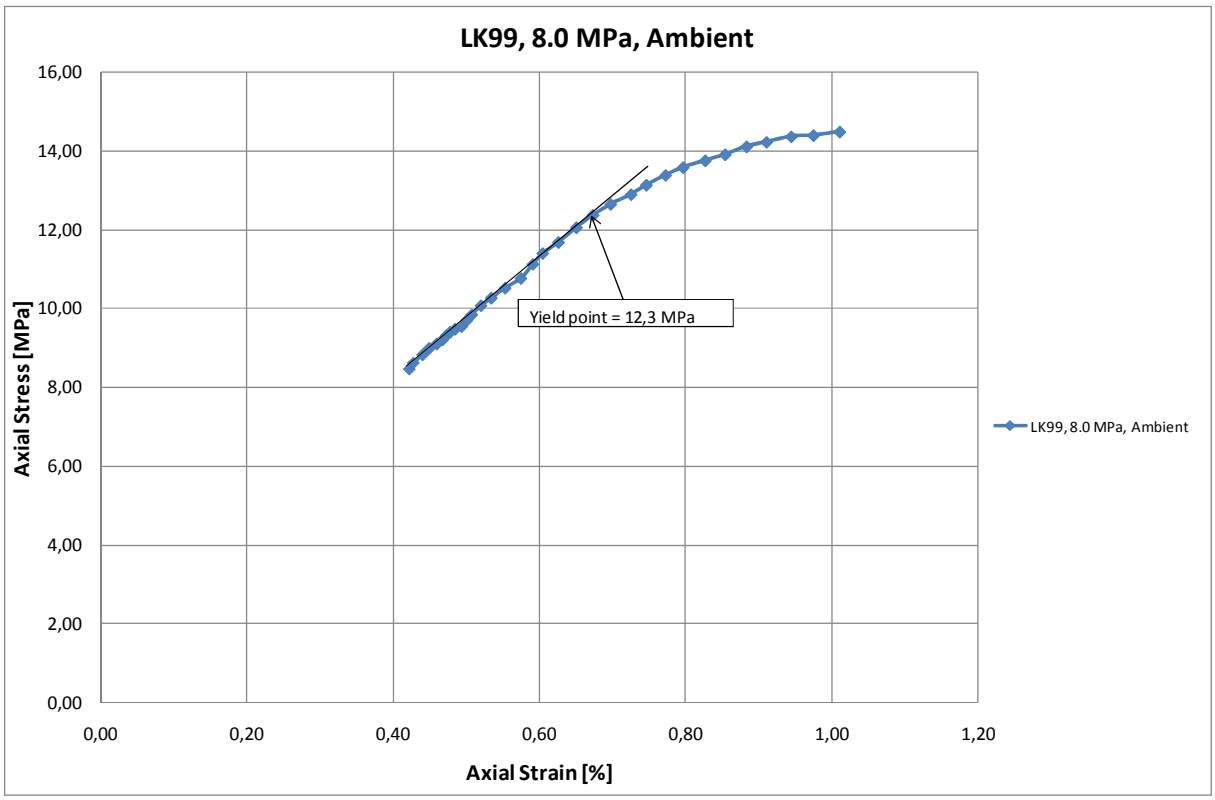


*Fig.A.19: Axial stress versus Axial strain plot for the 8.0 MPa deviatoirc test performed on LK99 with SSW flooding at ambient temperature*

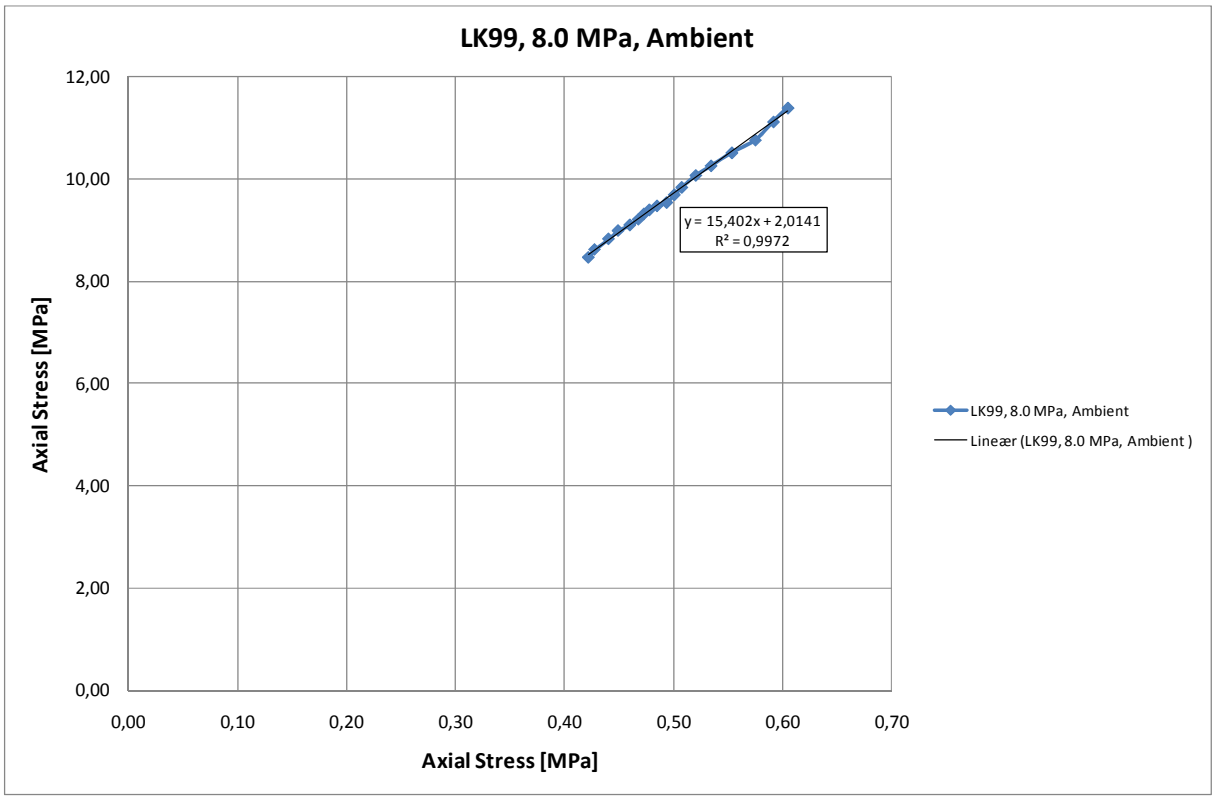


*Fig.A.20: Section of the Axial stress versus Axial strain plot for the 8.0 MPa deviatoirc test performed on LK99 with SSW flooding at ambient temperature used to estimate the Young's modulus.*

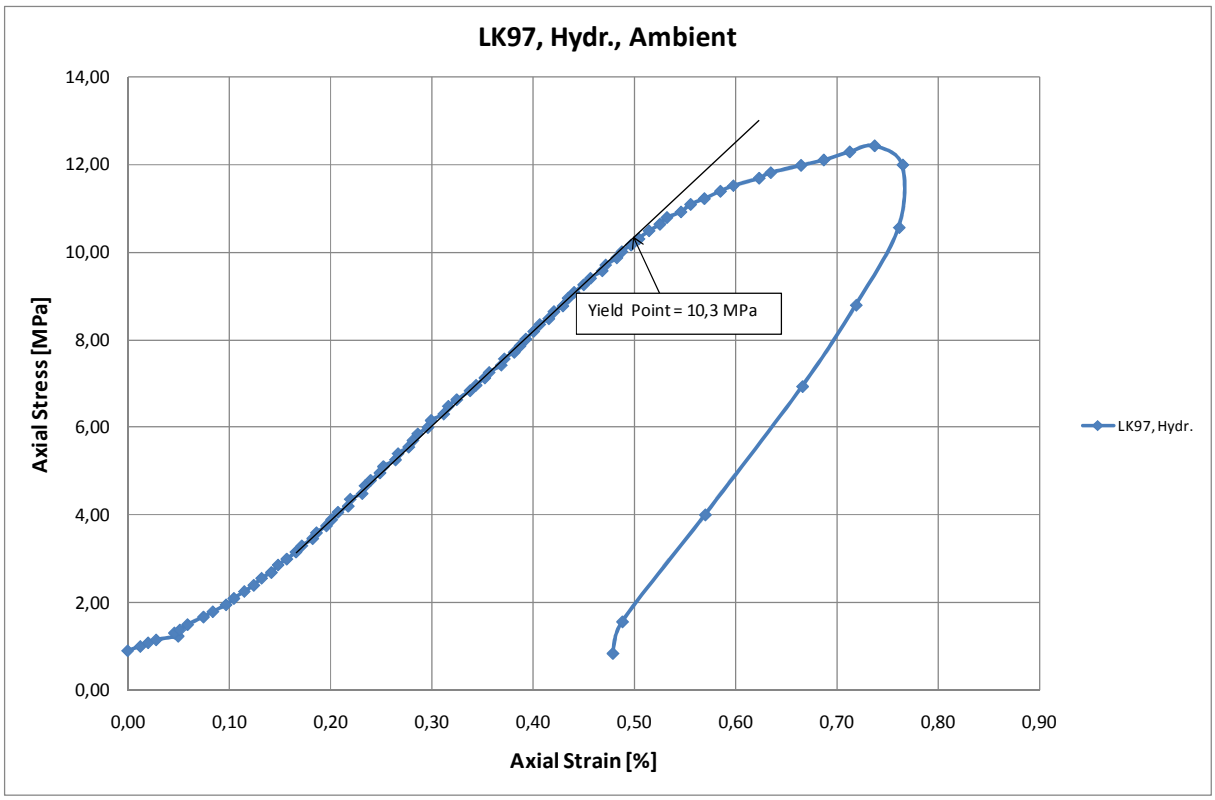


*Fig.A.21: Axial stress versus Axial strain plot for a hydrostatic test performed on LK97 with SSW flooding at ambient temperature*

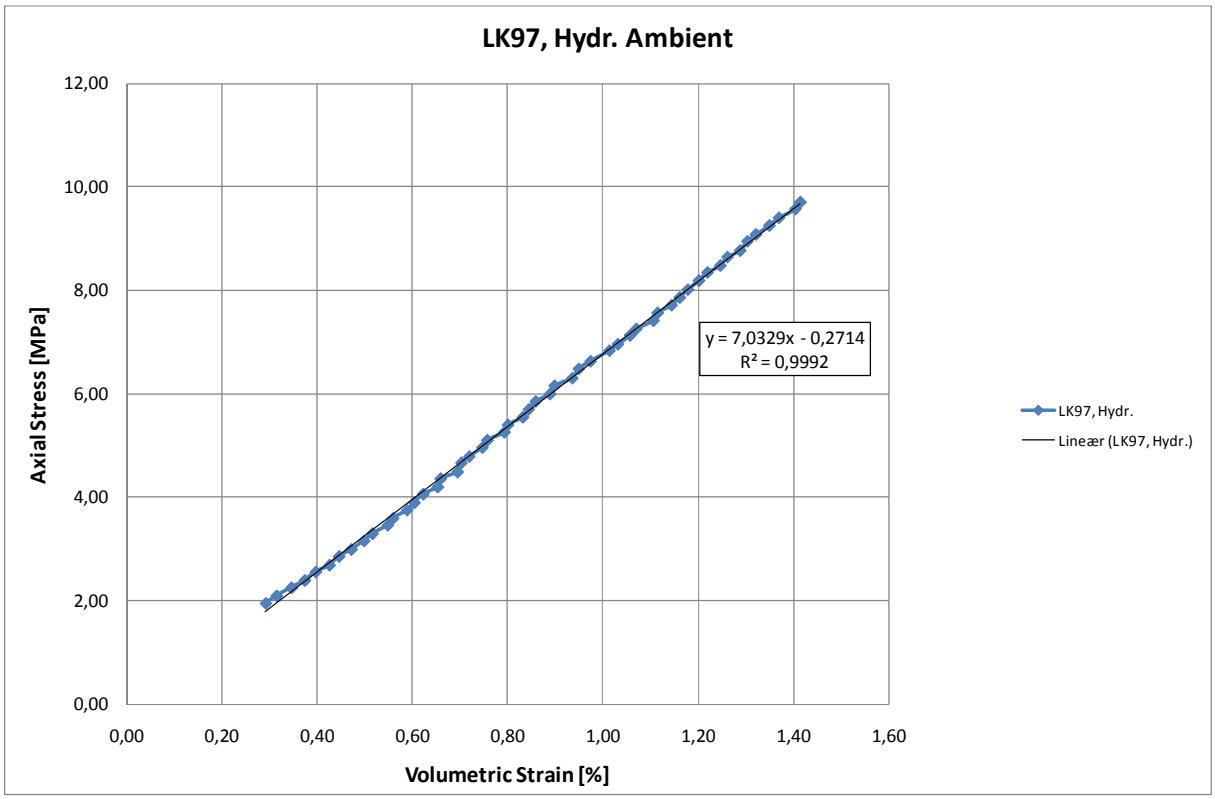


*Fig.A.22: Section of the Axial stress versus Volumetric strain plot the hydrostatic test performed on LK97 with SSW flooding at ambient temperature used to estimate the Bulk modulus.*

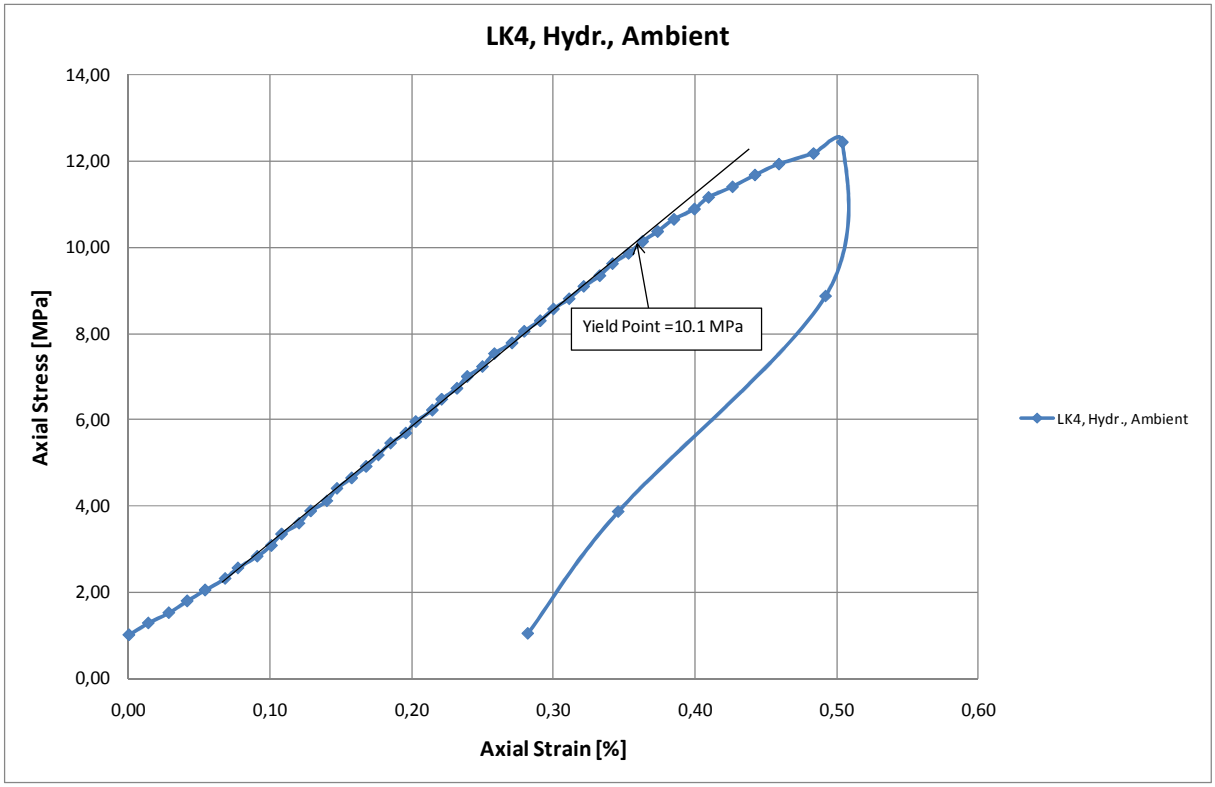


*Fig.A.23: Axial stress versus Axial strain plot for a hydrostatic test performed on LK4 with SSW flooding at ambient temperature*

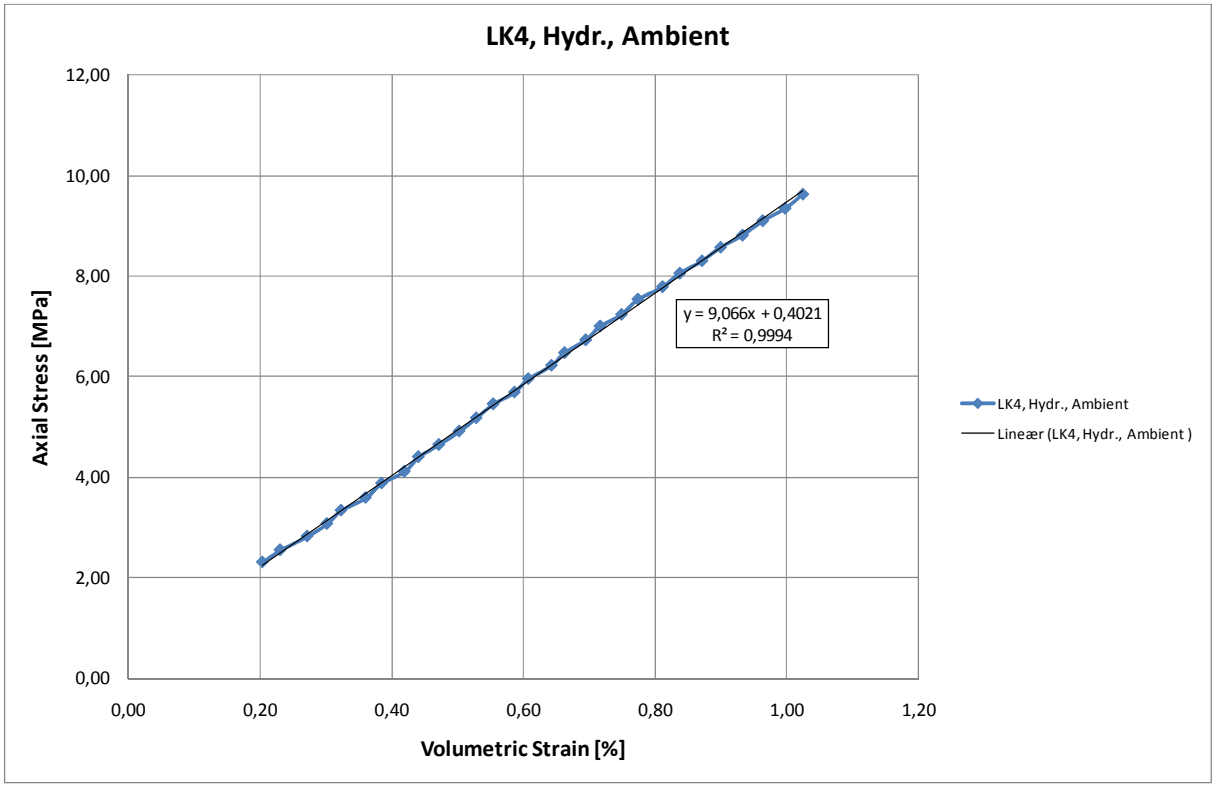


*Fig.A.24: Section of the Axial stress versus Volumetric strain plot the hydrostatic test performed on LK4 with SSW flooding at ambient temperature used to estimate the Bulk modulus.*

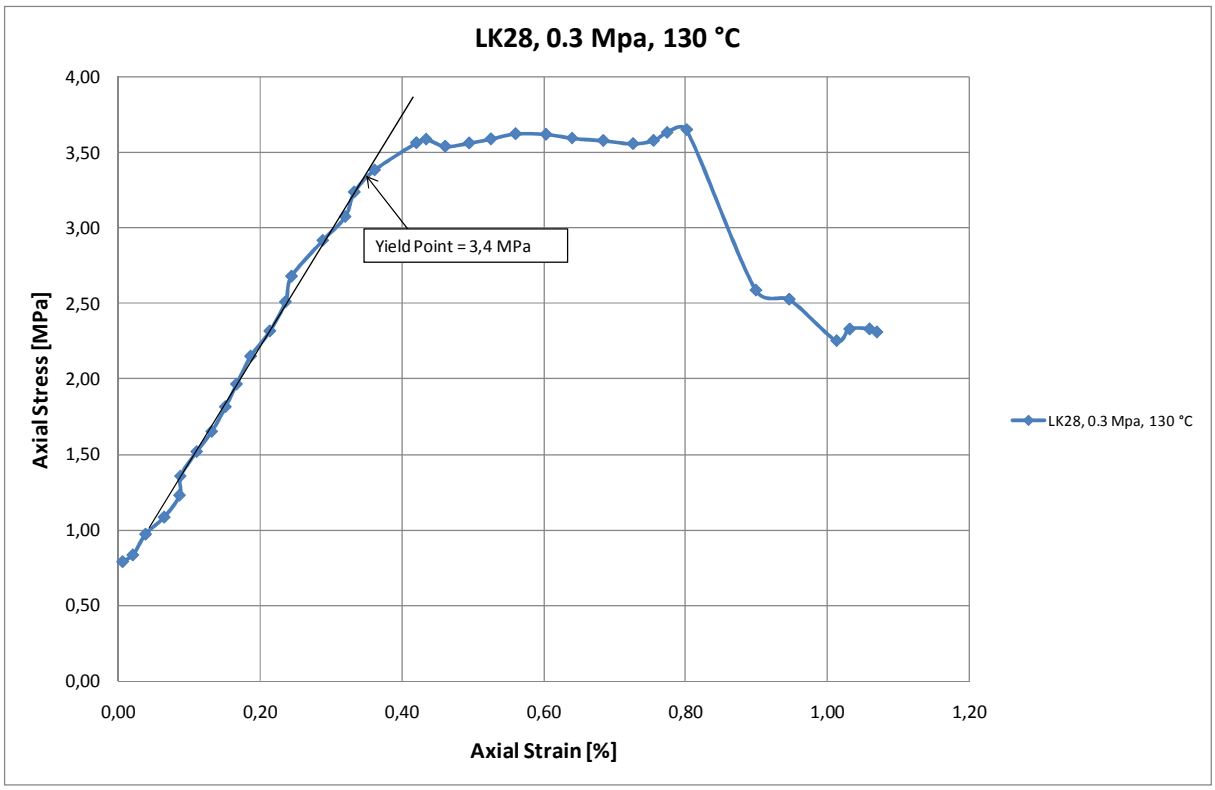


*Fig.A.25: Axial stress versus Axial strain plot for the 0.3 MPa deviatoirc test performed on LK28 with SSW flooding at 130 °C*

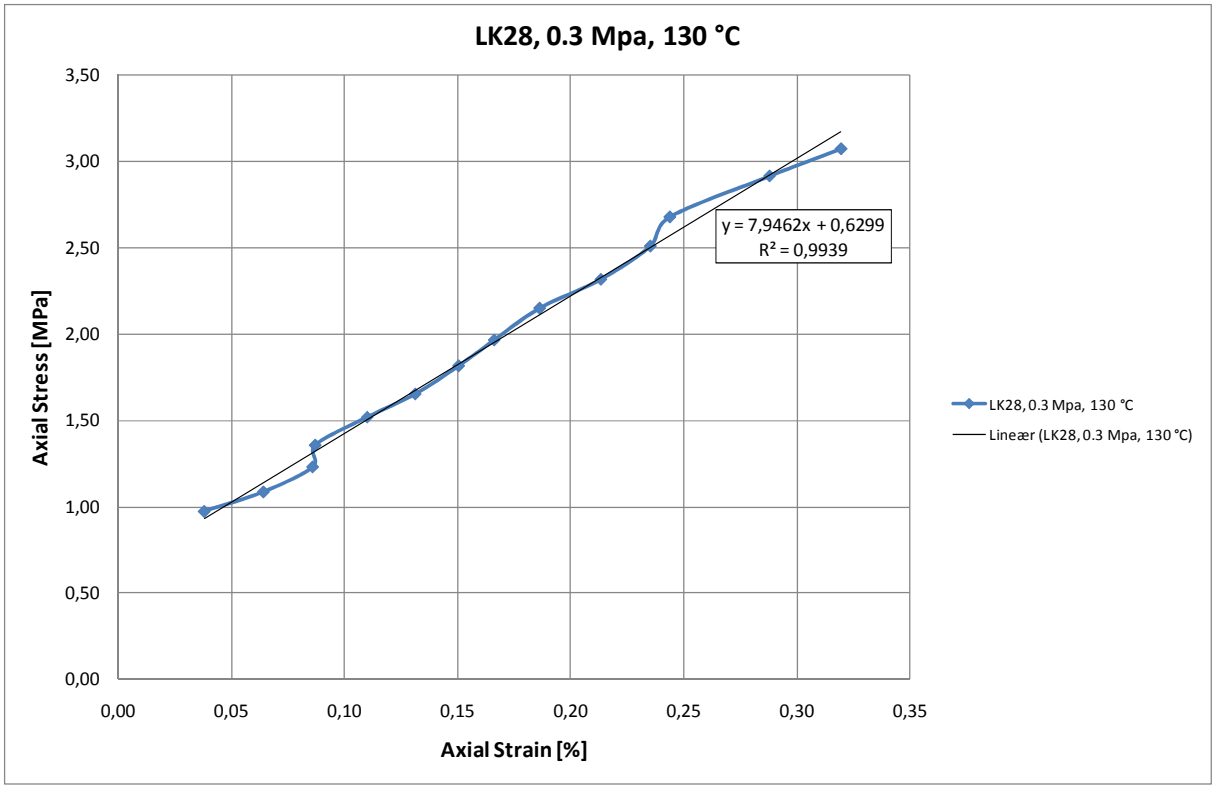


*Fig.A.26: Section of the Axial stress versus Axial strain plot for the 0.3 MPa deviatoirc test performed on LK28 with SSW flooding at 130 °C used to estimate the Young's modulus.*

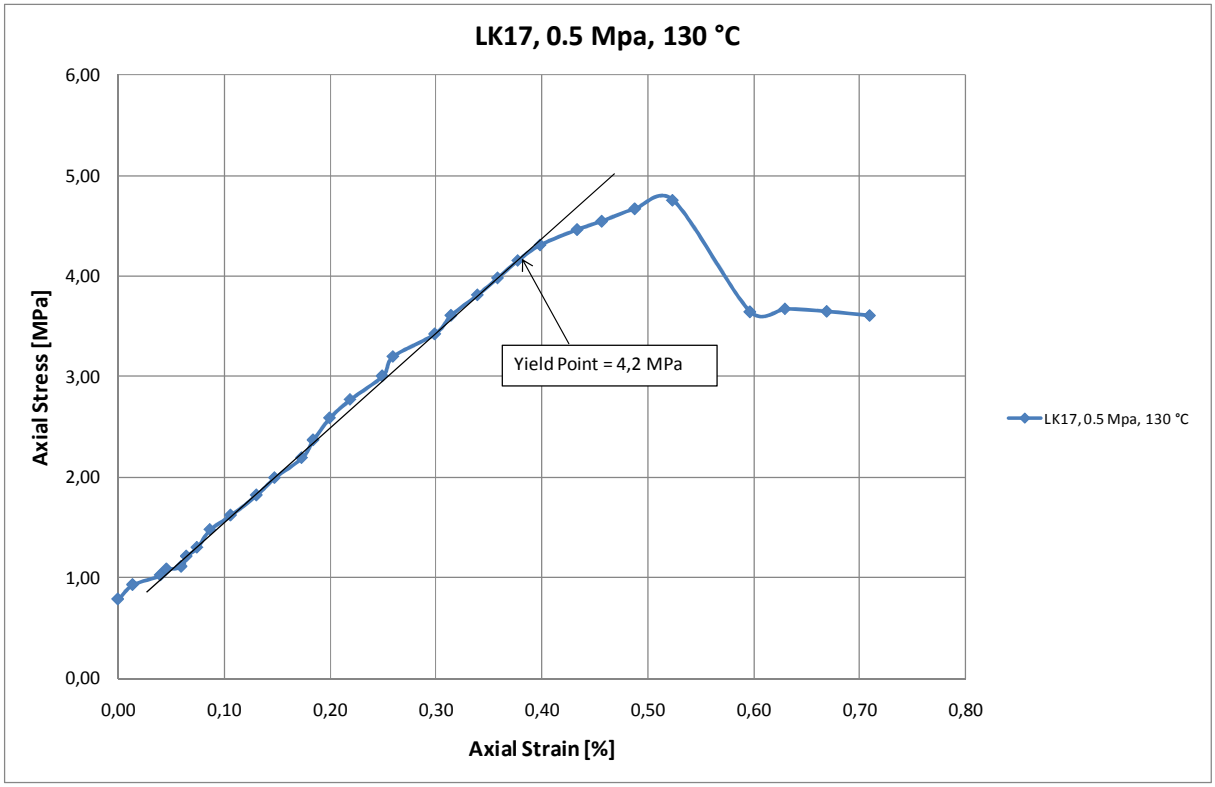


*Fig.A.27: Axial stress versus Axial strain plot for the 0.5 MPa deviatoirc test performed on LK17 with SSW flooding at 130 °C*

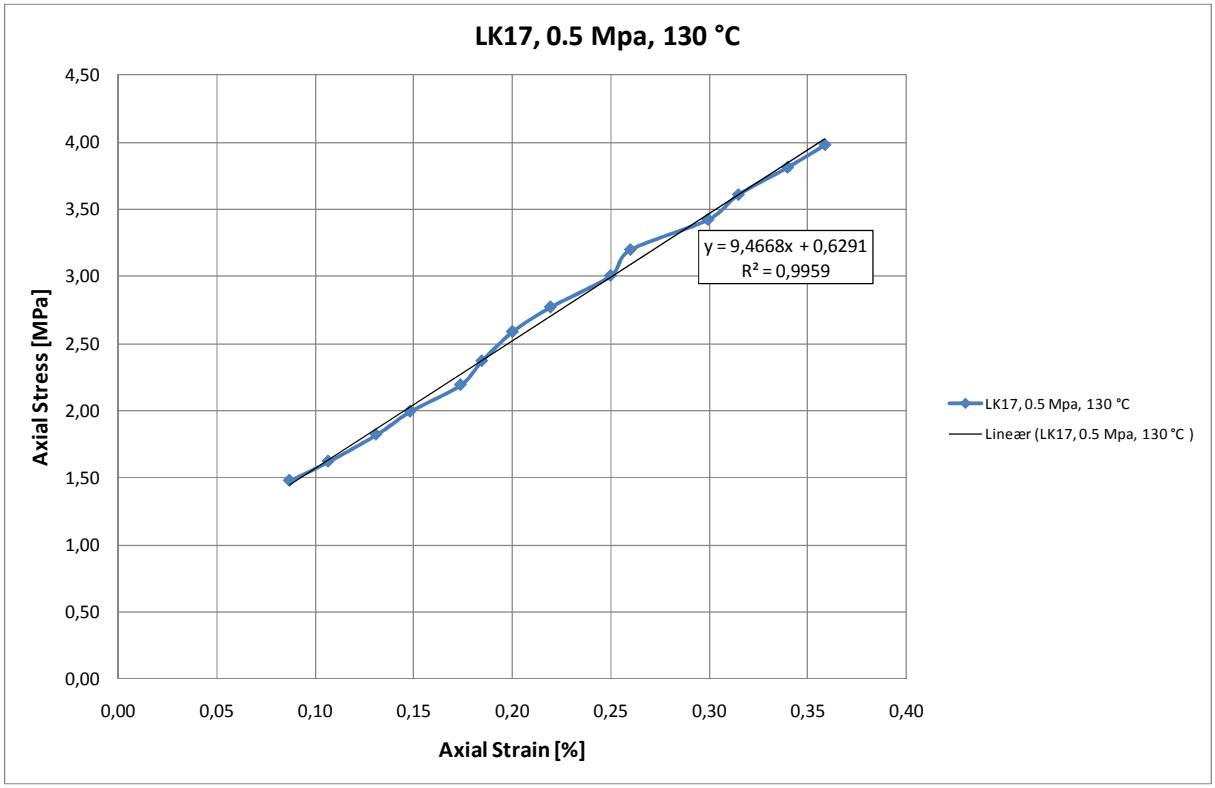


*Fig.A.28: Section of the Axial stress versus Axial strain plot for the 0.5 MPa deviatoirc test performed on LK17 with SSW flooding at 130 °C used to estimate the Young's modulus.*

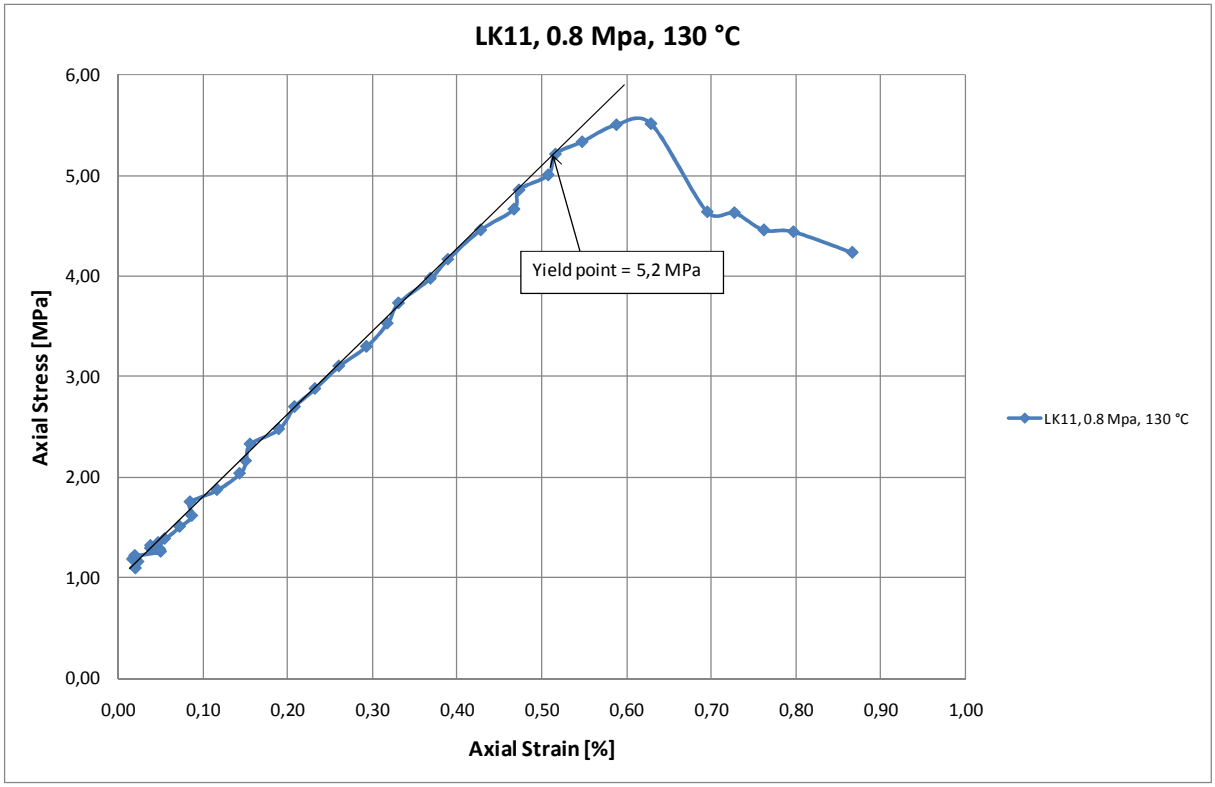


*Fig.A.29: Axial stress versus Axial strain plot for the 0.8 MPa deviatoirc test performed on LK11 with SSW flooding at 130 °C*

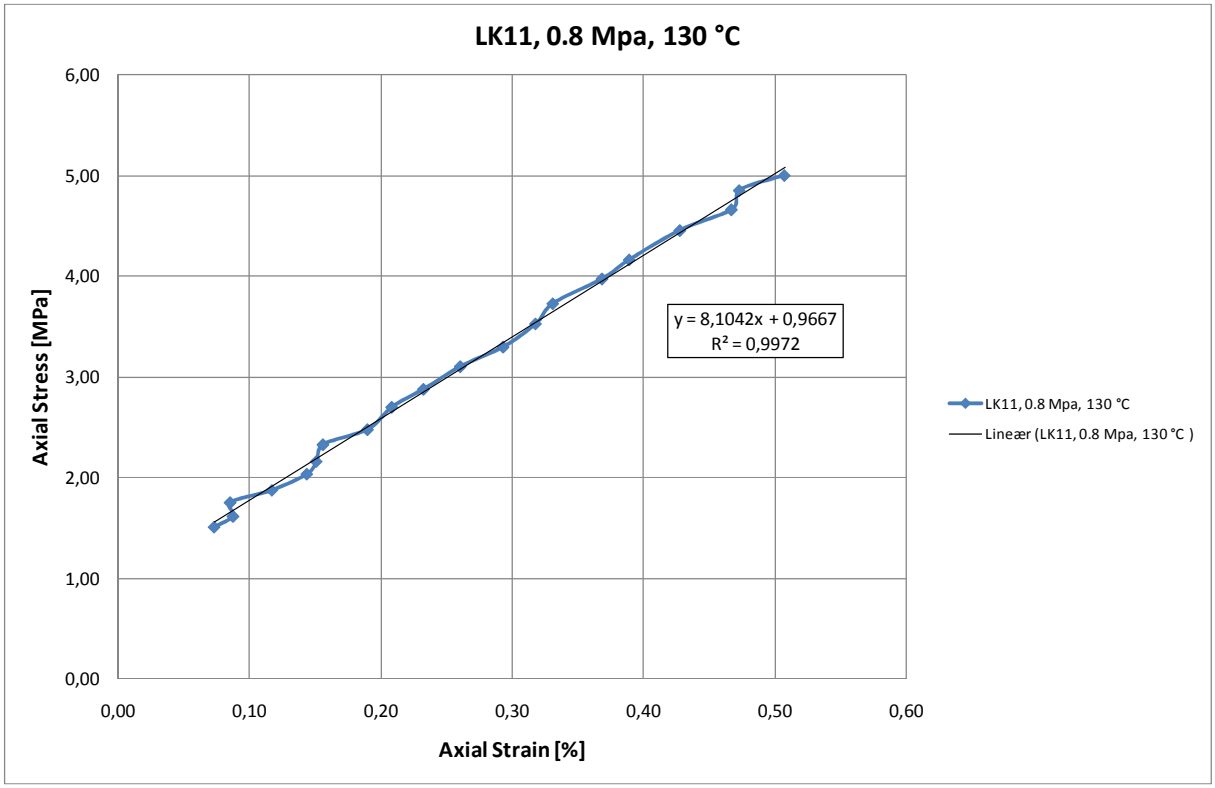


*Fig.A.30: Section of the Axial stress versus Axial strain plot for the 0.8 MPa deviatoirc test performed on LK11 with SSW flooding at 130 °C used to estimate the Young's modulus.*

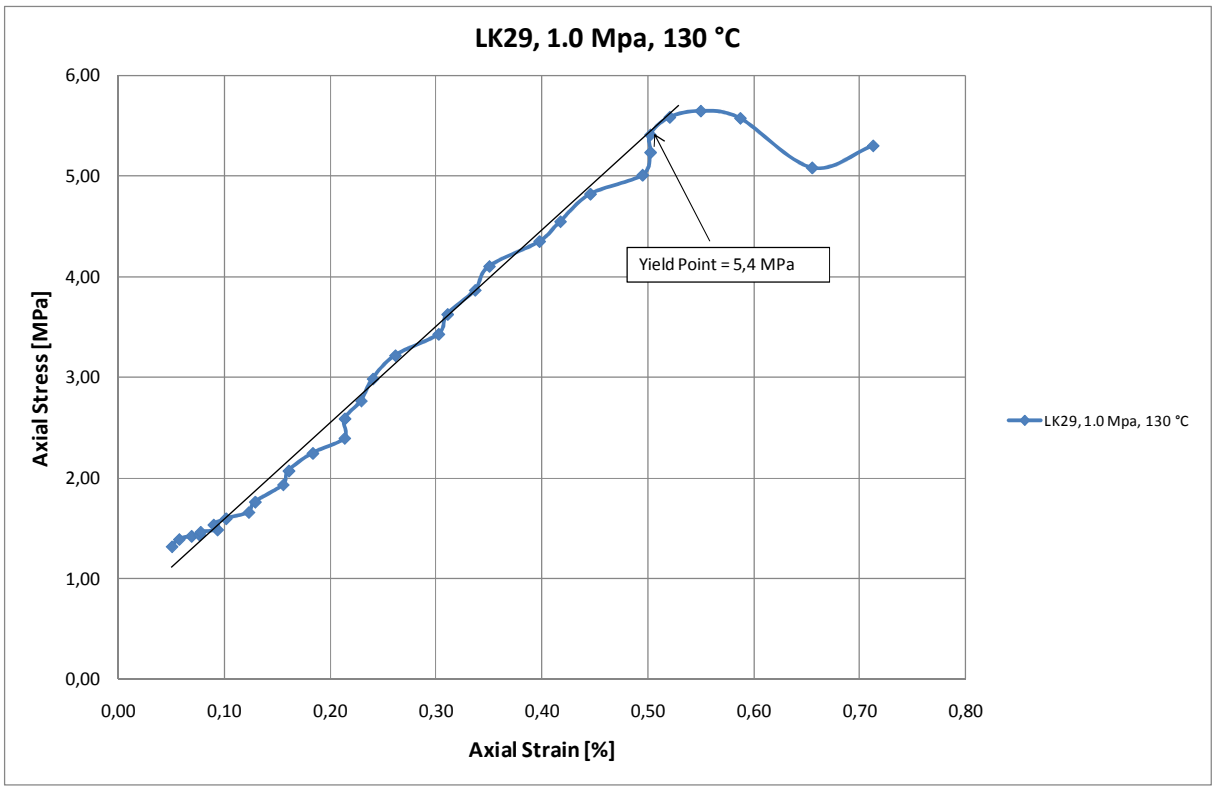


*Fig.A.31: Axial stress versus Axial strain plot for the 1.0 MPa deviatoirc test performed on LK29 with SSW flooding at 130 °C*

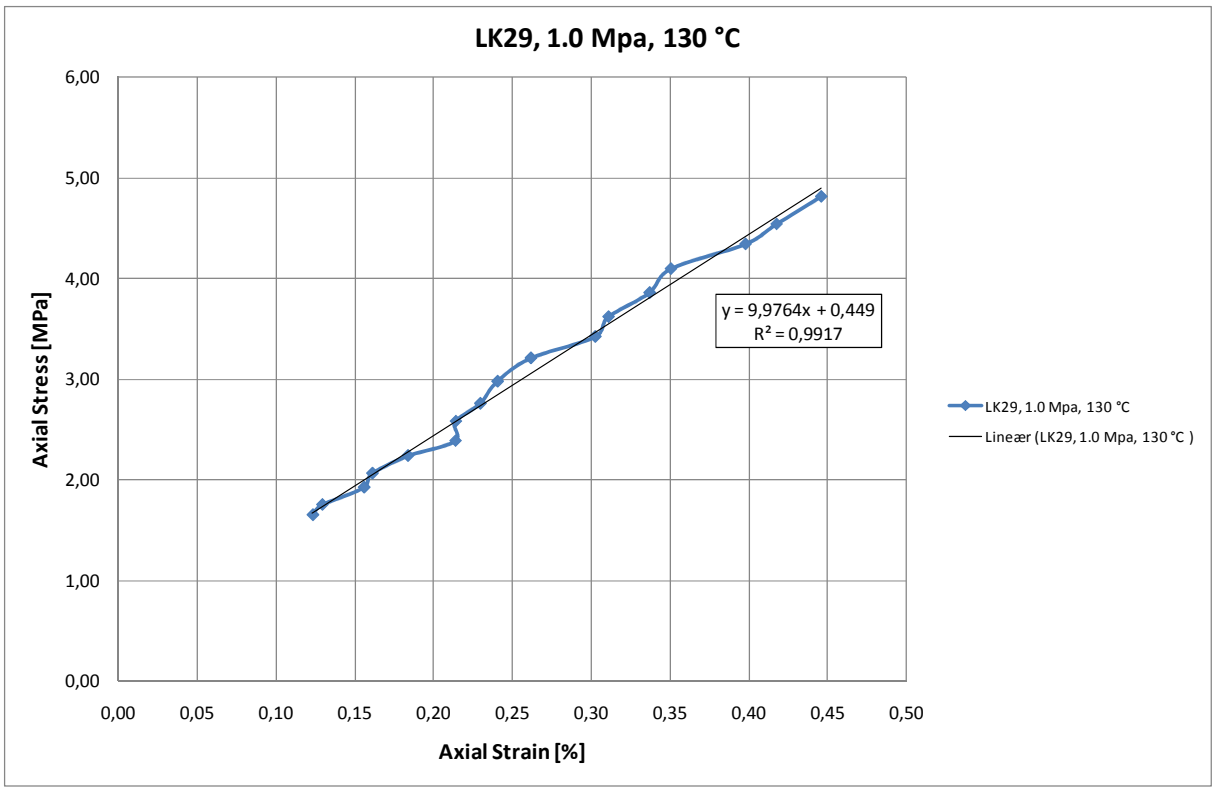


*Fig.A.32: Section of the Axial stress versus Axial strain plot for the 1.0 MPa deviatoirc test performed on LK29 with SSW flooding at 130 °C used to estimate the Young's modulus.*

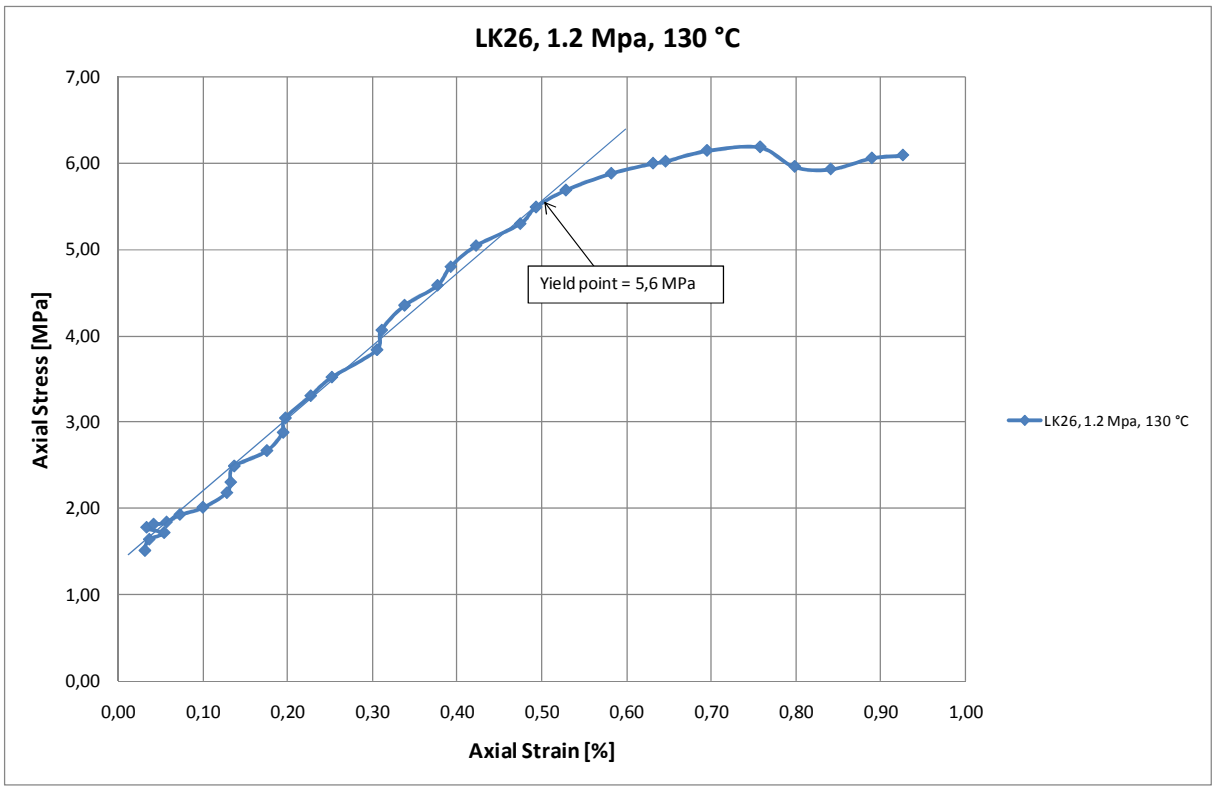


*Fig.A.33: Axial stress versus Axial strain plot for the 1.2 MPa deviatoirc test performed on LK26 with SSW flooding at 130 °C*

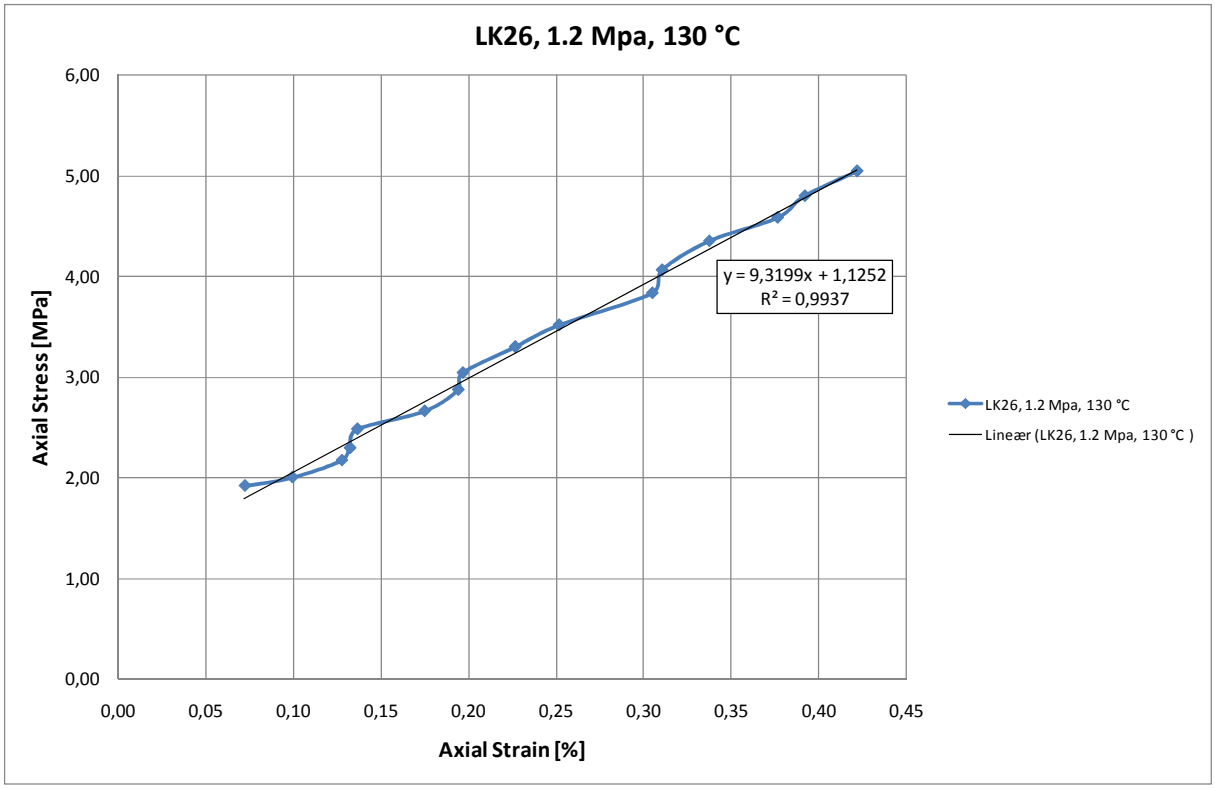


*Fig.A.34: Section of the Axial stress versus Axial strain plot for the 1.2 MPa deviatoirc test performed on LK26 with SSW flooding at 130 °C used to estimate the Young's modulus.*

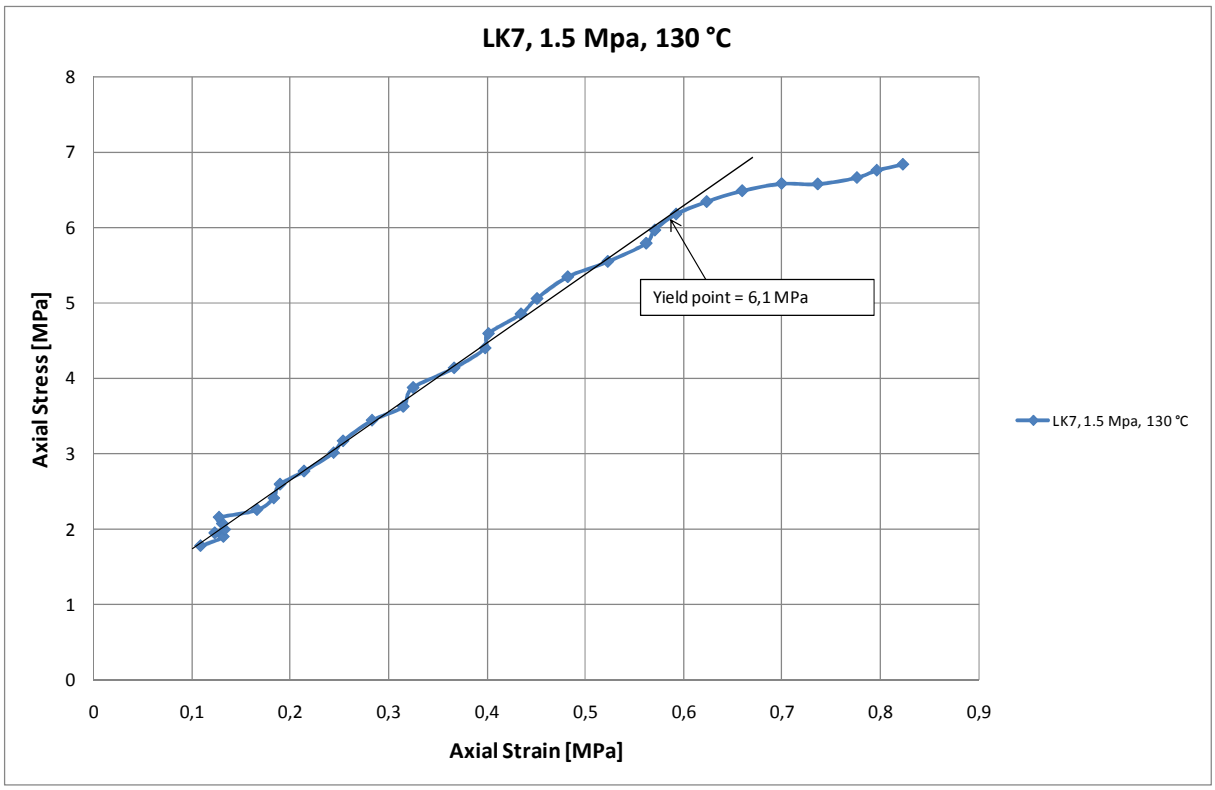


*Fig.A.35: Axial stress versus Axial strain plot for the 1.5 MPa deviatoirc test performed on LK7 with SSW flooding at 130 °C*

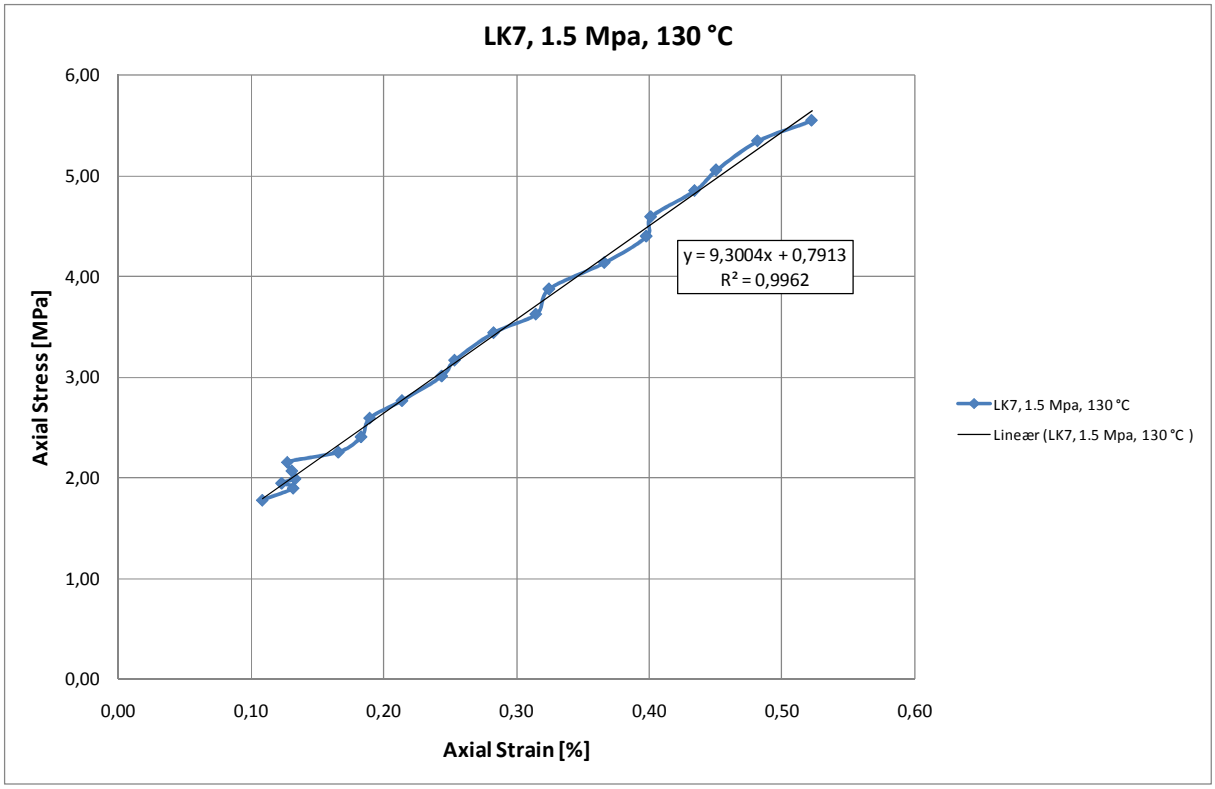


*Fig.A.36: Section of the Axial stress versus Axial strain plot for the 1.5 MPa deviatoirc test performed on LK7 with SSW flooding at 130 °C used to estimate the Young's modulus.*

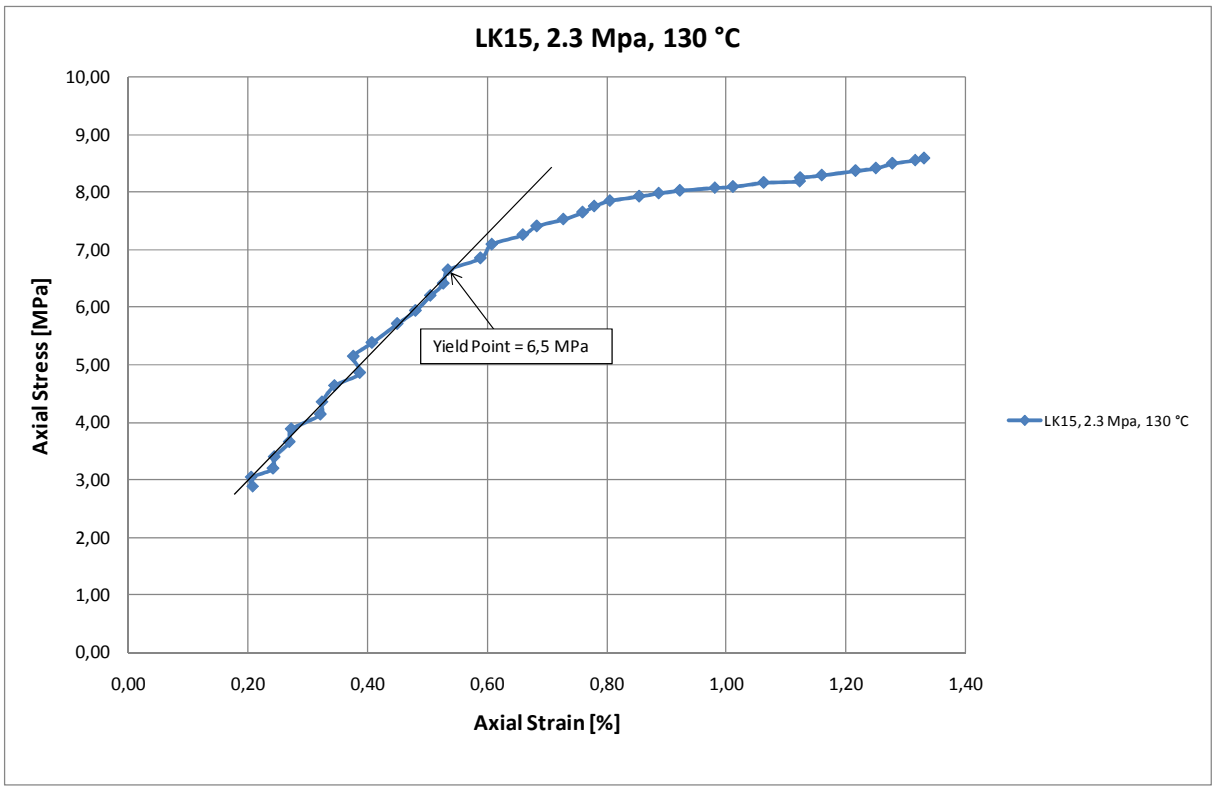


*Fig.A.37: Axial stress versus Axial strain plot for the 2.3 MPa deviatoirc test performed on LK15 with SSW flooding at 130 °C*

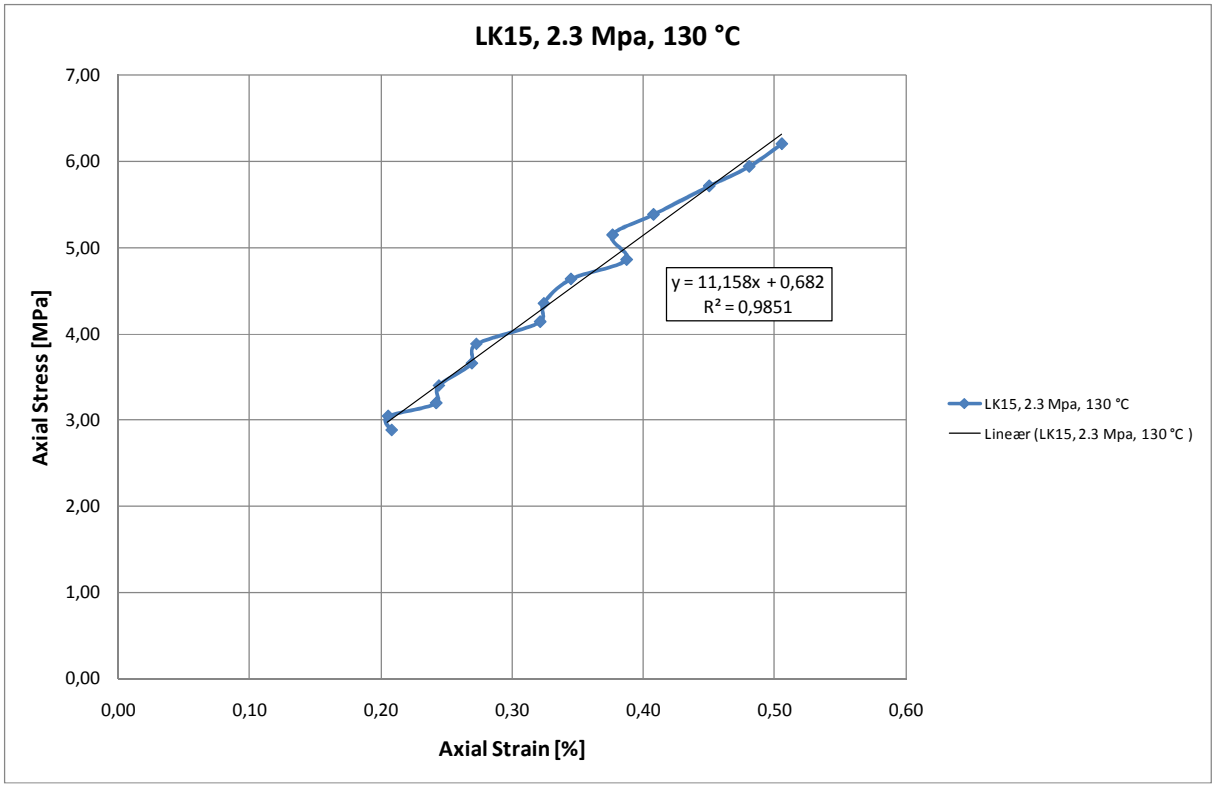


*Fig.A.38: Section of the Axial stress versus Axial strain plot for the 2.3 MPa deviatoirc test performed on LK15 with SSW flooding at 130 °C used to estimate the Young's modulus.*

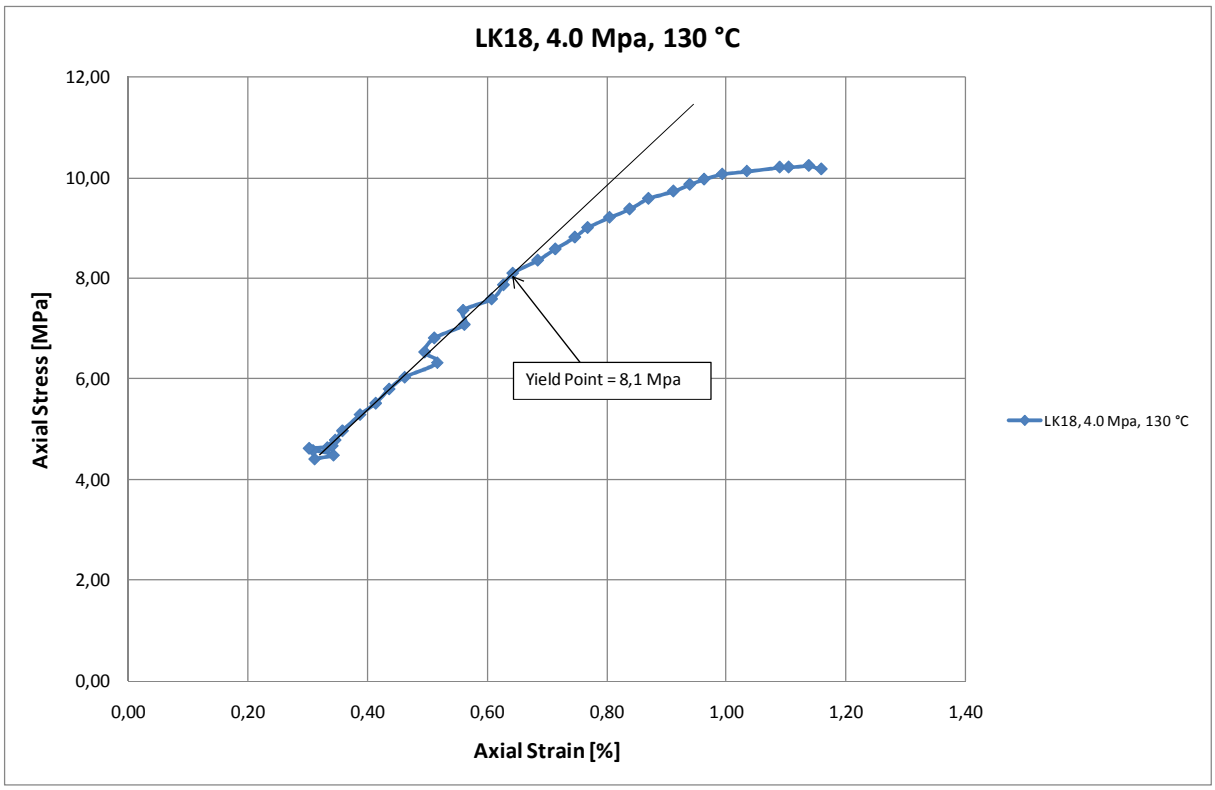


*Fig.A.39: Axial stress versus Axial strain plot for the 4.0 MPa deviatoirc test performed on LK18 with SSW flooding at 130 °C*

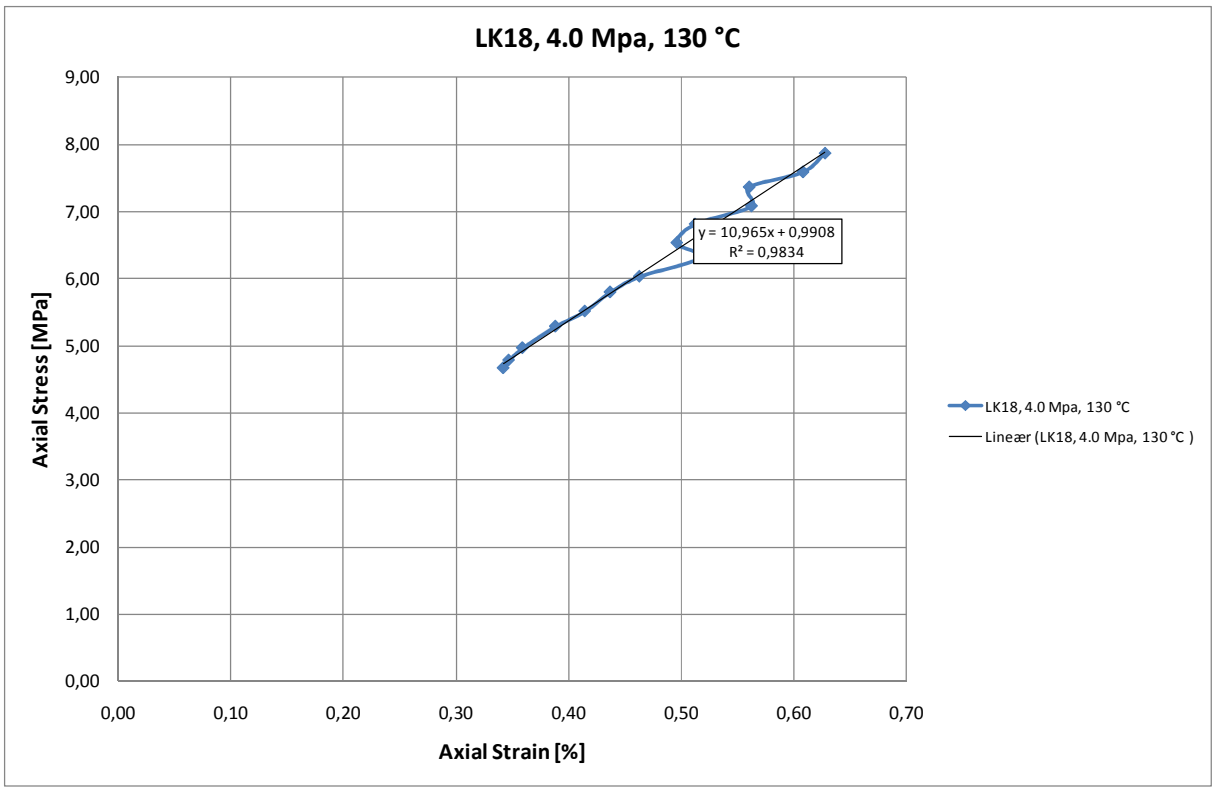


*Fig.A.40: Section of the Axial stress versus Axial strain plot for the 4.0 MPa deviatoirc test performed on LK18 with SSW flooding at 130 °C used to estimate the Young's modulus.*

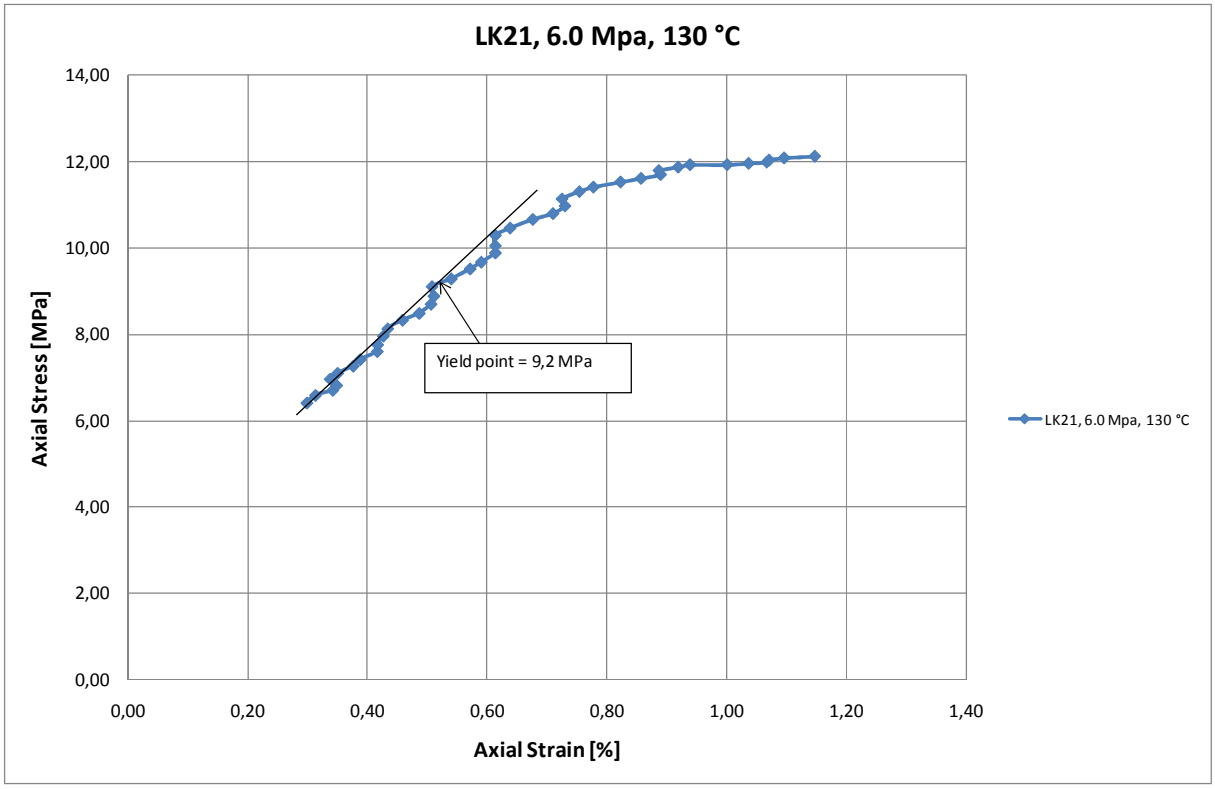


*Fig.A.41: Axial stress versus Axial strain plot for the 6.0 MPa deviatoirc test performed on LK21 with SSW flooding at 130 °C*

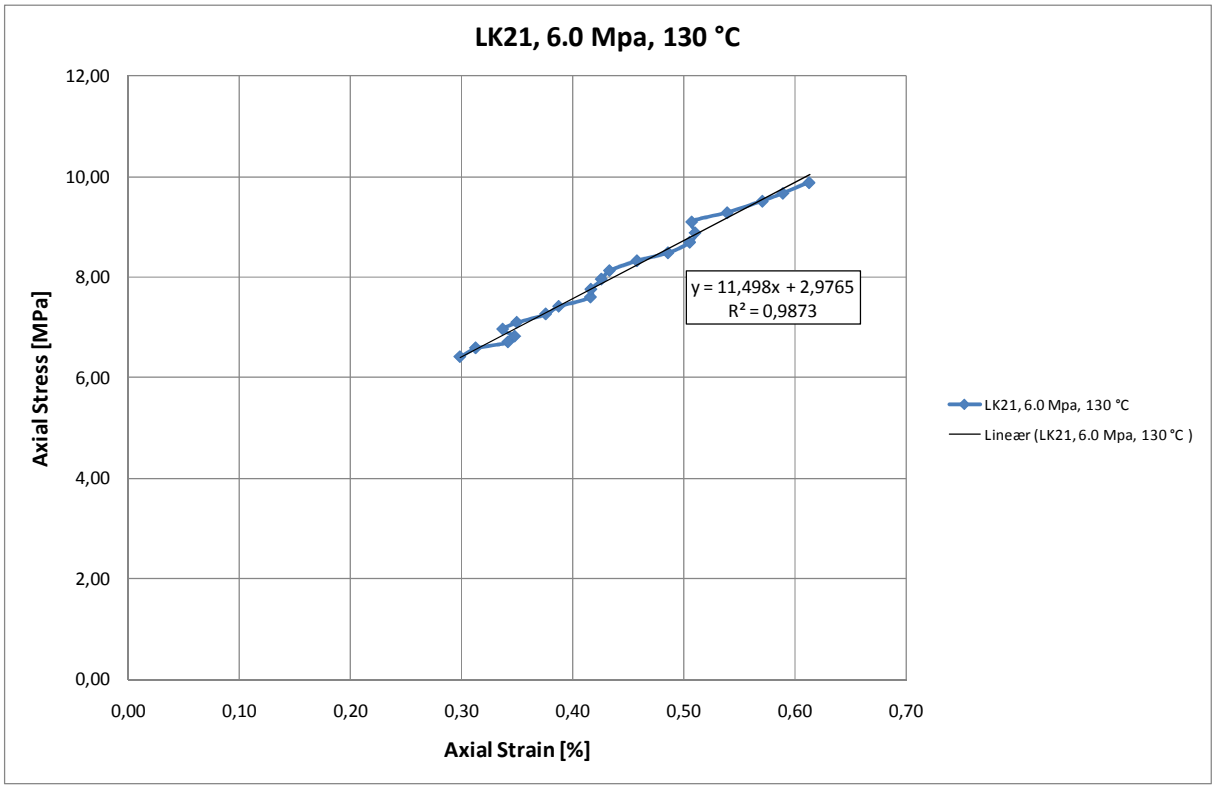


*Fig.A.42: Section of the Axial stress versus Axial strain plot for the 6.0 MPa deviatoirc test performed on LK21 with SSW flooding at 130 °C used to estimate the Young's modulus.*

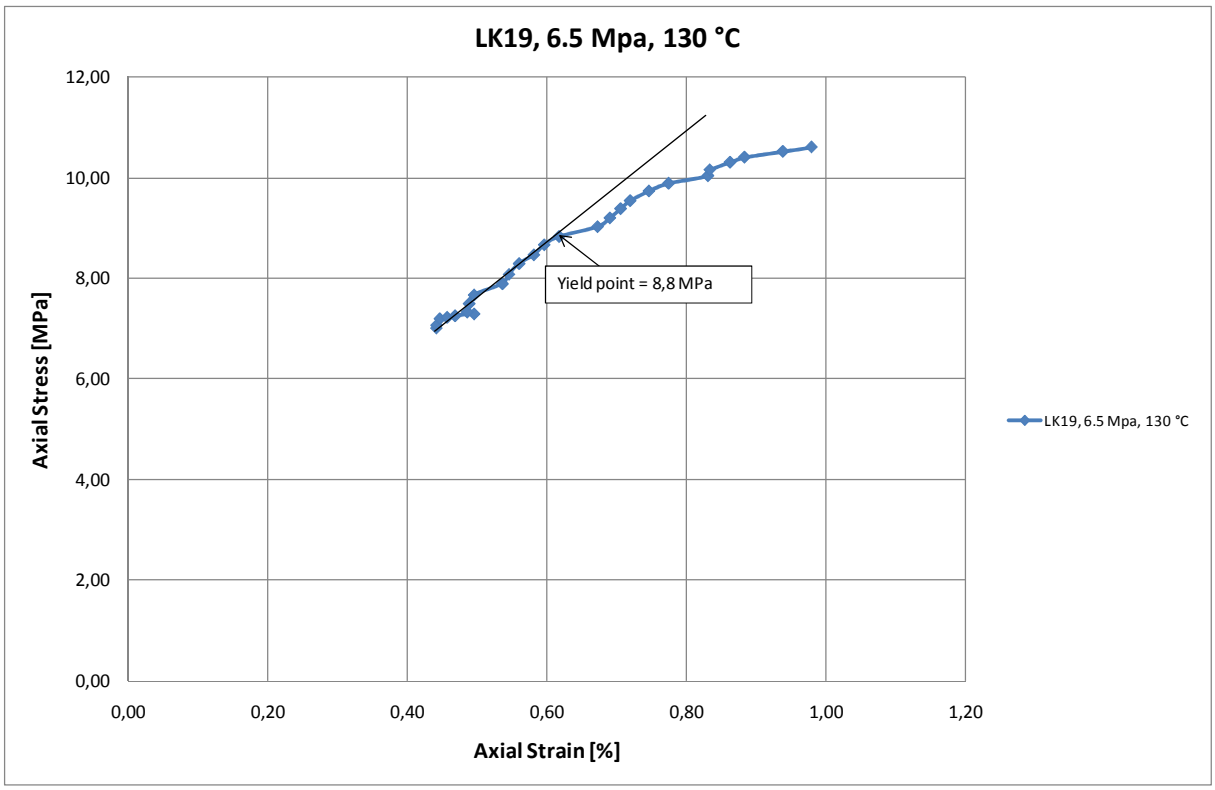


*Fig.A.43: Axial stress versus Axial strain plot for the 6.5 MPa deviatoirc test performed on LK19 with SSW flooding at 130 °C*

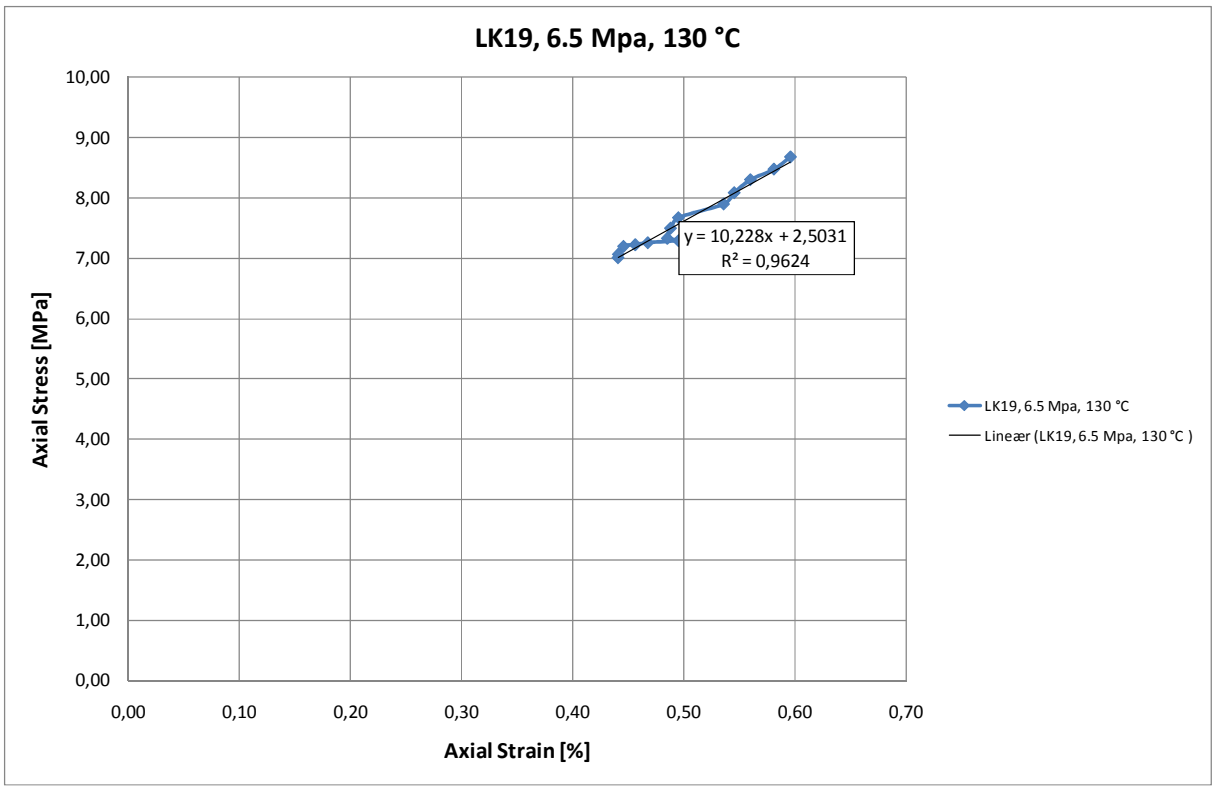


*Fig.A.44: Section of the Axial stress versus Axial strain plot for the 6.5 MPa deviatoirc test performed on LK19 with SSW flooding at 130 °C used to estimate the Young's modulus.*

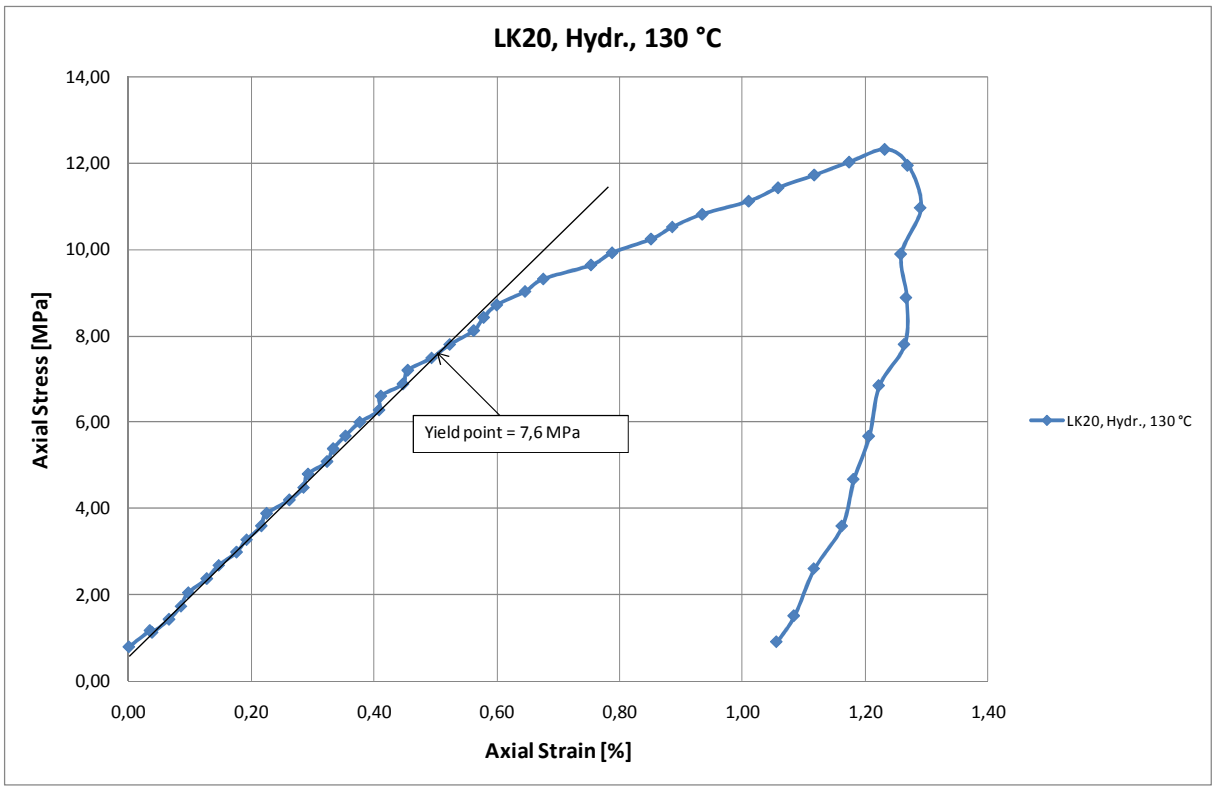


*Fig.A.45: Axial stress versus Axial strain plot for a hydrostatic test performed on LK20 with SSW flooding at ambient 130 °C*

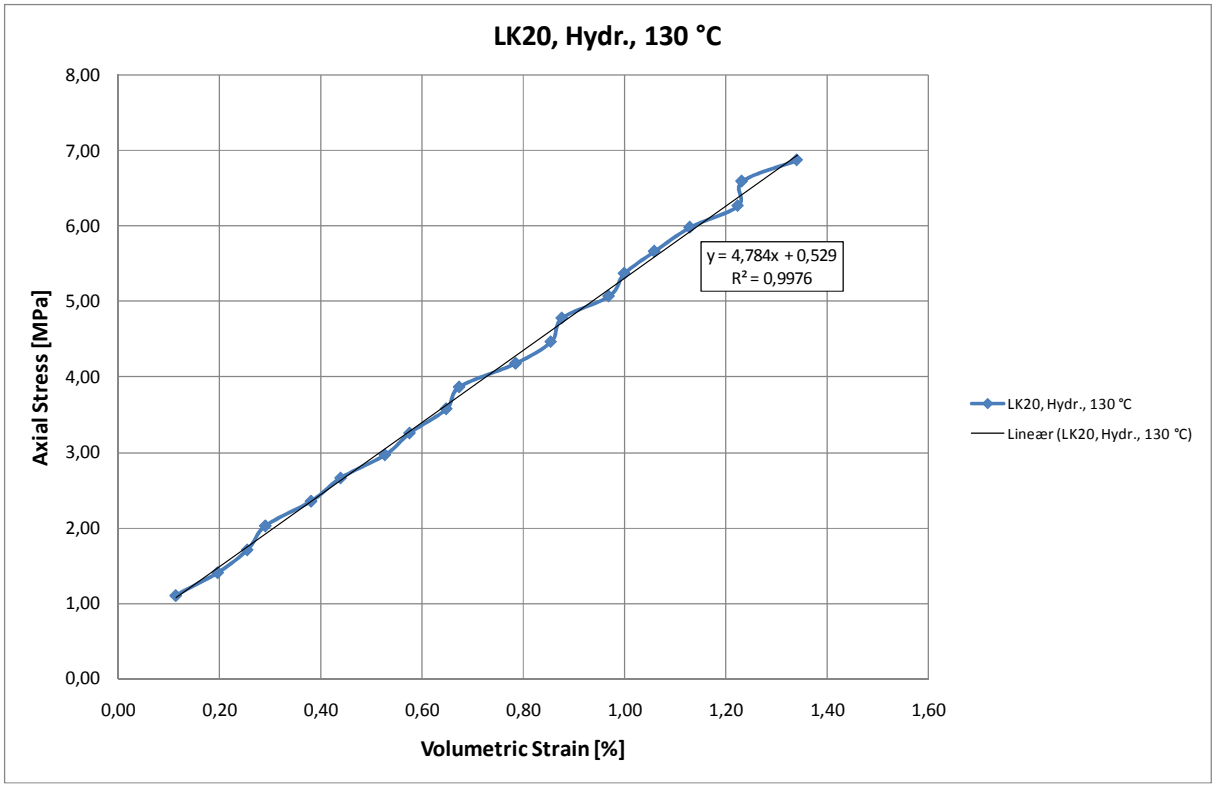


*Fig.A.46: Section of the Axial stress versus Volumetric strain plot the hydrostatic test performed on LK20 with SSW flooding at 130 °C used to estimate the Bulk modulus*

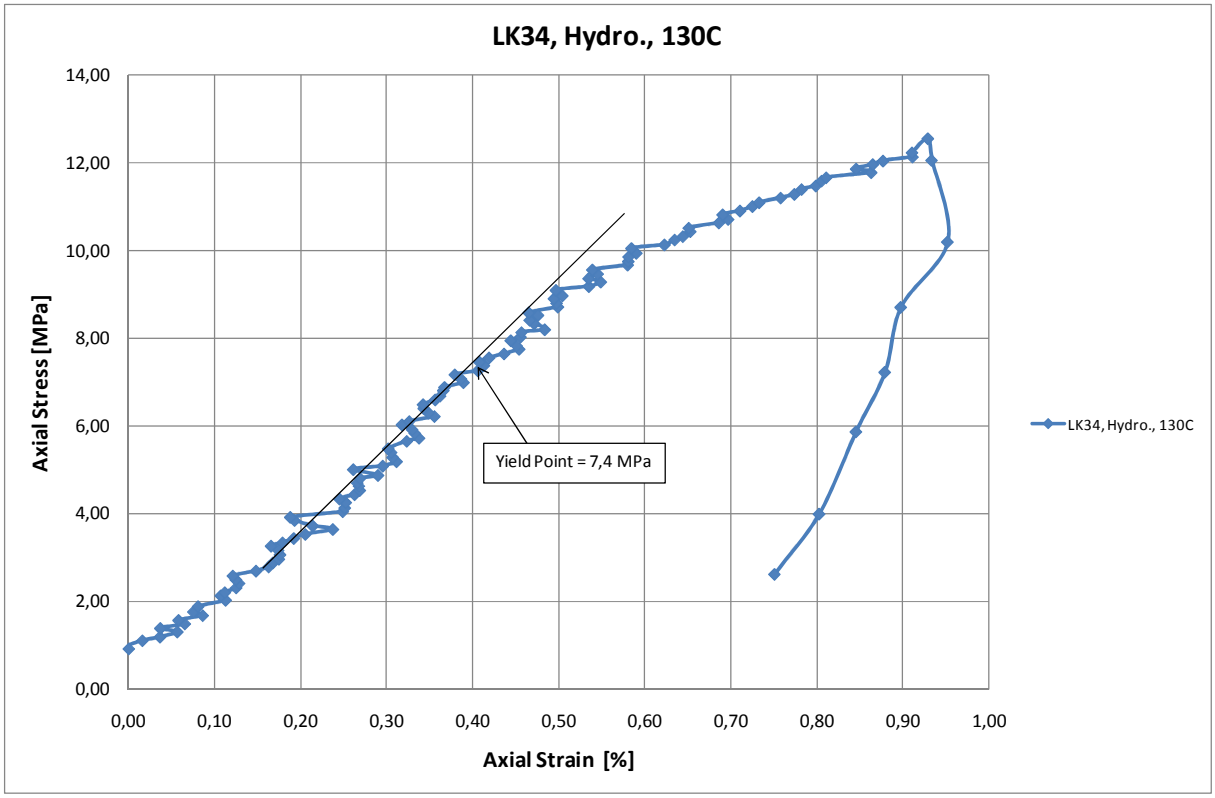


*Fig.A.47: Axial stress versus Axial strain plot for a hydrostatic test performed on LK34 with SSW flooding at ambient 130 °C*

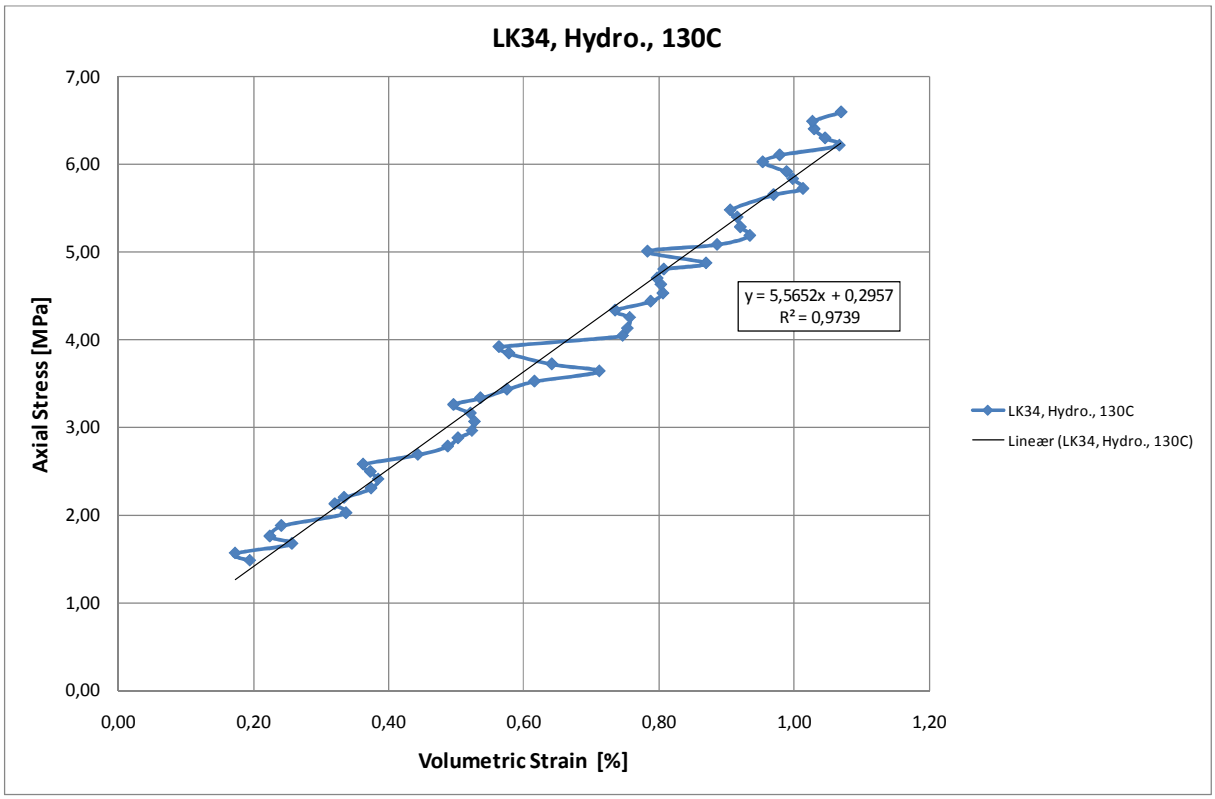


*Fig.A.48: Section of the Axial stress versus Volumetric strain plot the hydrostatic test performed on LK34 with SSW flooding at 130 °C used to estimate the Bulk modulus*

# 12 Appendix B- Tests saturated and flooded with SSW-(SO42-)

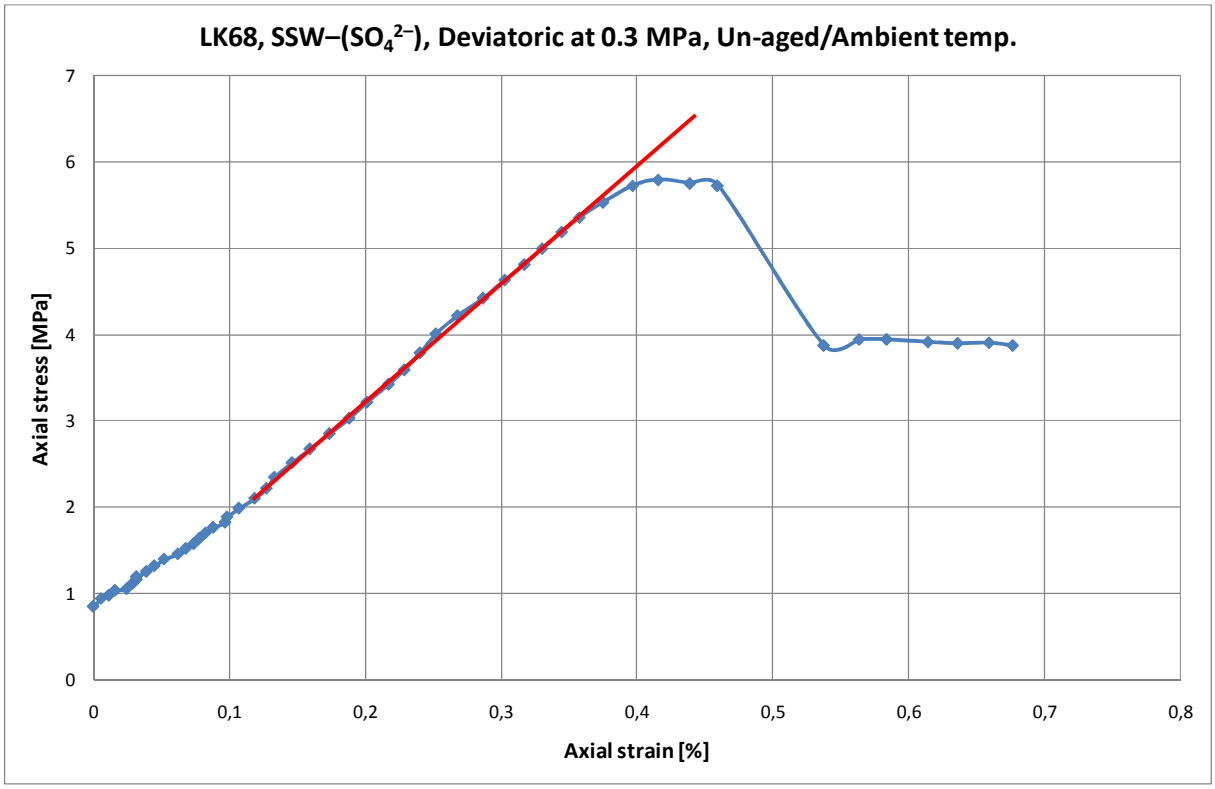


*Fig.B.1: Axial stress versus Axial strain plot for a 0.3 MPa deviatoirc test performed on LK68 with SSW-($SO_4^{2-}$) flooding at ambient temperature*

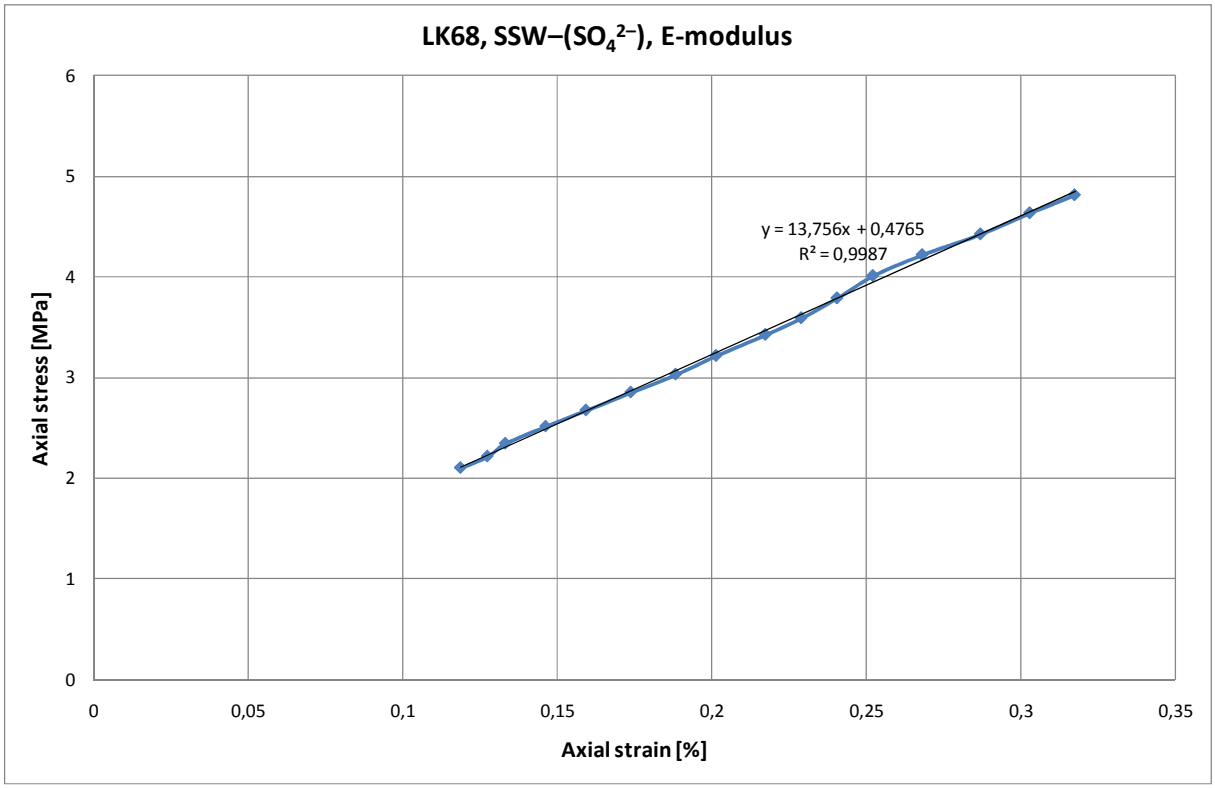


*Fig.B.2: Section of the Axial stress versus Axial strain plot for the 0.3 MPa deviatoirc test performed on LK68 with SSW-($SO_4^{2-}$) flooding at ambient temperature used to estimate the Young's modulus*

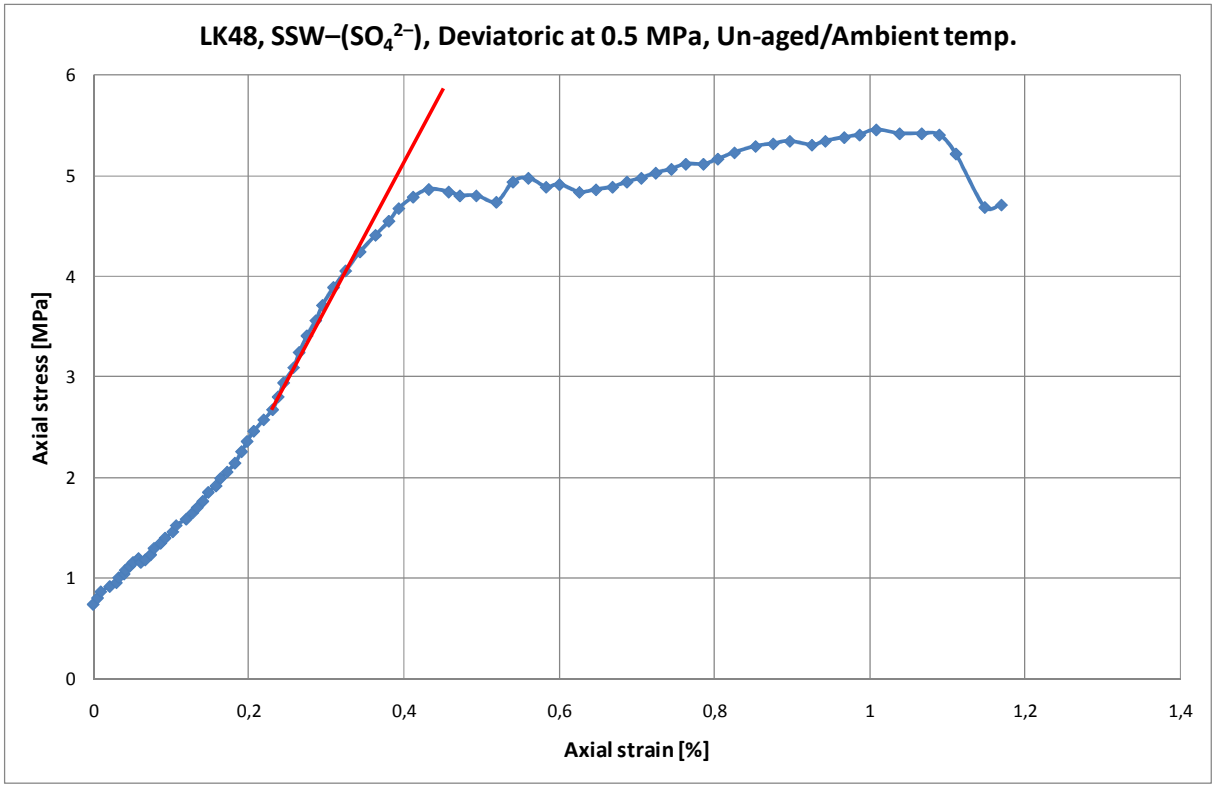


*Fig.B.3: Axial stress versus Axial strain plot for a 0.5 MPa deviatoirc test performed on LK48 with SSW-($SO_4^{2-}$) flooding at ambient temperature*

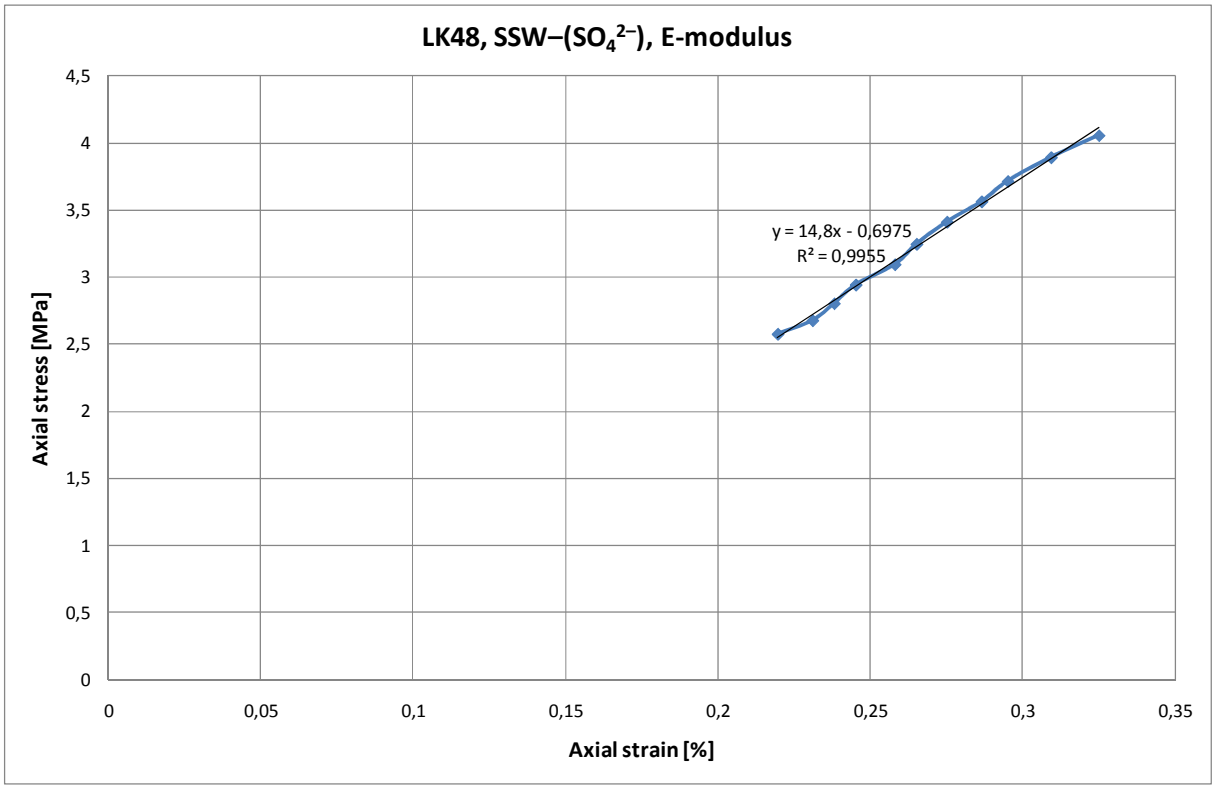


*Fig.B.4: Section of the Axial stress versus Axial strain plot for the 0.5 MPa deviatoirc test performed on LK48 with SSW-($SO_4^{2-}$) flooding at ambient temperature used to estimate the Young's modulus*

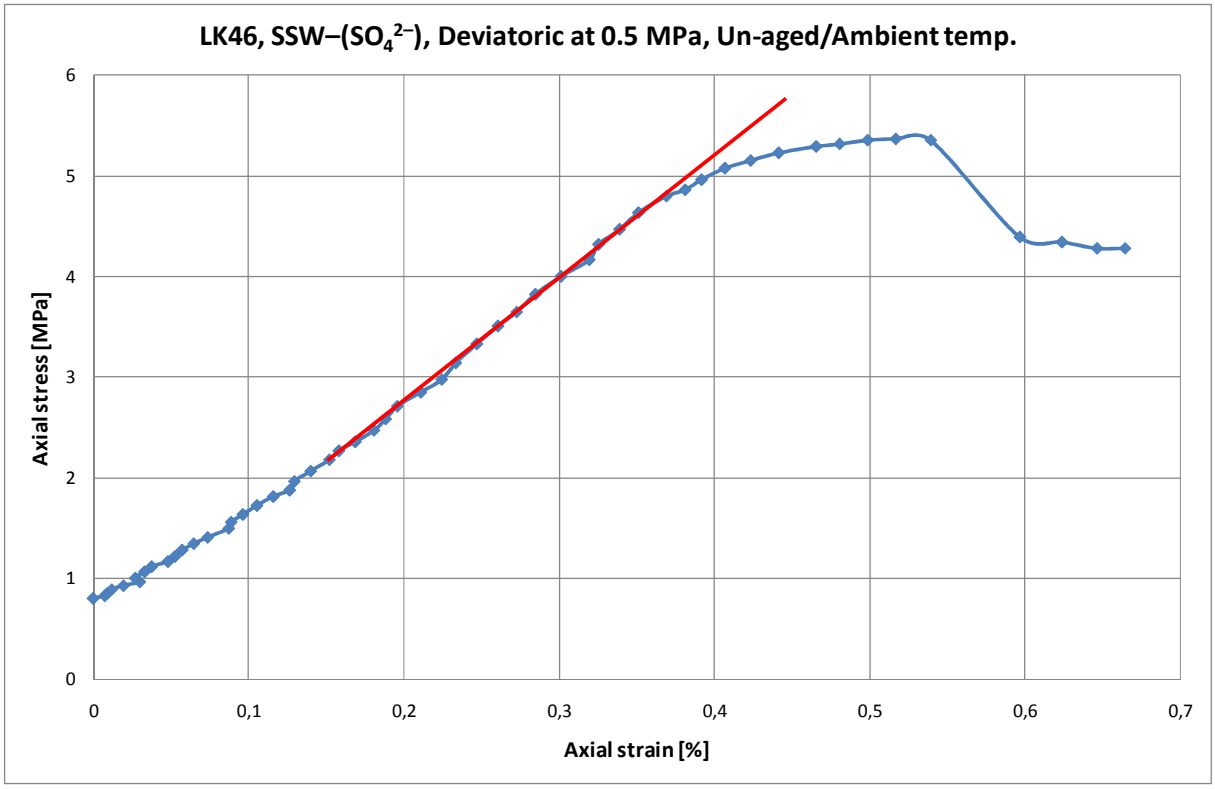


*Fig.B.5: Axial stress versus Axial strain plot for a 0.5 MPa deviatoirc test performed on LK46 with SSW-($SO_4^{2-}$) flooding at ambient temperature*

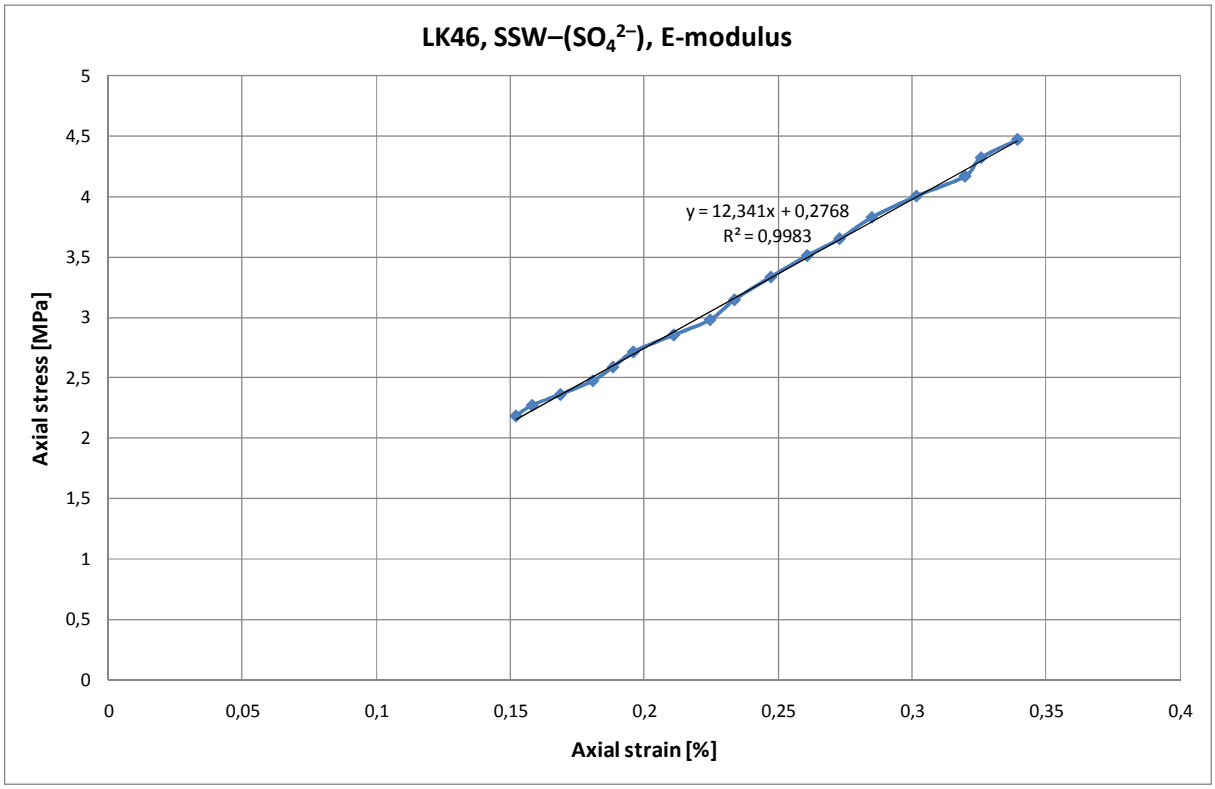


*Fig.B.6: Section of the Axial stress versus Axial strain plot for the 0.5 MPa deviatoirc test performed on LK46 with SSW-($SO_4^{2-}$) flooding at ambient temperature used to estimate the Young's modulus*

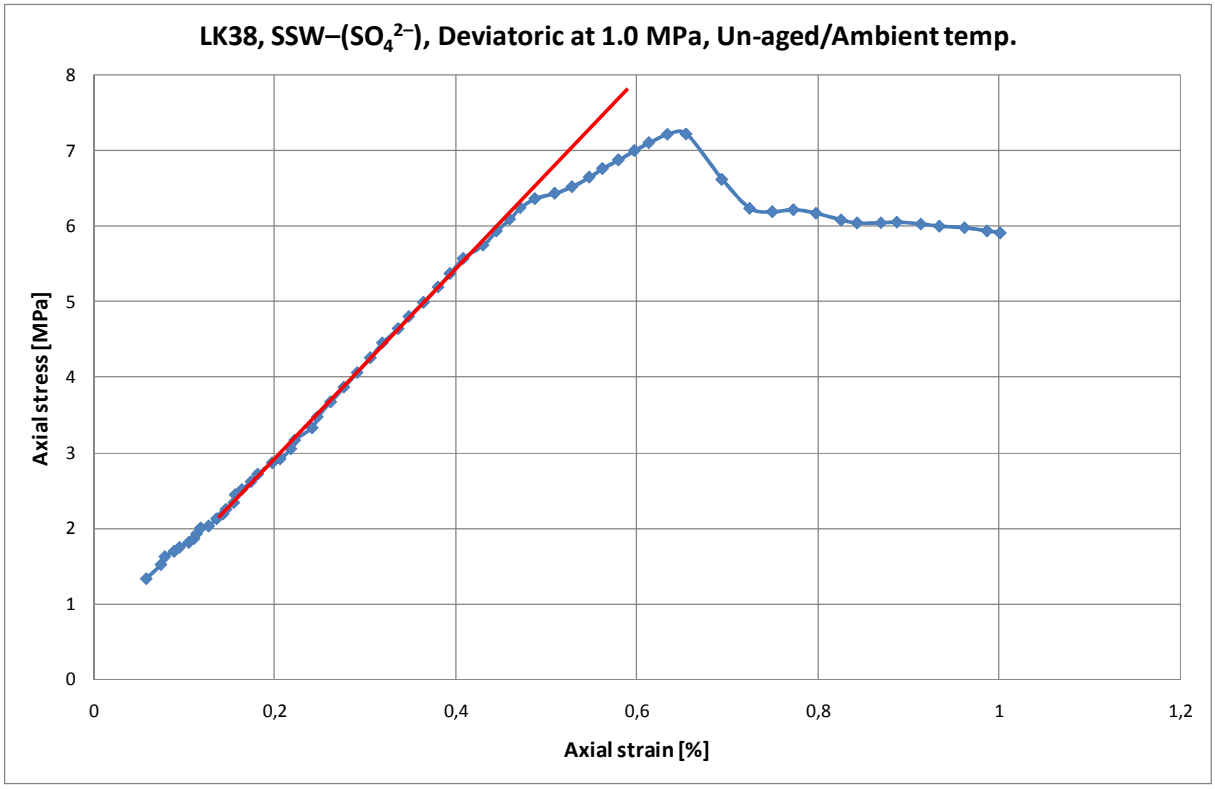


*Fig.B.7: Axial stress versus Axial strain plot for a 1.0 MPa deviatoirc test performed on LK38 with SSW-($SO_4^{2-}$) flooding at ambient temperature*

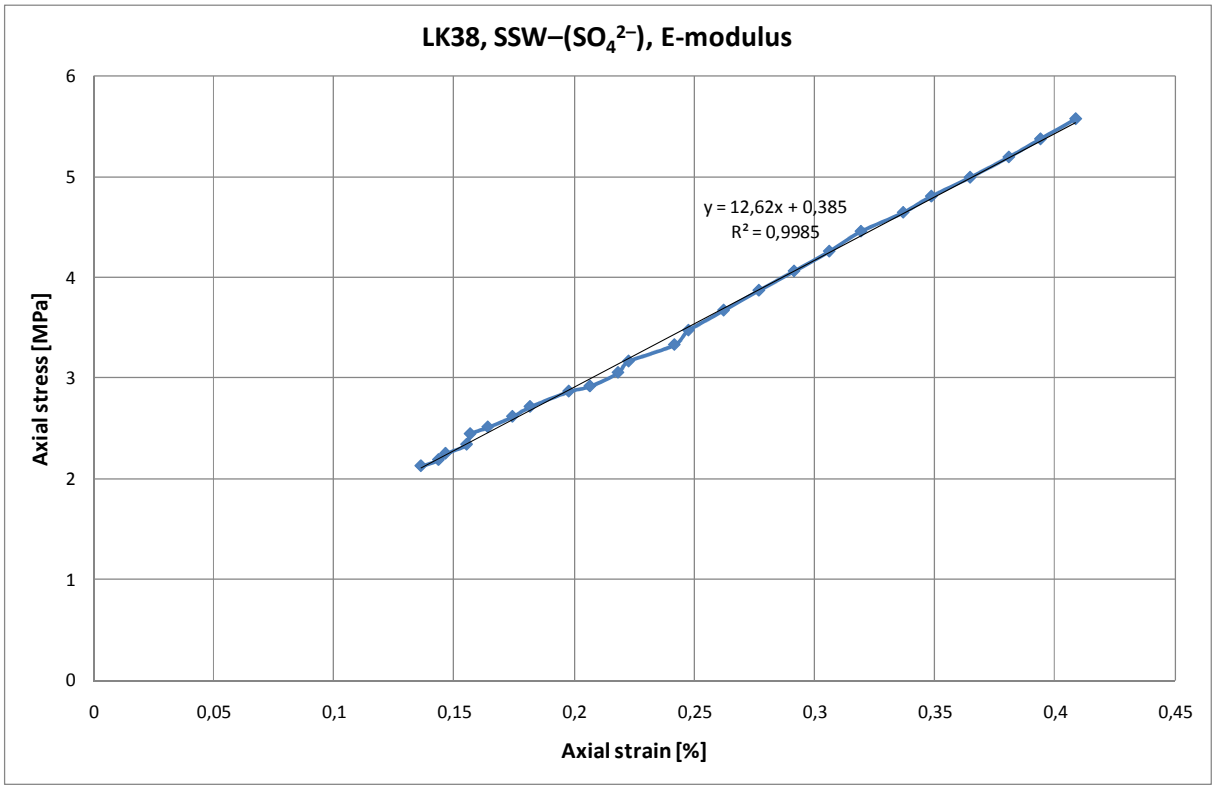


*Fig.B.8: Section of the Axial stress versus Axial strain plot for the 1.0 MPa deviatoirc test performed on LK38 with SSW-($SO_4^{2-}$) flooding at ambient temperature used to estimate the Young's modulus*

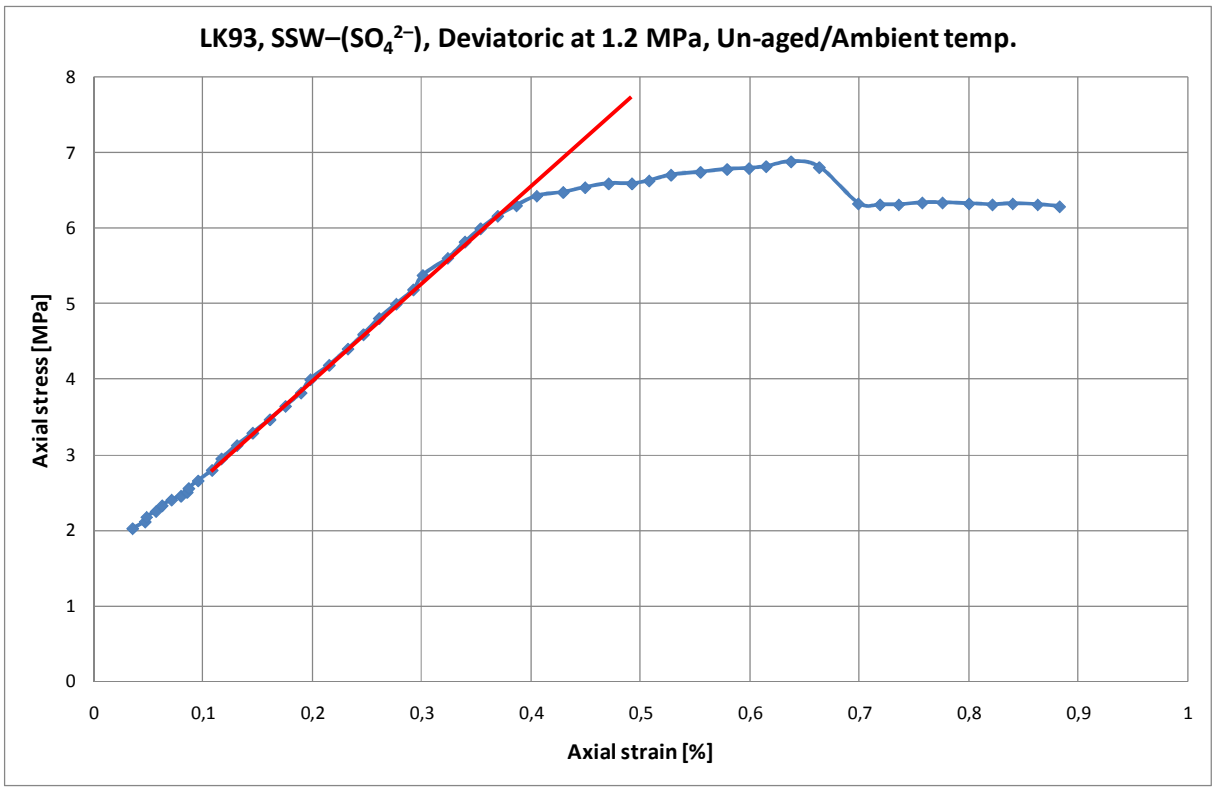


*Fig.B.9: Axial stress versus Axial strain plot for a 1.2 MPa deviatoirc test performed on LK93 with SSW-($SO_4^{2-}$) flooding at ambient temperature*

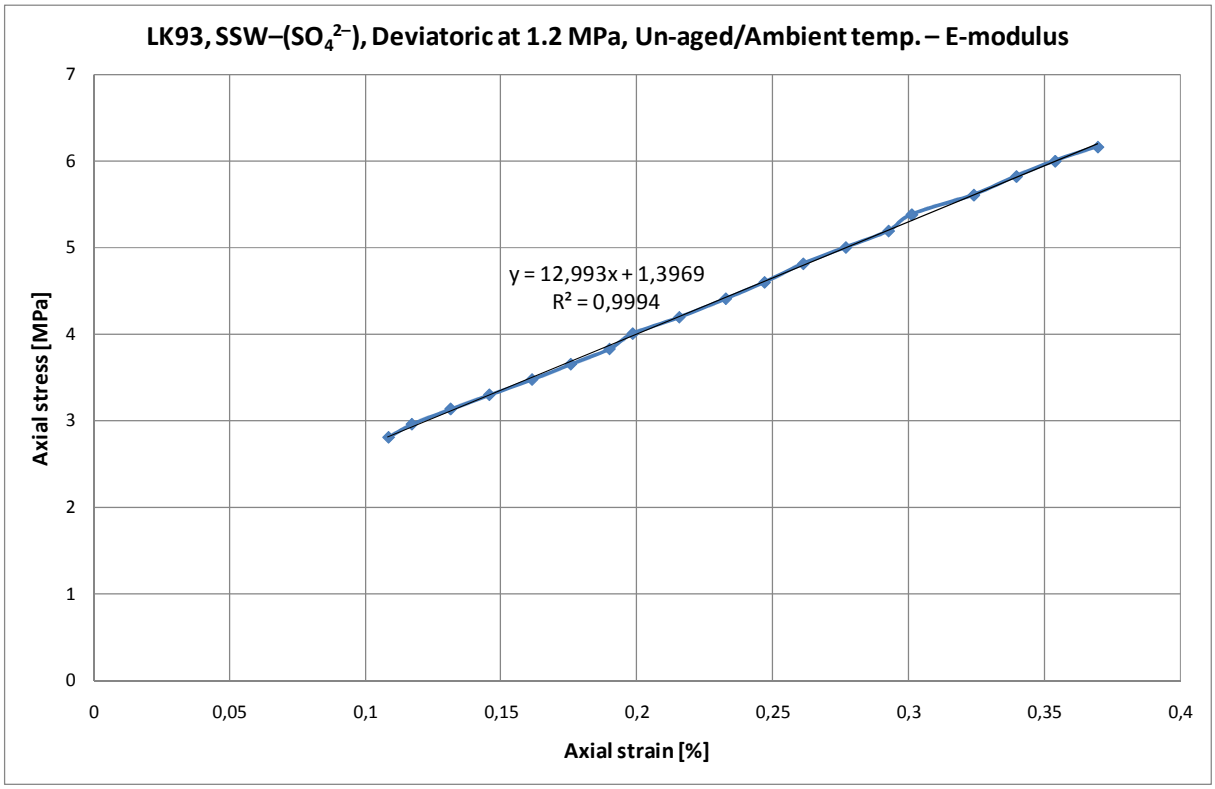


*Fig.B.10: Section of the Axial stress versus Axial strain plot for the 1.2 MPa deviatoirc test performed on LK93 with SSW-($SO_4^{2-}$) flooding at ambient temperature used to estimate the Young's modulus*

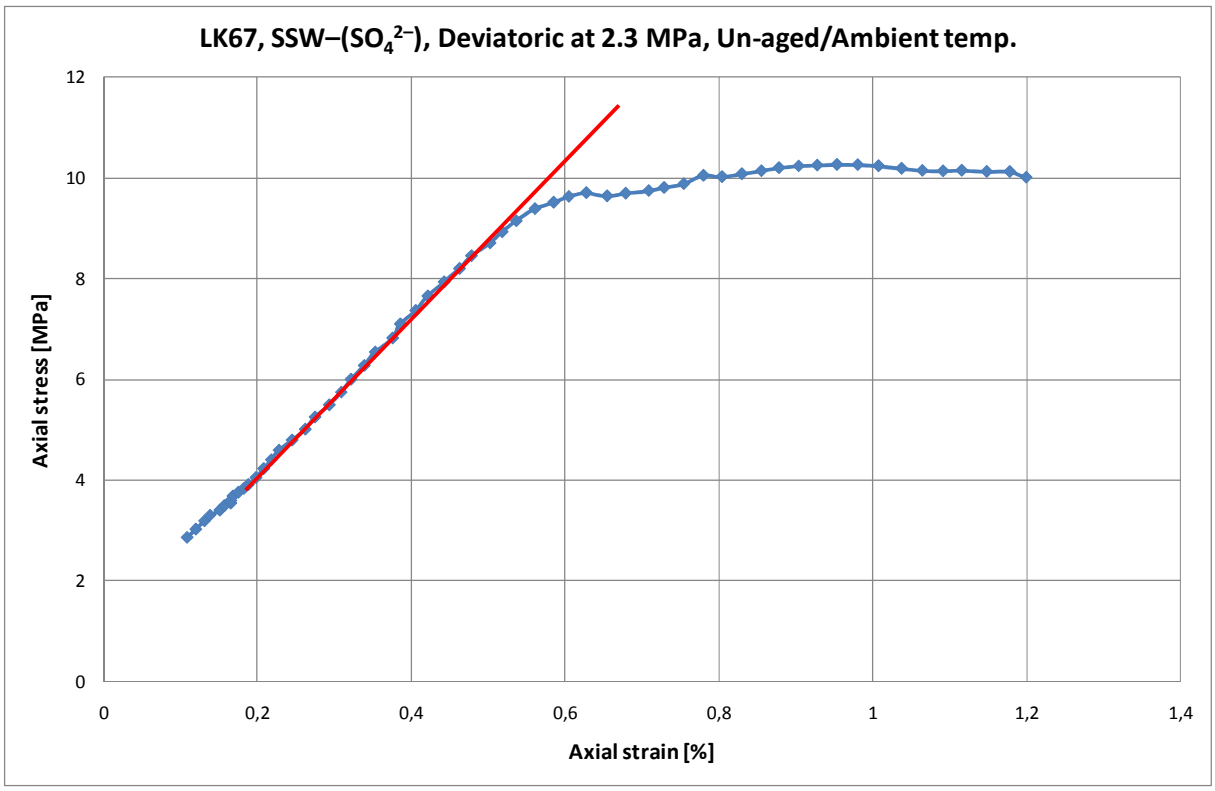


*Fig.B.11: Axial stress versus Axial strain plot for a 2.3 MPa deviatoirc test performed on LK67 with SSW-($SO_4^{2-}$) flooding at ambient temperature*

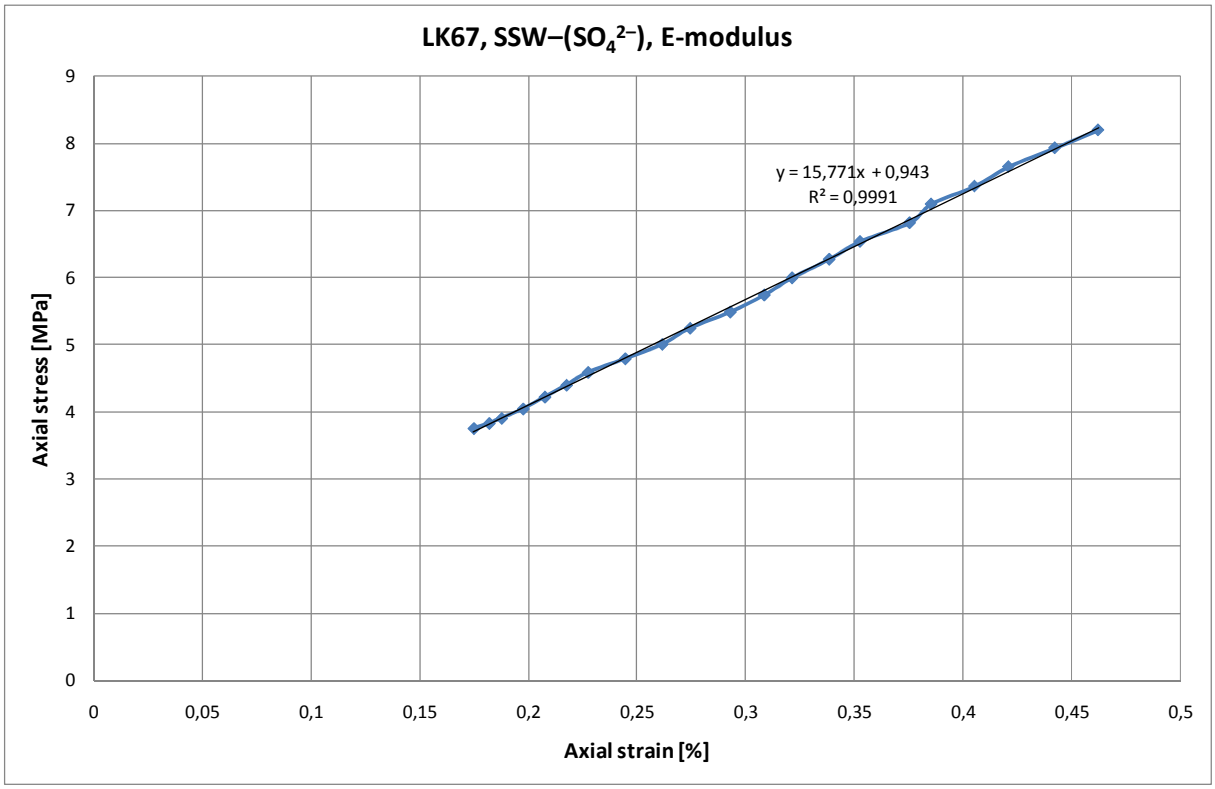


*Fig.B.12: Section of the Axial stress versus Axial strain plot for the 2.3 MPa deviatoirc test performed on LK67 with SSW-($SO_4^{2-}$) flooding at ambient temperature used to estimate the Young's modulus*

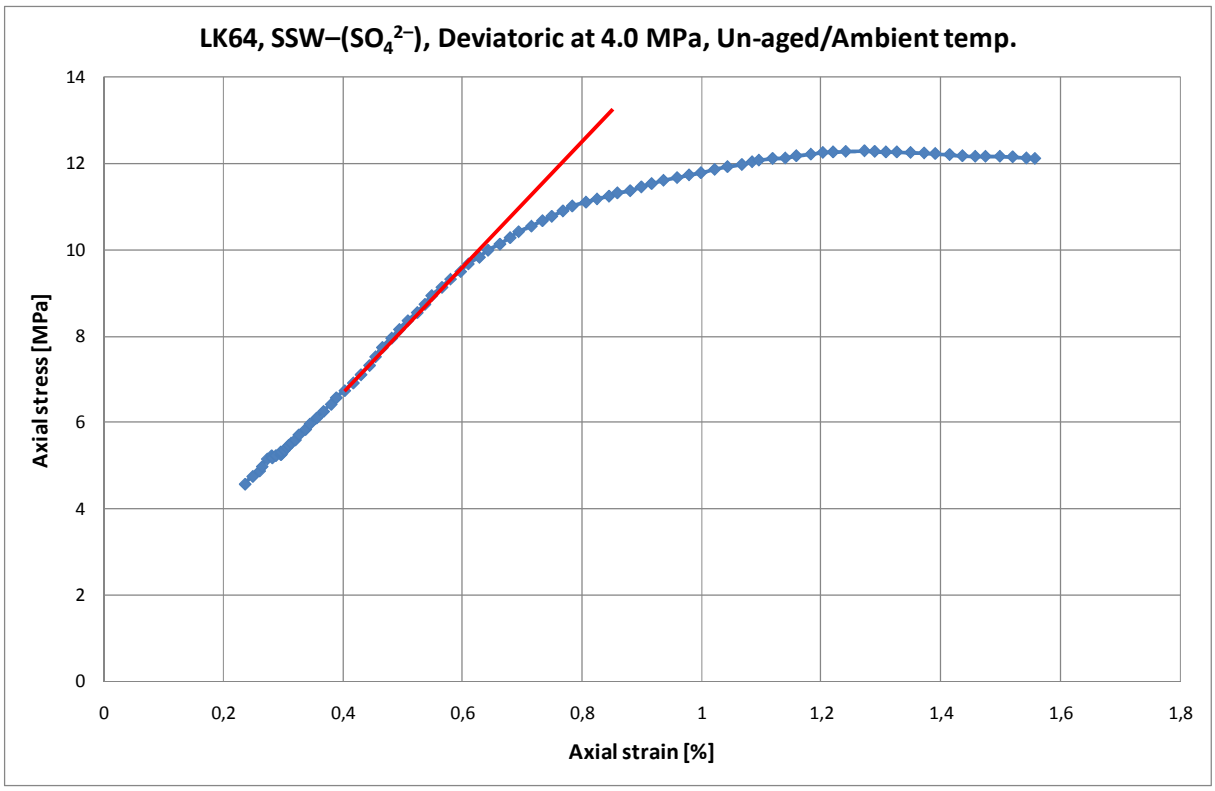


*Fig.B.13: Axial stress versus Axial strain plot for a 4.0 MPa deviatoirc test performed on LK64 with SSW-($SO_4^{2-}$) flooding at ambient temperature*

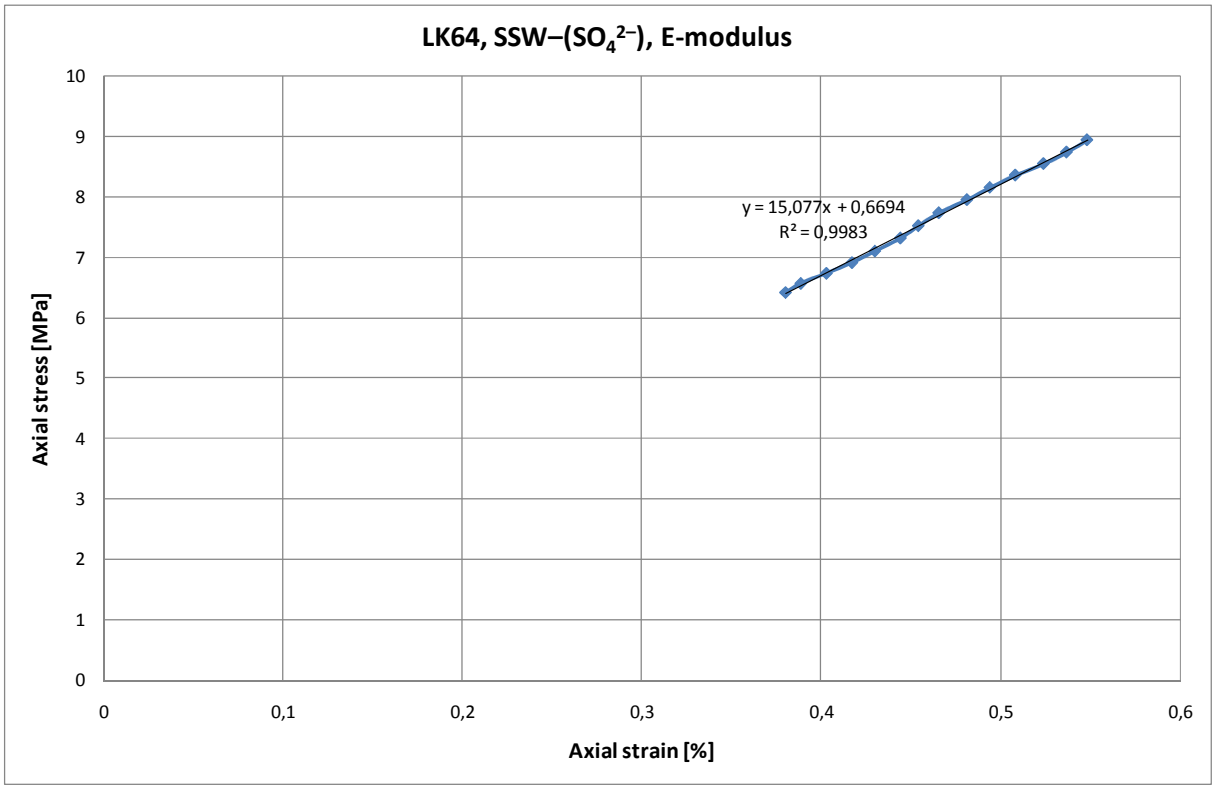


*Fig.B.14: Section of the Axial stress versus Axial strain plot for the 4.0 MPa deviatoirc test performed on LK64 with SSW-($SO_4^{2-}$) flooding at ambient temperature used to estimate the Young's modulus*

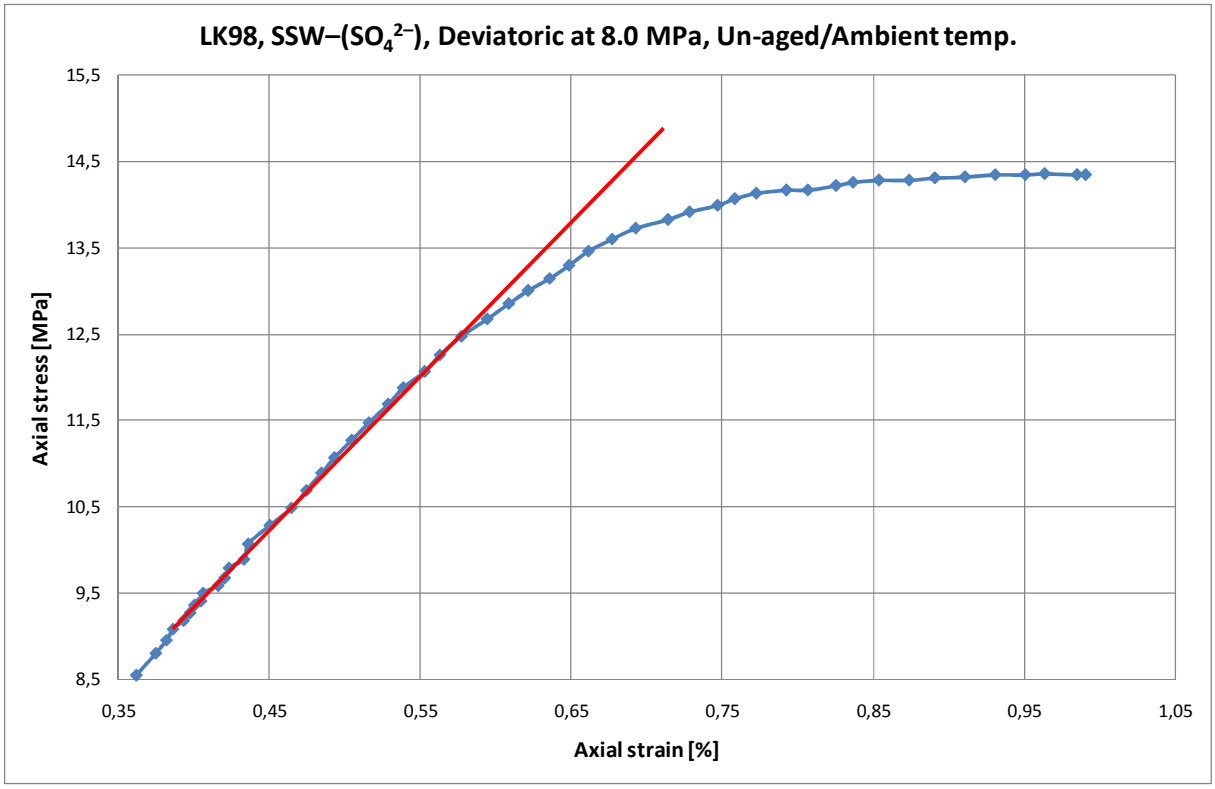


*Fig.B.15: Axial stress versus Axial strain plot for a 8.0 MPa deviatoirc test performed on LK98 with SSW-($SO_4^{2-}$) flooding at ambient temperature*

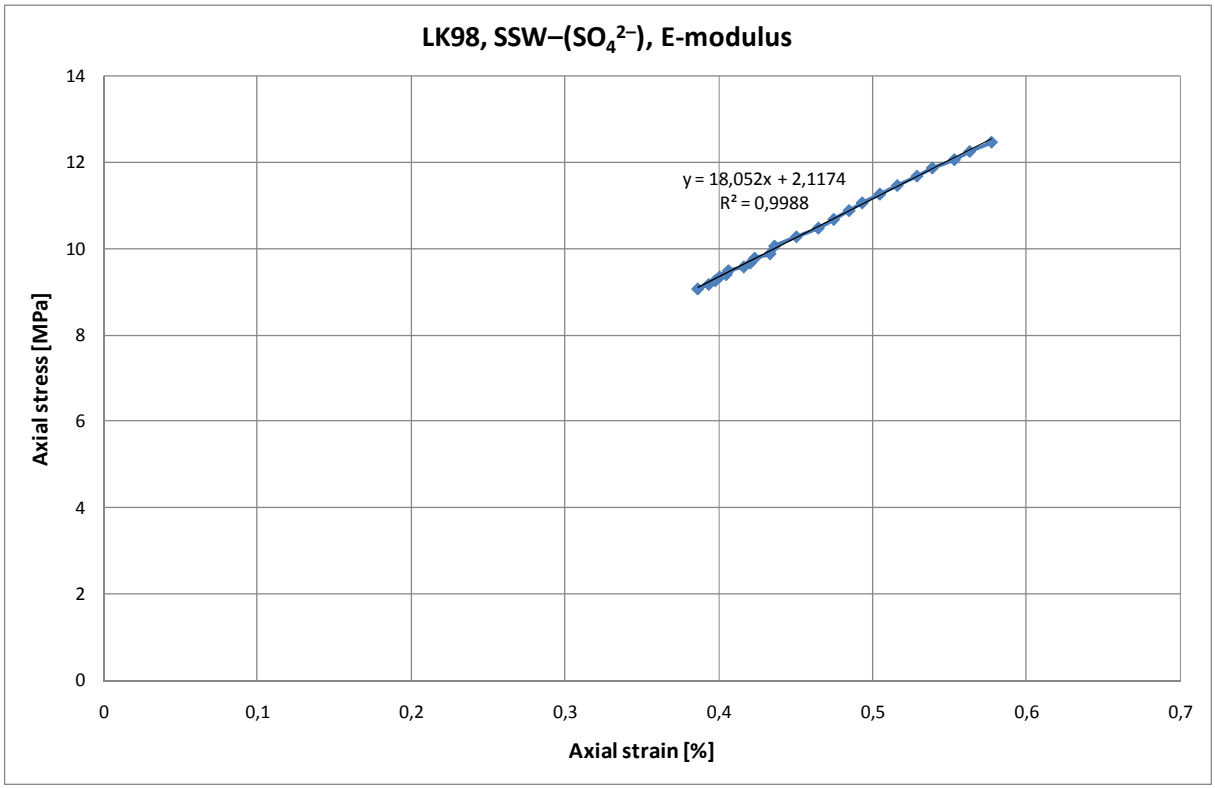


*Fig.B.16: Section of the Axial stress versus Axial strain plot for the 8.0 MPa deviatoirc test performed on LK98 with SSW-($SO_4^{2-}$) flooding at ambient temperature used to estimate the Young's modulus*

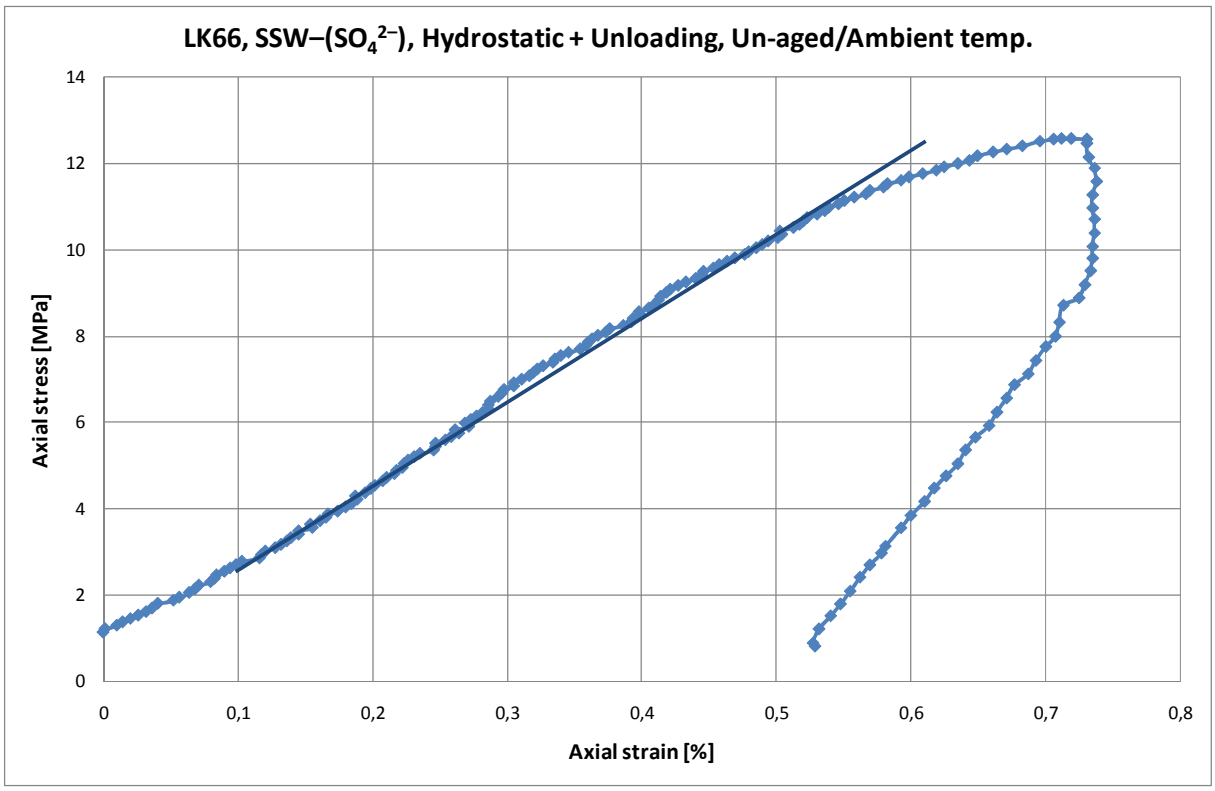


*Fig.B.17: Axial stress versus Axial strain plot for a hydrostatic test performed on LK66 with SSW-($SO_4^{2-}$) flooding at ambient temperature*

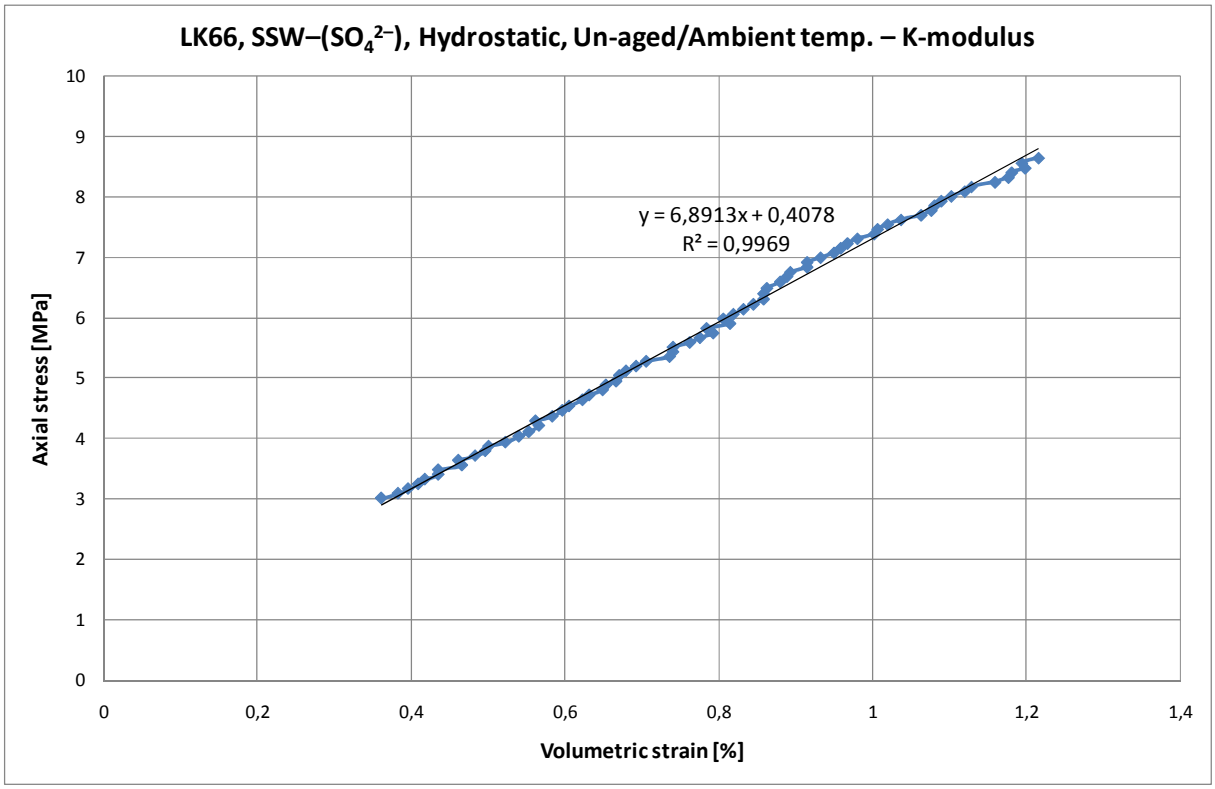


*Fig.B.18: Section of the Axial stress versus Volumetric strain plot the hydrostatic test performed on LK66 with SSW-($SO_4^{2-}$) flooding at ambient temperature used to estimate the Bulk modulus.*

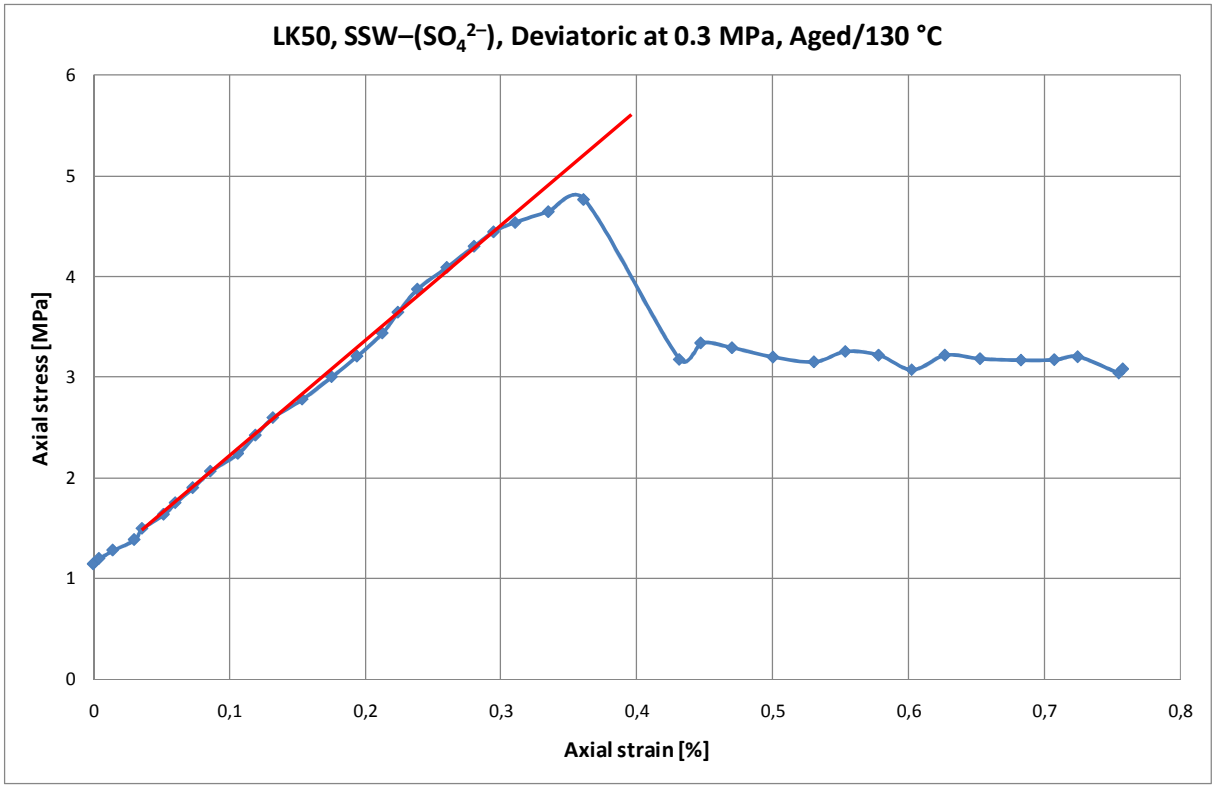


*Fig.B.19: Axial stress versus Axial strain plot for a 0.3 MPa deviatoirc test performed on LK50 with SSW-($SO_4^{2-}$) flooding at 130 °C*

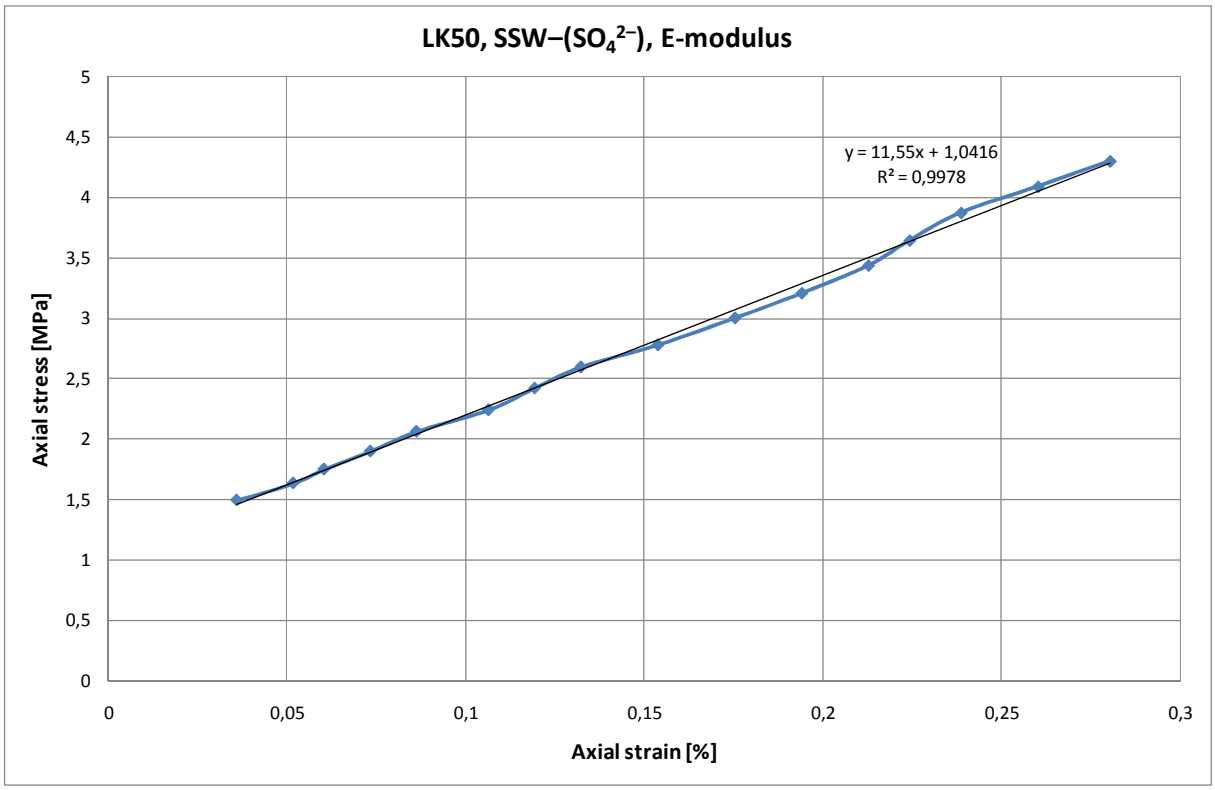


*Fig.B.20: Section of the Axial stress versus Axial strain plot for the 0.3 MPa deviatoirc test performed on LK50 with SSW-($SO_4^{2-}$) flooding at 130 °C used to estimate the Young's modulus*

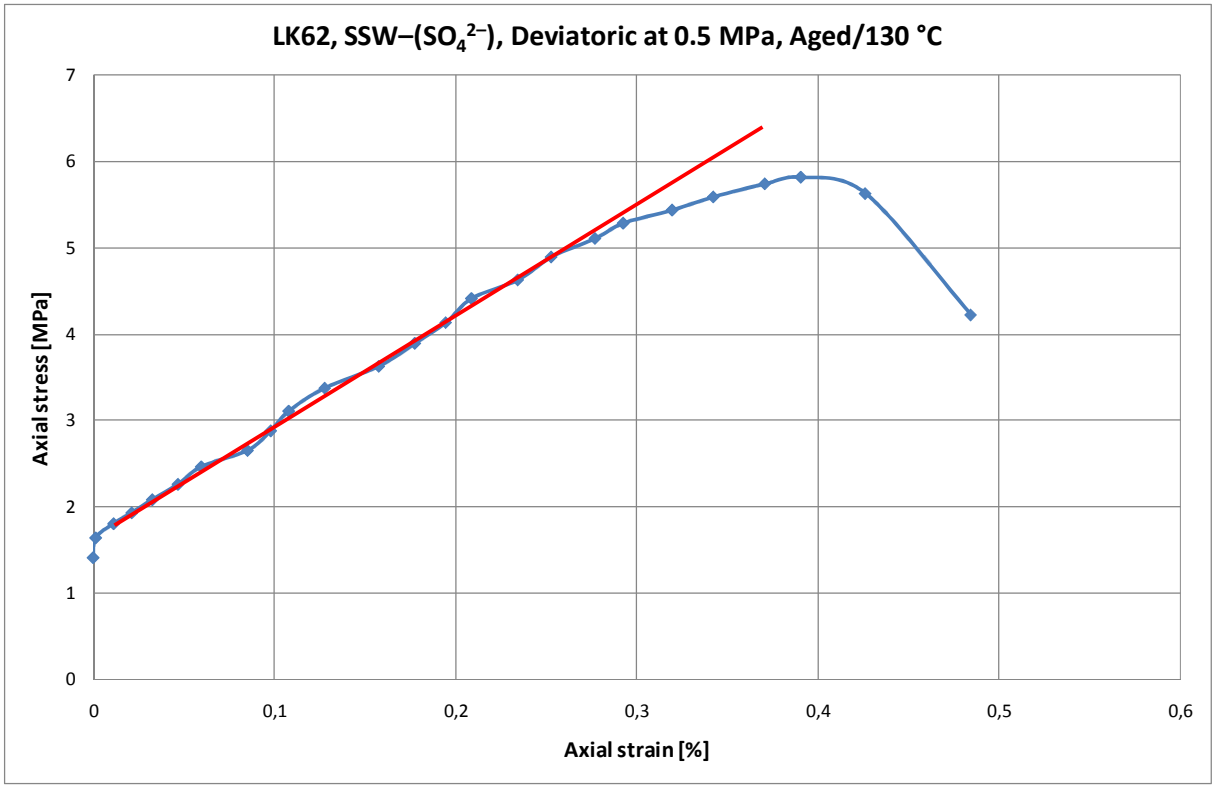


*Fig.B.21: Axial stress versus Axial strain plot for a 0.5 MPa deviatoirc test performed on LK62 with SSW-($SO_4^{2-}$) flooding at 130 °C*

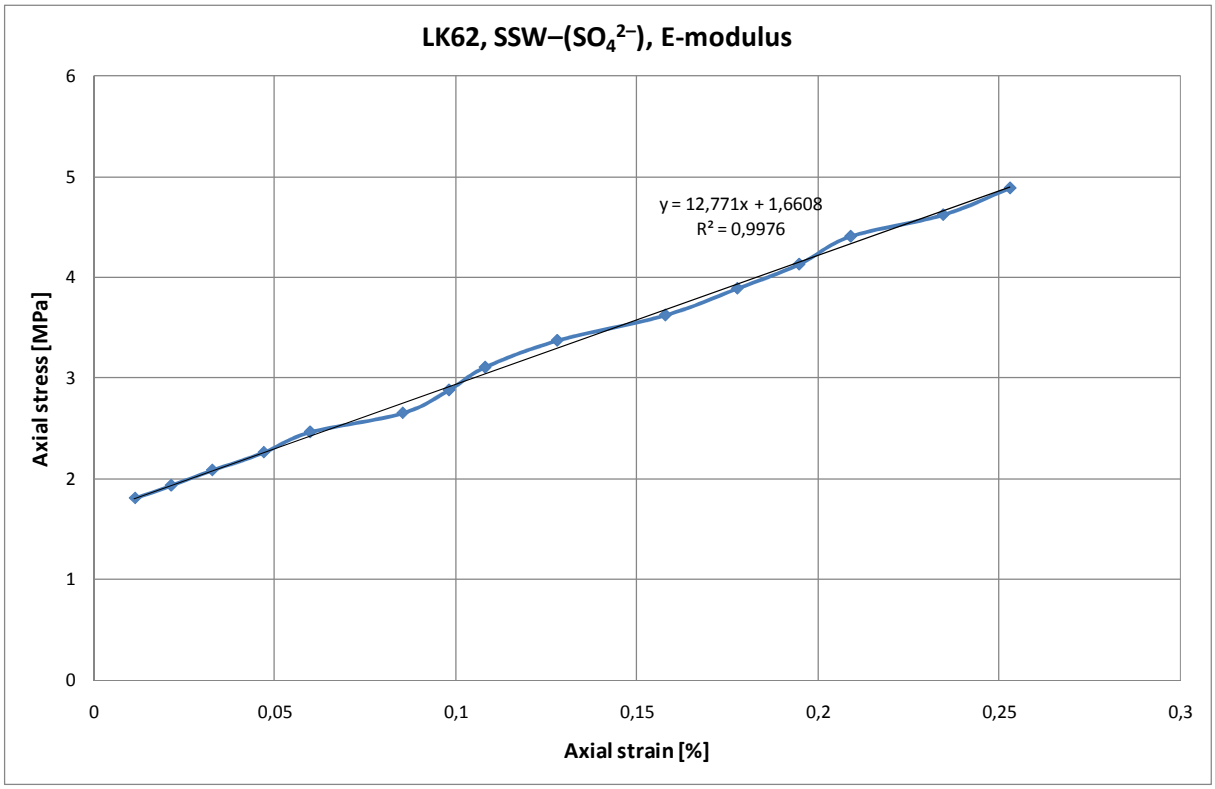


*Fig.B.22: Section of the Axial stress versus Axial strain plot for the 0.5 MPa deviatoirc test performed on LK62 with SSW-($SO_4^{2-}$) flooding at 130 °C used to estimate the Young's modulus*

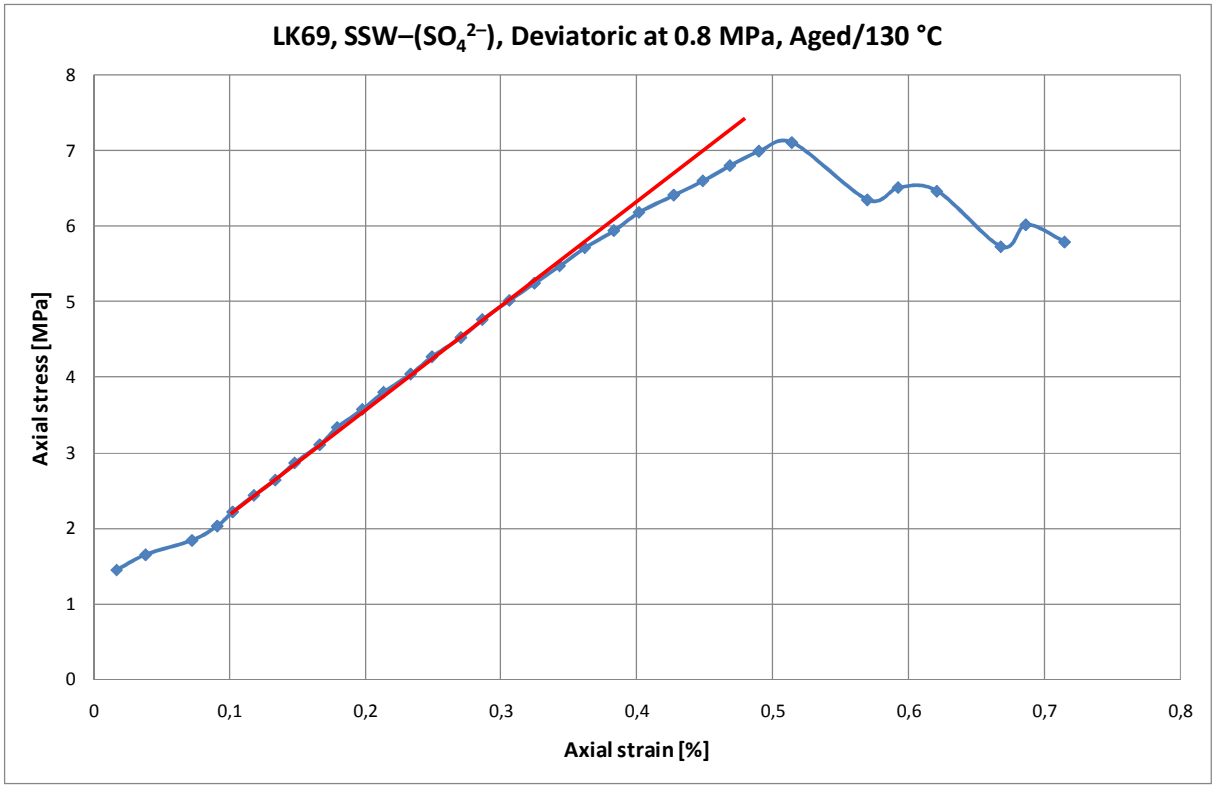


*Fig.B.23: Axial stress versus Axial strain plot for a 0.8 MPa deviatoirc test performed on LK69 with SSW-($SO_4^{2-}$) flooding at 130 °C*

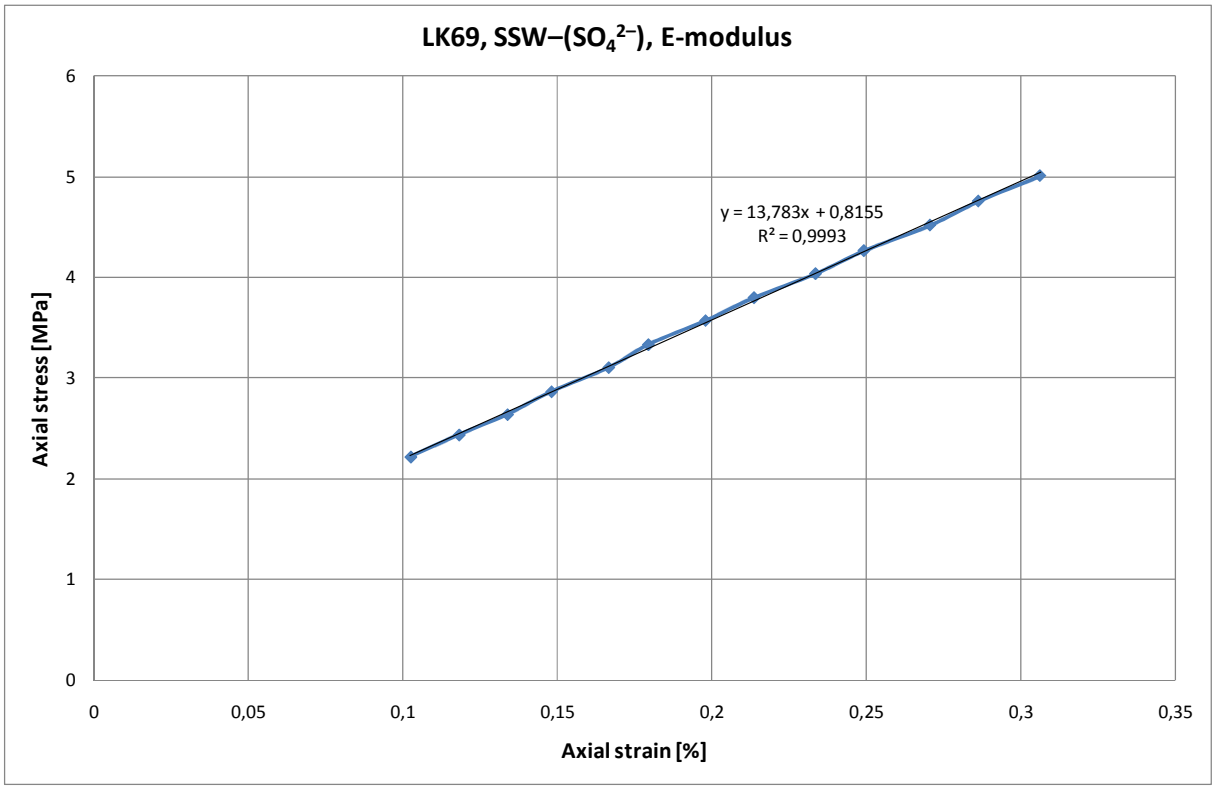


*Fig.B.24: Section of the Axial stress versus Axial strain plot for the 0.8 MPa deviatoirc test performed on LK69 with SSW-($SO_4^{2-}$) flooding at 130 °C used to estimate the Young's modulus*

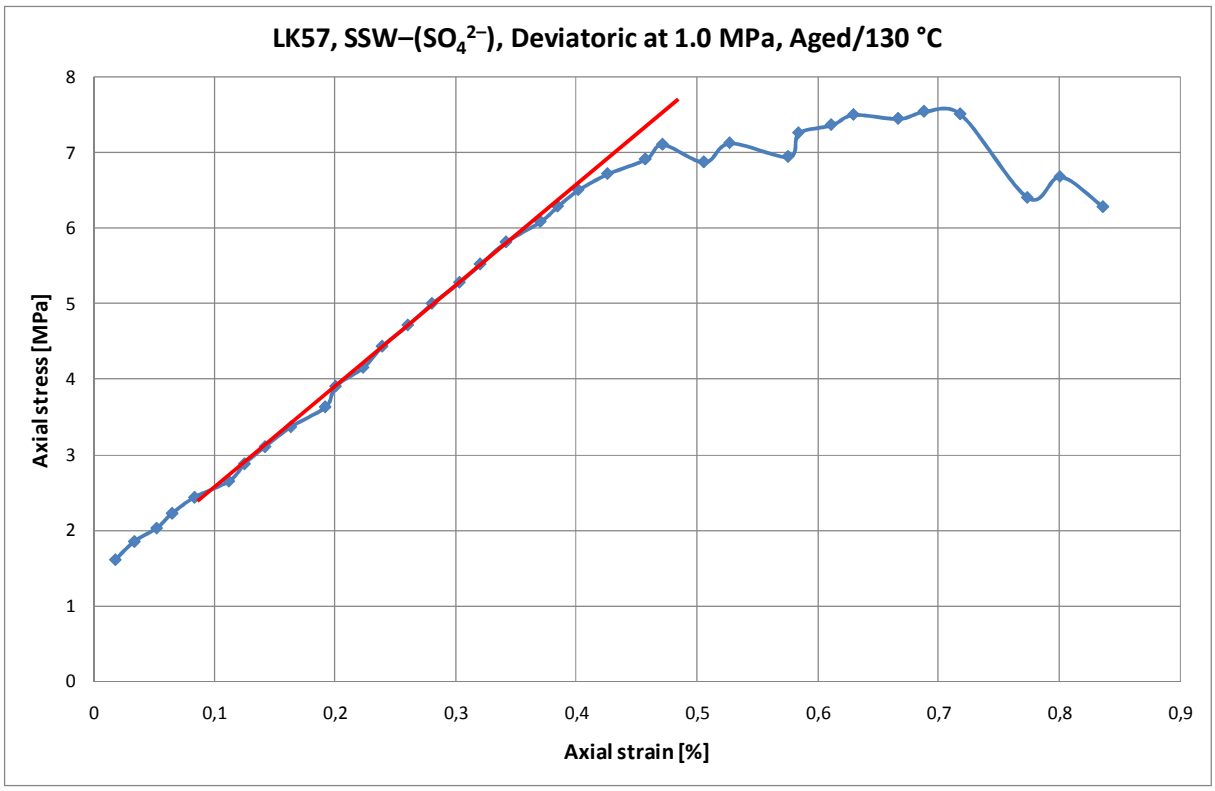


*Fig.B.25: Axial stress versus Axial strain plot for a 1.0 MPa deviatoirc test performed on LK57 with SSW-($SO_4^{2-}$) flooding at 130 °C*

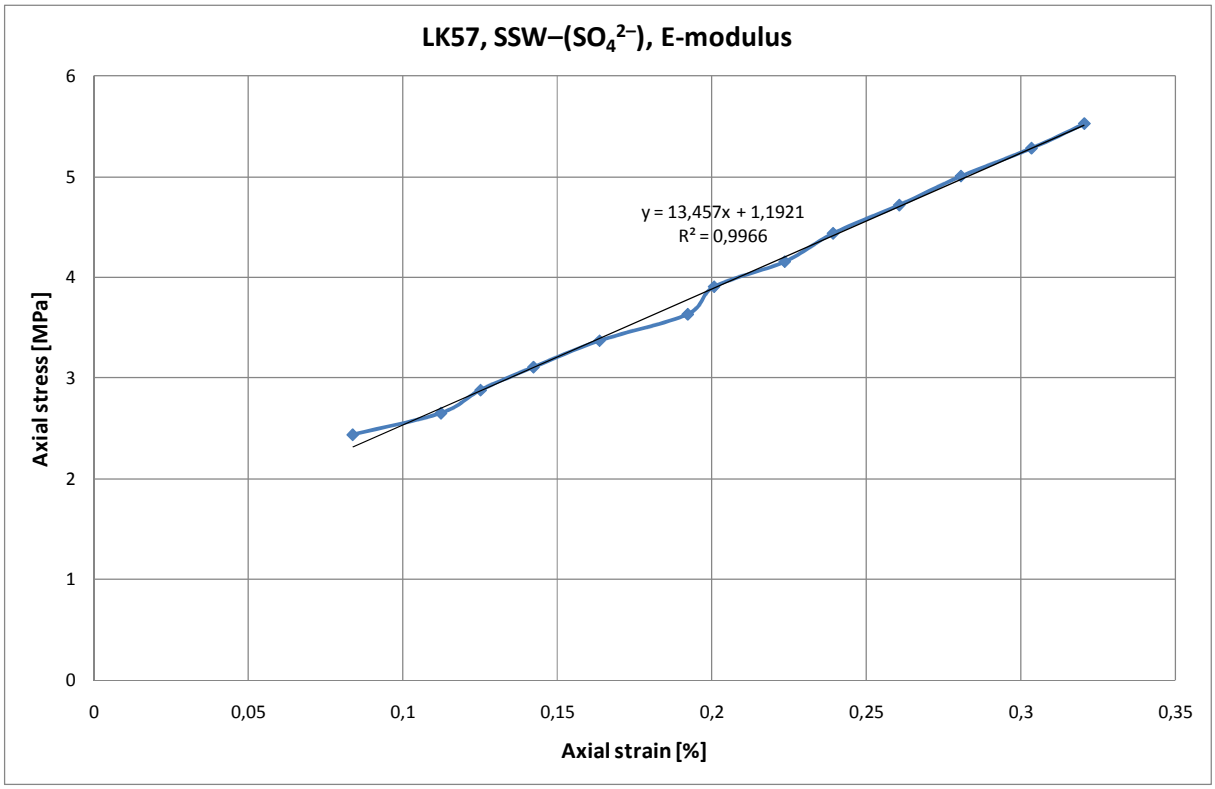


*Fig.B.26: Section of the Axial stress versus Axial strain plot for the 1.0 MPa deviatoirc test performed on LK57 with SSW-($SO_4^{2-}$) flooding at 130 °C used to estimate the Young's modulus*

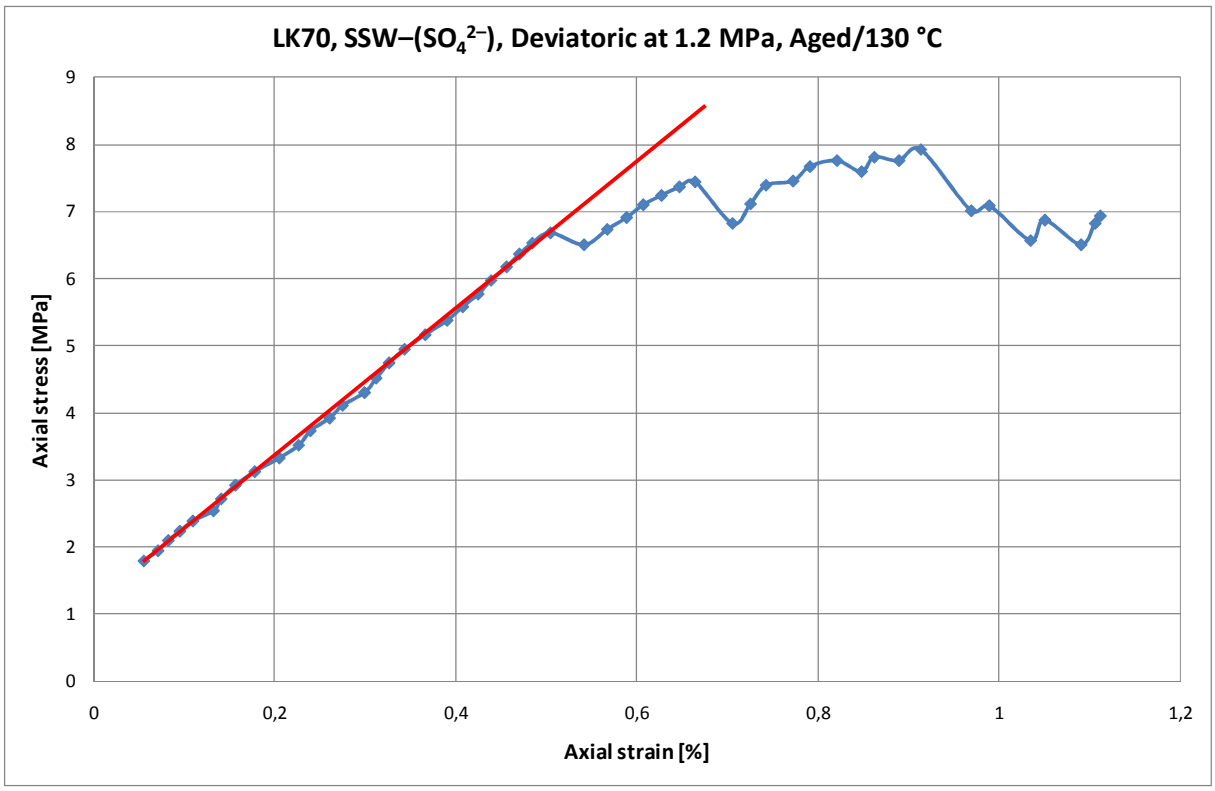


*Fig.B.27: Axial stress versus Axial strain plot for a 1.2 MPa deviatoirc test performed on LK70 with SSW-($SO_4^{2-}$) flooding at 130 °C*

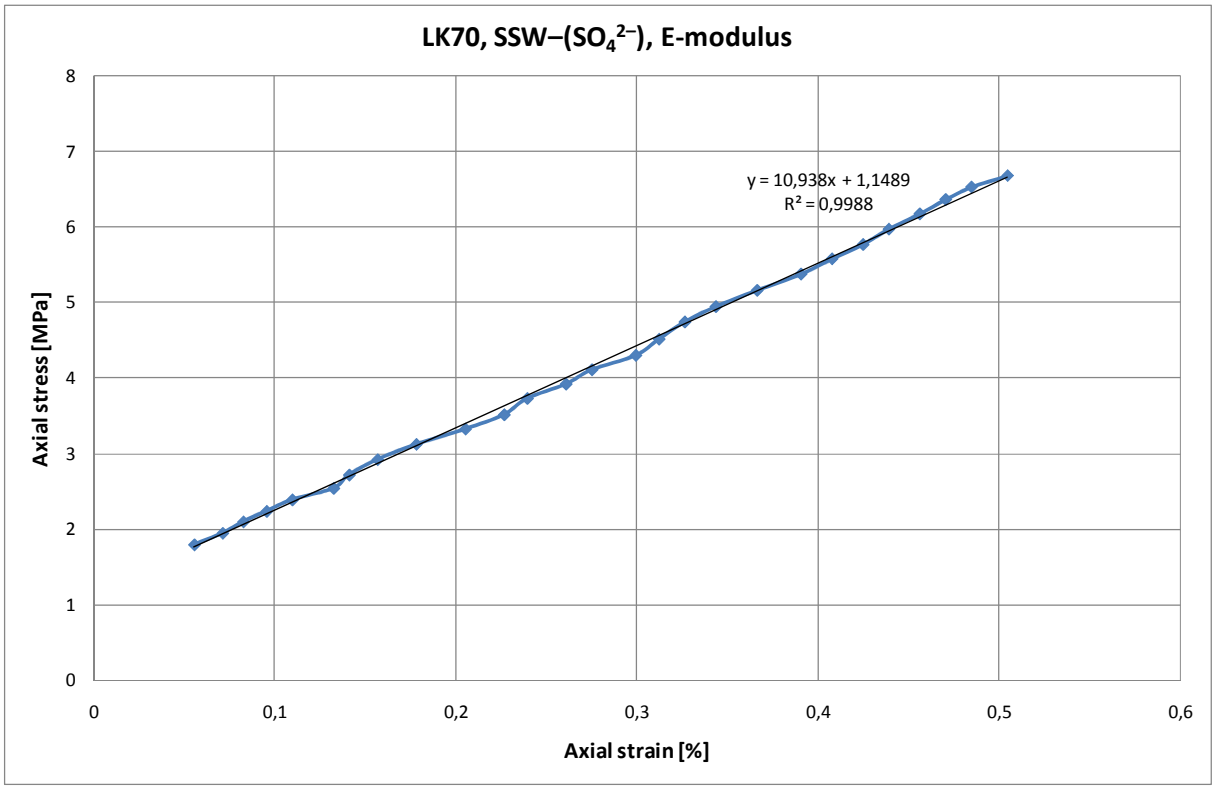


*Fig.B.28: Section of the Axial stress versus Axial strain plot for the 1.2 MPa deviatoirc test performed on LK57 with SSW-($SO_4^{2-}$) flooding at 130 °C used to estimate the Young's modulus*

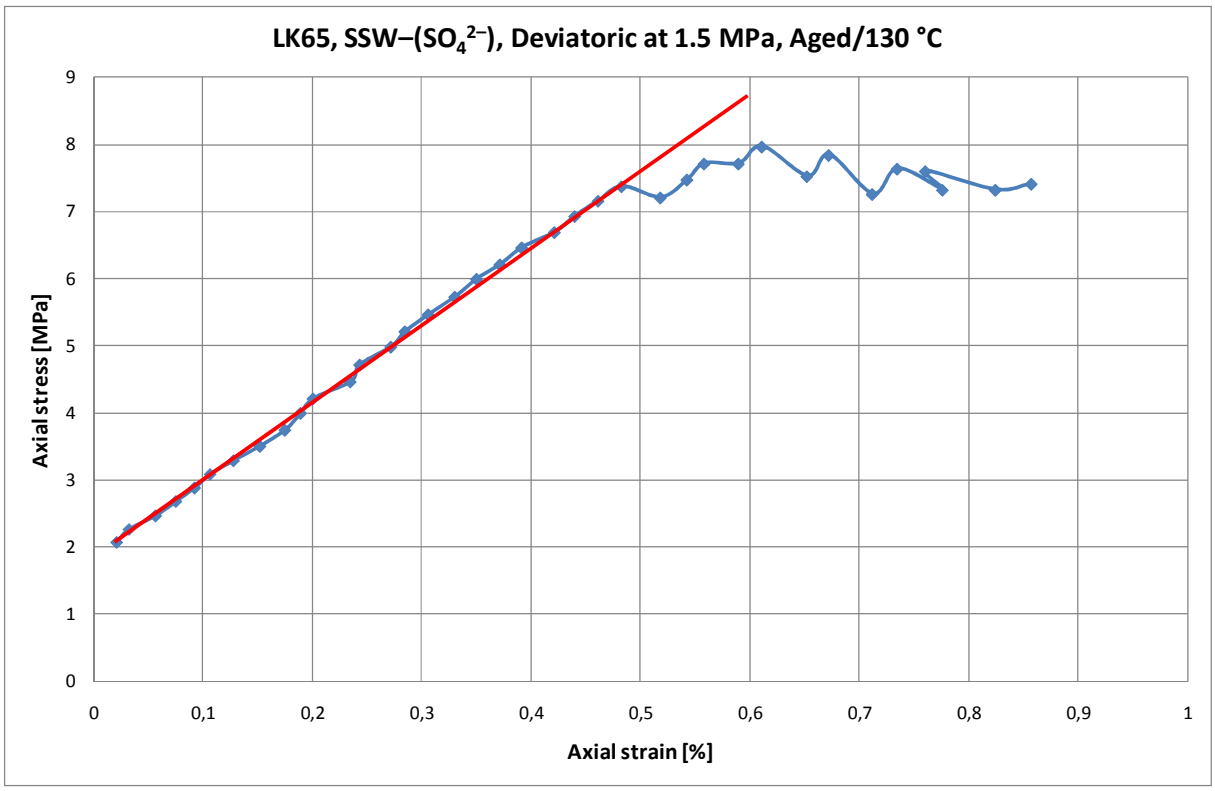


*Fig.B.29: Axial stress versus Axial strain plot for a 1.5 MPa deviatoirc test performed on LK65 with SSW-($SO_4^{2-}$) flooding at 130 °C*

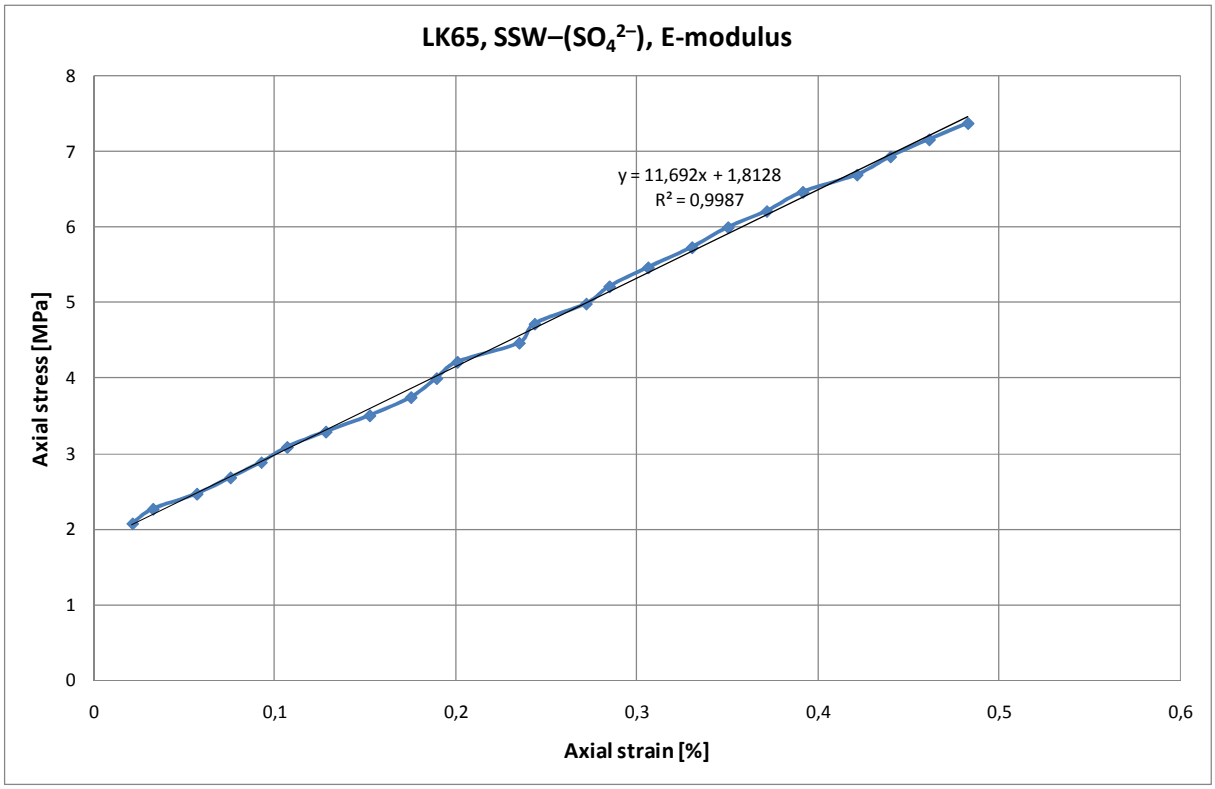


*Fig.B.30: Section of the Axial stress versus Axial strain plot for the 1.5 MPa deviatoirc test performed on LK65 with SSW-($SO_4^{2-}$) flooding at 130 °C used to estimate the Young's modulus*

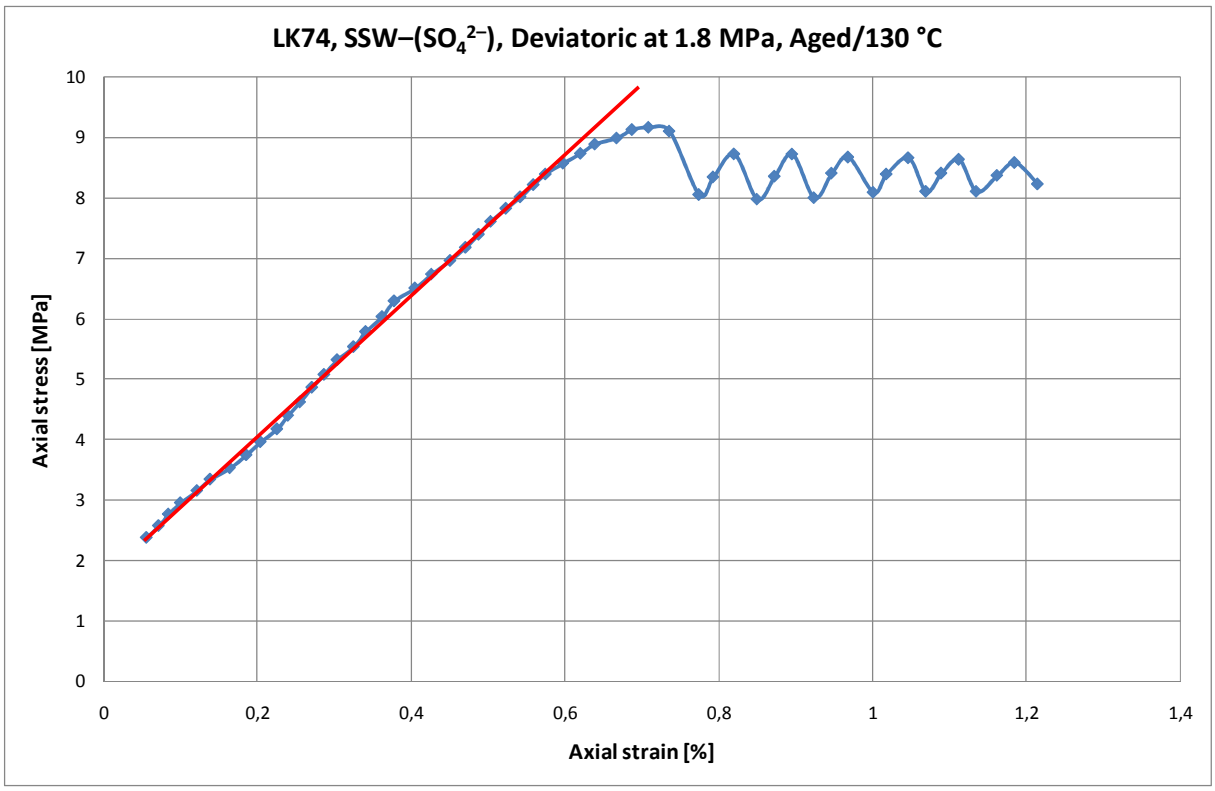


*Fig.B.31: Axial stress versus Axial strain plot for a 1.8 MPa deviatoirc test performed on LK74 with SSW-($SO_4^{2-}$) flooding at 130 °C*

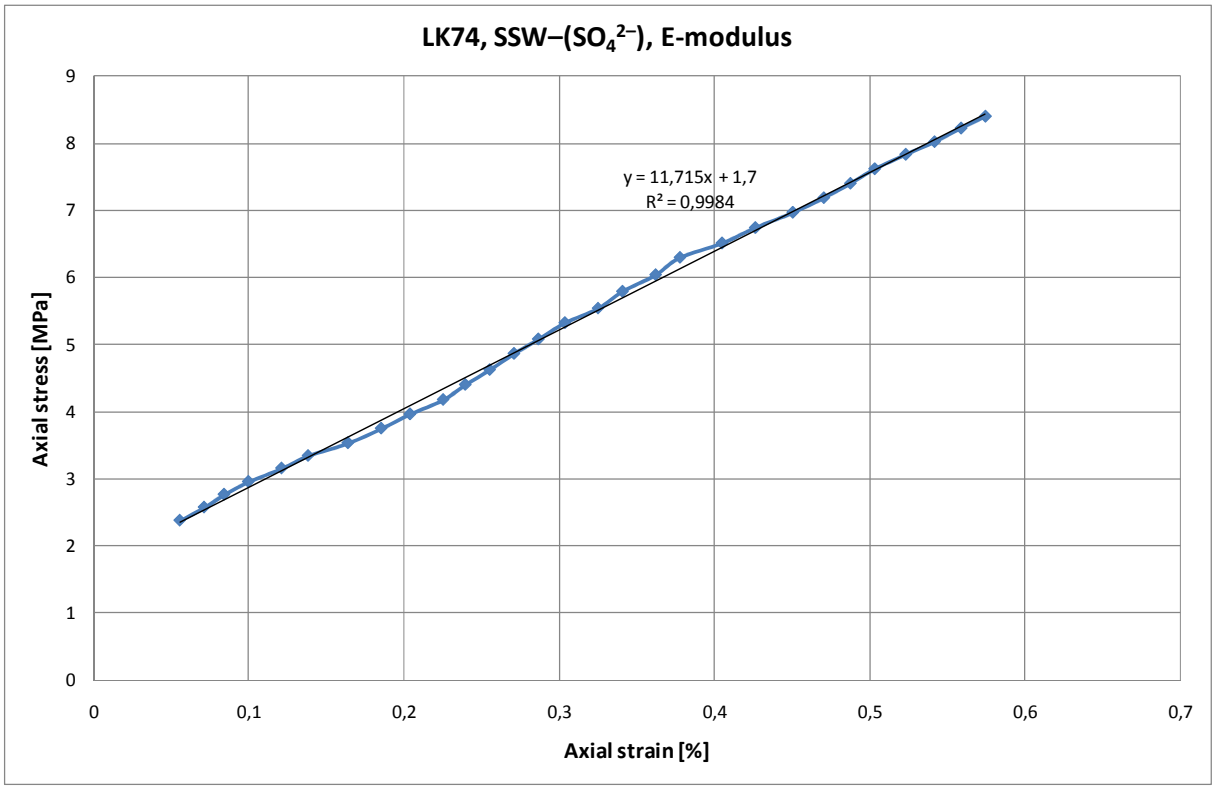


*Fig.B.32: Section of the Axial stress versus Axial strain plot for the 1.8 MPa deviatoirc test performed on LK74 with SSW-($SO_4^{2-}$) flooding at 130 °C used to estimate the Young's modulus*

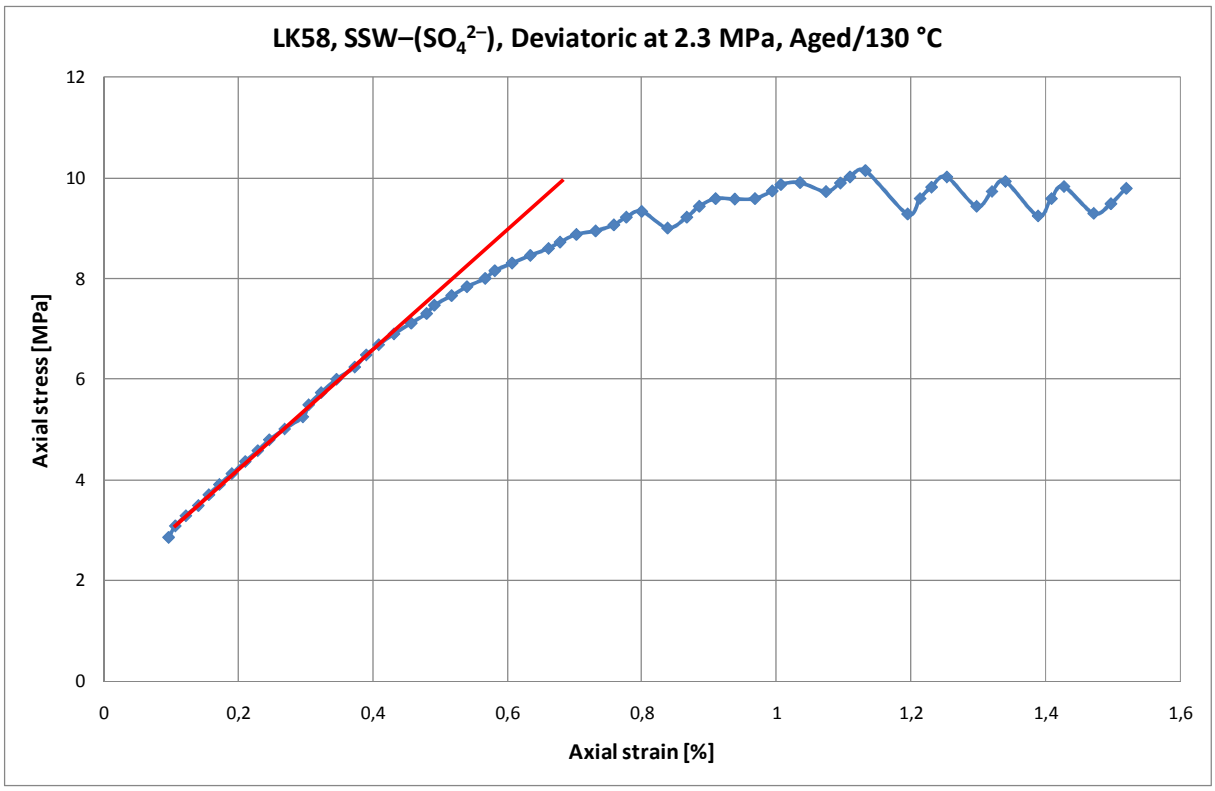


*Fig.B.33: Axial stress versus Axial strain plot for a 2.3 MPa deviatoirc test performed on LK58 with SSW-($SO_4^{2-}$) flooding at 130 °C*

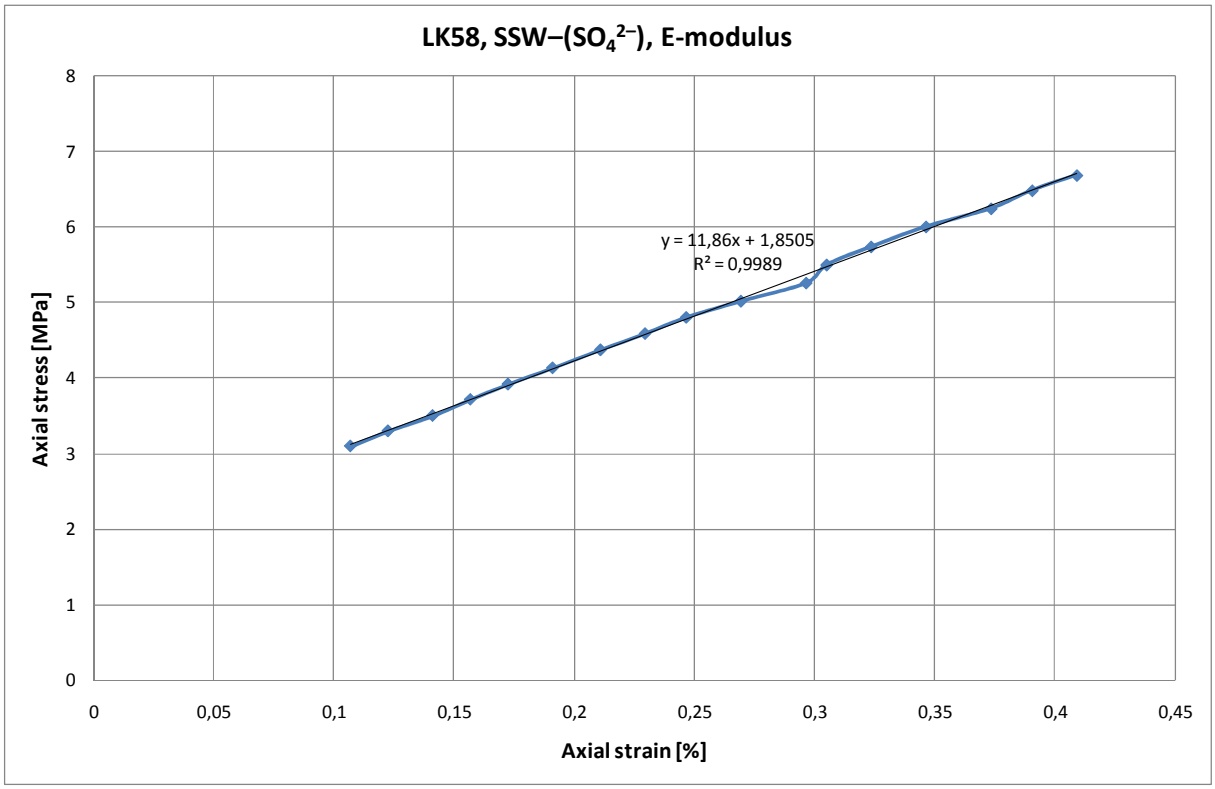


*Fig.B.34: Section of the Axial stress versus Axial strain plot for the 2.3 MPa deviatoirc test performed on LK58 with SSW-($SO_4^{2-}$) flooding at 130 °C used to estimate the Young's modulus*

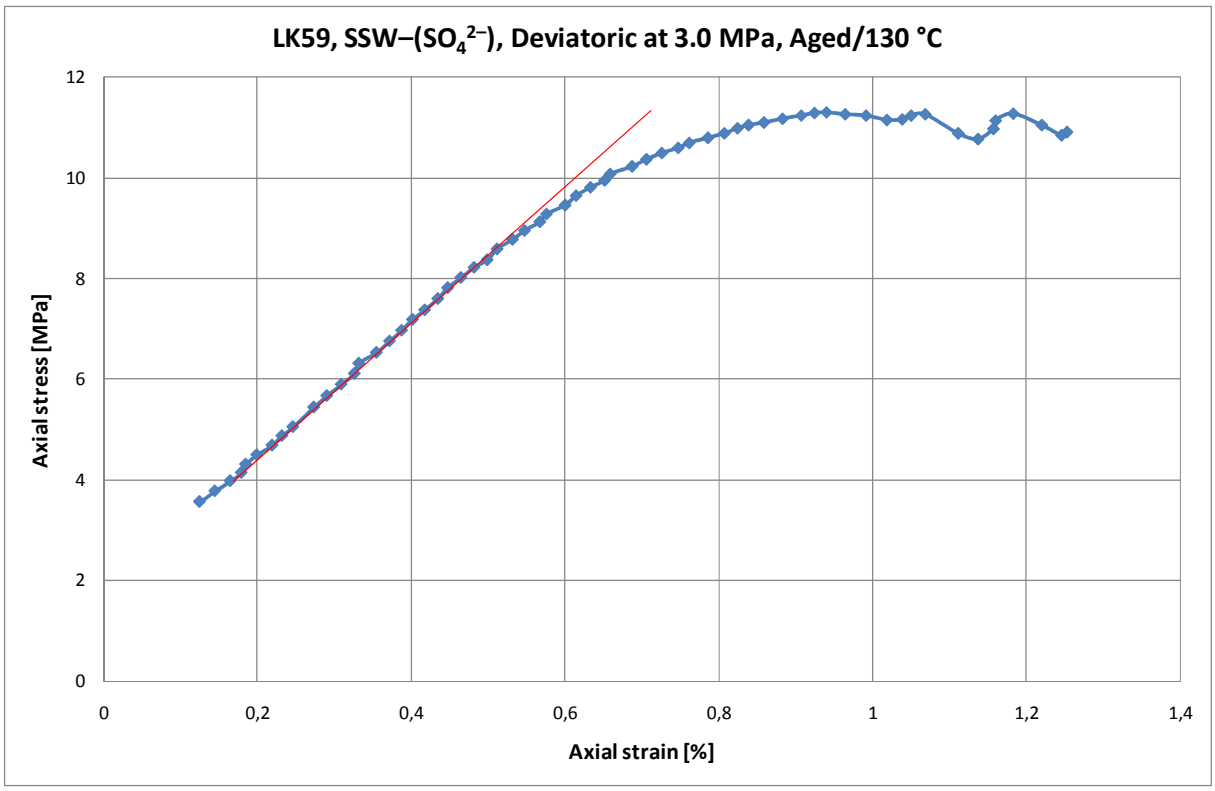


*Fig.B.35: Axial stress versus Axial strain plot for a 3.0 MPa deviatoirc test performed on LK59 with SSW-($SO_4^{2-}$) flooding at 130 °C*

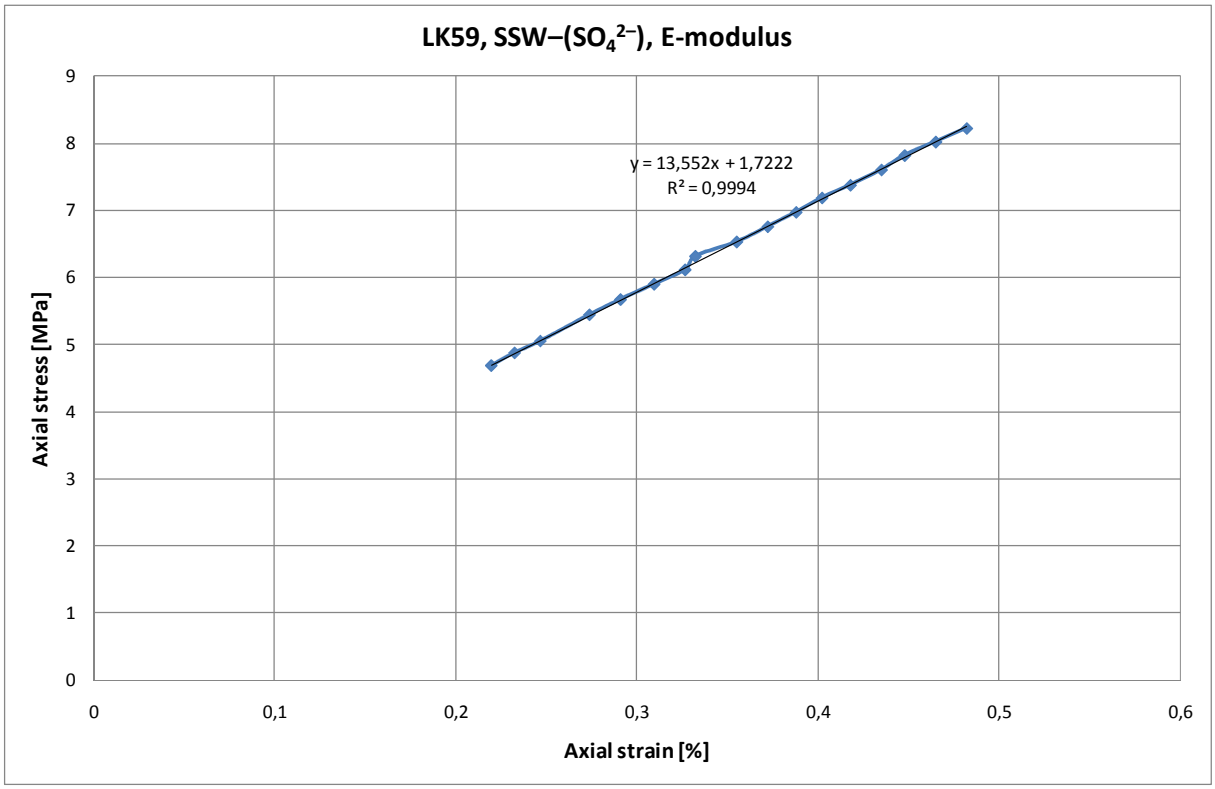


*Fig.B.36: Section of the Axial stress versus Axial strain plot for the 3.0 MPa deviatoirc test performed on LK59 with SSW-($SO_4^{2-}$) flooding at 130 °C used to estimate the Young's modulus*

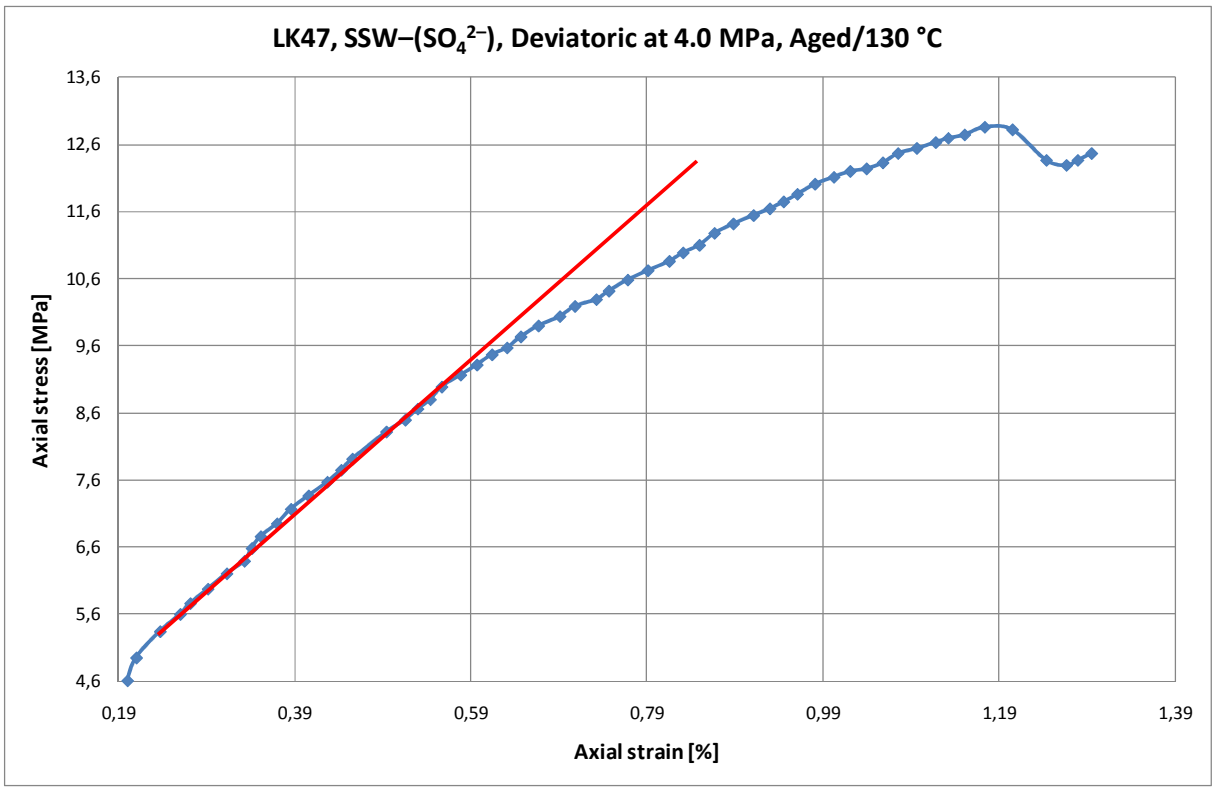


*Fig.B.37: Axial stress versus Axial strain plot for a 4.0 MPa deviatoirc test performed on LK47 with SSW-($SO_4^{2-}$) flooding at 130 °C*

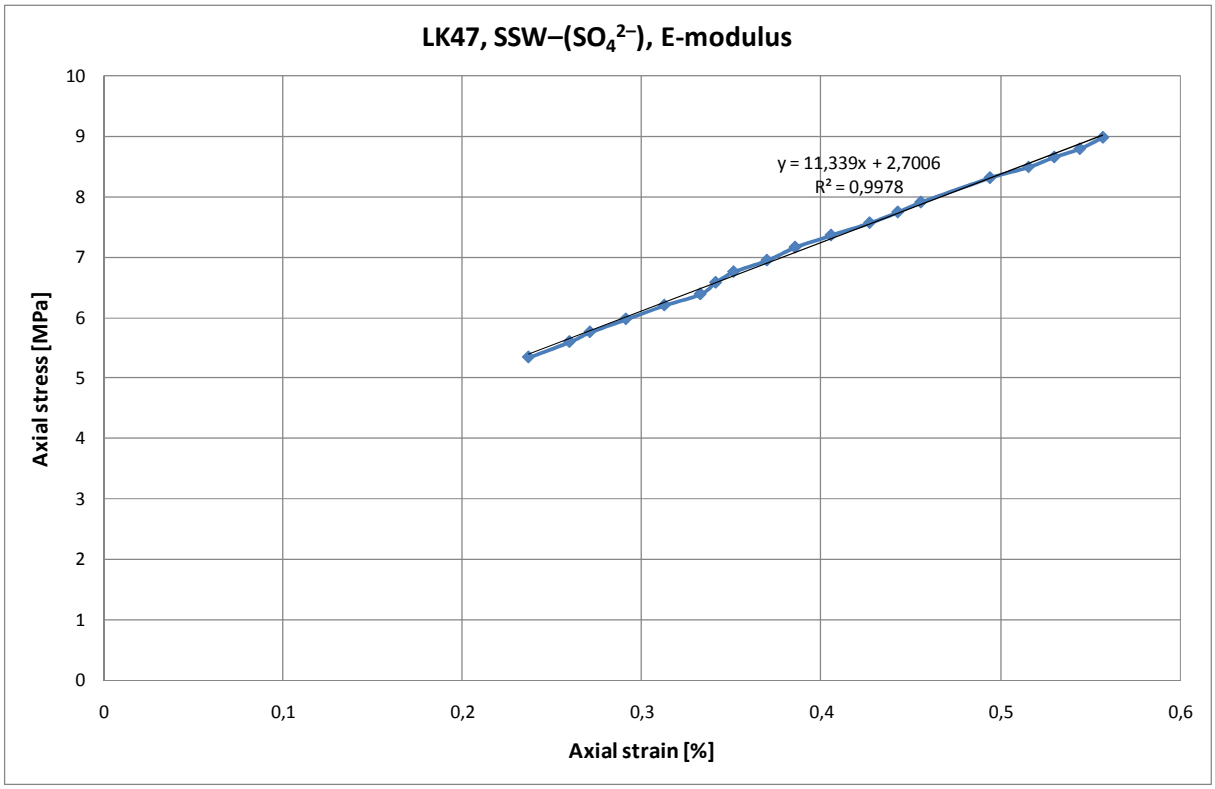


*Fig.B.38: Section of the Axial stress versus Axial strain plot for the 4.0 MPa deviatoirc test performed on LK57 with SSW-($SO_4^{2-}$) flooding at 130 °C used to estimate the Young's modulus*

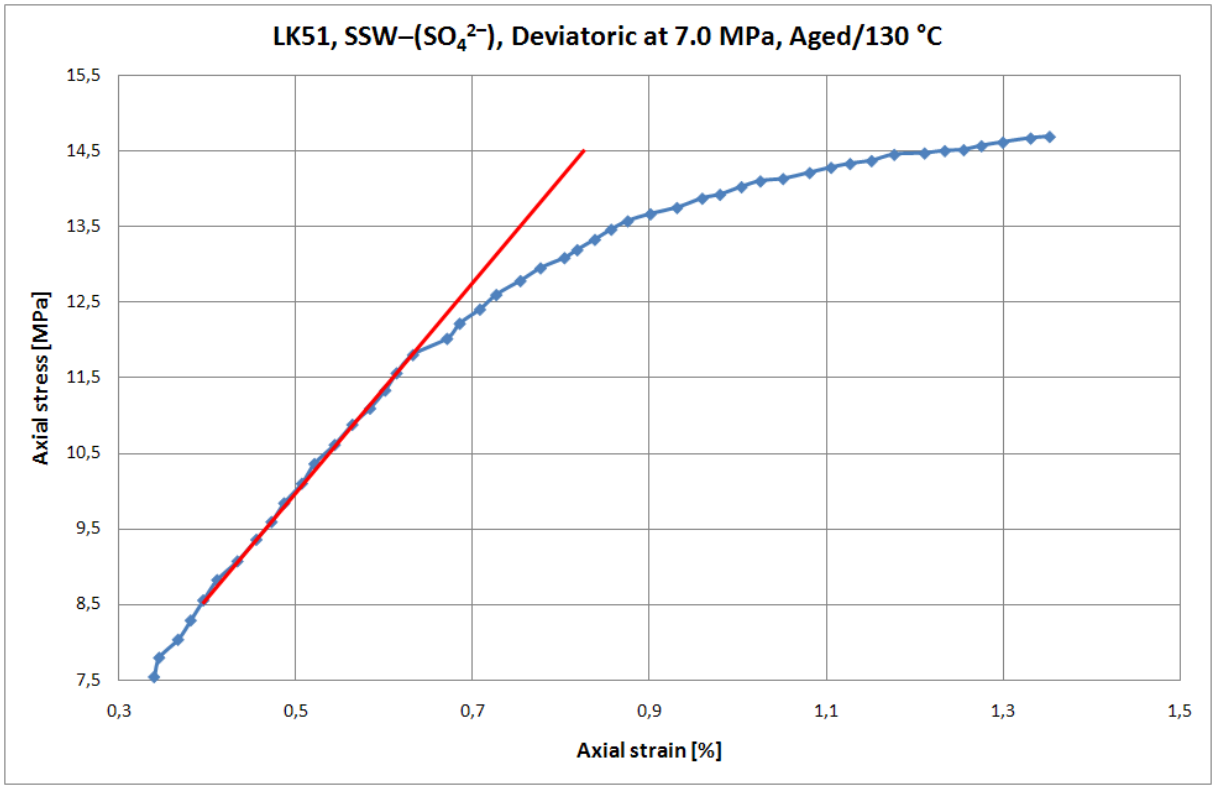


*Fig.B.39: Axial stress versus Axial strain plot for a 7.0 MPa deviatoirc test performed on LK51 with SSW-($SO_4^{2-}$) flooding at 130 °C*

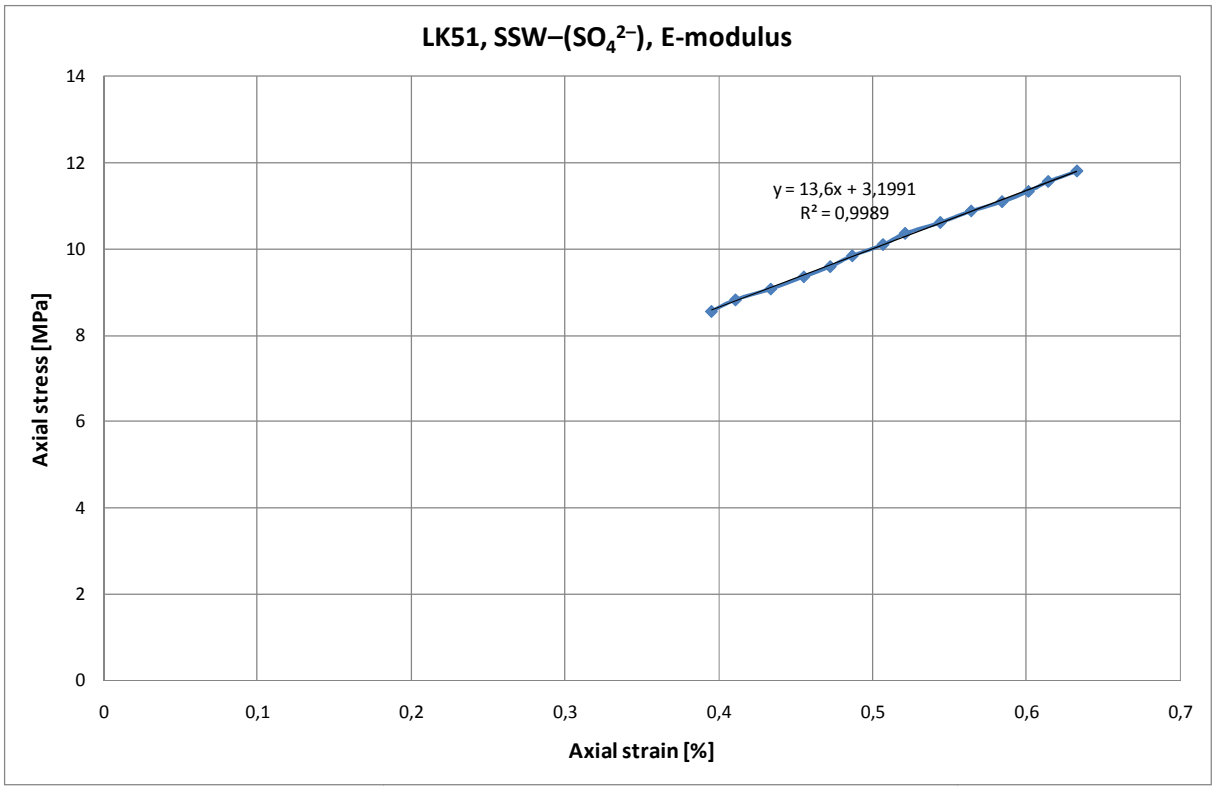


*Fig.B.40: Section of the Axial stress versus Axial strain plot for the 7.0 MPa deviatoirc test performed on LK51 with SSW-($SO_4^{2-}$) flooding at 130 °C used to estimate the Young's modulus*

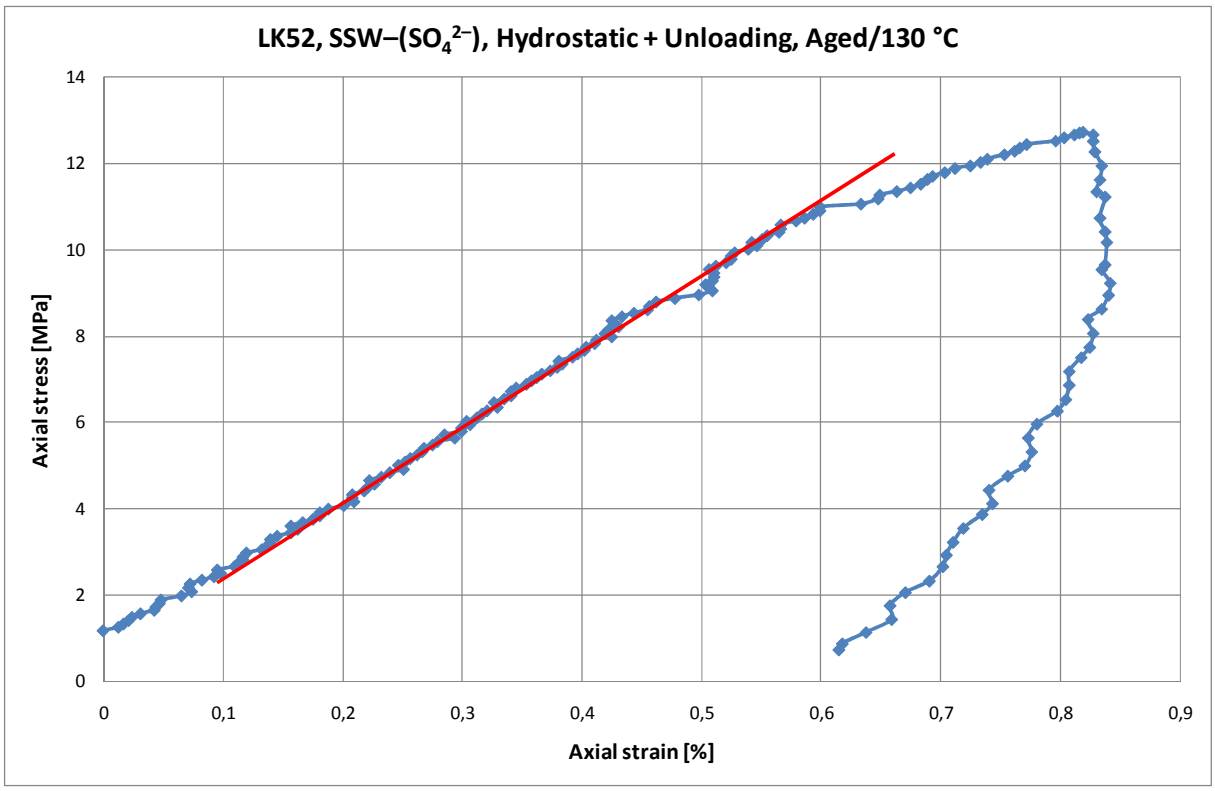


*Fig.B.41: Axial stress versus Axial strain plot for a hydrostatic test performed on LK52 with SSW-($SO_4^{2-}$) flooding at 130 °C*

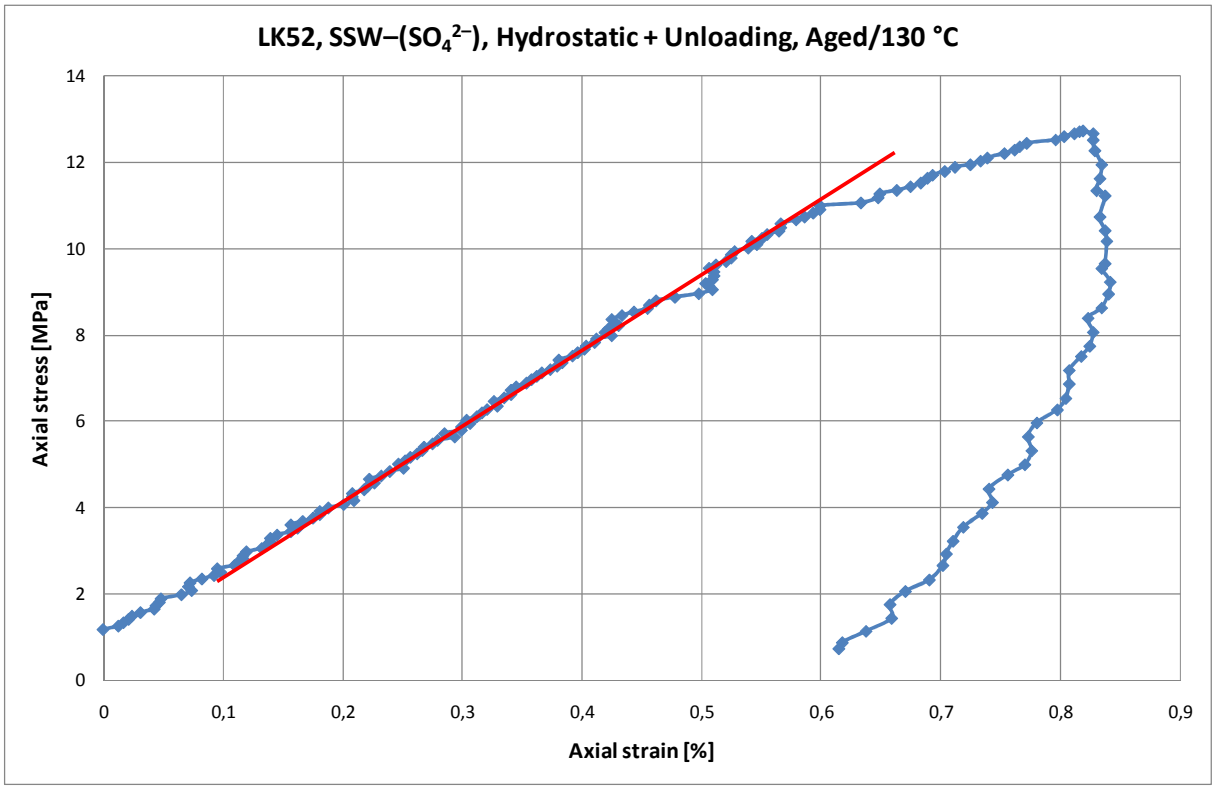


*Fig.B.18: Section of the Axial stress versus Volumetric strain plot the hydrostatic test performed on LK52 with SSW-($SO_4^{2-}$) flooding at 130 °Cused to estimate the Bulk modulus.*